3-2021

Optimizing Design Parameters for Active Flow Control Boundary-Layer Fence Performance Enhancement on a Delta Wing

Nathan L. Tedder

OPTIMIZING DESIGN PARAMETERS FOR ACTIVE FLOW CONTROL BOUNDARY-LAYER FENCE PERFORMANCE ENHANCEMENT ON A DELTA WING

THESIS

Nathan L. Tedder, First Lieutenant, USAF

AFIT-ENY-MS-21-M-322

DEPARTMENT OF THE AIR FORCE
AIR UNIVERSITY

AIR FORCE INSTITUTE OF TECHNOLOGY

Wright-Patterson Air Force Base, Ohio

AFIT-ENY-MS-21-M-322

OPTIMIZING DESIGN PARAMETERS FOR ACTIVE FLOW CONTROL BOUNDARY-LAYER FENCE PERFORMANCE ENHANCEMENT ON A DELTA WING

THESIS

Presented to the Faculty

Department of Aeronatical and Astronautical Engineering

Graduate School of Engineering and Management

Air Force Institute of Technology

Air University

Air Education and Training Command

in Partial Fulfillment of the Requirements for the

Degree of Master of Science in Aeronautical Engineering

Nathan L. Tedder, B.S.

First Lieutenant, USAF

March 2021

AFIT-ENY-MS-21-M-322

OPTIMIZING DESIGN PARAMETERS FOR ACTIVE FLOW CONTROL BOUNDARY-LAYER FENCE PERFORMANCE ENHANCEMENT ON A DELTA WING

THESIS

Nathan L. Tedder, B.S.
First Lieutenant, USAF

Committee Membership:

Michael M. Walker, LtCol, USAF, Ph.D.
Chair

Mark F. Reeder, Ph.D.
Member

Levi M. Thomas, Maj, USAF, Ph.D.
Member

Abstract

Utilizing computational fluid dynamic (CFD) simulations, the presented study is able to further the investigation of replicating and improving upon the performance of a NACA 0012 cropped half-span delta-wing at high angles-of-attack with an active flow control fluidic fence via wall-normal, steady blowing from an optimized single chordwise slot located at $z/b = 70\%$,. The data is generated using CREATE-AV Kestrel v10.1rc5 CFD software on the Department of Defense High Performance Computing systems. The flight regime is held constant at a Mach number of 0.18 and a Reynolds number (Re) of 5.0 x 10^5, based on the root chord. Computational solutions are successfully compared to previously obtained experimental wind tunnel results of three configurations; baseline, passive boundary-layer fence (BLF) and AFC slot of a single momentum coefficients ($C_\mu = 0.49\%$), to validate the CFD model prior to slot optimization. Optimization parameters include five reduced slot widths, five slot velocities and eight slot length. Performance parameters compared for validation and optimization are coefficients of lift, drag and pitching moment at angles-of-attack ranging from 0° to 30°. Surface flow visualization was produced via Tecplot 360 to evaluate unique AFC flow characteristics. AFC slot optimization successfully produce an overall dimension reduction and reduction in momentum input of 33% when compared to the experimental result's highest $C_\mu = 12\%$. With these reductions, the optimal AFC slot configuration yielded a $C_{Lmax,\%Gain} = 41\%$ at $\alpha = 22°$ compared to the baseline configuration. The optimal AFC slot configuration indicate no destabilizing pitching moment present. Visualization of the compared results show that the AFC slot allow for delay in vortex breakdown for some configurations which provide improved vortex generating lift across the wing surface at increasing angles-of-attack.

Dedicated to my devoted wife. I give you all love and thankfulness. Without your continual, never-ending love and support, I would never have been able to accomplish my life goals and aspirations nor be the person I am today.

Acknowledgements

First and foremost, I have to praise God for giving me health, mental fortitude and physical abilities that have propelled me to this moment in life.

To my children, thank you for being the driving force for me to be the best example that I can be for you. Through my accomplishments, I hope you grow to see that with hard work and dedication you can achieve whatever you set your mind to.

To my parents and grandparents, thank you for instilling in me a love for God and family, and an incredible work ethic. I love you.

To my family, thank you for the complete understanding and never ending support given from afar. I cannot express my love for you enough.

To LtCol Michael Walker, Maj Shawn Naigle, AFIT faculty, staff and peers, thank you for sharing your knowledge and providing support throughout this work.

To all those outside of AFIT who provided top notch support, thank you. To name a few: Capt Matthew Clarey (AFRL/XP), Mr. Charles Lynch (CREATE-AV Kestrel) and a huge thanks to Dr. Brent Rankin (AFRL/RQTC), without your generosity, this task would have never been accomplish.

Finally, to Capt Luke Steinberg, thank you for the friendship that we have built and for the daily lunch sessions. Fishing will be lonely!

Nathan L. Tedder

Table of Contents

Page

List of Figures

List of Tables

List of Abbreviations, Acronyms and Symbols

A	wing axial force (Fy)
AR	aspect ratio
A_{slot}	slot area
BR	blowing ratio
C_D	coefficient of drag
C_L	coefficient of lift
C_M	pitching moment coefficient
C_p	compressible pressure distribution
C_{Lmax}	maximum coefficient of lift
C_μ	momentum coefficient
$C_{p,0}$	incompressible pressure distribution
D	drag
L	lift
MAC	mean aerodynamic chord
N	wing normal force (Fx)
PM	wing pitching moment (Mz)
Re	Reynolds number
S	wing planform area
V_∞	freestream velocity
α	angle-of-attack
$\bar{c}$	wing mean chord
β	Prandtl-Glauert Factor
$\dot{V}$	volumetric flow rate
$\dot{m}_{slot}$	slot mass flow rate

ρ_∞	freestream density
b	wing half-span
c	speed of sound
c_{root}	wing root chord
c_{tip}	wingtip chord
y^+	initial cell wall spacing
2D	two-dimensional
3D	three-dimensional
AD	Advective Damping
AFC	active flow control
AMR	adaptive mesh refinement
BC	boundary conditions
BLF	boundary-layer fence
CAD	computer-aided design
CFD	computational fluid dynamics
CREATE-AV	Computational Research Engineering Acquisition Tools and Environments – Air Vehicles
DDES	Delayed-Detached Eddy Simulation
DoD	Department of Defense
ERDC	Engineering Research and Development Center
EX	slot extent (length)
FCV	finite control volume
GPGPU	general-purpose graphic processing unit
GPU	graphic processing unit
HPC	high performance computing
IDDES	Improved Delayed-Detached Eddy Simulation

LES	large eddy simulation
LEV	leading-edge votex
M	Mach
MLA	Machine Learning Accelerator
N-S	Navier-Stokes
NACA	National Advisory Committee for Aeronautics
PFLOPS	peta (10^{15}) floating points operations per second
PIV	particle image velocimetry
RANS	Reynolds Averaged Navier-Stokes
RC	rotation correction
RCS	radar cross sections
S-A	Spalart-Allmaras
std	standard deviation
SW	slot width
TS	Time Step
UG	User's Guide

OPTIMIZING DESIGN PARAMETERS FOR ACTIVE FLOW CONTROL
BOUNDARY-LAYER FENCE PERFORMANCE ENHANCEMENT
ON A DELTA WING

I. Introduction

1.1 Background and Motivation

When considering the lifting body geometry of a majority of modern fighter, low observable aircraft and blended wing body concepts, research on improved delta-wing aircraft performance characteristics is of significant interest. Particularly, addressing high angle-of-attack flow separation which leads to wing stall and/or reduced aerodynamic performance envelopes. A variety of flow control strategies have been devised in an attempt to postpone stall, improve lift performance and reduce undesirable moment characteristics.

Expanding in delta-wing performance envelopes without the use of geometric modifications that protrude into the airflow (avoiding creating increased radar cross sections (RCS) and drag) would be optimal. Initially, passive flow control methods such as winglets, boundary-layer trips and wing fences [1] were found to be effective at delaying flow separation within certain conditions and provide insight into swept wing stall reduction. Development of active flow control (AFC) strategies, such as fluidic oscillators [2], pulsed jets [3] and fluidic fences [4] provide similar performance enhancements with the ability to activate as needed while avoiding the undesired effects that geometry modifications create. However, additional energy expenditures are necessary for AFC operation, meaning the benefit must outweigh the cost.

Future development of modern aircraft tends to avoid performance enhancement solutions that would detract from stealth capabilities, specifically increased RCS, or contribute to unnecessary drag, especially above sonic speeds. Fortunately, the use of AFC techniques to replicate performance enhancements of passive flow control methods satisfy the requirements of future modern aircraft and provides a solution for flow separation leading to wing stall and undesirable moment characteristics. With the potential for an overall increase in performance at extreme flight envelopes, this development expands the trade space for future delta-wing configuration development.

1.2 Problem Statement

The focus of the presented study is to further the investigation of replication and enhancement of a National Advisory Committee for Aeronautics (NACA) 0012 cropped delta-wing performance at high angles-of-attack using an active flow control wall-normal, steady blowing, fluidic fence from a single slot. Through the use of computational fluid dynamics (CFD) tools, fluidic performance solutions will be compared and validated against previously obtained experimental wind tunnel results. Furthermore, the study seeks to optimize the AFC slot configuration by maximizing AFC performance gains while minimizing required energy input.

1.3 Methodology

Gathering data regarding the effects of high angle-of-attack (α) on any operational air asset in real-world scenarios is a challenging process. Testing within an airframe's stall region at low speeds can also prove to be potentially dangerous. However, CFD allows for these high-risk scenarios to be modeled and investigated without the risk and cost associated with experimental testing.

The CFD simulations used in this study were solved with the Computational

Research Engineering Acquisition Tools and Environments – Air Vehicles (CREATE-AV) software Kestrel v10.4rc5 and computed on the U.S. Army Engineering Research and Development Center (ERDC) high performance computing (HPC) systems. This software is widely used by the Department of Defense (DoD) aerospace community to generate data for various fixed wing aircraft scenarios. The wide range of uses and recommendations provide heightened level of confidence in the accuracy of results and robustness of the solver [5, 6]. The software also allows for the use of adaptive mesh refinement (AMR) which allows Kestrel to refine and coarsen the computational grid as necessary for more accurate distribution of computational resources as prescribed by the user.

Three configurations, based upon previous studies, will be modeled and compared to wind-tunnel performance results under similar conditions to determine CFD model accuracy. These configurations will all be based on a NACA 0012 cropped delta-wing with performance results attained from Demoret et al. for a baseline control, passive boundary-layer fence and an AFC fluidic fence. Furthermore, the AFC fluidic fence slot will be optimized under those same flow conditions. Performance characteristics will be quantified as changes in global forces and moments (specifically lift, drag and pitch). A more detailed discussion of the methodology can be found in Chapter III.

1.4 Assumptions and Limitations

This investigation focuses on the ability of an AFC fluidic fence to improve performance of a delta wing. Limited AFC research has been accomplished with respect to swept wings and delta wings. Thus, the focus of the investigation centers around proof of concept and negates application and operational recommendation of the technology implementation.

The original experiment involved an internal chamber being filled from an external

pressurized air source and did not examine the feasibility of including a fluidic fence into a standard wing structure nor the air source within an operational aircraft (bleed air from the engine, ect.). Additionally, the study does not include details regarding how a fluidic fence would integrate into the stability and control system of the aircraft.

This investigation looks to utilize Demoret et al.'s delta-wing experimental results. For this reason, the same configuration was modeled with a relatively thick airfoil that may not directly be applicable to fourth- and fifth-generation delta-wing fighter aircraft. Additionally, the dimensions of the model and free-stream velocity corresponded to a Reynolds number of 5.0×10^5, while an fourth- and fifth-generation high-speed flight envelopes reach Reynolds numbers on the order of 10^8.

II. Literature Review

2.1 Wing Theory

2.1.1 Straight Wing

While considering a symmetric airfoil configured as a straight wing at low speed, lift is generated as angle-of-attack increases due to a pressure differential between the low-pressure upper and high-pressure lower surfaces. The majority of lift is generated over the upper first third of the airfoil section, traveling from leading to trailing edge, with the development of a low pressure region known as a suction peak [7]. The suction peak generally aligns with the angle of the leading-edge sweep as seen in Figure 1. For straight wings, airflow typically travels parallel to the chord or perpendicular to the leading edge due to no leading-edge sweep [8]. The flow for a high aspect ratio straight wing, flow can be considered quasi two-dimensional (2D), where separation and at some point stall generally begins near the trailing edge and propagates toward the leading edge in a uniform manner relative to spanwise location [9].

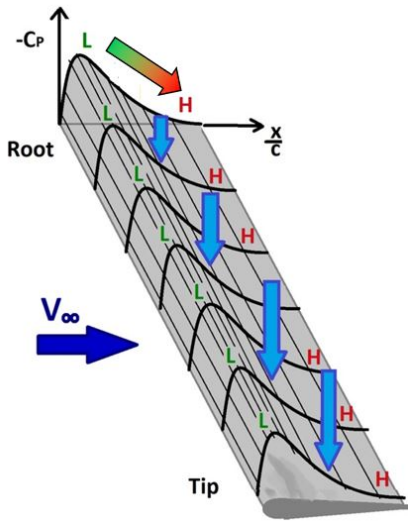

Figure 1. Suction Peak Example [9]

2.1.2 Swept Wing

Likewise, a symmetric airfoil configuration as a swept wing at low speed compares to the straight wing with suction peaks aligning with the leading-edge sweep. However, the outboard neighboring suction peak, moving from root chord to tip, is offset aft. The low-pressure suction peak now aligns with an inboard high-pressure region which develops an outboard, spanwise flow that increases in momentum as the flow moves toward the wing tip and trailing edge. Just as swept-wing theory suggested, streamwise velocity components can now be divided into components normal and parallel to the leading edge[10]. Generally, at increased angles-of-attack, the spanwise component of the flow increases while lift generated by the wing is decreased [11]. Ultimately, a non-uniform separation and wing stall generates, beginning at the wingtip and propagates inboard 3-dimensionally, due to the introduction of the crossflow component. Furthermore, as angle-of-attack increases and separation and stall propagation develop, a non-uniform lift distribution occurs along the wing creating a complex pitching moment. The introduction of an abrupt loss of lift at the wing tip can cause a shift in the aerodynamic center, which if considerable, can cause substantial instability of the wing.

2.1.3 Delta Wing

Further development of the swept rectangular wing brought about the delta wing; a triangular planform area swept wing with a large root chord. Similar to swept rectangular wings, separation and stall propagation occurs at the wingtip and propagates inboard beginning at the trailing edge, creeping toward the leading edge [9]. However, highly-swept delta wings ($\Lambda > 45°$), at increasing angles-of-attack, develop a leading-edge votex (LEV) [12]. The steep sweep of the delta-wing allows high-pressure air to rotate around the leading edge and interact with the adjacent suction peak which

creates a high-energy vortical motion of the air along the upper surface of the wing seen in Figure 2. Overall lift is increased as a result of vortex lift generation, seen in Figure 3. The result is a nonlinear lift curve, which is a result of a reduced upper surface pressure aft of the leading edge due to the vortex's low static pressure [13].

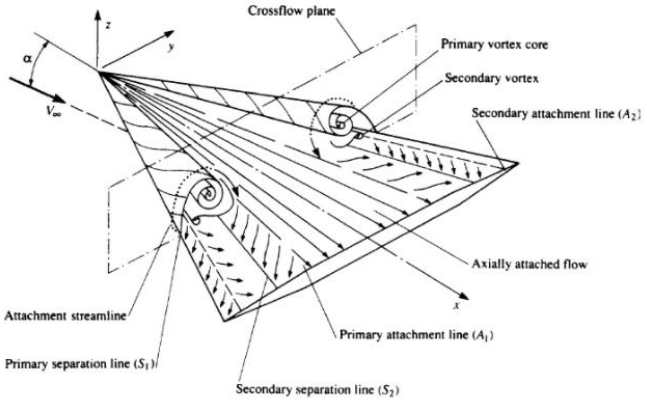

Figure 2. Subsonic Delta-Wing Flow Field [14]

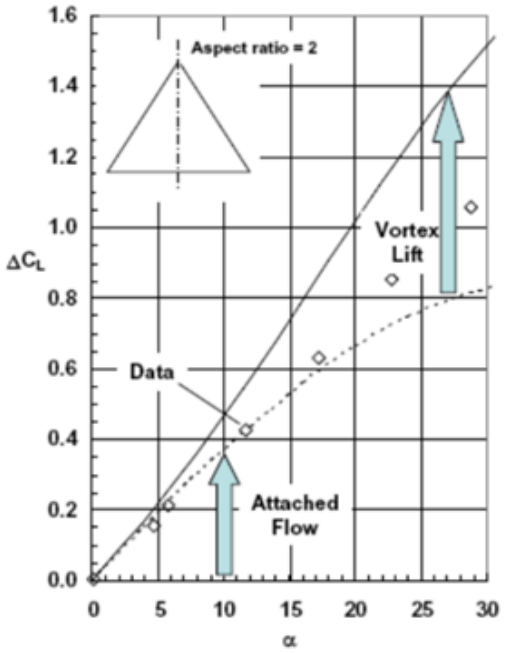

Figure 3. Blunt Delta-Wing Lift-Curve Characteristics (AR = 2) [12]

Vortex flow solution and propagation, along with lift dependence, has been demon-

strated to be a function of both α and Λ as depicted in Figure 4 [14, 15]. This relationship and prediction shows that the vortex flow features can be tracked and accurately related to prior results. Additionally, it can be used for computational model validation through visualization of the vortex core and comparison to these expected results. As delta-wing angle-of-attack increases, LEVs lose momentum,

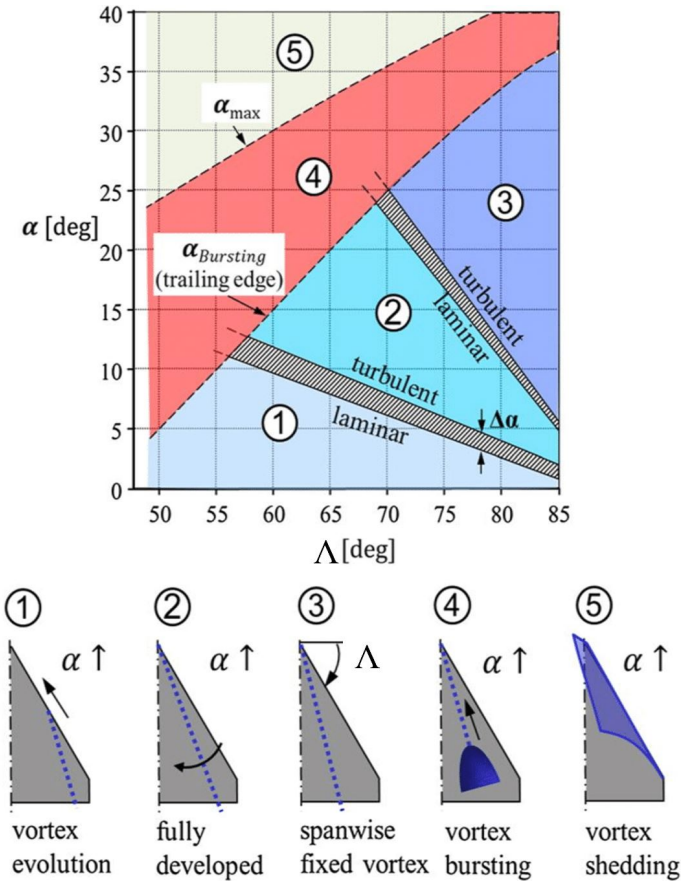

Figure 4. Delta-Wing Vortex Stages: Wing Sweep (Λ) vs Angle-of-Attack (α) [14]

separate from the surface and break down. The performance gains are lost resulting in overall loss of lift and unsteady spanwise flow developing across the wing surface, as described previously during swept-wing separation and stall propagation. Spanwise flow moving across a vortex was theorized to reduce vortex core energy leading to the breakdown of the LEV and successive stall of the delta wing [16]. During stall of a delta wing, the aerodynamic center of the wing is shifted forward, similar to a straight

wing. However, delta-wing configurations center of gravity generally lay further aft on the body due to the increased mass associated with the triangular geometry. With this sudden forward shift of the aerodynamic center due to stall, the wing becomes statically unstable as seen in Figure 5. This condition produces destabilizing control characteristic resulting in a drastic pitch up motion at an already high angle-of-attack, unlike straight-wing and most swept-wing configurations which experiencing a pitch down characteristic during stall. This condition occurring at low altitude and at low velocities has resulted in unrecoverable, catastrophic events. For this reason, delta-wing configurations avoid low-speed, high angle-of-attack conditions and have detracted from delta-wing use in large body aircraft.

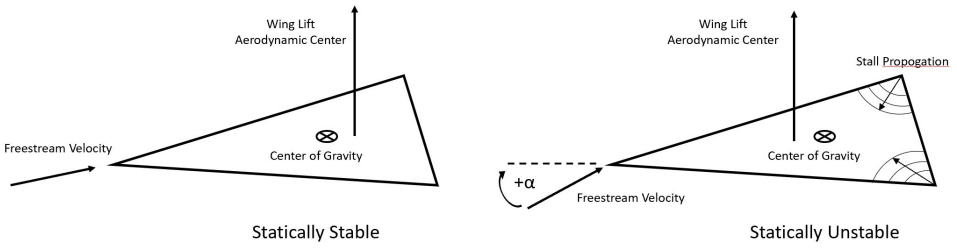

Figure 5. Delta-Wing Static Stability

Many modern platforms, the F-22, F-35 and the J-20 fifth-generation fighter aircraft, use cropped delta-wings with forward-swept trailing edges with sweep angles between 34° and 47° [17]. Therefore, the present study chose a moderate 45° sweep delta wing to mimic current modern airframes. Unlike high-swept delta wings, which produce higher energy LEV, the 45° sweep delta wing is anticipated to produce lower energy LEV with performance results comparable to prior swept-wing studies.

2.2 Flow Control

The practice of manipulating airflow over an aerodynamic body in an attempt to positively impact designated performance characteristics is generally characterized as aerodynamic flow control. This control can be implemented either passively, with geometric modifications to the wing, or actively with fluidic actuators that add momentum, generally quantified as a nondimensional momentum coefficient (C_μ), or energy to the flow through entrainment.

2.2.1 Passive Flow Control

Aerodynamic improvement by means of passive, or physical mechanisms, was the initial solution to halt or redirect crossflow over a swept-wing geometry. The passive boundary-layer fence (BLF), a flat plate fixed vertically to the upper surface of the wing, attempts to allow areas of the wing outboard of the fence to regain streamwise flow, thus creating lift and preventing stall as illustrated in Figure 6. The passive BLF was initially used in 1938 by Wolfgang Liebe and has been utilized for many years on various US and forgein military aircraft: the Convair F-102 Delta Dagger, the Mikoyan-Gurevich MiG-15, the Mikoyan-Gurevich MiG-17, the Sukhoi Su-17 and the Russian OKB-1 150 bomber [18]. Through experimental research and real-world application, certain passive BLF characteristics have proven to be more productive than others. Attributes documented (negative and positive) include effects related to height of the boundary-layer fence relative to the actual boundary-layer thickness and increased performance relative to chordwise fence placement. Furthermore, optimal spanwise location for a single wing fence was found to be between $z/b = 0.5$ and 0.8 with multiple BLFs out-performing single fences configurations [19, 1, 20, 18].

Salmi's study of a NACA 63_1-A012 swept wing ($AR = 8$, $\lambda = 0.45$, $\Lambda = 45°$, 2b = 29 in) in a 19 ft wind tunnel at a Reynolds number of 6.0 x 10^6 detail the benefits

Figure 6. Mig-15 Passive Boundary-Layer Fences [21]

of passive BLFs related to stall propagation [1]. Salmi's baseline wing and passive BLF configurations, shown in Figure 7, at an $\alpha = 26°$ and 29° respectively depict stall by hash marks and location of the passive fence (highlighted in blue). Analysis of the wing surface reveal the effects of the passive system which allowed continued lift generation outboard of the fence versus the baseline being stalled. Salmi further indicated the most effective passive BLF location, with restrictions, to be between z/b = 0.50 and 0.80 [1].

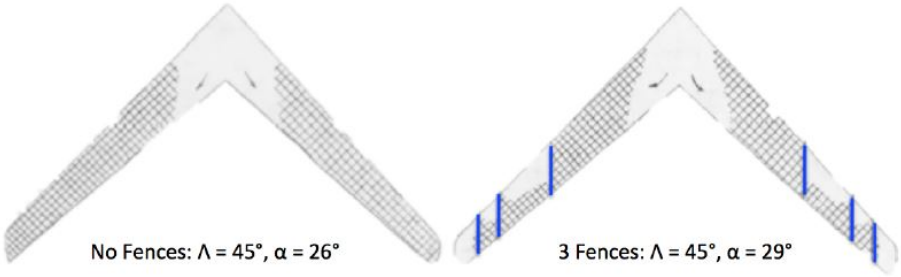

Figure 7. Swept-Wing Passive Flow Control Stall Propagation [1]

Pratt and Shields published a 1952 NACA study considered assorted passive flow control devices on a 45° swept wing, seen in Figure 8. Analysis of fence location and BLF configurations of length and height revealed varying performance gains dependent on configuration. Performance gains varied from the baseline configuration

with a 5.9% increase in C_{Lmax} at a location of $z/b = 0.575$ with a partial fence that does not wrap around the leading edge and has moderate height, to a 28.7% increase in C_{Lmax} at a location of $z/b = 0.575$ with a moderate height, leading edge wrapped BLF. These passive flow control methods producing greater performance gains when the fence continues around the leading edge to the bottom surface of the wing. Furthermore, increased gains were also determined to increase as the fence spanned the entire streamwise length of the upper surface [20].

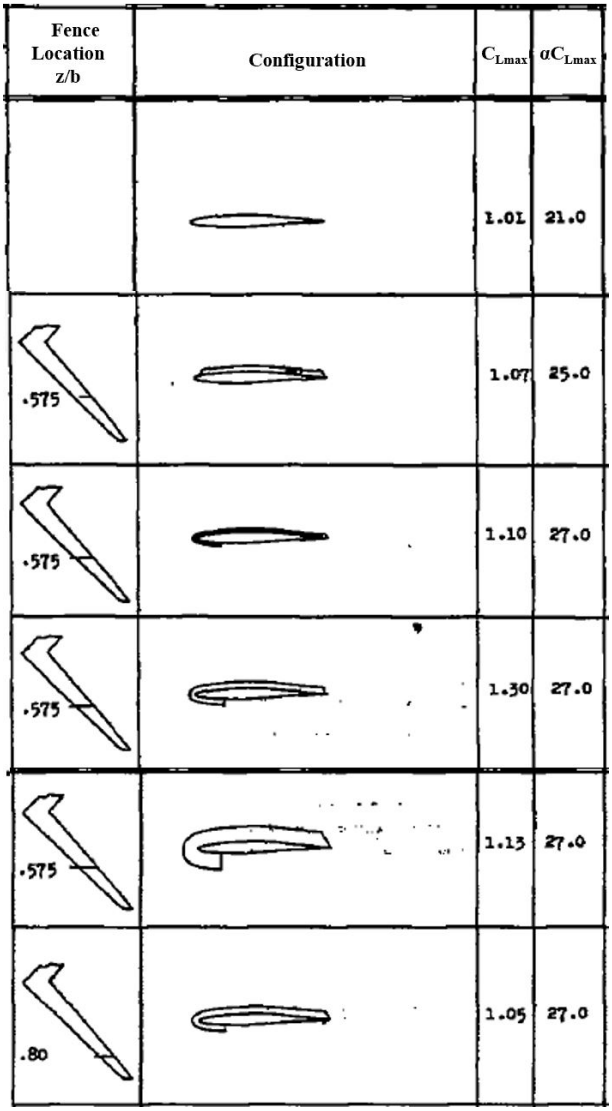

Figure 8. Low-Speed Flow Control Characteristics on a 45° Sweptback Wing (AR = 8) [20]

Demoret et al.'s study of the passive BLF on a cropped NACA 0012 delta-wing with the fence located at a spanwise position of 0.7 z/b and beginning at 0.25 x/c on the high-pressure surface which then wrapped the leading edge to extend the entire streamwise length of the low-pressure surface. This configuration resulted in an 8.7% increase in C_{Lmax} as compared to the baseline wing, pictured in Figure 9. Also, no destabilizing pitching moment characteristics was produced and no significant change in stall angle-of-attack was reported [22].

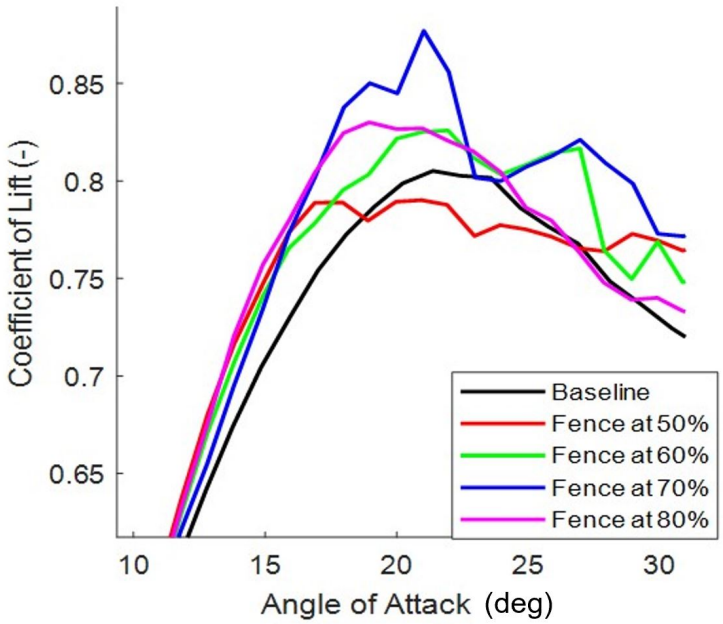

Figure 9. Demoret NACA 0012 Cropped Delta-Wing Passive Boundary-Layer Fence C_L Results [22]

Physical fences, in most cases, are not retractable and are a permanent fixture through all phases of flight. This is a particular issue for many aircraft during cruise when drag penalties due to physical outcroppings diminish flight efficiency. Furthermore, with the requirement for a minimized RCS signature requirement on military low observable aircraft, passive fences are not considered viable solutions for wing performance increase.

2.2.2 Active Flow Control

With the application of current knowledge related to swept-wing fluid interaction and passive flow control methods, application of active flow control (AFC) to swept wing geometries was believed as the next step in swept-wing performance improvement. The majority of AFC research centers around straight-wing planforms with recent studies involving swept-wing geometries. Tewes, Greenblatt, Walker and Demoret all document significant performance enhancement with various AFC methods when applied to swept wings, specifically at increased angles-of-attack [11, 23, 9, 22].

Various oscillatory flow research was conducted by both Seifert, in 2008 and Tewes, in 2014. Both studies investigated both straight- and swept-wing interactions with similar conclusions being formulated. Seifert inferred that oscillatory blowing was able to delay stall on a swept wing more effectively than steady blowing and the location of the momentum injection was significant to reduction of the separation bubble [24, 25, 26]. Tewes utilized fluidic oscillators (Figure 10) at a location of $x/c = 70\%$ on the trailing edge of a NACA 0012 flapped wing. Tewes reported the actuators behaved similar to fluidic fences by reducing the spanwise flow through partial or full flow re-orientation. Furthermore, he suggested momentum added to the flow by the actuators behave similar to vortex generators that bring about counter rotating streamwise vorticity that energizes the boundary-layer and thus allowing flow to remain attached and producing lift [11].

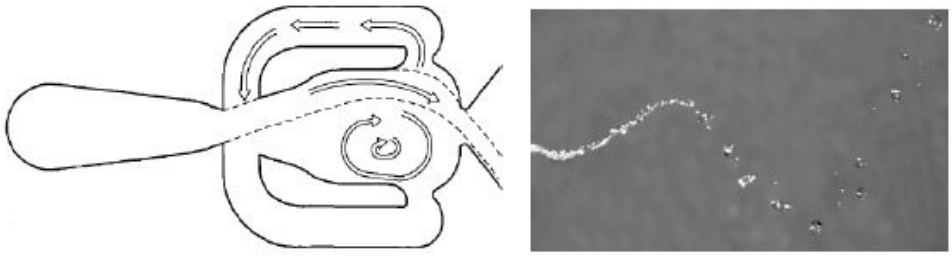

Figure 10. Fluidic Oscillator Function [11]

Additionally, Greenblatt et al.'s study demonstrated the effectiveness of AFC in 3D flows. Specifically the study focused on low aspect ratio (AR) swept wings blowing slot application producing parallel flow relative to the leading edge, illustrated in Figure 11, for separation control within the post-stall flight domain. The product of the research revealed an increase in C_{Lmax} and continued lift being generated after stall. Furthermore, the study deducted that the slot re-energized the leading-edge vortex which contributed to the performance gains mentioned [23].

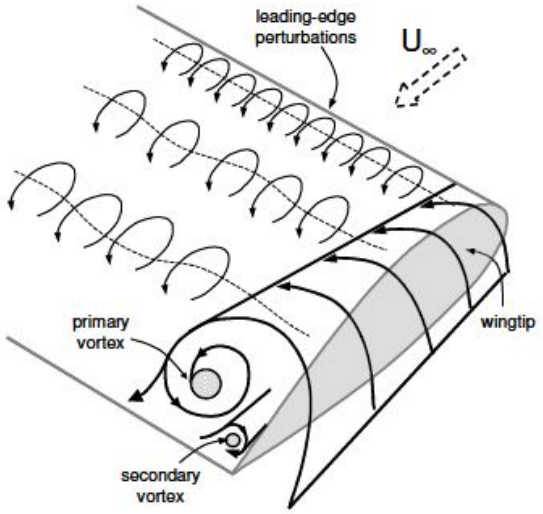

Figure 11. 2D Leading-Edge Perturbation Separation Control [23]

The most applicable research related to the current investigation was documented by Walker et al., in 2018 and Demoret et al., in 2020. Walker et al. applied a wall-normal constant blowing velocity AFC slot configuration to a NACA 64_3-618 baseline swept wing ($\Lambda = 30°, \lambda = 4.3$) at $Re = 1.0\text{x}10^5$. The AFC slot configurations, pictured in Figure 12, was a direct replacement for a passive BLF located at 0.7 z/b runs streamwise from 0.25 x/c_{eff} on the high pressure side of the wing to 0.75 x/c_{eff} on the low pressure side at a width of 0.4 mm. Shown in Figure 13, the study revealed a 12.8% gain in ΔC_{Lmax} for the AFC slot at an isentropic blowing ratio (BR) of 4 ($C_\mu = 11.08\%$), shown in Equation 1, versus 14.3% gain for the passive fence that

spanned to an additional 0.25 x/c_{eff} along the low pressure side of the wing [9].

$$BR = \frac{U_{slot,avg}}{U_{edge}} \tag{1}$$

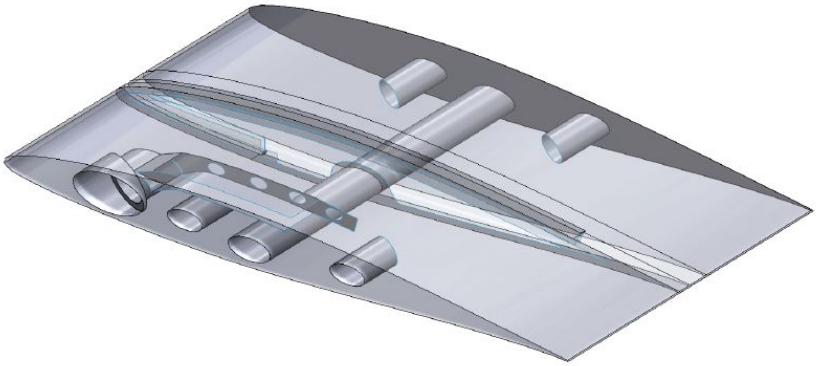

Figure 12. Walker NACA 64_3-618 30° Swept-Wing AFC Slot Geometry [4]

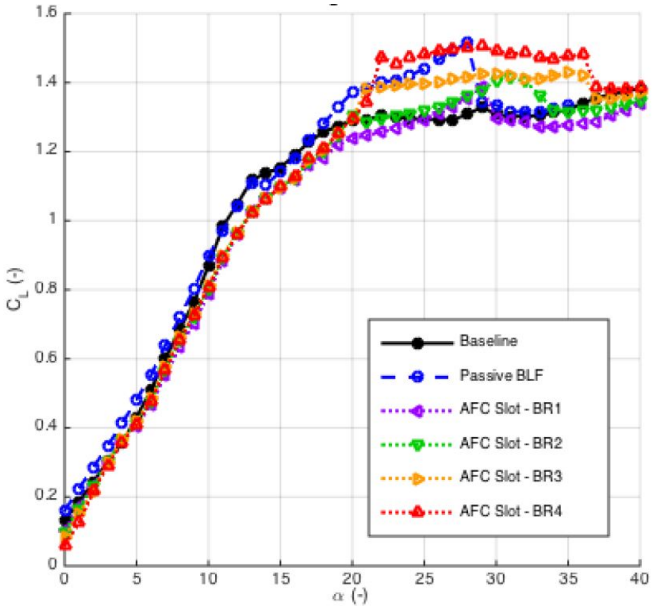

Figure 13. Walker NACA 64_3-618 30° Swept-Wing C_L at Re = 1.0x10^5: Baseline, Passive BLF and AFC Slot [4]

However, the most visible improvement Walker discovered was the disparity in C_M at high angels of attack, presented in Figure 14. The baseline configuration experiences an increase in C_M starting at 14° angle-of-attack which indicates the onset of

stall and a steep, but more gradual, pitch up motion. The BLF configuration successfully delayed the onset of stall an additional 14°, to 28° angle-of-attack. However, the BLF C_M drastically increased, indicating a sudden pitch up condition, when the wing approached stall and was therefore identified as a destabilizing control characteristic [9]. The active flow control method successfully delayed the onset of the negative destabilizing control characteristic another 7°, to 35° angle-of-attack. Although the destabilizing condition existed with the AFC slot, reduction of the magnitude and delay of the onset was successfully achieved [9]. This finding seemingly opened the trade space for slotted wall-normal AFC configuration application to wing geometries that experiences more drastic destabilizing control characteristics, the delta-wing.

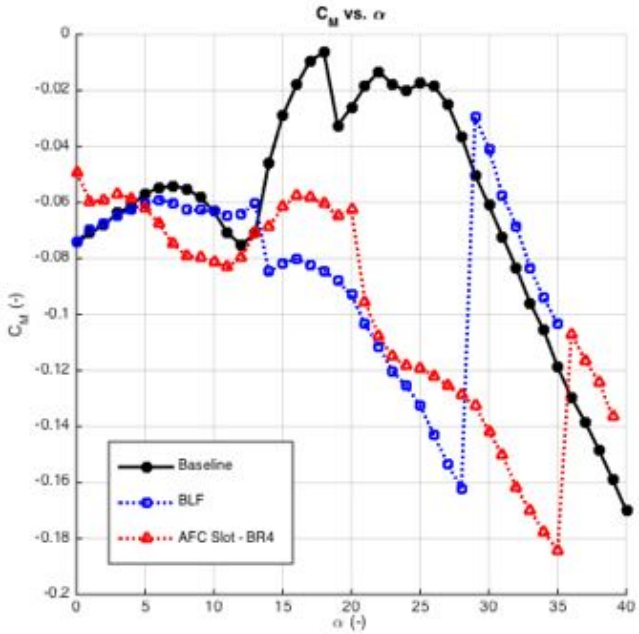

Figure 14. Walker NACA 64_3-618 30° Swept Wing C_M at Re = 1.0x10^5: Baseline, Passive BLF and AFC Slot [4]

Walker's stereo-PIV data, illustrated in Figure 15, revealed the creation of two counter rotating vortices, a wingtip vortex and a tip vortex generated by the BLF and AFC slot. Both vortices provide additional momentum by redirecting the flow back down into the boundary-layer, resulting in the increased lift and delay in stall

[9].

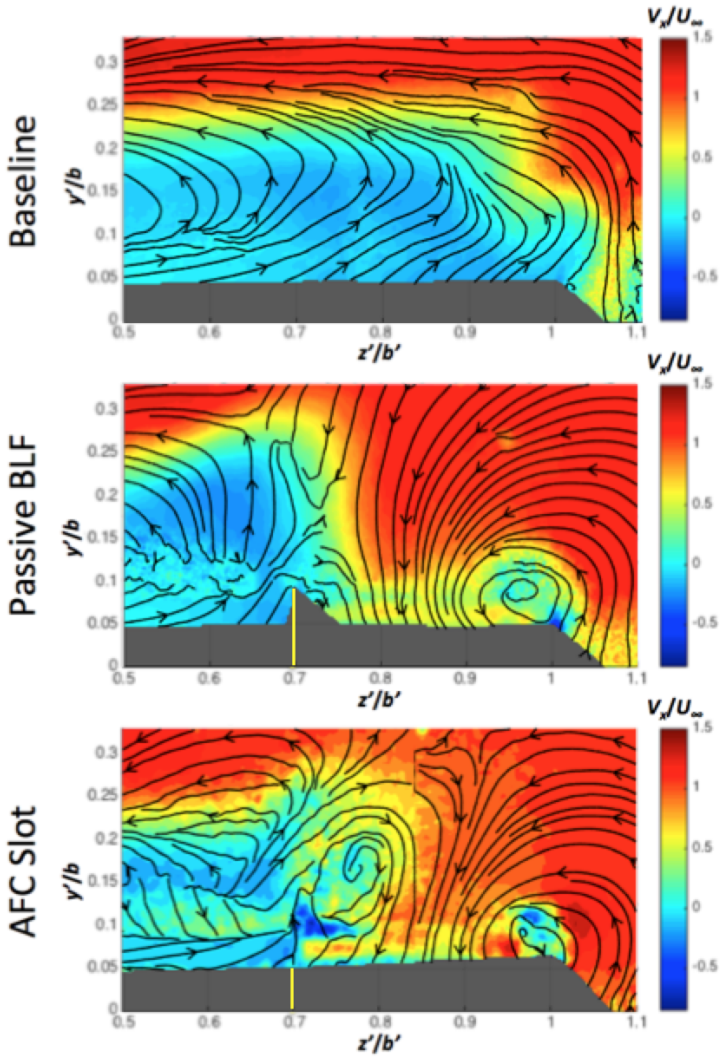

Figure 15. Walker 3D Flow-field comparison of Baseline, Passive BLF and AFC Slot ($BR = 4$) in the y'-z' Plane at $x'/c = 0.8$ ($\alpha = 25°$); Plot of V_X/U_∞ with Streamlines of V_Y/U_∞ and V_Z/U_∞ [9]

A continuation of Walker et al. findings were applied to a cropped NACA 0012 delta-wing (c_{root} = 14in, c_{tip} = 2.8in, $\Lambda = 45°$, $2b$ = 23.5in) at Re = 5.0 x 10^5 by Demoret. The study attempted to replicate performance improvements of a passive BLF utilizing a wall-normal AFC slot. The constant velocity AFC slot configuration, pictured in Figure 16, was a direct replacement for the passive BLF located at 0.7 z/b which extended chordwise from 0.25 x/c_{eff} on the high pressure side of the wing to

0.75 x/c_{eff} on the low pressure side with a width of 1 mm. However, the passive BLF configuration extended an additional 0.25 x/c_{eff} on the low pressure side of the wing from 0.75 x/c_{eff} to the trailing edge. A gain in C_{Lmax} = 60.3% was produced with the AFC slot operating at C_μ = 12.22%. These results far exceeded the passive fence configuration, annotated in Figure 17 and delayed the onset of stall an additional 7° [22].

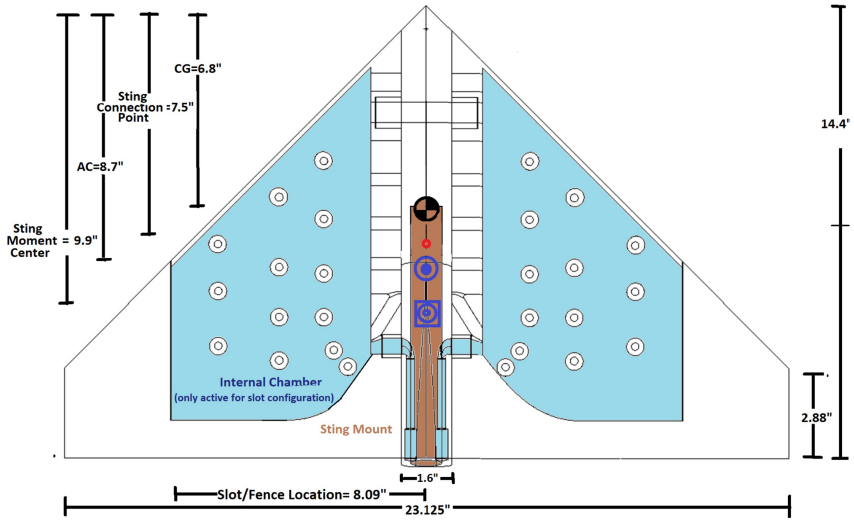

Figure 16. Demoret NACA 0012 Cropped Delta-Wing AFC Slot Configuration [22]

Similarly to Walker et.al. findings, the baseline and passive BLF of Demoret et.al. revealed less drastic destabilizing moment characteristics, illustrated in Figure 18. However, the AFC slot configurations showed no destabilizing pitching moment present over the entirety of the angle-of-attack sweep [22].

Demoret et.al. florescent tuft surface flow visualization at both 25° (Figure 19) and 33° (Figure 20) angle-of-attack demonstrate significant areas of streamwise flow being maintained for the AFC slot, indicating attached flow providing lift, versus the BLF showing spanwise flow, indicating stall. These results support C_L data provided in Figure 17 above. Demoret noted the increased streamwise flow captured outboard of the AFC slot, demostrating the ability of to halt spanwise flow comparatively to

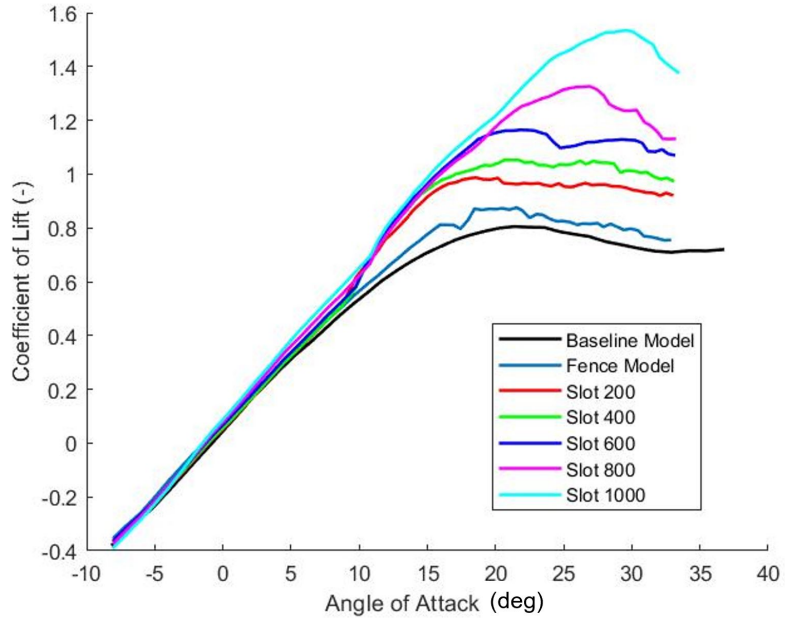

Figure 17. Demoret NACA 0012 Cropped Delta-Wing C_L at Re = 5.0 x 10^5: Baseline, Passive BLF and AFC Slot [22]

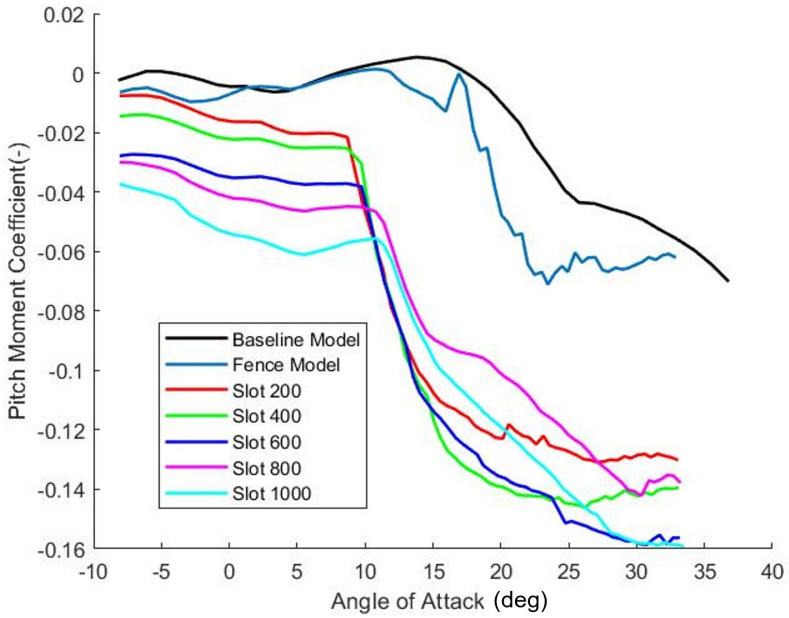

Figure 18. Demoret NACA 0012 Cropped Delta-Wing C_M at Re = 5.0 x 10^5: Baseline, Passive BLF and AFC Slot [22]

the BLF, while also noting the similiar streamwise flow inboard of the slot where the BLF model produces spanwise flow characteristics [22]. The area inboard of the

slot appears to be the source of the improved performance characteristics due to the momentum injection interaction, due to the steady blowing slot, with the naturally occurring vortex formed from swept-wing geometries. Additional investigation was recommended to confirm the flow interaction and its contribution to the performance gains.

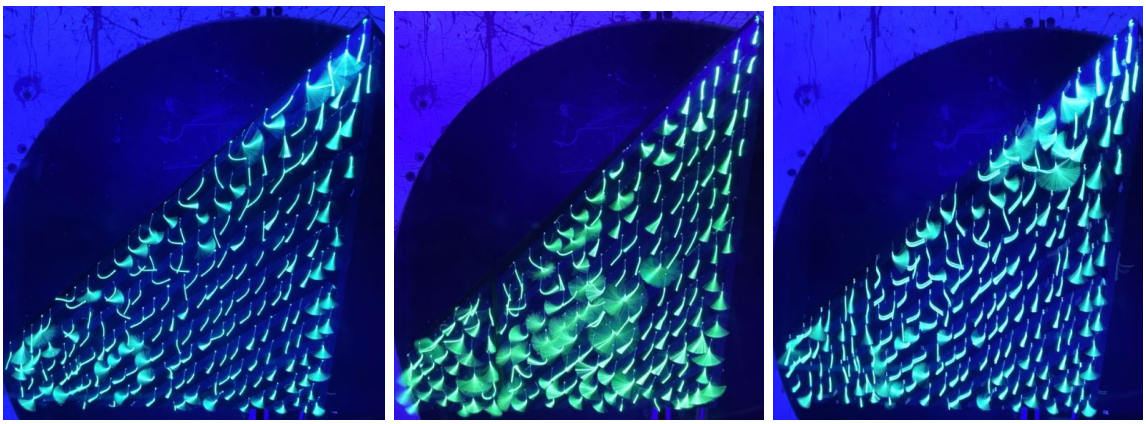

(a) Baseline Model (b) Fence Model (c) Slot Model, $C_\mu = 7.82\%$

Figure 19. Demoret NACA 0012 Cropped Delta-Wing Fluorescent-Tuft Visualization, $\alpha = 25^\circ$ [22]

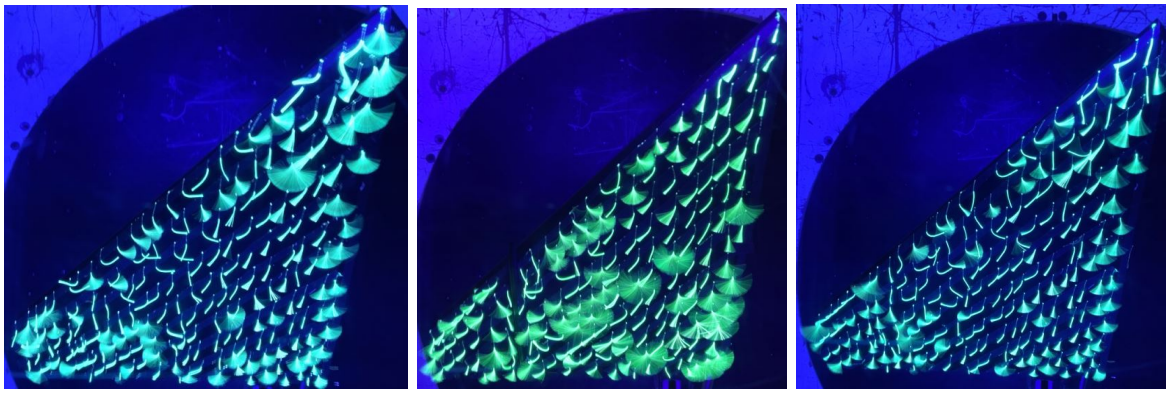

(a) Baseline Model (b) Fence Model (c) Slot Model, $C_\mu = 7.82\%$

Figure 20. Demoret NACA 0012 Cropped Delta-Wing Fluorescent-Tuft Visualization, $\alpha = 33^\circ$ [22]

As a means of validating Demoret's baseline configuration experimental data, direct comparison of Marzanek et al. presented water tunnel stereo-PIV research,

which utilized a NACA 0012 non-cropped delta-wing with $\Lambda = 45°$ at $Re = 3.0\text{x}10^5$, revealed similar results [27]. Overlay of C_L and C_D versus α data, Figures 21 and 22 respectively, affirm Demoret's data by following similar baseline wing trends and producing a baseline wing stall angle-of-attack identical to Marzanek.

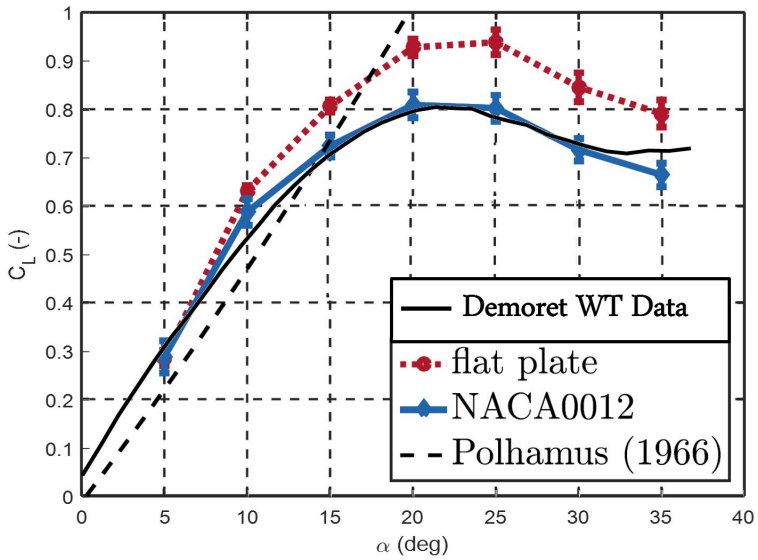

Figure 21. C_L vs. α NACA 0012 Delta-Wing: Demoret (Cropped, Re = 5.0x10^5) Marzanek (Non-cropped, Re = 3.0x10^5) [27]

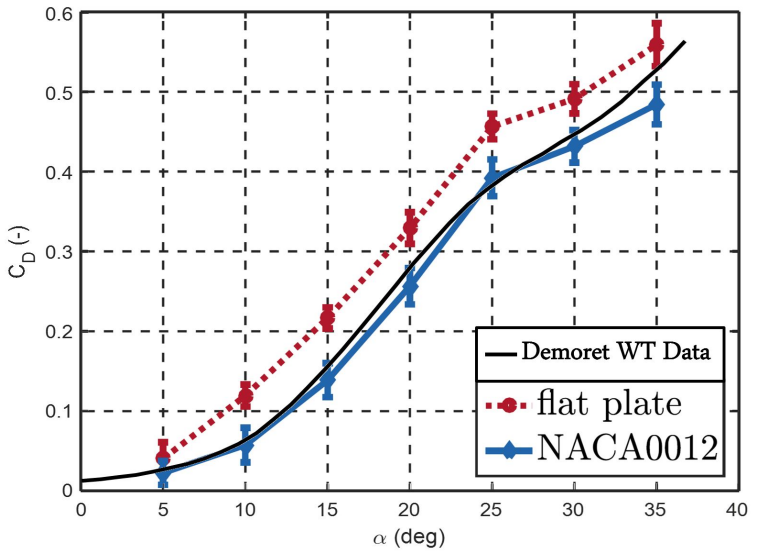

Figure 22. C_L vs. α NACA 0012 Delta-Wing: Demoret (Cropped, Re = 5.0x10^5) Marzanek (Non-cropped, Re = 3.0x10^5) [27]

Considering Walker et al. and Demoret et al. gains associated with the AFC slot, it was understood that physical, full scale production of a volumetric flow capable of reaching C_μ values listed were would be difficult. However, overall gains in wing performance was captured at lower scale momentum coefficients that continued to outperform the passive system improvement. The next phase in the evolution of the wall-normal AFC technique would be to optimize the slot relative to full-scaled geometry and attempt to minimize momentum injection while being able to produce similar performance gains demonstrated in the reviewed research.

2.2.3 Viscous Effects

Active flow control relies heavily on viscous fluid interactions through fluid entrainment. This is accomplished by energizing the flow with an injection of momentum into the naturally occurring swept wing separation-induced vortex [28]. Vortex theory reveals that viscous losses attribute to vortex breakdown resulting in the eventual loss of swept wing performance at high angles-of-attack [28]. AFC performance gains over that of the passive systems can be attributed to the viscous flow interaction of the vortex and AFC mechanism, specifically at high angles-of-attack. Solfelt and Williams show through computational results that boundary-layer fence performance enhancement success was attributed to vortex generation [29, 30]. These vortices are shown as having the strongest vortical motion when performance benefit are at their peak. Likewise, Walker and Demoret AFC studies revealed a direct relationship between an increase in viscous flow interaction through momentum input within the flow over a wing and an increase in overall wing performance, far exceeding that of passive systems [4, 22].

2.3 Computational Fluid Dynamic Theory

The primary purpose of CFD modeling is to provide insight into the flow features around a body. CFD models continually become more robust and closer resemblance of experimental values as computational capabilities advance. Furthermore, with these advances, it allows increasingly more complex flows to be investigated at a comparatively lower cost than experimental tests.

2.3.1 Governing Equations

The Navier-Stokes (N-S) equations are the governing equations upon which CFD simulations function. These equations provide the foundation for fluid conservation of mass, momentum and energy. Solving these equations in a closed form has yet to be accomplished without assumptions being applied about the nature of the turbulent fluid flow and its boundary conditions (BC). However, the equations can be solved numerically and iteratively to obtain values of the flow properties.

Within a CFD solution, convergence is achieved when either designated flow feature property values do not change outside of a set tolerance or, in the case of unsteady flow, the average flow feature property values do not change outside of a set tolerance.

For calculation simplification, the fluid flow is treated as a finite control volume (FCV) with application of the N-S equations [31]. The specifications of the computational grid or mesh establish the size of each FCV. Creating small volumes allow for the use of mass, momentum and energy conservation laws which states what mass, momentum and energy leaves one control volume is equal to the mass, momentum and energy entering the adjacent control volume. As these control volumes become smaller, both the accuracy of the results and the computational requirements needed to solve the model increase. Adaptive mesh refinement (AMR) was developed to contest with this ever-increasing requirement cycle.

2.3.2 Adaptive Mesh Refinement

To ensure accurate flow solutions are being produced, computational fluid dynamic simulations require important flow features to be properly resolved and captured. While modeling supersonic flow, shock generation and development is crucial to produce an accurate flow solution, as are laminar and turbulent flow boundaries and vortex shedding to subsonic flow solutions. To sufficiently capture these flow features, the mesh or grid must be precisely aligned with the flow feature and be fine enough to resolve the conservation laws as stated previously. The manual generation of a mesh that perfectly aligns with the different variety of flow features can be tedious and time consuming as each flow feature location must be estimated or calculated, computationally tested, observed and refined manually as needed. However, the application of AMR refines this process and allows the CFD solver to determine where the mesh requires coarsening or refinement based upon flow property gradients to properly balance the accuracy of results and the computational requirements needed to achieve a solution [32]. Figure 23 illustrates the basic concept of AMR where cells are coarsened, or large, in the flow field far away from the body of interest and systematically refined as cells approach the body surface or fluid flow features.

2.3.3 Turbulence Models

CFD is extraordinarily complex due to the subsequent chaotic nature of fluid flow patterns, or turbulence. The application of AMR aids in solving for turbulent flow regions which exhibit highly unsteady flow features, but greatly increases computational requirements due to solving more complex governing equations. Various models have been proposed to manage the bulk properties of the unpredictability of turbulent flow in the utilization of Reynolds Averaged Navier-Stokes (RANS) equations [31]. Users are limited to two RANS models while utilizing Kestrel: Spalart-Allmaras

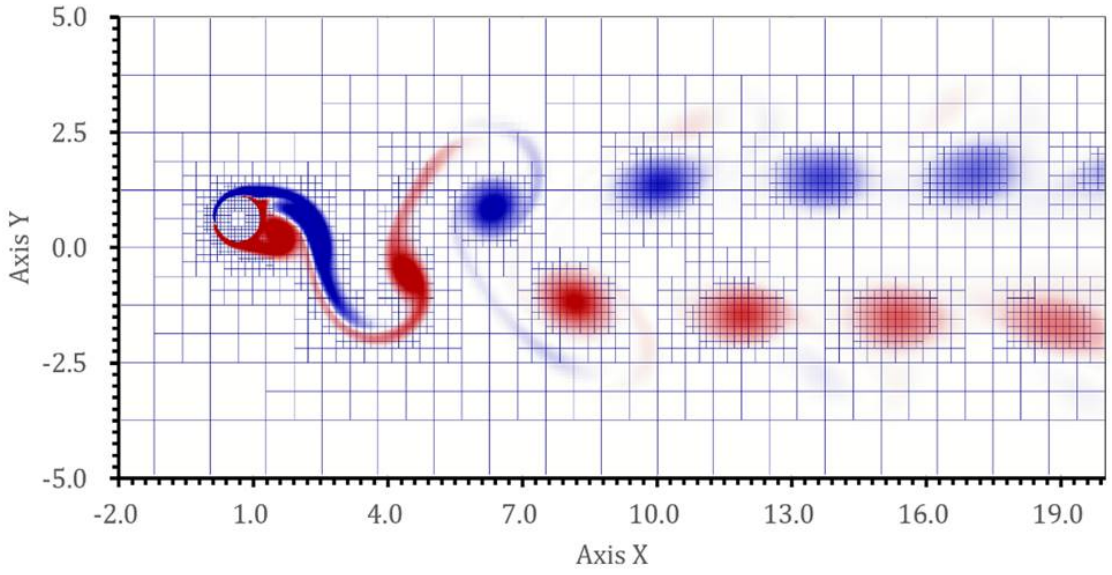

Figure 23. Active Mesh Refinement (AMR) Cell Density Example [33]

(S-A) and Menter. According to the Kestrel User's Guide (UG), S-A methods are more appropriate for external flow while Menter is better suited for internal flows [34]. As the S-A one-equation turbulence model was chosen for the presented study, Equation 2 represents the complete S-A turbulence model in dimensional, differential form. Table 1 lists the closure coefficients that were calibrated from empirical data in the literature [35]. In the S-A equation, ν is kinematic viscosity, $\tilde{\nu}$ is a parameter related to kinematic eddy viscosity and u is velocity. On the right hand side of the equation, the first term corresponds to the production of $\tilde{\nu}$, the second term corresponds to the destruction of $\tilde{\nu}$ and the last term corresponds to the diffusion of ν [35]. To fully compute Equation 2, the intermediate functions for f_{v1}, f_{v2}, f_{v3}, S, f_w, g and r are provided in Equations 3 - 10, respectively [35]. In these equations, κ is the turbulence kinetic energy, d is the distance to the nearest wall, S is the magnitude of the vorticity and σ is the turbulent Prandtl number.

$$\frac{\partial \tilde{\nu}}{\partial t} + u_j \frac{\partial \tilde{\nu}}{\partial x_j} = c_{b1}\tilde{S}\tilde{\nu} - c_{w1} f_w \left(\frac{\tilde{\nu}}{d}\right)^2 + \frac{1}{\sigma}\left[\frac{\partial}{\partial x_j}\left(\left(\tilde{\nu}+\nu\right)\frac{\partial \tilde{\nu}}{\partial x_j}\right) + c_{b2}\left(\frac{\partial \tilde{\nu}}{\partial x_i}\right)\right] \quad (2)$$

Variable	Value
c_{b1}	0.1355
c_{b2}	0.622
σ	0.6667
κ	0.41
c_{w1}	3.239
c_{w2}	0.3
c_{w3}	2
c_1	7.1
c_2	5

Table 1. Spalart-Allmaras Closure Constants [35]

$$\chi = \frac{\tilde{\nu}}{d} \quad (3)$$

$$f_{v1} = \frac{\chi^3}{\chi^3 + c_{v1}^3} \quad (4)$$

$$f_{v2} = \frac{1}{\left(1 + \chi / c_{v2}^3\right)} \quad (5)$$

$$f_{v3} = \frac{\left(1 + \chi f_{v1}\right)\left(1 + f_{v2}\right)}{max\left(\chi, 0.001\right)} \quad (6)$$

$$\tilde{S} = f_{v3} S + \left(\frac{\tilde{\nu}}{\kappa^2 d^2}\right) f_{v2} \quad (7)$$

$$f_w = g\left[\frac{1 + c_{w3}^6}{g^6 + c_{w3}^6}\right]^{1/6} \quad (8)$$

$$g = r + c_{w2}\left(r^6 - r\right) \tag{9}$$

$$r = \frac{\tilde{\nu}}{\tilde{S}\kappa^2 d^2} \tag{10}$$

The RANS equations introduce Reynolds stress to the N-S equations. Reynolds stress associates with the unsteadiness of the flow but allow for the separation of the fluid velocity and the turbulent fluctuations [31]. RANS methods are typically used for resolving near wall turbulent flow regions near a body and tend to produce inaccurate results where larger eddies form and flow is separated [31]. To solve this issue, large eddy simulation (LES) is utilized to sufficiently capture the large eddies in the separated flow. The combination of RANS and LES gave way to the creation of the Delayed-Detached Eddy Simulation (DDES) and further the Improved Delayed-Detached Eddy Simulation (IDDES) within Kestrel. IDDES resolves the issues related with using both LES and RANS in the boundary-layer by reducing or eliminating the mismatch in values between the two simulations by utilizing a switching function to alternate between RANS and LES based upon grid characteristics and a wall-length scale [36].

Spalart provides a guide to proper gridding practices when using these turbulence models as well as RANS, LES and IDDES methods [37]. For the purposes of the presented study, the S-A turbulence model with IDDES was chosen due to the primary flow being external, vortices being formed from increasing AoA and from the AFC slot jet and large eddies occurring in the separated regions at high AoA. All of which will be simultaneously resolved. For some aerodynamic applications, the S-A model produces similar results to other models but typically reaches solutions faster and thus increases computational efficiency [31].

2.3.4 Initial Cell Wall Distance

To accurately model the boundary-layer of a flow, the near wall cells in a mesh or grid must be properly sized to resolve the boundary-layer flow when utilizing turbulence models. This sizing comes in the form of the non-dimensional distance normal to the wall, y^+ [31]. The equation for this term is presented in Equation 11, where y represents the dimensional distance normal to the wall, τ_w is the wall shear stress, ρ is density of the fluid and ν is the kinematic viscosity of the fluid. Spalart recommends a y^+ value of less than 1 being necessary to properly resolve the boundary-layer flow when using the S-A one-equation turbulence model [37]. The settings and values used to establish an appropriate mesh size for this study are discussed in more detail in Chapter III.

$$y^+ = \frac{y\sqrt{\frac{\tau_w}{\rho}}}{\nu} \tag{11}$$

2.4 Compressibility Correction

With the onset of increasing flow velocities, compressibility factors must be addressed when computing flow solutions. With a large majority of original NACA data existing within the incompressible realm, simple compressibility corrections were developed to allow this data to be applied up to high velocity compressible flow scenarios, with maximum Mach comparisons around M = 0.7 [38]. The Prandtle-Glauert compressibility correction is the simplest and easiest correction applied to very low speed cases, such as this study. This method is based upon the linearized perturbation velocity potential equation shown in Equation 12 where perturbation velocity potential is given by $\hat{\phi}$ in the x and y direction [38]. Prandtl-Glauert assumes the airfoil is thin and that α is small as to simplify Equation 12 to the approximation shown in Equation 13, named the Prandtl-Glauert factor (β) [38].

$$\left(1 - M_\infty^2\right) \frac{\partial \hat{\phi}}{\partial x^2} + \frac{\partial \hat{\phi}}{\partial y^2} = 0 \tag{12}$$

$$\beta \equiv \sqrt{1 - M_\infty^2} \tag{13}$$

Application of the Prandtl-Glauert factor to compresssible and incompressible pressure distribution through the form of pressure coefficients, the Prandtl-Glauert rule was developed. Given in Equation 14, the rule states it the incompressible pressure distribution ($C_{p,0}$) over an airfoil is known, then the compressible pressure distribution (C_p) can be calculated over the same airfoil [38].

$$C_p = \frac{C_{p,0}}{\sqrt{1 - M_\infty^2}} \tag{14}$$

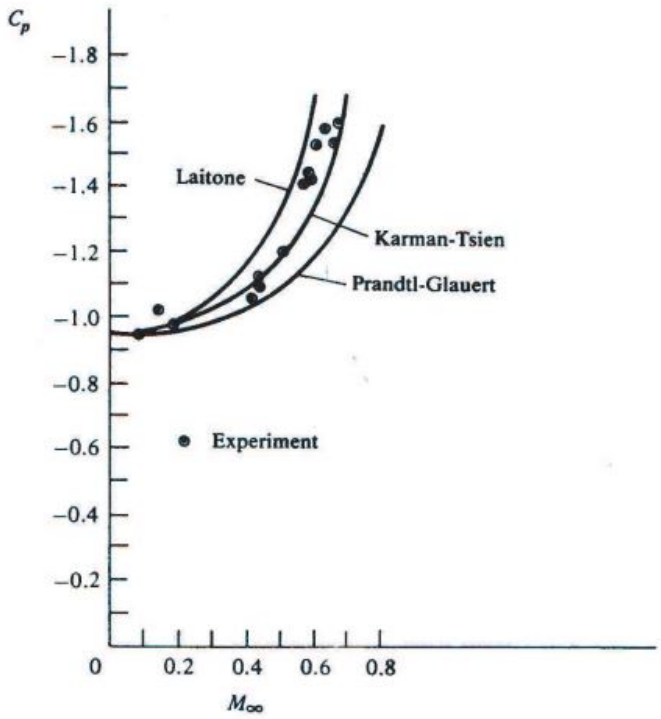

Figure 24. Compressibility Correction Comparison [38]

Due to the limited application and proven errors associated with the Prandtl-Glauert rule at high angle-of-attack and high mach numbers, improvements to the compressibility correction were made. Popular formulas developed include the Karman-Tsien rule and the Laitone rule which account for the shortcomings of the Prandtl-Glauert rule [38]. Comparison of the rules versus experimental results are shown in Figure 24 and indicate the Prandlt-Glauert rule under-predicts results at high mach numbers. However, the solutions converge to similar results at very low Mach numbers making the Prandtl-Glauert rule an appropriate compressibility correction approximation for this study.

III. Methodology

Computational fluid dynamics simulations require thoughtful application of settings when applied to mesh generation and solver operation to produce accurate and plausible flow solutions. A clear understanding of the operational flow regime, including compressibility and turbulence effects, and flow structure prediction, by anticipating fluid flow physics developed from the wing geometry interaction, was necessary when constructing CFD simulations. Settings used were developed based upon trial and error, solution comparison to physical results for model validation and focused recommendations refined by software manufactures and professionals utilizing the solver to create accurate predictions of similar cases.

3.1 Wind Tunnel Model Characteristics

Utilizing the NACA 0012 airfoil coordinates found in NACA Technical Note 3361 and measurements obtained from Demoret's study, listed in Table 2, the delta-wing 3D digital geometry was created with SolidWorks v2019 solid modeling computer-aided design (CAD) software[22, 39].

Wing Geometry	
Root Chord (c_{root})	14 in
Tip Chord (c_{tip})	2.88 in
Wing Sweep (Λ)	45°
Wing Half-Span (b)	11.5625 in
Angle-of-Attack (α)	$0°to30°$
Planform Area (S)	195.16 in^2
Mean Aerodynamic Chord (MAC)	9.66 in
Aerodynamic Center (AC)	8.7 in
Center of Gravity (CG)	6.8 in

Free-stream Settings	
Reynolds Number (Re)	500,000
Temperature (T)	300K
Pressure (P)	28.95 in Hg
Free-stream Flow Mach (M_∞)	0.059 ($V_\infty = 45mph$)

Passive BLF Geometry	
Location (z/b) *	70% (8.225 in from c_{root})
Airfoil Thickness @ 70% z/b (t)	0.74 in
Height (0.6t)	0.444 in
BLF Thickness	0.037 in
Extent/Height	See Figure 25 (a)

* Spanwise Location (z)

AFC Slot Geometry	
Extent	See Figure 25 (b)
Thickness	0.037 in
Air Flow Velocity	See Table 6
Volumetric Flow Rate	200, 400, 600, 800, 1,000 SLPM

Table 2. Demoret et al.'s Wind Tunnel Delta-Wing Geometry/Flow Settings

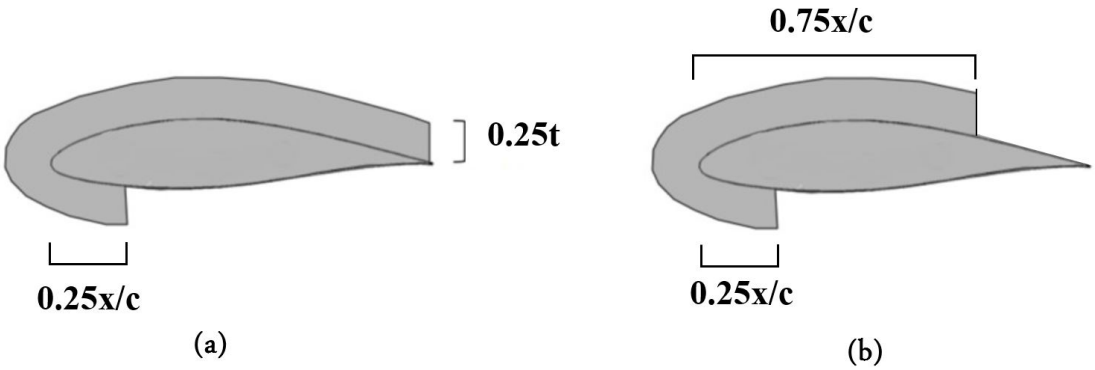

Figure 25. CFD Model Passive BLF (a) and AFC Slot (b) Configurations [22]

Production of three models, Figures 26, 27 and 28, represent the CAD geometries used throughout the study. Each model was developed utilizing the dimensions listed in Table 2 above.

3.2 Mesh Generation

Mesh generation began with the import of the developed CAD file geometry coordinate database, file type .IGS, into Pointwise v19.1 CFD mesh generation software [40]. Specific settings related to overall mesh generation are listed in Table 3. These

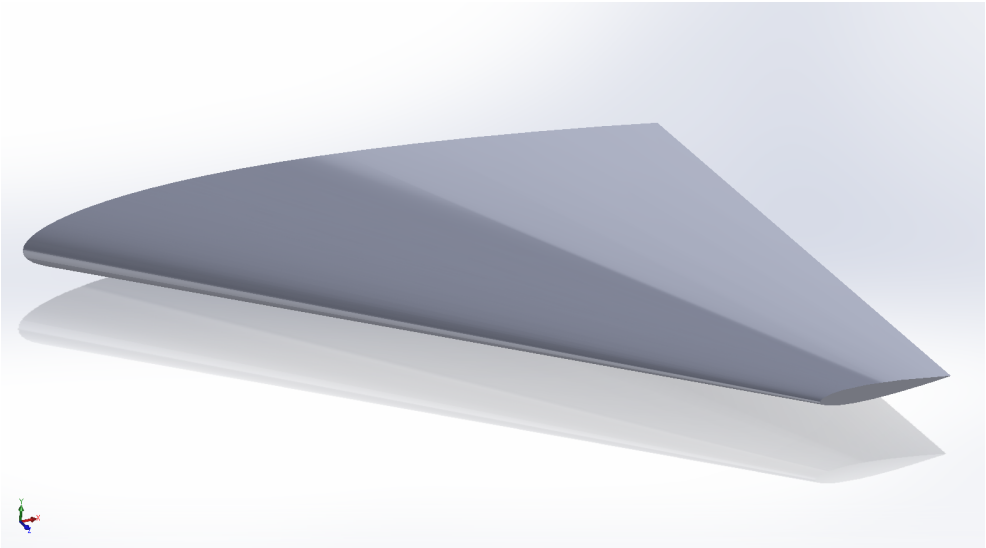

Figure 26. Baseline Cropped Delta-Wing Configuration

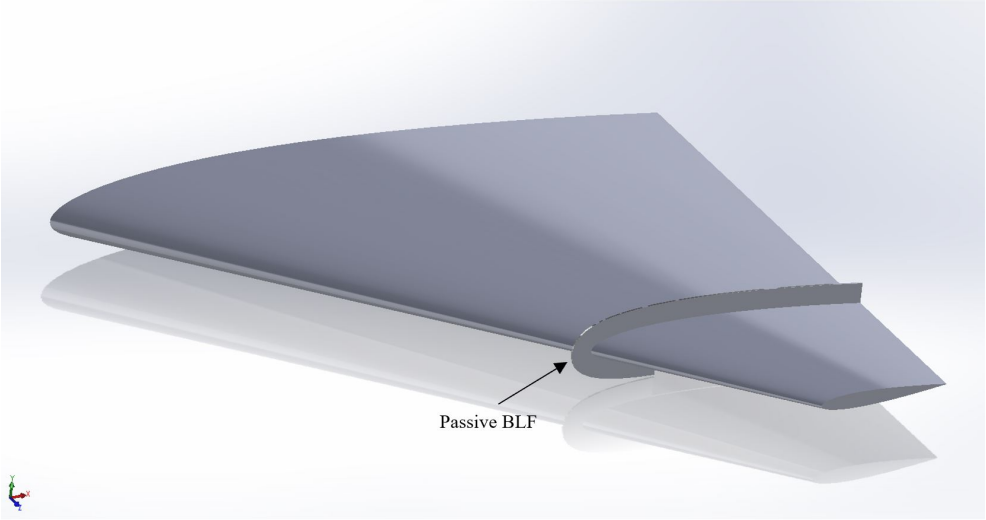

Figure 27. Passive Boundary-Layer Fence (BLF) Cropped Delta-Wing Configuration

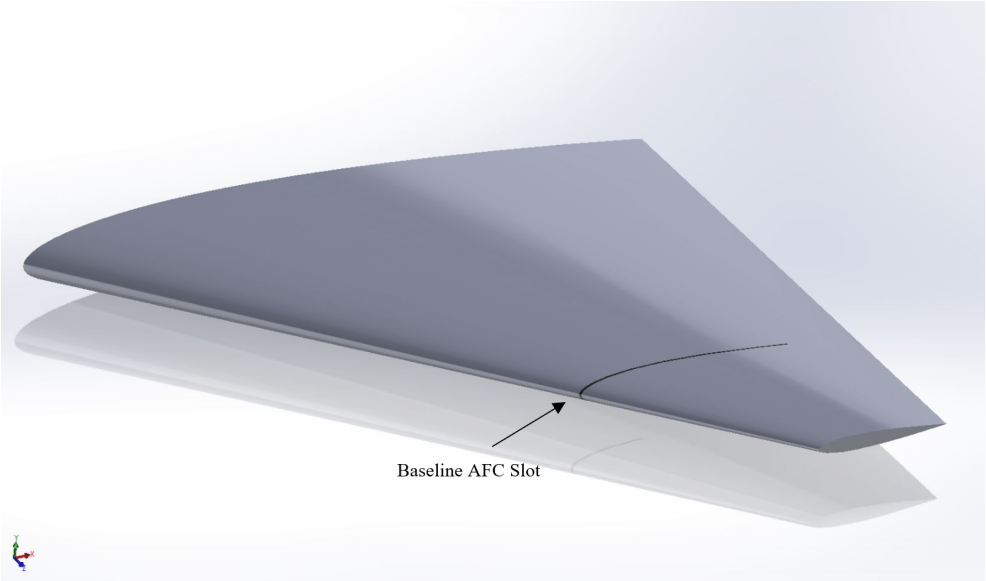

Figure 28. Active Flow Control (AFC) Cropped Delta-Wing Configuration

setting produced an initial cell spacing ($y^+ < 1$), as required for the solver to accurately develop near wall fluid interaction while utilizing the Spalart-Allmaras one-equation turbulence model [34]. The 3D anisotropic tetrahedral extrusion (T-Rex) tool was used to generate cells that accurately capture near wall fluid flow development in the boundary-layer [40]. Cell growth rate was recommended at 1.15 to accurately resolve boundary-layer physics [34]. Furthermore, utilizing a maximum

included angle less than 170° assisted in production of an aspect ratio of less than 40 to minimize cell skewness, a mesh characteristic shown at values greater than 40 to produce non-physical flow resulting in reduced solution accuracy [41].

Appropriate boundary conditions were applied to support Demoret et al. wind tunnel flow conditions as detailed in Figure 29. A half-delta wing was modeled as a method to reduce computational expenditure. However, a symmetry plain was utilized to account for the delta wing's omitted geometry and its inclusion of fluid interaction while compiling the simulation solution. Additionally, an outline of the critical flow region was created on the symmetry plain to extend the concentration of cells into the volume above the surface of the wing, depicted in Figure 30. This strategy was implemented to capture predicted flow features, outlined in Section 2.1.3, inherent of the swept delta wing at high angles-of-attack.

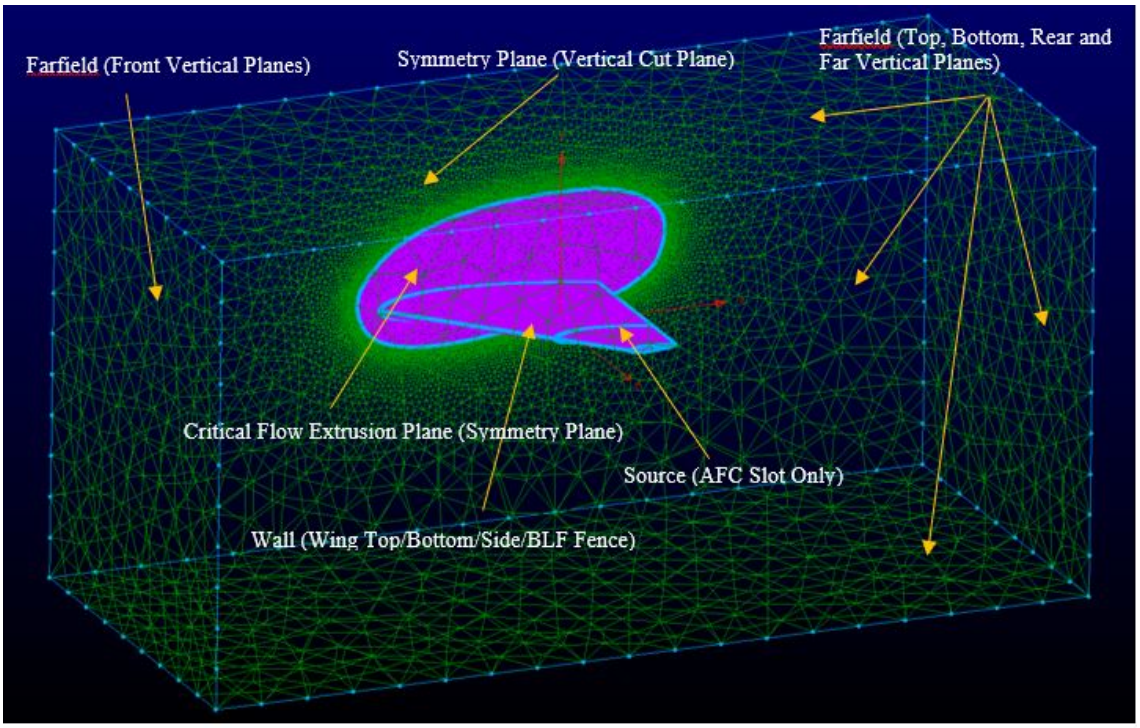

Figure 29. General Pointwise Mesh Generation, Boundary Conditions and Critical Flow Region

General Settings		
CAE:	**Solver**	Kestrel
	Dimension	3D
	Boundary Conditions	Symmetry
		Far-field
		No Slip Wall
		Interface Plane (Source)

Connectors	
Nodes	∼80 per unit measure
Spacing Constraints	0.001 (Tip Chord Curvature Regions)
	0.003-0.004 (Passive BLF and AFC Slot Curvature/BC Interaction Regions)
	0.005 (Root Chord Curvature Regions)

Domain Settings		
Attributes:	**Mesh Generation**	Unstructured
	Algorithm	Delauney
	Geometry	Triangles
	Surface Shape	Database, Closest Point
	Cells Max Angle	160
	Boundary Decay	0.99 (Wing Surface, Flow Field Concentration
		0.96 (Far-field)
TREX (Symmetry Plane)	**Max Layers**	20
	Full Layers	0
	Growth Rate	1.15
	Geometry	Triangles and Quads
	Boundary Conditions	Type Match - Symetry Plane
		Type Wall - Wing Edge (s = 0.001)
Note: Refine each surface until all cell geometries are fully resolved (i.e. cell count did not change)		

Block		
Attributes	**Boundary Decay**	0.96
	Max Edge Growth Rate	1.8
	Aspect Ratio	0.6
TREX	**Max Layers**	20
	Full Layers	0
	Growth Rate	1.15
	Isotropic Seed Layers	2
	Collision Buffer	2
	Aniso-Iso Blend	0.6
	Skew Criteria Max Angle	162.5
	Boundary Conditions	Type Match - Symetry Plane
		Type Wall - Wing and AFC Slot Surfaces (s = 0.001)

Table 3. Pointwise Mesh Generation General Settings

3.3 Simulation Setup

3.3.1 Free-stream Flow Correction

Reference conditions were chosen based upon the scaled geometry and Demoret et al. wind tunnel experimental conditions. However, initial simulation results of the baseline configuration failed to capture accurate flow solutions at high angles-of-

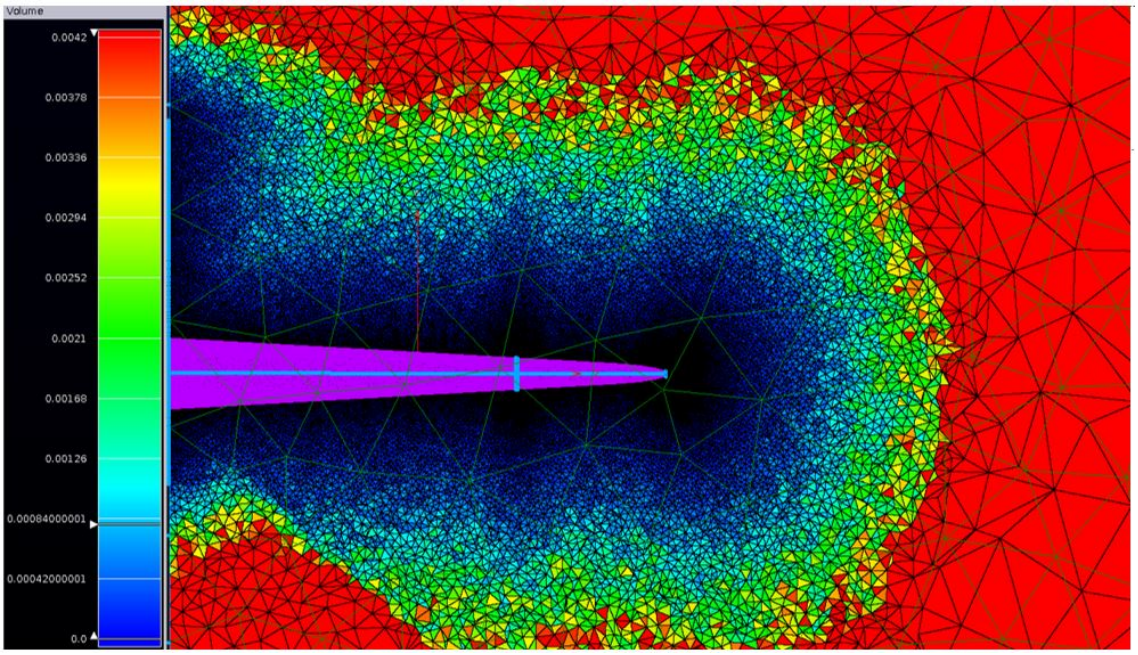

Figure 30. AFC Mesh Critical Flow Region Slice at 11.2 in x/c$_{root}$ (in^3)

attack ($\alpha > 20°$) while utilizing the relatively low experimental free-stream velocity (45 mph at Mach 0.059). Flow visualization indicated no flow separation and raw data revealed a linear progression of C_L, with no indication of wing stall. Demoret et al. experimental results indicated wing stall and flow separation at an approximate $\alpha \approx 21°$. Increase of the interation quantity and free-stream velocity was recommended for the CFD solver to generate a computational flow solution that accurately captured the simulation flow physics. Detailed in Section 2.4 and computed in Table 4, the Prandtl-Glauert transformation through the Prandtl-Glauert factor (β) indicated that a change in free-stream Mach number can be accounted for and was found to be within approximately 1.5%. The free-stream Mach number of the flow was therefore increased to 0.18 while maintaining the experimental Reynolds number ($Re = 5.0\text{x}10^5$) with the CFD simulation and experimental results continuing to remain comparable. Reynolds number was computed with Equation 15 utilizing the

free-stream velocity (U_∞), wing root chord (c_{root}) and kinematic viscosity (ν).

$$Re = \frac{U_\infty c_{root}}{\nu} \tag{15}$$

Free-stream Mach	β	% Change
0.059	0.9983	1.483
0.18	0.9837	

Table 4. Prandtl-Glauert Factor Computation

3.3.2 Flow Solver Settings

For the three individual model validation studies and AFC slot optimization study, Table 5 detailed CREATE-AV Kestrel general solver settings pertinent to all cases. Kestrel User Guide recommended the Spalart-Allmaras turbulence model to be used in external flow scenarios involving aircraft structures [34]. Rotation correction (RC) was implemented for enhanced modeling of vortical flows which are prominent flow structures inherent of swept delta-wings, detailed in Section 2.1.3, and expected with implementation of AFC slot steady blowing [34]. Additionally, with the expectation of unsteady, separated flow at high angels of attack, improved delayed-detached eddy simulation (IDDES) was implemented and was cited to improve the solution accuracy for such cases [34]. IDDES was selected to implement hybrid RANS-LES model that behaves as wall-modeled large eddy simulation (LES) when there turbulent inflow exists and a traditional delayed-detached eddy simulation (DDES) model when it does not [34]. Utilizing global time stepping, ranging from 1 (steady, incompressible flow) to 10 (transient, unsteady, incompressible flow), a moderate sub-iteration count of 5 was used to capture the unsteady (time-accurate), compressible flow physics more accurately [34]. The turbulent length scale was chosen relative to the airfoil thickness at the mean aerodynamic chord (MAC) [41]. Due to the CAD model and

mesh being generated in units of inches, Kestrel units also followed the imported settings. With that, Kestrel utilizes an uncommon standard unit of mass, the snail, which equates to 1 snail for every 12 slugs. Units of force continue to be in units of pound-force ($snail * in/s^2$). Additionally, the AFC slot "source" boundary condition, further detailed in Section 3.4, utilized a constant slot velocity, static pressure and static temperature. With these constant inputs set, the mass flow input was allowed to "float" and computed by the Kestrel software as necessary.

3.3.3 Cartesian Off-Body Settings

To capture flow interaction located in the far-field region of the computational volume, a structured Cartesian of-body mesh was generated, shown in Figure 31. Within Kestrel, SAMAir, a fifth-order, finite-volume solver, was used to generate a controlled far-field region of cells and their volumes with an overlaid grid of refining cells. This dual structured mesh system provided active mesh refinement (AMR), discussed in Section 2.3, and was set to execute after completion of 250 iterations and every 250 iterations thereafter within the far-field region. The focus of AMR, within the Cartesian mesh, was to recognize high gradient flow regions for refinement and coarsens elsewhere, when necessary. Additionally, an overset mesh was used to translate the near-body mesh interactions to and from the far-field. SAMAir coarsens cells by a factor of 4 outward from the near-body mesh to the Cartesian domain extents, excluding the strong gradients regions that require refinement. Furthermore, the Cartesian mesh was solved separately from the near-body mesh as to increase Kestrel's efficiency through reduced far-field cell density and parallel computation [34].

SAMAir inputs included extent bounds of the far-field region and refinement area around the near-body mesh. Based upon the free-stream flow conditions being com-

Simulation Control			
Units	ISS (inches, snails, seconds) $_{Note1}$		
Startup Iterations	0		
Scale	1		
Global CFD Solver Parameters			
Equation Set	Turbulent Navier-Stokes		
Compressible	Yes		
RANS Model	Spalart-Allmaras,Vorticity Based		
RC	Yes	**Transition Solver**	None
IDDES	Yes	**QRC**	No
CFD Actions			
Iterations	3500	**Time Step** $_{Note3}$	$5*10^{-5}$
Advective Damping Start	0.5	**Sub-Iterations**	5
Advective Temporal Damping $_{Note3}$	0.01	**Damping Ramp Fraction**	0.0
Spatial Accuracy Ramp Fraction	0.0		
Details	Time-Accurate Time Solution, Second-Order Spatial and Temporal Accuracy, Newton Nonlinear Convergence Solution Strategy		
KCFD Actions			
Enable Wall Function	Yes	**Theta**	1.0°
Max Solution Average	300	**Relaxation**	0.9
Fixed Sweeps	No	**Max Sweeps**	32
Sweeps Convergence Criteria	$1.0*10^{-6}$	**Min Sweeps**	15
Details	HLLE++ Inviscid Flux, LDD+ Viscous Flux, Weighted Gradient Type, Standard Viscous Flux Jacobian Scheme		
Free-stream Conditions			
Known Conditions	P-Re-Mach	**Reynolds Length**	14 (root chord)
Mach	0.18	**Turbulent Intensity**	-1.0 $_{Note2}$
Static Pressure	14.2415 psi	**Beta**	0 °
Re	500000	**Temp Increment**	0.0
α	0, 10, 14, 16, 18, 20, 22, 24, 26, 28, 30 (deg)		
Details	Native Perfect Gas (Air), Standard Atmosphere Model		
Boundary Conditions			
No Slip Wall (Wing Surface)	Adiabatic Force Account: True Force Account Absolute: True		
Symmetry	Force Account: False Patch Force Account Absolute: True		
Far-field	Force Account: True Patch Force Account Absolute: True Method: Reimann Invariant Include Momentum Loads: No		
Source: **(AFC Slot Only)**	Force Account: True Patch Force Account Absolute: True Method: Constant Total Properties (Specify Static Properties) Include Momentum Loads: Add Reference Frame: Body Turbulence: -1.0, -1.0 $_{Note2}$ Mach: Table 6 Static Pressure: 15 psi $_{Note4}$ Static Temperature: 1255.43 R $_{Note5}$ Mass Flow: -1.0 $_{Note2}$ Swirl: 0.0, 0.0, 0.0		
Mesh Definition			
Mesh Output Ref Length	1.0 1.0 1.0 (in)		
Mesh Output Ref Point	9.66, 0.0, 0.0 (in)		
Mesh Output Reference Area	97.58 in^2		
Note 1: 1 snail = 12 slugs Note 2: Float value Note 3: Required time step study to validate Note 4: Increased to prevent reverse flow, based upon max surface pressure CFD results Note 5: Based upon M 0.18, Re = $5 * 10^5$ reference conditions			

Table 5. Kestrel Model Validation and AFC Slot Optimization General Settings

pressible and subsonic, that the far-field bounds were set at 20 chords aft and 10 chords in all other directions, excluding the symmetry plane, to capture low-speed fluid interaction appropriately, seen in Figure 31 [31]. Additionally, the near-body mesh, seen in Figure 29, was trimmed to accommodate the overset mesh required for SAMAir application, depicted in Figure 32. Using the Kestrel Mesh Manipulation

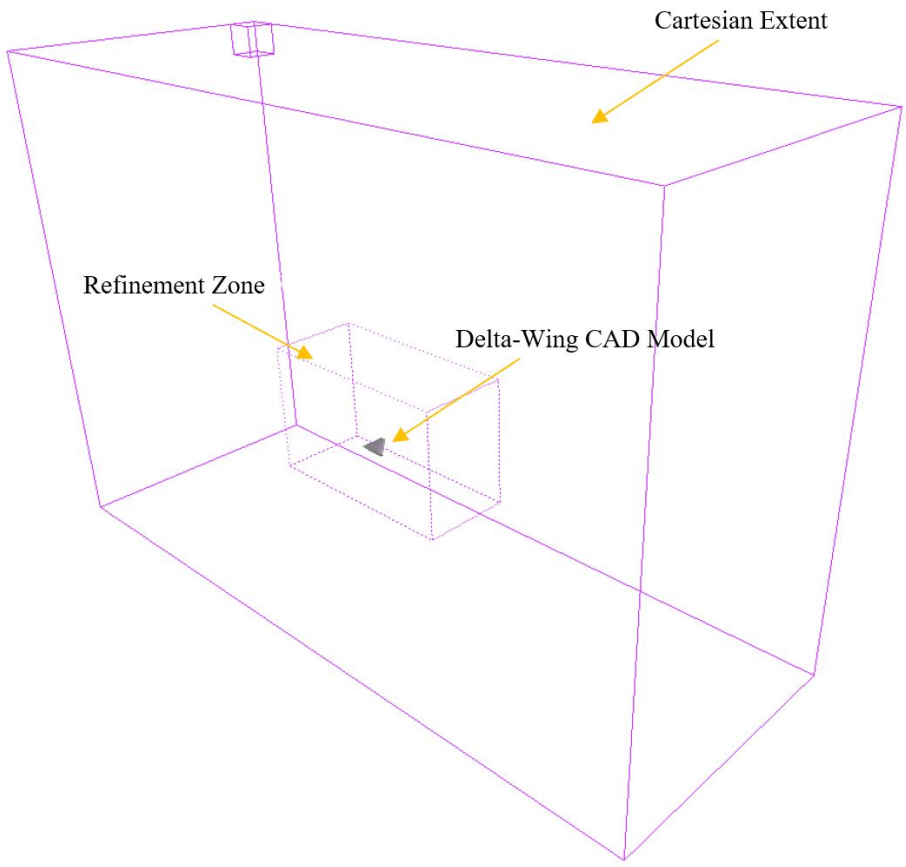

Figure 31. SAMAir Refinement Zone and Cartesian Extents

tool, each mesh was trimmed to within 9 inches from the surface of the wing, outside of the critical flow region designated previously. This allowed for the primary, finely resolved mesh to capture all boundary-layer flow interactions and develop near-body flow structures prior to translating those values to the overset mesh for far-field interaction.

3.4 Performance Parameters

Using simulation output force files, time averaged global forces and moment measurements in the body fixed reference frame, detailed in Figure 33, were averaged over the final 1000 iterations for each case after sufficient convergence had been ob-

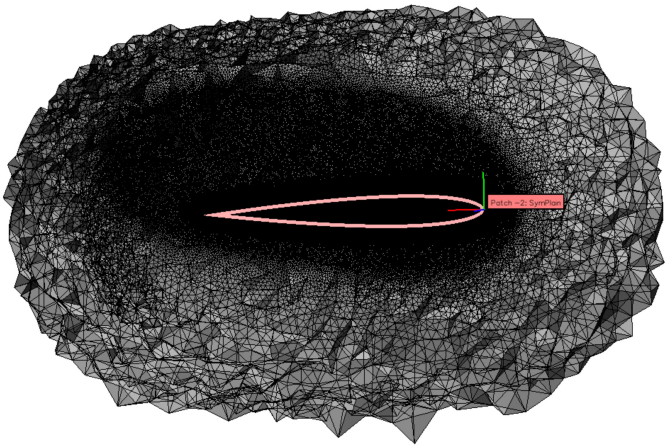

Figure 32. Near-Body Mesh Trimmed for SAMAir Refinement Zone

tained. This data was used to generate lift (L), drag (D) and pitch moment (PM), presented in the form of non-dimensional coefficients of lift (C_L), drag (C_D) and moment (C_M), with respect to angle-of-attack (α), outlined in Equations 18 - 22. These coefficients will be used to determine the performance of each wing configuration. Variables within these equations are defined as density (ρ), free-stream velocity (V_∞), the planform area of the wing (S given in Equation 16), the mean chord of the wing ($\bar{c}$), wing half-span (b), wing root chord (c_{root}), wingtip chord (c_{tip}) and the x-location of the axis about which the pitching moment was calculated (x_{cm}). Below are the equations for lift and drag as a function of normal force (N) and axial force (A) with the axis transformed to x-back, y-up and z-left [34].

$$S = \frac{b(c_{root} - c_{tip})}{2} + (c_{tip}b) \tag{16}$$

$$D = Nsin(\alpha) - Acos(\alpha) \tag{17}$$

$$L = Ncos(\alpha) - Asin(\alpha) \tag{18}$$

$$PM = M_z - [Lcos(\alpha) - Dsin(\alpha)]\, x_{cm} \tag{19}$$

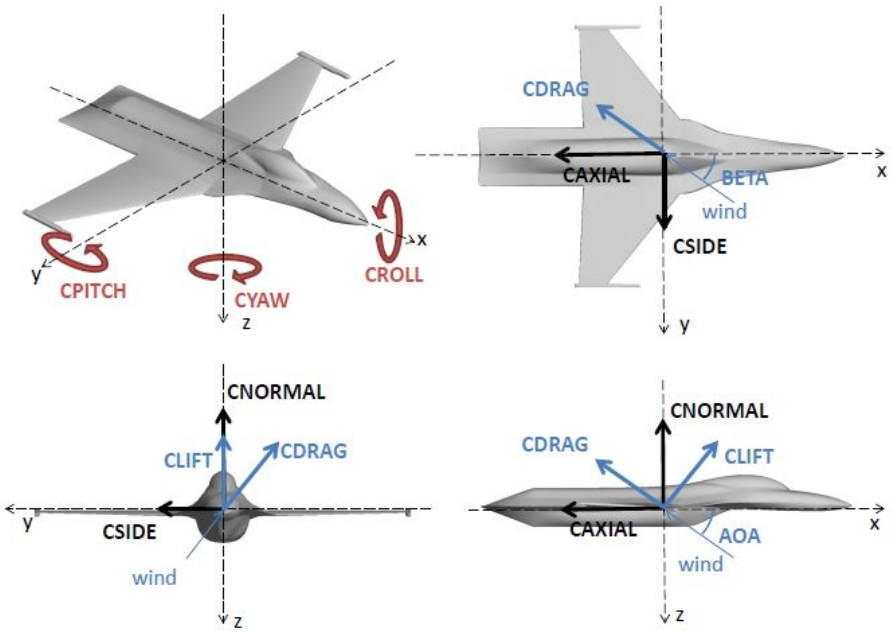

Figure 33. Components of Aerodynamic Force [34]

$$C_D = \frac{D}{\frac{1}{2}\ \rho\ V_\infty^2\ S} \tag{20}$$

$$C_L = \frac{L}{\frac{1}{2}\ \rho\ V_\infty^2\ S} \tag{21}$$

$$C_M = \frac{PM}{\frac{1}{2}\ \rho\ V_\infty^2\ S\ \bar{c}} \tag{22}$$

The momentum coefficient (C_μ), used to quantify the momentum energy being added to the system, was calculated with the incorporated variables slot area (A_{slot}), mass flow rate ($\dot{m}_{slot}$), wing planform area (S), volumetric flow rate through the slot ($\dot{V}$), free-stream velocity (V_∞) and the assumption of incompressible flow ($\rho_\infty = \rho_{slot}$). Initial wind tunnel C_μ values were calculated at Mach 0.059 and listed in Table 6 along with estimated baseline slot velocities with respect to Demoret et al. measured volumetric flow rates.

$$C_\mu = \frac{\dot{m}_{slot}\ V_{slot}}{\frac{1}{2}\ \rho_\infty\ V_\infty^2\ S} * 100 \tag{23}$$

where

$$\dot{m}_{slot} = A_{slot}\ \rho_{slot}\ V_{slot} \tag{24}$$

and

$$V_{slot} = \dot{V}/A_{slot} \tag{25}$$

Combining Equations 23 - 25 into a more robust equation yields:

$$C_\mu = 2\ \frac{A_{slot}}{S}\ \frac{\rho_{slot}}{\rho_\infty}\ \frac{(\dot{V}_{slot}/A_{slot})^2}{V_\infty^2} * 100 \tag{26}$$

Kestrel "source" AFC slot boundary condition settings for constant velocity were input as a Mach number (M). With the increase in free-stream Mach number to 0.18 while maintaining an experimental Re and static pressure, wind tunnel AFC slot volumetric flow parameters required conversion to a scaled slot flow Mach number with respect to updated free-stream conditions. Utilizing the Equation 23 and experimental wind tunnel C_μ values, Table 6 detailed wind tunnel slot settings and applicable converted settings for simulation utilization, with applicable designators for each Mach configuration. Additionally, while maintaining the previously identified experimental constants, Kestrel was able to "float," or adjust, free-stream density, temperature and viscosity as necessary. As a result, free-stream density and viscosity reduced while temperature increased which also allowed Kestrel to produce an increased free-stream speed of sound (c) of 20,841.6 in/s. This value was utilized in the production of Mach numbers computed using Equation 27 and listed in Table 6.

$$M_{slot} = \frac{V_{slot}}{c} \tag{27}$$

Comparison of gains or reduction in performance parameters versus momentum quantities, via C_μ, were attained utilizing Equation 28 and plotted to that perfor-

	Mach 0.059			Mach 0.18		
$\dot{V}_{slot}$ (SLPM)	C_μ(%)	V_{slot} (in/s)	M_{slot}	V_{slot} (in/s)	M_{slot}	Designator
200	0.49	777.52	0.0574	3,643.67	0.1748	M1
400	1.95	1,551.06	0.1145	7,268.72	0.3488	M2
600	4.4	2,329.90	0.1720	10,918.61	0.5239	M3
800	7.82	3,106.10	0.2293	14,556.07	0.6984	M4
1,000	12.22	3,882.82	0.2867	18,196.02	0.8731	M5

Table 6. AFC Slot (Source) Boundary Condition Conversion

mance parameter's percent gain or reduction. Variable $A_{initial}$ and B_{final} are arbitrary values and were implemented based upon the performance parameter being analyzed. The comparison plots were used for visual aids during analysis of the AFC slot to select the most suitable configuration based upon optimal performance.

$$\%_{gain} = \frac{B_{final} - A_{initial}}{A_{initial}} \tag{28}$$

3.5 Convergence Criteria

Confirming computational simulation convergence varied with software application. The Kestrel UG outlined it's specific criteria used for convergence. Output parameters located within the tracking file required plotting for visual inspection of steady-state values occurring. Which specific values that reflected convergence was dependent on the simulation being performed. Initial inspection across all variables within the tracking file was required to identify those parameters exhibiting large, non-uniform oscillations or non-constant values. Furthermore, the number of variable sweeps was to be checked to confirm that parameter was not fixed it's maximum value of 32. If so, the final value was not likely to be accurate. Thus, time-resolution settings were to be adjusted in accordance with the Kestrel UG. Finally, the error and warning logs were also to be checked for complications the simulation experienced throughout the simulation execution. Also, if warnings existed, the solution produced

may not be accurate and solutions to those warnings were to be addressed [34].

3.6 Testing Procedure

3.6.1 Initial Testing

3.6.1.1 Time-Resolution Study

Recommended by the Kestrel UG to reduce error in key performance indicators and improve convergence, a time-resolution study was performed. Listed in Table 7, solver time-resolution settings analyzed included variations in time step and temporal damping, designated as runs 1 thru 4. While using higher order solvers, increased time to solution was longer for a given step size but production of temporal error was reduced [34]. Furthermore, with the prediction of highly separated, unsteady flow at high angles-of-attack, time step and temporal damping were reduced to allow the solver to fully resolve flow features. The Kestrel UG provided rough orders of magnitude of 1.0x10^{-3} to 1.0x10^{-4} seconds for initial sizing of the time step and 0.1 to 0.01 for temporal damping [34]. The time-resolution study was conducted at a relatively high angle of attach, 22°, utilizing the baseline configuration, so convergence criteria could be attained during production of flow separation and unsteadiness. Normal and axial forces along with the pitching moment, outlined in Section 3.4 for each run were compared for convergence criteria, detailed in Section 3.5, and production of steady state values.

Run	Time Step	Adv Temp Damp
1	5x10^{-5}	0.01
2	2x10^{-5}	0.1
3	5x10^{-5}	0.1
4	5x10^{-4}	0.01

Table 7. Time Step Study Parameters

3.6.1.2 Mesh Refinement

To validate the mesh's computational application while also reducing computational expense, or computational time, while also achieving a sufficiently converged solution, a grid independence study was performed. For each physical geometry, a total of three independent meshes; coarse, medium and fine, were generated at approximately ±20% of the medium mesh cell count, detailed in Table 8. Each mesh was required to meet the minimum requirements previously discussed in Section 2.3 for turbulent flow criteria and a $y^+ < 1$ for near wall boundary-layer interaction. Furthermore, performance measures, outlined in Section 3.4, specifically normal (Fx) forces, axial (Fy) forces and the moment about the z-axis (Mz), were compared within individual groupings of wing geometries at each mesh size to determine mesh convergence, outlined in Section 3.5, and minimal computational utilization to meet that criteria. Due to the study concentrating on improvement of delta-wing performance at high angles-of-attack, at or beyond stall conditions, an angle-of-attack (α) of 22° was chosen for the mesh refinement study so convergence criteria could be attained during production of flow separation and unsteadiness. Those results were indicators of the mesh to be utilized for the remainder of the study for each given geometry.

Configuration	**Coarse Mesh**		**Medium Mesh**		**Fine Mesh**	
	Cell Count	y^+	**Cell Count**	y^+	**Cell Count**	y^+
Baseline Wing	26,592,298	0.9432	31,181,731	0.9386	39,353,985	0.8624
Passive BLF	36,274,945	0.9109	42,726,349	0.9015	54,686,837	0.9016
AFC Slot	28,815,082	0.9192	31,562,845	0.8996	48,909,625	0.9223

Table 8. Grid Independence Cell Count and Initial Cell Spacing (y^+)

3.6.1.3 CFD Model Validation

Computational model performance affirmation with respect to physical data and theory allow confidence in results produced. Furthermore, that confidence allows the

models to be used outside of the comparison to further research and test limits in ways that previously may not have been capable. In this study, all three CFD model configurations were validated through comparison with previously obtained wind tunnel results prior to proceeding with AFC slot optimization. For the experimental baseline and passive BLF model validations, the configurations were replicated utilizing CAD geometries, with mesh generation and Kestrels settings outlined in Sections 3.2 and 3.3 respectively. Furthermore, these configurations were compared to theoretical and experimental results to validate vortical flow features formation within the flow field, via vortex leading edge location and angular propagation based upon α. The AFC slot validation focused on a single volumetric flow rate chosen from Demoret's investigation, 200 SLPM or C_μ=0.49%, to produce comparison data. For all geometries, the flow performance measurements compared included coefficient listed in Section 3.4 and were evaluated for convergence as described in Section 3.5. All three configurations were simulated at α's of 0°, 10° and 14° to 30° in 2° increments. Qualitatively, each performance measure plot was expected to follow trends with respect to Demoret et al. wind tunnel data and quantitatively expected be within 5% of those experimental values. This margin of error incorporates Demoret et al.'s calculated experimental accuracy and uncertainty calculation of approximately ±2.5% with an additional error margin of ±2.5% for compressibility correction and general configuration variations [22].

3.6.2 Primary Testing

Energy expenditure within an aircraft requires that the benefits of that expenditure outweigh the penalty imposed on the system. Optimization of the AFC slot configuration was necessary to ascertain if performance gains witnessed in the preceding wind tunnel experiment can potentially be replicated through reduction of

momentum energy input by means of geometry and slot flow rate reconfiguration.

3.6.2.1 AFC Slot Width Optimization

Comparison of the primary slot width characteristics from wind tunnel model to a scaled model potentially 17 to 20 times the model's size revealed the original slot width was not suitable for real-world application. Thus, a focus on slot geometry, specifically reduced slot widths (SW), would potentially capture the more realistic, real-world scaled slot geometry while also analyzing the reduced momentum injection effects on the system. This was also a means of optimizing energy input into the system. Utilizing Demoret et al.'s wind tunnel experimental method with the five scaled slot Mach numbers, listed in Table 6, along with the five varying slot width geometries, listed in Table 9, the AFC slot performance of the 25 individual configurations was evaluated through comparison of performance coefficients described in Section 3.4. Furthermore, convergence criteria was also enforced as outlined in Section 3.5. Due to the large quantity and computational expense required to produce detailed, CFD simulation, full angle-of-attack performance parameter curves of 25 configurations, a single angle-of-attack was chosen to represent the configuration's performance based upon Demoret et al. wind tunnel experimental results, illustrated in Figure 17, which also coincide with validated CFD model results. An angle-of-attack of 24° was chosen as the focus for this analysis due to existing beyond the baseline model stall ($\alpha = 22°$), an α which all other configurations showed improvement and prior to AFC slot low C_μ models experienced the onset of stall. This angle-of-attack also produces sufficient variation between AFC slot C_μ modifications as to differentiate between configurations with improved performance. Percentage gains in performance coefficients, specifically coefficient of lift (C_L), with respect to momentum coefficient (C_μ), listed in Table 6 and Table 10, will be used to determine the optimal slot width

configuration.

Designator	L_{slot} (in)	W_{slot} (in)	A_{slot} (in^2)
SW1 (Original)	6.85	0.037	0.25345
SW2 (80% SW1)		0.0296	0.20276
SW3 (60% SW1)		0.0222	0.15207
SW4 (40% SW1)		0.0148	0.10138
SW5 (20% SW1)		0.0074	0.05069

Table 9. Slot Width Geometry Characteristics

SW2	C(μ) %
M1	0.392
M2	1.56
M3	3.52
M4	6.256
M5	9.776

SW3	C(μ) %
M1	0.294
M2	1.17
M3	2.64
M4	4.692
M5	7.332

SW4	C(μ) %
M1	0.196
M2	0.78
M3	1.76
M4	3.128
M5	4.888

SW5	C(μ) %
M1	0.098
M2	0.39
M3	0.88
M4	1.564
M5	2.444

Table 10. Cμ as a Function of Slot Width (SW) and Mach (M)

3.6.2.2 AFC Slot Length Optimization

Using the analyzed optimal slot width performance results outlined in Section 3.6.2.1, continued optimization of the AFC slot configuration focused on variation in slot length, or extent (EX), with specific dimensions listed in Table 11 and detailed in Figure 25. Utilizing the optimal slot width configuration and slot velocity, Table 11 was updated to reflect coefficients of momentum (C_μ) obtained from each extent configuration using Equation 26, detailed in Section 3.4. Each configuration was simulated at a single angle-of-attack, 24° for purposes described in Section 3.6.2.1 and was evaluated for convergence as detailed in Section 3.5. Analysis was performed in accordance with Section 3.4 with the generation of performance parameters C_L, C_D and C_M along with performance gain comparisons versus C_μ to determine the optimal configuration.

Designator	Surface Measurement (x/c)
EX1	-0.25 to 0.75
EX2	-0.25 to 1.0
EX3	-0.25 to 0.5
EX4	0 to 0.75
EX5	0 to 0.5
EX6	0 to 0.25
EX7	0 to 1.0
EX8	0.25 to 1.0
Note: - Zero indicates the leading edge - Negative values follow the bottom surface - Positive values follows the top surface	

Table 11. Extent Configuration Dimensions

3.6.3 Flow Visualization

Using Tecplot 360 visualization software, the CFD generated flow fields of the baseline, passive BLF, best performing AFC slot wind tunnel configurations and optimized AFC slot configuration were generated in 2D and 3D imagery to compared critical flow feature variations that reveal performance enhancement interactions. Flow field variables to be visualized included surface pressure contours, y-z plane pressure distributions, surface particle streamtraces, velocity magnitude vector fields and velocity magnitude iso-surfaces.

3.7 Data Processing

The full MATLAB code for processing the Kestrel output files collected for each run can be found in Appendix A thru I. The general process for producing comparative data visualizations is outlined as follows:

1. Import the *force.dat* files for sweep of angles-of-attack being analyzed

2. Input final iteration count to average data collection over

3. Calculate lift, drag and pitching moment based upon imported body axis reference frame data

4. Calculate coefficients of lift, drag and pitching moment

5. Using and iterative approach, adjust measured distance between mean aerodynamic chord and aerodynamic center (x_{cm}) for determination of pitching moment coefficient

6. Plot data

7. Determine optimized configuration solution based upon criteria outlined in Section 3.4 and parameter being analyzed

8. Determine extent C_μ based on chosen optimized slot width and Mach configuration

9. Implement processes 1-7 for slot extent optimization

10. Plot and compare performance parameters outlined in Section 3.4 against baseline, passive BLF, wind tunnel AFC Slot results and CFD optimal solution to determine overall performance gains and total energy conserved.

11. Analyze flow field using visualizations as outlined in Section 3.6.3.

3.8 Computational Resources

To produce computational results within a suitable and timely manner, it was necessary to use the HPC system described in Chapter 1. Within the HPC network, all simulations conducted were performed on the Onyx system. This system consists of 4,810 standard compute nodes, 4 large-memory compute nodes, 32 GPU compute nodes, 32 Knights Landing (Phi) compute nodes and 64 Machine Learning Accelerator

(MLA) multi-GPGPU nodes (a total of 4,942 compute nodes or 217,128 compute cores) rated at 6.06 peak PFLOPS [42]. Each simulation utilized 44 computational cores per node while varying the number of cores used based upon iterations, mesh size and system availability. For this study, approximately 165 nodes for 1.2 wall-clock hours were utilized to compute 3,500 iterations. An estimate of 87 independent jobs were simulated resulting in approximately 760,000 HPC computational hours used.

IV. Results and Analysis

4.1 Initial Testing

4.1.1 Time-Resolution Analysis

Using the baseline NACA 0012 cropped delta-wing configuration at an angle-of-attack of 22° and configured as outlined in Section 3.6.1.1 and detailed in Table 7, normal and axial forces along with the pitching moment for each run were compared for convergence criteria and production of steady state values as defined in Section 3.5. Summarized parametric analysis of the performance parameters are listed in Table 12 and plotted results are listed in Appendix A. No errors or warnings were indicated in the output log files and variable sweeps were at the minimal value of 15 at the end of each run.

Run Number	**1** (**TS = 5x10^{-5} AD = 0.01**)	**2** (**TS = 2x10^{-5} AD = 0.1**)	**3** (**TS = 5x10^{-5} AD = 0.1**)	**4** (**TS = 5x10^{-4} AD = 0.01**)
Fx (lb_f)	1.267	1.178	0.8662	1.548
Fx$_{std}$ (lb_f)	0.1099	0.2641	0.3183	0.1332
Fy (lb_f)	27.84	30.22	29.02	29.73
Fy$_{std}$ (lb_f)	0.4978	1.131	0.9926	1.146
Mz (lb_f-in)	39.89	41.02	39.34	42.26
Mz$_{std}$ (lb_f-in)	1.506	2.008	3.254	1.847
Time to Conv (Iter)	1500	No Convergence	No Convergence	1500
Note: All values averaged over 1,000 iterations, time step (TS), advective damping (AD), standard deviation (std)				

Table 12. CFD Time-Resolution Parametric Analysis: Baseline Model (α = 22°)

Qualitatively, steady state values for the three performance parameters had begun to converge for Runs 1 and 4 at approximately 1,500 iterations. Analysis of the steady-state axial (Fx) and moment (Mz) values for Runs 2 and 3 indicated no minimum convergence criteria being met for these settings as the plots continued to have a positive trend upon conclusion of the simulation. Thus, Runs 2 and 3 were eliminated as potential setting parameters. Further comparison of Runs 1 and 4 reveal a reduced

standard deviation (std) and amplitude across the the final 1,000 iterations being average for Run 1, giving a more consistent solution satisfying convergence criteria. For this reason, Run 1 parameters (TS = 5x10^{-5}s and AD = 0.01) will be utilized for the remainder of the study for all simulation configurations.

4.1.2 Mesh Refinement Analysis

Using the NACA 0012 cropped delta-wing baseline, passive BLF and AFC slot $C_\mu = 0.49\%$ CFD models at an angle-of-attack of 22° and configured as outlined in Section 3.6.1.2 and detailed in Table 8, normal and axial forces along with the pitching moment for each configuration were averaged over 1,000 iterations and analyzed for convergence criteria and steady state values as defined in Section 3.5. Summarized parametric analysis of the performance parameters were listed in Table 13 and plotted results listed were presented in Appendix B. No errors or warnings were indicated in the output log files and variable sweeps were at the minimal value of 15 at the end of each configuration's solution. Flow solution unsteadiness between adjacent values was anticipated due to the mesh study being conduced for each configuration at an angle-of-attack beyond stall conditions. Thus steady state was determined to be minimal oscillation about an average value over 1,000 iterations yielding a small standard deviation (std).

Comparison of the coarse (26x10^6), medium (31x10^6) and fine (39x10^6) mesh cell counts of the baseline CFD configuration produced convergence at approximately 1,500 iterations, for the fine mesh, with small oscillations across all three performance parameters annotated in Table 13. Visual analysis of the moment data about the z-axis for the coarse and medium cell counts, illustrated in Appendix B Figure 67, revealed the solution had not achieved steady state within the 1,000 iterations being averaged due to high amplitude deviations being present in the solution. Re-

	CFD Baseline ($\alpha = 22°$)			CFD Passive BLF ($\alpha = 22°$)			CFD AFC Slot (C_μ=0.49%, $\alpha = 22°$)		
Mesh Cell Count	**26 x10^6**	**31x10^6**	**39x10^6**	**36x10^6**	**43x10^6**	**54x10^6**	**28x10^6**	**31x10^6**	**39x10^6**
Fx (lb_f)	0.5241	0.9225	1.267	0.9672	0.6087	0.3914	1.298	0.9168	1.718
Fx$_{std}$ (lb_f)	0.2609	0.1499	0.1099	0.2266	0.2316	0.1551	0.1428	0.1041	0.1168
Fy (lb_f)	26.28	27.57	27.84	28.09	26.71	25.91	29.25	27.67	30.52
Fy$_{std}$ (lb_f)	1.137	0.9448	0.4978	1.266	1.493	1.136	1.024	0.4689	0.3545
Mz (lb_f-in)	36.07	38.97	39.89	9.226	7.612	6.873	23.12	19.21	24.33
Mz$_{std}$ (lb_f-in)	4.147	2.345	1.506	3.891	3.393	2.614	0.6118	0.8849	0.5491
Time to Conv (iter)	NA	NA	1500	NA	NA	2500	NA	NA	2200
Note: All values averaged over 1,000 iterations, TS = 5x10^{-5}, AD = 0.01, standard deviation (std)									

Table 13. CFD Mesh Refinement Parametric Comparison: Baseline, Passive BLF and AFC Slot Models ($\alpha = 22°$)

sults concluded that the fine mesh achieved the designated convergence criteria and prompted the fine baseline mesh to be utilized in the baseline CFD model validation study.

Comparison of the coarse (36x10^6), medium (43x10^6) and fine (54x10^6) mesh cell counts of the passive BLF CFD configuration produced convergence at approximately 2,500 iterations, for the fine mesh, and small oscillations across all three performance parameters annotated in Table 13. Visual analysis of the axial force data for the coarse and medium cell counts, illustrated in Appendix B Figure 68, revealed the solution had not achieved steady state within the 1,000 iterations being averaged due to high amplitude deviations being present in the solution. Results concluded that the fine mesh achieved the designated convergence criteria and prompted the fine BLF mesh to be utilization in the passive BLF CFD model validation study.

Comparison of the coarse (28x10^6), medium (31x10^6) and fine (49x10^6) mesh cell count of the AFC slot $C_\mu = 0.49\%$ CFD configuration produced convergence at approximately 2,500 iterations, for the fine mesh, and small oscillations across all three performance parameters annotated in Table 13. Analysis of the axial forces data and momentum data about the z-axis for the coarse and medium cell counts, illustrated in Appendix B Figures 71, 73 respectively, revealed that the solutions

had not achieved steady state within the 1,000 iterations being averaged due to high amplitude deviations being present in the solution. Results concluded that the fine mesh achieves the designated convergence criteria and prompted the fine AFC slot mesh to be utilized the AFC slot, $C_\mu = 0.49\%$, CFD model validation study.

4.1.3 CFD Model Validation Analysis

The computational model validation of the NACA 0012 cropped delta-wing baseline, passive BLF and AFC slot $C_\mu = 0.49\%$ CFD configurations were compared to Demoret et al. wind tunnel experimental data and utilized time-resolution results, listed in Section 4.1.1, and mesh refinement results, listed in Section 4.1.2. Performance parameters, outlined in Section 3.4, were summarized in Table 14 for each of the three CFD model configurations. Each performance, parameter at its given configuration, was averaged over 1,000 iterations and met convergence criteria as outlined in Section 3.5.

		Baseline	BLF	AFC Slot (C_μ=0.49%)
CFD Max % Deviation From Wind Tunnel (%)	C_D	2.6	3.7	4.8
	C_L	3.9	7.3	4.9
	C_M	9.8	35.9	45.7
C_{Lmax} (-)	Wind Tunnel Model	0.8051	0.873	0.8886
	CFD Model	0.8077	0.8226	0.8773
Distance from Aero Center (in) (All Wind Tunnel Models = 1.189 in)		1.32	0.99	1.28

Table 14. CFD Validation Parametric Comparison versus Wind Tunnel Data: Baseline, Passive BLF and AFC Slot Models

4.1.3.1 Baseline CFD Model Validation Analysis

Analysis of the baseline CFD configuration with respect to Demoret et al. wind tunnel experimental data reveal a maximum deviation in coefficient of drag (C_D) and lift (C_L) performance measures, listed in Table 14, to within 5%, as anticipated. Furthermore, C_D and C_L performance curves trended as expected with minimal variation throughout the angle-of-attack sweep, shown in Figures 34 and 35 respectively. Coefficient of momentum (C_M) experienced a maximum deviation of more than the anticipated 5% at $\alpha = 10°$, shown in Figure 36. However, the following moment solution values trend as expected with the experimental data.

Further validation of the baseline configuration with respect to flow physics generation included visual analysis of vortex core development and location at varying angles-of-attack. Previous studies, discussed in Section 2.1.3 and Figure 4, indicated a shift in the vortex spanwise location, relative to the leading edge, and change in

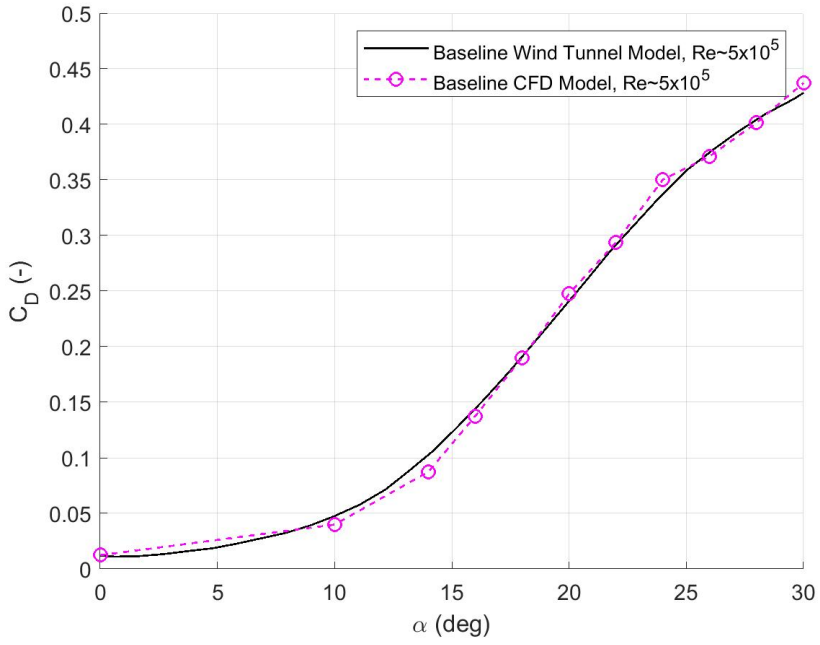

Figure 34. NACA 0012 Cropped Delta-Wing Baseline Coefficient of Drag (C_D) CFD Model and Wind Tunnel Comparison, $\alpha = 0°$ to $30°$, Re = 5x10^5

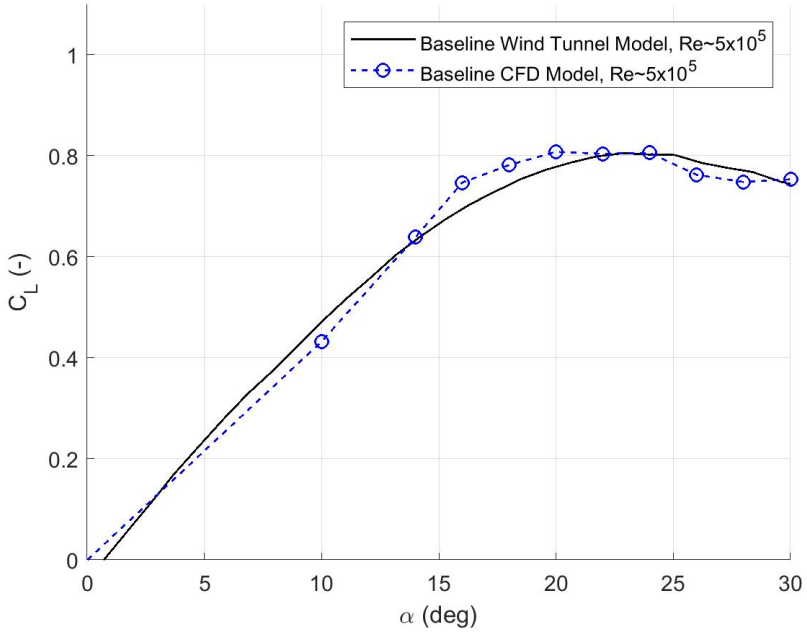

Figure 35. NACA 0012 Cropped Delta-Wing Baseline Coefficient of Lift (C_L) CFD Model and Wind Tunnel Comparison, $\alpha = 0^\circ$ to 30°, Re = 5x10^5

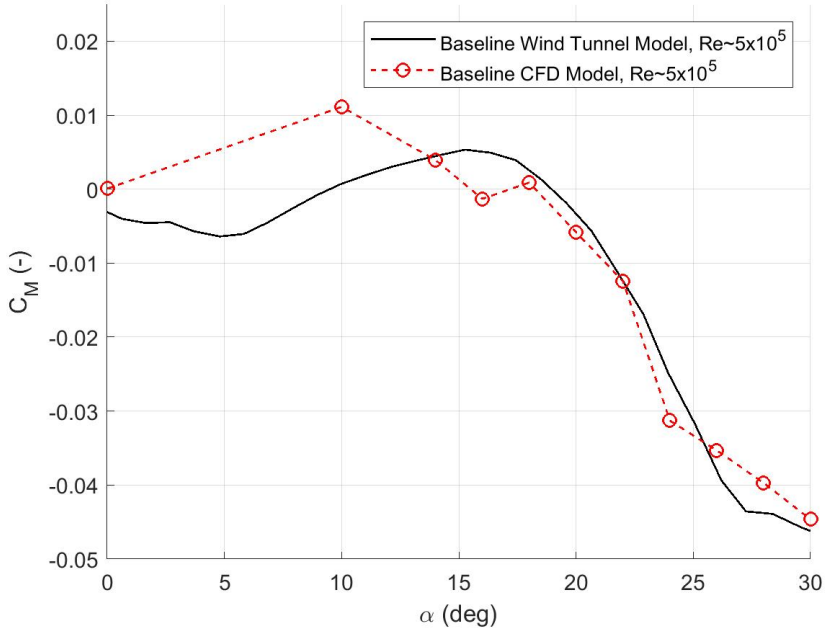

Figure 36. NACA 0012 Cropped Delta-Wing Baseline Pitching Moment Coefficient (C_M) CFD Model and Wind Tunnel Comparison, $\alpha = 0^\circ$ to 30°, Re = 5x10^5

vortex sweep angle, based upon α, should occur. Baseline CFD model primary vortex core visualizations were produced at $\alpha = 18°$ and 24°, shown in Figure 37, and confirm variations consistent with literature with a shift in the vortex core, both in sweep and spanwise location. Sweep variation was measured with $\alpha = 18°$ having a 63° sweep and $\alpha = 24°$ having a 74° sweep, increasing with angle-of-attack. Furthermore, the spanwise location of the vortex interaction on the leading edge moved inboard as angle-of-attack increased from $\alpha = 18°$ at 3.8in and $\alpha = 24°$ at 1in from the root chord (c_{root}). Taking all three performance parameters trends, equivalent performance solutions and flow physics into consideration, the baseline CFD model was confirmed to be accurate and valid for the purposes of this study.

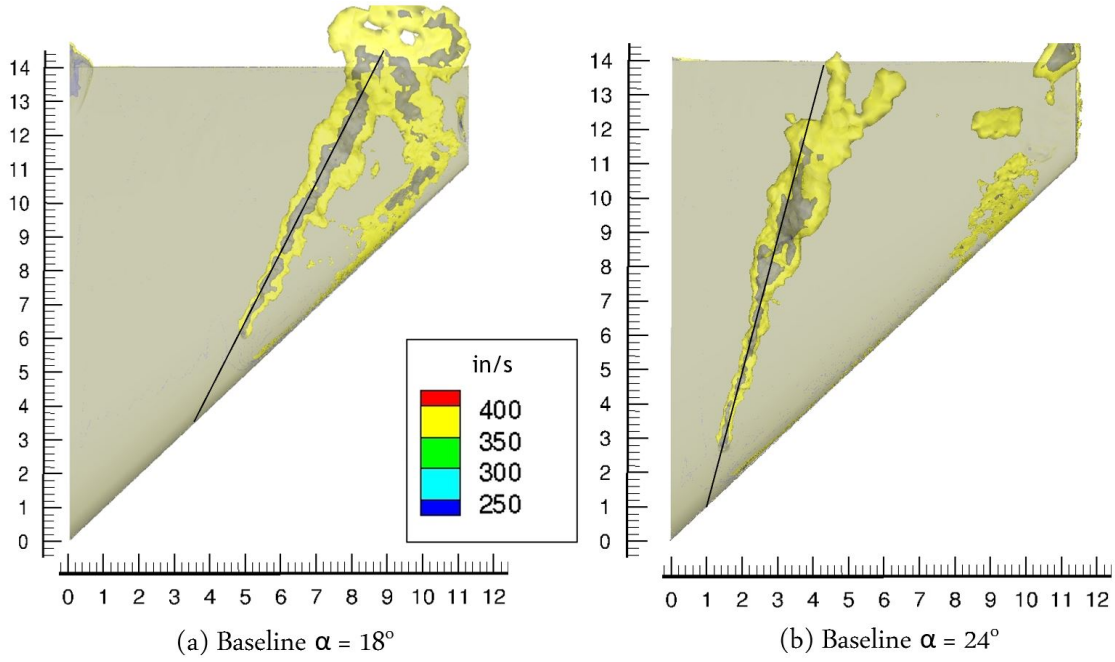

Figure 37. NACA 0012 Cropped Delta-Wing Baseline CFD Model Vortex Core Comparison, $\alpha = 18°$ and 24°, Re = 5x10^5, Iso-Surface Velocity Magnitude

4.1.3.2 Passive BLF CFD Model Validation Analysis

Analysis of the passive BLF CFD configuration with respect to Demoret et al. wind tunnel experimental data reveal a maximum deviation in coefficient of drag (C_D)

performance measures, listed in Table 14, to within 5%, as anticipated. Furthermore, the C_D performance curve trend as expected with minimal variation throughout the angle-of-attack sweep, shown in Figures 38. Coefficients of lift (C_L) and momentum (C_M) experienced a maximum deviation of more than the anticipated 5%, shown in Figures 35 and 36 respectively. The lift coefficient curve, Figures 35, trended with the experimental data until stall propagation and varied with a constant negative offset of approximately 7.3% from $\alpha = 20°$ to 30°. There was no immediate explanation presented as to the source of the displacement. Further investigation was required to resolve the issue. Due to the passive BLF configuration not being the focus of the primary optimization study and C_L data trends being comparable with experimental trends, produced C_L CFD results were accepted. The pitching moment coefficient curve, Figure 36, showed maximum variation in the region of a dramatic decrease in moment, from $\alpha = 20°$ to 22°. However, all other C_M data followed experimental trends and was within the data constraints.

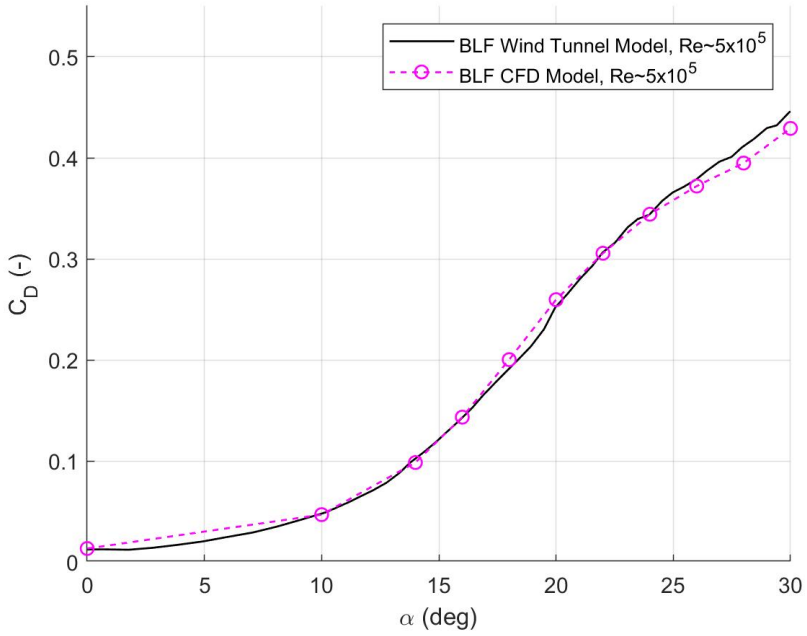

Figure 38. NACA 0012 Cropped Delta-Wing Passive BLF Coefficient of Drag (C_D) CFD Model and Wind Tunnel Comparison, $\alpha = 0°$ to 30°, Re = 5x10^5

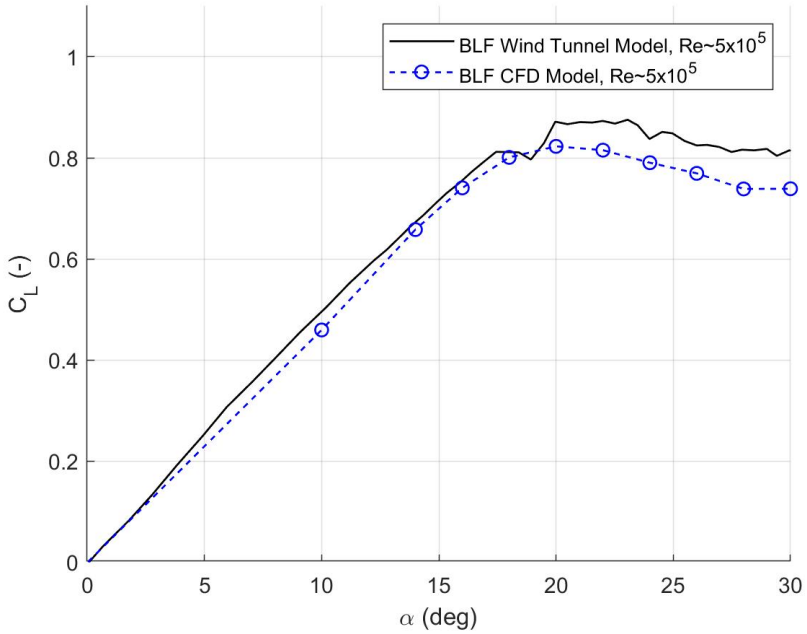

Figure 39. NACA 0012 Cropped Delta-Wing Passive BLF Coefficient of Lift (C_L) CFD Model and Wind Tunnel Comparison, $\alpha = 0^\circ$ to 30°, Re = 5x10^5

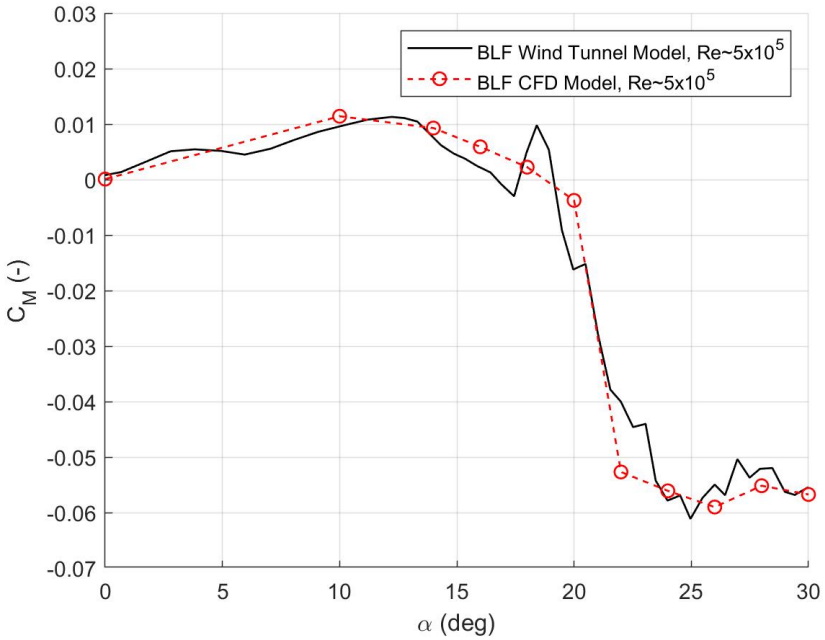

Figure 40. NACA 0012 Cropped Delta-Wing Passive BLF Pitching Moment Coefficient (C_M) CFD Model and Wind Tunnel Comparison, $\alpha = 0^\circ$ to 30°, Re = 5x10^5

Further validation of the passive BLF configuration flow physics included analysis of the primary vortex core development and location at varying angles-of-attack. Analogous to the baseline CFD model, a shift in the vortex spanwise location, relative to the leading edge, and change in sweep angle based upon angle-of-attack was indicated. Passive BLF CFD model primary vortex core visualizations were produced at $\alpha = 18°$ and $24°$, Figure 41, and confirmed variations consistent with literature with a shift in the vortex core, both in sweep and spanwise location. Sweep variation was measured with $\alpha = 18°$ having a $70°$ sweep and $\alpha = 24°$ having a $77°$ sweep, increasing with angle-of-attack. Furthermore, the spanwise location of the vortex interaction on the leading edge moved inboard as angle-of-attack increased from $\alpha = 18°$ at 2.8 in and $\alpha = 24°$ at 0.8 in from the root chord (c_{root}). Taking all three performance parameters trends, equivalent performance solutions and flow physics into consideration, the passive BLF CFD model was confirmed to be accurate and valid for the purposes of this study.

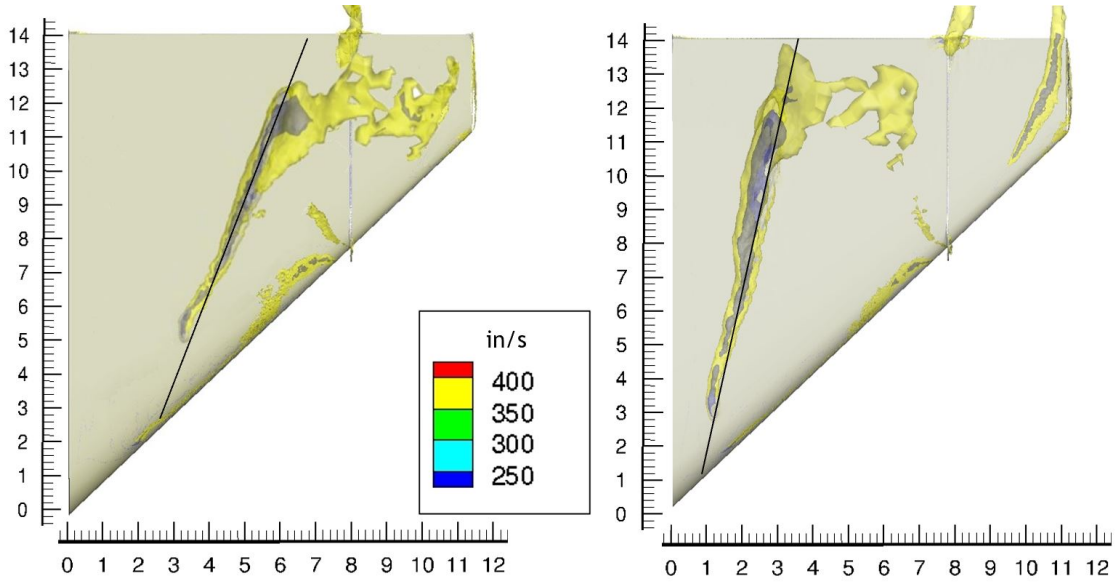

Figure 41. NACA 0012 Cropped Delta-Wing Passive BLF CFD Model Vortex Core Comparison, $\alpha = 18°$ and $24°$, Re = 5x10^5, Iso-Surface Velocity Magnitude

4.1.3.3 AFC Slot CFD Model Validation Analysis

Analysis of the AFC Slot $C_\mu = 0.49\%$ CFD configuration with respect to Demoret et al. wind tunnel experimental data reveal a maximum deviation in coefficient of drag (C_D) and lift (C_L) performance measures, listed in Table 14, being within 5% anticipated. Furthermore, the C_D and C_L CFD values trended as expected with minimal variation throughout the angle-of-attack sweep, shown in Figures 42 and 43 respectively, with maximum deviations occurring beyond indicated stall angle-of-attack. Coefficient of momentum experienced a maximum deviation of more than the anticipated 5% at $\alpha = 24°$, shown in Figure 44. However, all other solution values with corresponding angles-of-attack trend as expected with the experimental data indicating this solution as a possible outlier.

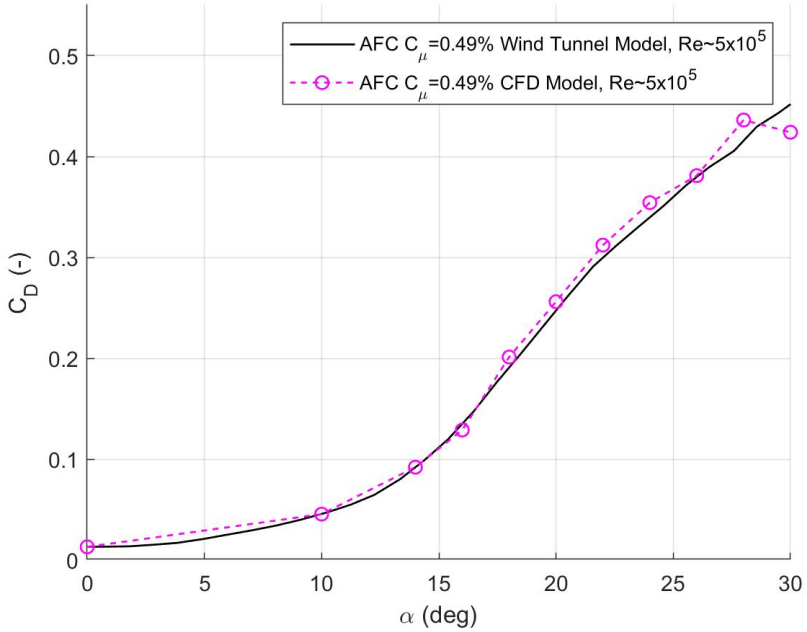

Figure 42. NACA 0012 Cropped Delta-Wing AFC Slot Coefficient of Drag (C_D) CFD Model and Wind Tunnel Comparison, $\alpha = 0°$ to $30°$, Re = 5x10^5, $C_\mu = 0.49\%$

Further validation of the AFC Slot $C_\mu = 0.49\%$ configuration flow physics included analysis of the primary vortex core development and location at varying angles-of-

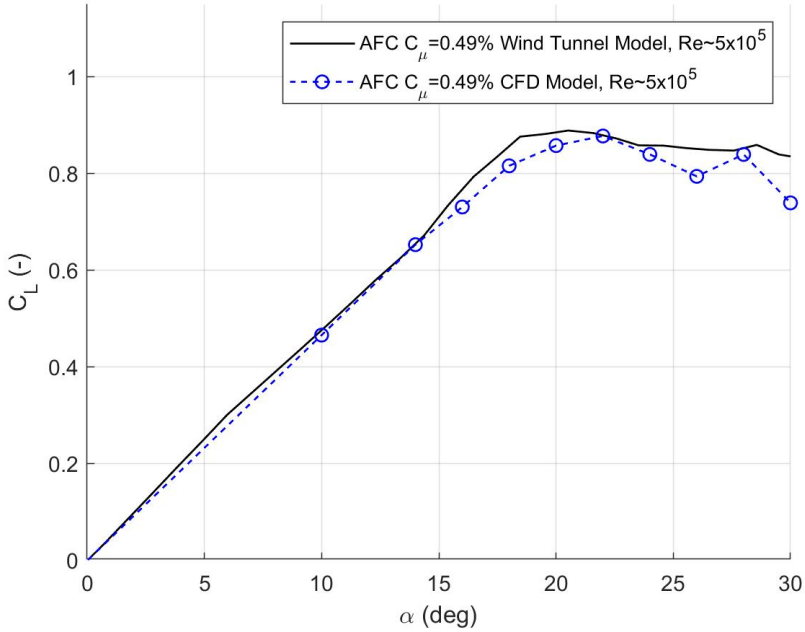

Figure 43. NACA 0012 Cropped Delta-Wing AFC Slot Coefficient of Lift (C_L) CFD Model and Wind Tunnel Comparison, $\alpha = 0^\circ$ to 30°, Re = 5x10^5, $C_\mu = 0.49\%$

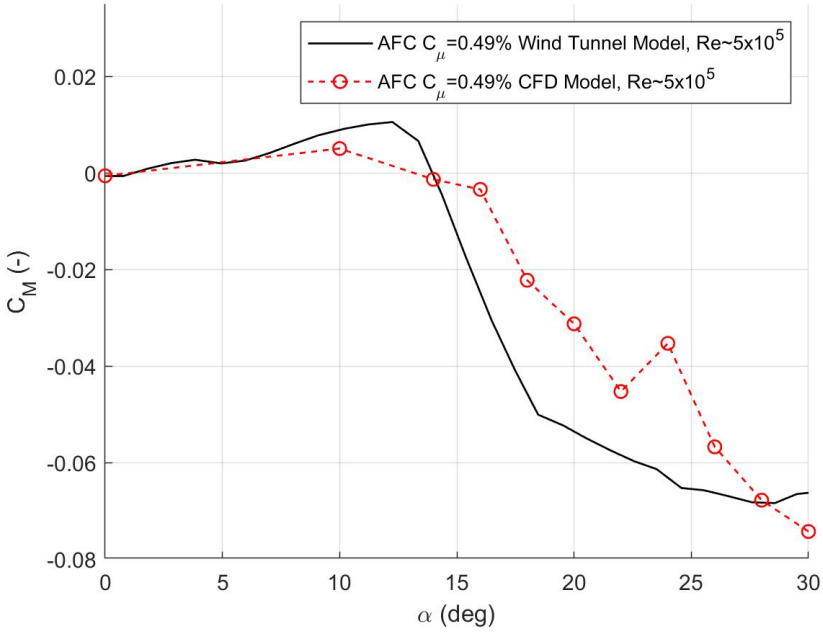

Figure 44. NACA 0012 Cropped Delta-Wing AFC Slot Pitching Moment Coefficient (C_M) CFD Model and Wind Tunnel Comparison, $\alpha = 0^\circ$ to 30°, Re = 5x10^5, $C_\mu = 0.49\%$

attack. Analogous to the baseline and passive BLF CFD models, a shift in the vortex spanwise location, relative to the leading edge, and change in sweep angle based upon angle-of-attack was indicated. Passive AFC slot model primary vortex core visualizations were produced at $\alpha = 18°$ and $24°$, Figure 45, and confirm variations consistent with literature with a shift in the vortex core, both in sweep and spanwise location. Sweep variation was measured with $\alpha = 18°$ having a $65°$ sweep and $\alpha = 24°$ having a $74°$ sweep, increasing with angle-of-attack. Furthermore, the spanwise location of the vortex interaction on the leading edge moved inboard as angle-of-attack increased from $\alpha = 18°$ at 2.6 in and $\alpha = 24°$ at 0.8 in from the root chord (c_{root}). Taking all three performance parameters trends, equivalent performance solutions and flow physics into consideration, the AFC Slot $C_\mu = 0.49\%$, CFD model was confirmed to be accurate and valid for the purposes of this study.

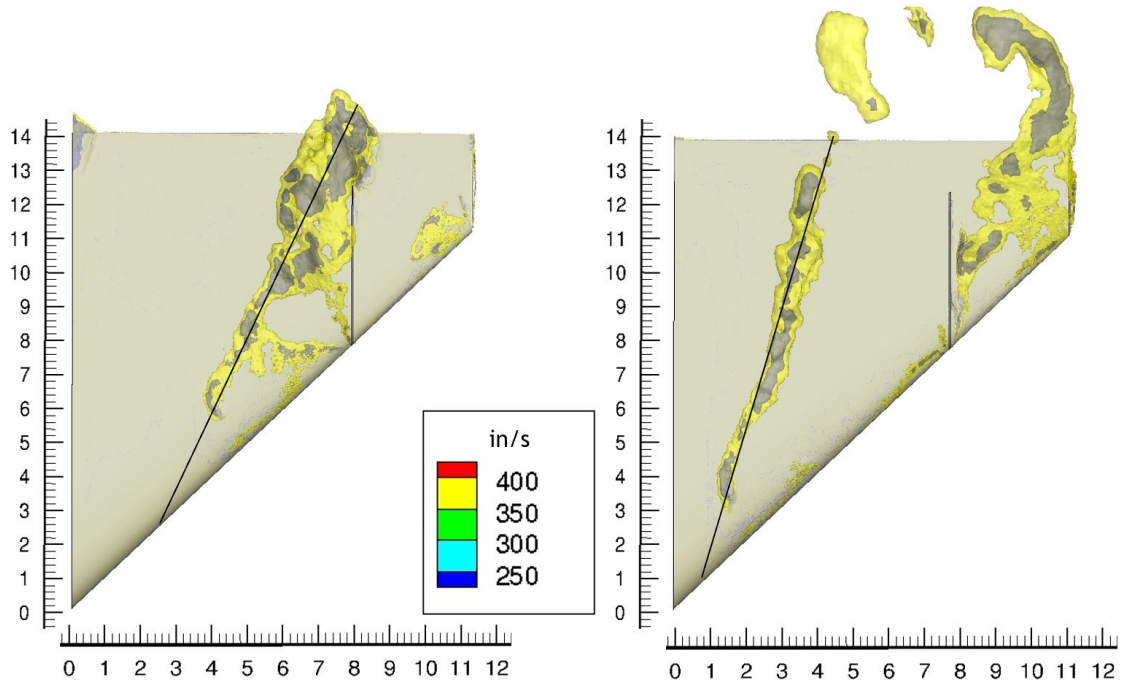

Figure 45. NACA 0012 Cropped Delta-Wing AFC Slot, $C_\mu = 0.49\%$, CFD Model Vortex Core Comparison, $\alpha = 18°$ and $24°$, Re = 5x10^5, Iso-Surface Velocity Magnitude

4.2 Primary Testing Results

4.2.1 AFC Slot Width Optimization Results

The active flow control (AFC) slot width optimization study utilized the five scaled slot Mach numbers (M1-M5) listed in Table 6, which related slot velocity and ultimately mass flow, along with the five varying slot width (SW1-SW5) geometries, listed in Table 9. The 25 individual AFC slot performance configurations were simulated and performance coefficients described in Section 3.4 were produced for comparison and listed in Table 15. Coefficient of lift (C_L) indicated the highest performance gain overall, based upon Demoret et al. experimental results, thus C_L was focused on as a suitable initial comparative performance measure. All data was gathered at $\alpha = 24^\circ$ for each configuration as outlined in Section 3.6.2.1.

Calculation of the coefficient of lift percent gains ($C_{L,\%Gain}$) versus baseline CFD coefficient of lift ($C_{Lmax,Baseline} = 0.8021$) indicated the highest performing configurations with respect to increased lift. Comparison of these results revealed the highest lift performance configurations for each slot width (SW) was composed of the highest slot velocity (M5), or Mach, within that grouping. This indicates that the performance of the slot was directly related to momentum introduced to the system (C_μ). This deduction was a parallel assessment to Demoret et al. wind tunnel experimental results. However, with regards to energy reduction, in the form of $C_{L,\%Gain}$ per C_μ, the smallest slot velocity (M1) produced the most efficient use of the momentum added to the system with the least amount of overall gain in lift.

Of the highest lift performance configurations, four solutions produced significant gains which indicated potential candidates for selection as the optimized configuration. Arrangements included two experimental configurations (SW1 at M5 and SW1 at M4), which slot width reduction was deemed necessary for real-world use and removed them from contention, and the highest performing configurations from SW2

	Designator	$C_{L,\alpha=24^\circ}$	Δ $C_{L,Baseline}$	$C_{L,\%Gain}$ vs. $C_{Lmax,CFDBaseline}$	Cμ (%)	$C_{L,\%Gain}$/ Cμ
Wind Tunnel	**Baseline**	0.8021	0.0000	0.00	0	NA
	Passive BLF	0.8505	0.0484	6.03	0	NA
	SW1M1	0.8508	0.0487	6.07	0.49	12.39
	SW1M2	0.8861	0.0840	10.47	1.95	5.37
	SW1M3	0.9891	0.1870	23.32	4.4	5.30
	SW1M4	1.1013	0.2992	37.31	7.82	4.77
	SW1M5	1.1484	0.3463	43.17	12.22	3.53
CFD	**SW1M1**	0.8608	0.0587	7.32	0.49	14.94
	SW1M2	0.9165	0.1144	14.27	1.95	7.32
	SW1M3	0.8694	0.0673	8.39	4.4	1.91
	SW1M4	1.0366	0.2345	29.23	7.82	3.74
	SW1M5	1.0891	0.2870	35.78	12.22	2.93
	SW2M1	0.8887	0.0866	10.80	0.392	27.56
	SW2M2	0.8408	0.0387	4.82	1.56	3.09
	SW2M3	0.9017	0.0996	12.42	3.52	3.53
	SW2M4	0.9645	0.1624	20.24	6.256	3.24
	SW2M5	1.0391	0.2370	29.55	9.776	3.02
	SW3M1	0.9245	0.1224	15.26	0.294	51.91
	SW3M2	0.9211	0.1190	14.83	1.17	12.68
	SW3M3	0.9020	0.0999	12.46	2.64	4.72
	SW3M4	0.9434	0.1413	17.62	4.692	3.75
	SW3M5	0.9984	0.1963	24.48	7.332	3.34
	SW4M1	0.8682	0.0661	8.24	0.196	42.06
	SW4M2	0.8998	0.0977	12.18	0.78	15.61
	SW4M3	0.9147	0.1126	14.04	1.76	7.98
	SW4M4	0.9241	0.1220	15.21	3.128	4.86
	SW4M5	0.8754	0.0733	9.14	4.888	1.87
	SW5M1	0.8615	0.0594	7.41	0.098	75.59
	SW5M2	0.8637	0.0616	7.69	0.39	19.71
	SW5M3	0.9236	0.1215	15.14	0.88	17.21
	SW5M4	0.8928	0.0907	11.30	1.564	7.23
	SW5M5	0.8948	0.0927	11.56	2.444	4.73

Note:
- All Measurements at $\alpha = 24^\circ$,
- CFD Baseline $C_{Lmax} = 0.8021$

Table 15. NACA 0012 Cropped Delta-Wing AFC Slot Width CFD Optimization Data Comparison, $\alpha = 24^\circ$, Re = 5x10^5

(80% of SW1) and SW3 (60% of SW1) utilizing the highest Mach setting, M5. Comparison of the latter configurations revealed a variation in C_L of approximately 4%, in favor of SW2 at M5, with a significant variation in C_μ of approximately 33%, favoring SW3 at M5. Furthermore, visualization of the data, $C_{L,\%Gain}$ versus C_μ in Figure 46, reveal the overall performance of SW3 as producing lift performance gains with a consistent reduction in output momentum, specifically at low C_μ values. For the above-mentioned attributes of the SW3 (0.0222 in) at M5 (Mach = 0.8731) and momentum conservation outweighing the minimal variation in lift gain from SW2 at M5, the afore mentioned configuration was chosen as the optimal selection for use in

the continued AFC slot optimization study.

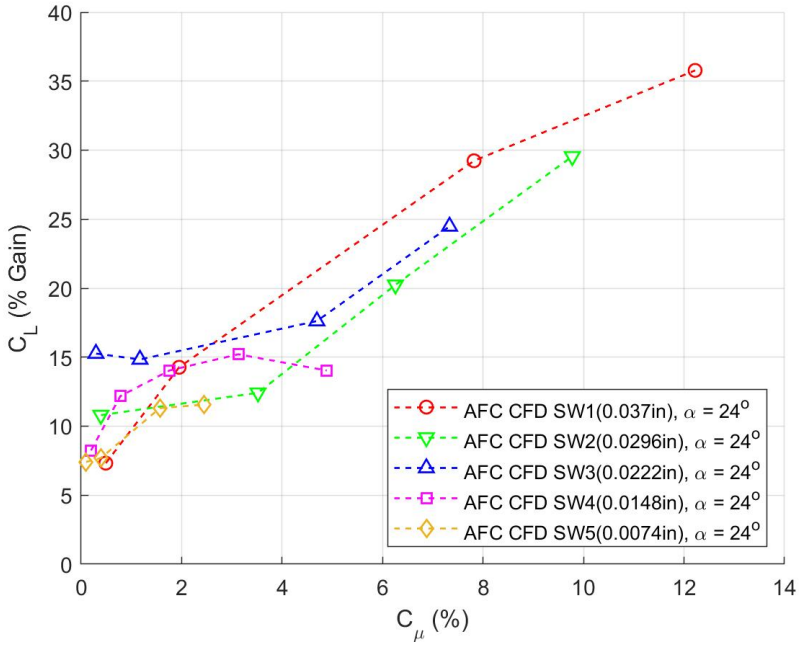

Figure 46. NACA 0012 Cropped Delta-Wing AFC Slot Width Optimization: Coefficient of Lift Percent Gain ($C_{L,\%Gain}$) vs. Coefficient of Momentum (C_μ) Comparison, $\alpha = 24°$, Re = 5x10^5

4.2.2 AFC Slot Length Optimization Results

The active flow control (AFC) slot length, or extent, optimization study utilized the eight configurations (EX1 thru EX8) outlined in Table 11 along with slot width optimized results described in Section 4.2.1. Updated configuration parameters were computed utilizing the optimized slot width and Mach (SW3 = 0.0222 in at M5 = 0.8731) and listed in Table 16 along with AFC slot performance coefficients, described in Section 3.4. Coefficient of lift (C_L) captured the highest performance gain overall, as stated in Section 4.2.1, thus C_L was focused on as a suitable initial comparative performance measure. All data was gathered at $\alpha = 24°$ for each configuration as outlined in Section 3.6.2.2.

Similar to the slot width optimization, calculation of the coefficient of lift percent

gains ($C_{L,\%Gain}$) versus baseline CFD coefficient of lift ($C_{Lmax,Baseline} = 0.8021$) indicated the highest performing configurations with respect to increased lift. Comparison of the results annotated in Table 16 revealed the highest lift performance configurations for each slot extent (EX) integrated the largest slot areas in the simulation, in turn relating increased momentum with performance gains. However, configurations incorporating the lower surface of the AFC slot (-0.25 to 0 x/c) had reduced performance output, with increased C_μ, compared to the configuration with equal upper surface AFC slot length, with reduced C_μ.

Designator	**Surface Measurement (x/c)**	**Area (in^2), Constant SW3**	**C$_{L,\alpha=24^\circ}$**	**Δ C$_{L,Baseline}$**	**C$_{L,\%Gain}$ vs. C$_{Lmax,CFDBaseline}$**	**C$_\mu$ (%)**	**C$_{L,\%Gain}$/ Cμ**
EX1	-0.25 to 0.75	0.1521	0.9984	0.1963	24.47	7.332	3.34
EX2	-0.25 to 1.0	0.1901	1.0701	0.268	33.41	9.165	3.65
EX3	-0.25 to 0.5	0.1141	0.9398	0.1377	17.17	5.499	3.12
EX4	0 to 0.75	0.1141	0.9992	0.1971	24.57	5.499	4.47
EX5	0 to 0.5	0.0760	0.9558	0.1537	19.16	3.666	5.23
EX6	0 to 0.25	0.0380	0.9065	0.1044	13.02	1.833	7.10
EX7	0 to 1.0	0.1521	1.1089	0.3068	38.25	7.332	5.22
EX8	0.25 to 1.0	0.1141	1.0399	0.2378	29.65	5.499	5.39

Note:
- All measurements simulated at $\alpha = 24^\circ$
- CFD Baseline C$_L$ = 0.8021
- Zero indicates the leading edge
- Negative values follow the bottom surface
- Positive values follows the top surface

Table 16. NACA 0012 Cropped Delta-Wing, with Optimized Slot Width (SW3 = 0.0222 in), Slot Extent CFD Optimization Data Comparison, $\alpha = 24^\circ$, Re = 5x10^5

Results from Table 16 were plotted in Figure 47 and likewise detail the increased performance with removal of the lower portion of the AFC slot (-0.25 to 0 x/c). Furthermore, analysis of similar slot areas, specifically, EX3, EX4 and EX8, experiences a continuous increase in C_L performance gains as initial slot interaction moved away from the leading edge toward the trailing edge. This indicated that the AFC slot gains were dependent on where the slot interacted chordwise with the flow Interactions further aft on the wing surface produced higher performance gains compared with interactions near the leading edge. With these reductions in scale and energy injection, the AFC slot was optimized. Additionally, unlike the passive BLF which wraps around the leading edge, the AFC slot hindered performance gains when the

slot momentum interacts with the lower surface of the wing. Section 4.3 detailed the flow field interactions.

Considering the highest coefficient of lift percent gains ($C_{L,\%Gain}$) with substantial $C_{L,\%Gain}/C\mu$ output, EX7 produced a 38.25% gain, an increase of 13.77% from the slot width analysis, without an increase in momentum. Thus, the optimal configuration with respect to slot width and extent optimization consisted of the configuration designators SW3 (0.0222 in) with EX7 (0 to 1.0 x/c) at M5 (Mach = 0.8731). The final computational comparison utilized this configuration for optimized performance parameter generation.

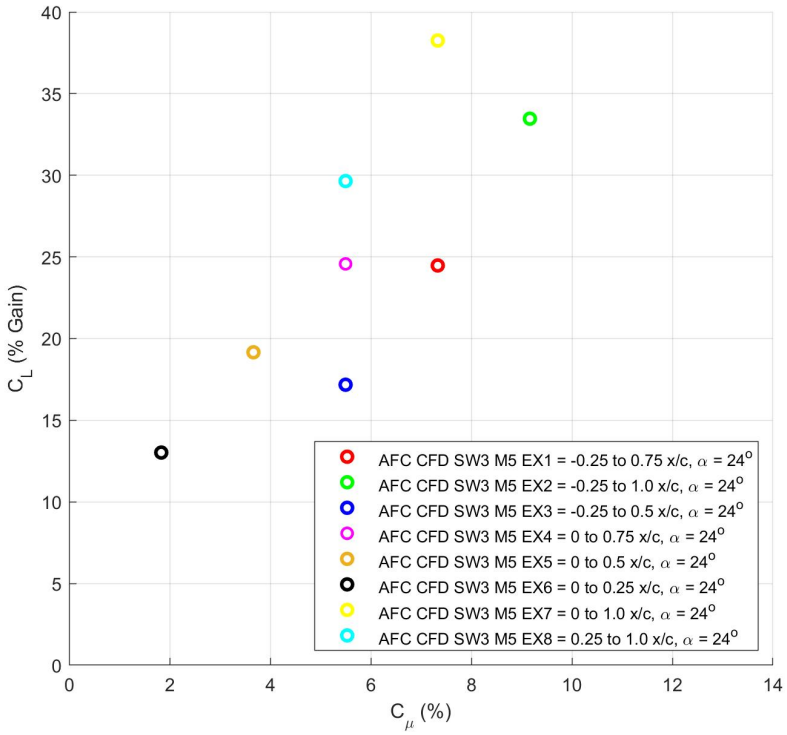

Figure 47. NACA 0012 Cropped Delta-Wing AFC Slot Length (Extent) Comparison: Coefficient of Lift Percent Gain ($C_{L,\%Gain}$) vs. Coefficient of Momentum (C_μ), $\alpha = 24°$, Re = 5x10^5, Slot Width (SW3) = 0.0222 in, Mach (M5) = 0.8731

4.3 Flow Visualization

The CFD generated flow fields of the baseline, passive BLF, best performing AFC slot wind tunnel configuration and optimized AFC slot configuration were compared to assess the critical flow features participating in the flow control performance enhancements. These visualizations provide insight into the mechanisms which aided previously reported configurations to outperform applied flow control methods.

Qualitative analysis of the surface pressure contour plots of the upper and lower surfaces of the NACA 0012 cropped delta-wing, Figures 48 and 49 respectively, reveal low and high pressure interactions with the various flow control configurations. Comparison of the upper surface pressure contour reveal large low pressure regions inboard of the AFC slot configurations, (c and d of Figure 48 with slot indicated by the arrow). These low-pressure regions produce suction on the surface which can be attributed to the significant increase in lift performance when compared to the baseline (a) and passive BLF (b with fence location indicated by the arrow). Compared to the passive BLF (b), the AFC slot configurations produce more low-pressure outboard of the slot. Comparison of the slot configurations (c and d) reveal the optimized solution (d) with the longer slot extent produced a larger surface area of low-pressure outboard of the slot. However, the increased momentum of the original wind tunnel model (c) generated a larger area of low-pressure inboard of the AFC slot. Analysis of the AFC slot configuration upper surfaces do not clearly indicate how the optimized AFC slot configuration outperformed the wind tunnel configuration at $\alpha = 24^{\circ}$ due to both surface pressure contours being similar in average pressure over the upper surface and not indicating any large disparities.

Analysis of the lower surfaces pressure contours, Figure 49, immediately revealed the distinction among the flow control models. The wind tunnel AFC slot configuration (c) wrapped around the leading edge of the wing, similar to the passive BLF (b),

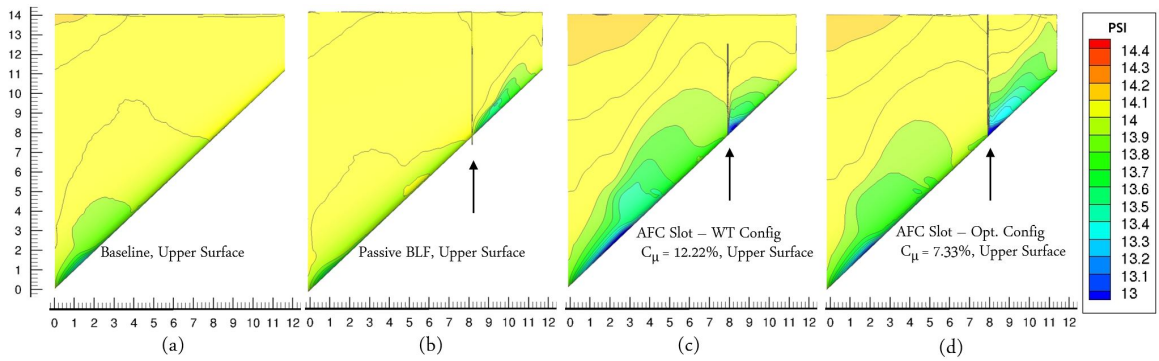

Figure 48. NACA 0012 Cropped Delta-Wing Upper Surface Pressure (PSI) Contour Plot, $\alpha = 24°$, Re = 5x10^5: (a) Baseline Configuration, (b) Passive BLF Configuration, (c) AFC Slot Wind Tunnel (WT) Configuration, $C_\mu = 12.22\%$, (d) AFC Slot Optimized Configuration, $C_\mu = 7.33\%$

and injected airflow on the lower surface of the wing. This airflow injection disrupted the high-pressure region necessary to produce lift. The optimized slot configuration (d) does not disrupt the high-pressure region, thus allowing this configuration to outperform the wind tunnel model with increased lift generation.

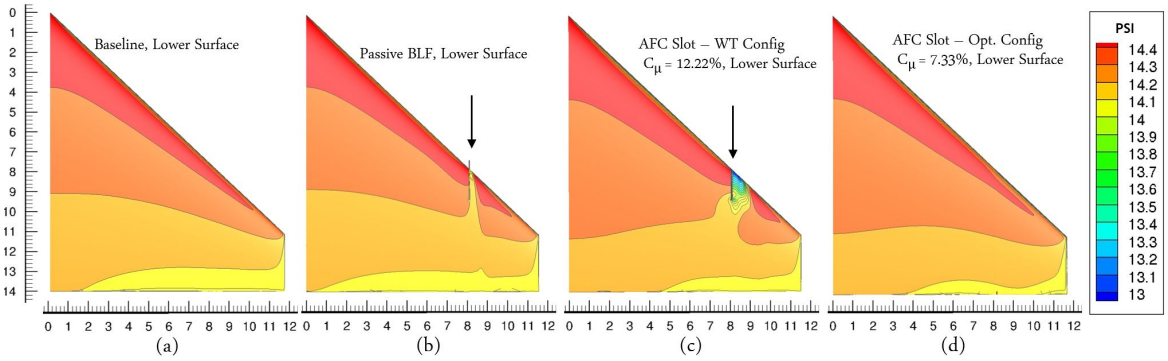

Figure 49. NACA 0012 Cropped Delta-Wing Lower Surface Pressure (PSI) Contour Plot, $\alpha = 24°$, Re = 5x10^5: (a) Baseline Configuration, (b) Passive BLF Configuration, (c) AFC Slot Wind Tunnel (WT) Configuration, $C_\mu = 12.22\%$, (d) AFC Slot Optimized Configuration, $C_\mu = 7.33\%$

Extension of the surface contour into slices within the y-z plane provided an additional dimension of the pressure profile above and below the wing's surface. Slices taken at 60% and 80% chord, shown in Figure 50, revealed the large lower pressure regions created above the surface by the AFC slot configurations in columns (c) and (d). At the 80% chord location, the low-pressure region extends further inboard for

the optimized solution compared to the wind tunnel configuration as well as extending outboard of the AFC slot, marked with an arrow. Furthermore, the previously identified wind tunnel AFC slot interference along the lower high-pressure region was plainly identified at the 80% chord slice. The raised circular shape of the low pressure regions across all configurations indicate the presence of the vortex core, identified through delta-wing research and visualized in Section 4.1.3 while validating the CFD models.

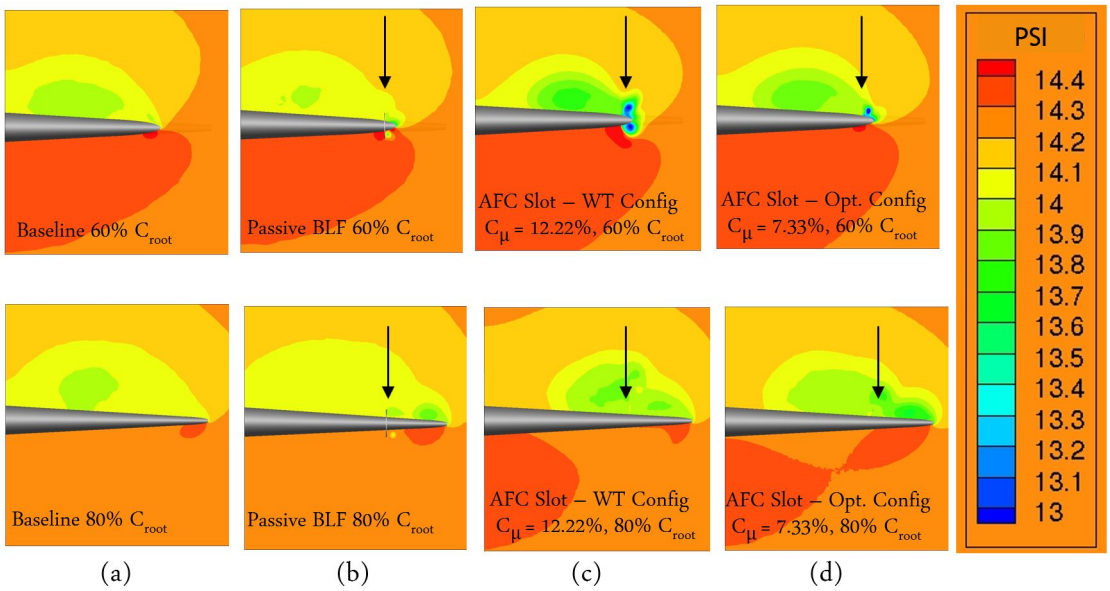

Figure 50. NACA 0012 Cropped Delta-Wing Y-Z Plane Pressure (PSI) Slice, 60% and 80% Chord, $\alpha = 24°$, Re = 5x10^5: (a) Baseline Configuration, (b) Passive BLF Configuration, (c) AFC Slot Wind Tunnel (WT) Configuration, $C_\mu = 12.22\%$, (d) AFC Slot Optimized Configuration, $C_\mu = 7.33\%$

Visualization of surface particle streamtraces provided insight into surface flow interaction related to stall propagation. Delta wing theory, detailed in Section 2.1.3, described stall propagation emanating from the wingtip trailing edge and spreading inboard and toward the leading edge. Furthermore, spanwise flow also indicated regions of stall, thus the implementation of the passive BLF to halt spanwise flow and permit streamwise flow to resume outboard of the fence. Figure 51 provided insight into the particle interactions with the flow control mechanisms on the upper

surface of the wing. The baseline configuration (a) was well beyond its stall limits at $\alpha = 24°$ and clearly show spanwise flow across the majority of the upper surface. The passive BLF (b), with the physical fence marked with an arrow, indicated spanwise flow disruption inboard of the fence and streamwise flow resuming outboard of the fence to the wingtip. The wind tunnel AFC model (c), with the slot marked with an arrow, revealed the flow continuing its streamwise propagation aft of the slot due to the upper surface slot extent of 0 to 0.75 x/c and not continuing to the trailing edge of the wing. Thus, streamwise flow only reoccurred directly outboard of the AFC slot but resumed a spanwise flow direction upon interaction with the unimpeded flow aft of the slot. The optimized AFC slot (d), with the slot indicated by an arrow, continues to the trailing edge and impeded all spanwise flow, similar to the passive BLF. This physical interaction further explained the substantial decrease in surface pressure outboard of the slot, visualized in Figure 48 for the optimized configuration (d).

Continued analysis of lower surface particle streamtraces, illustrated in Figure 52, indicated flow disruption produced by the wind tunnel AFC slot configuration (c). This flow disruption was analogous to the pressure disruption visualized in the

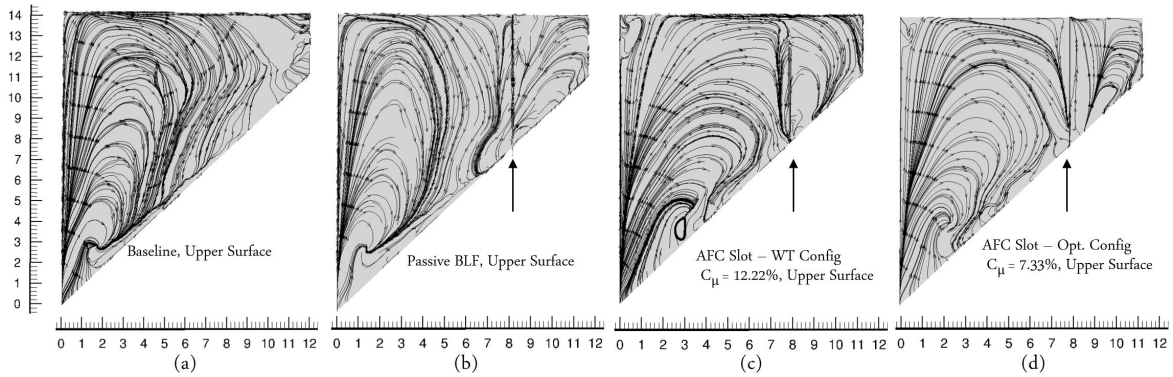

Figure 51. NACA 0012 Cropped Delta-Wing Upper Surface Particle Streamtrace, α = 24°, Re = 5x10^5: (a) Baseline Configuration, (b) Passive BLF Configuration, (c) AFC Slot Wind Tunnel (WT) Configuration, C_μ = 12.22%, (d) AFC Slot Optimized Configuration, C_μ = 7.33%

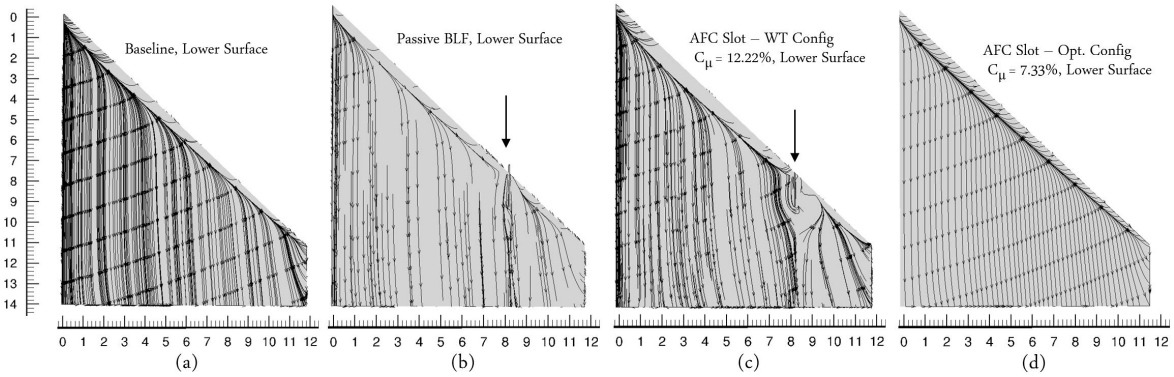

Figure 52. NACA 0012 Cropped Delta-Wing Lower Surface Particle Streamtrace, α = 24°, Re = 5x10^5: (a) Baseline Configuration, (b) Passive BLF Configuration, (c) AFC Slot Wind Tunnel (WT) Configuration, C_μ = 12.22%, (d) AFC Slot Optimized Configuration, C_μ = 7.33%

lower surface pressure contour plot for this configuration, Figure 49(c), affirming the reduced performance being a result of this interaction.

Creation of vector field slices along the y-z plane allowed visualization of the flow field direction while also viewing the magnitude of the flow field velocity. At 40% chord, the vector field provided initial visualization of the primary, leading edge vortex formation along the upper surface of the wing, shown in Figure 53. Specifically, the dark blue coloration indicated a well-developed vortex core propagating inboard toward the root chord (c_{root}), shown in the baseline (a) and passive BLF (b) configurations. The AFC slot configurations, wind tunnel (c) and optimized (d), illustrate higher velocity flow above the vortex core, attributed to the AFC slot airflow injection, seemingly driving the core consistently towards the leading edge for both AFC slot configurations.

At 60% chord, the vector field interacted with the flow control devices indicated by arrows in Figure 54. For the baseline (a) and passive BLF (b) configurations, the low velocity primary leading edge vortex core continued within close proximity to the c_{root} while the primary leading edge vortex core for the AFC slot configurations continued along a path relative to the leading-edge sweep, indicating entrainment of

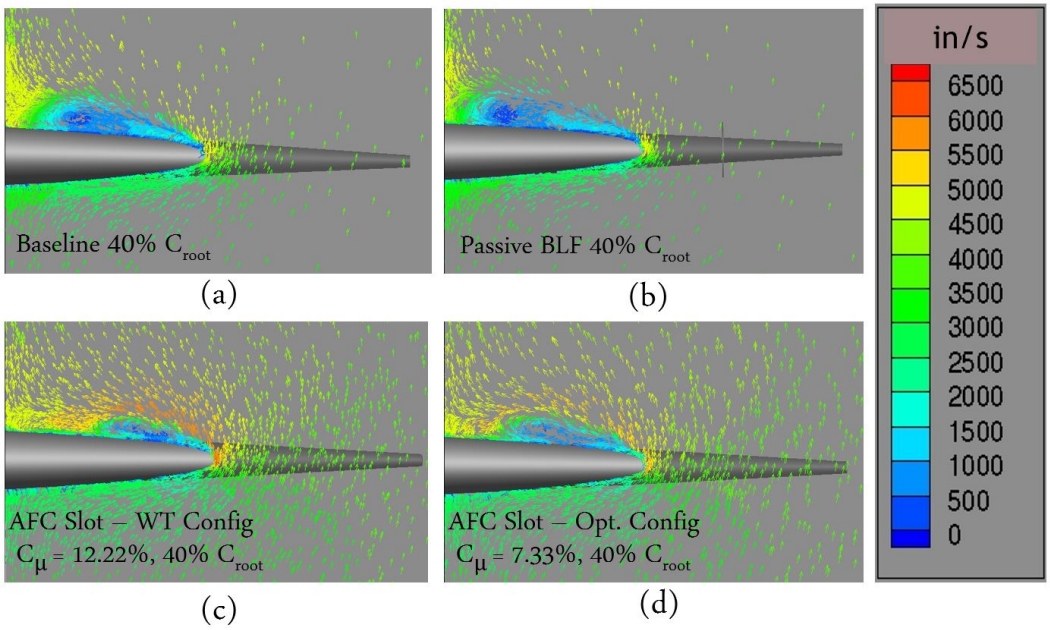

Figure 53. NACA 0012 Cropped Delta-Wing Y-Z Plane Vector Slice Colored by Velocity Magnitude (in/s) 40% Chord, $\alpha = 24°$, Re = 5x10^5: (a) Baseline Configuration, (b) Passive BLF Configuration, (c) AFC Slot Wind Tunnel (WT) Configuration, C_μ = 12.22%, (d) AFC Slot Optimized Configuration, C_μ = 7.33%

the primary leading edge vortex with the AFC slot airflow.

At 80% chord, the vector field interacted with the flow control devices indicated by arrows in Figure 55. For the baseline (a) and passive BLF (b) configurations, the low velocity primary leading edge vortex core continues near the c_{root} and visualization of the wing tip vortex comes into view. The passive BLF configuration was seen to have additional flow interaction outboard of the passive fence similar to the interactions illustrated with the wind tunnel (c) and optimized (d) AFC slot configurations. The vortex cores for the AFC slot configurations remained inboard of the slot with a large spiraling vortex remaining over the majority of the wing's upper surface, a further indication of the primary lifting vortex entrainment with the AFC slot airflow. Furthermore, the wingtip vortex of both AFC slot models showed interaction with the slot airflow in a counter rotating manner.

At 100% chord, the vector field interacted with the flow control devices indicated

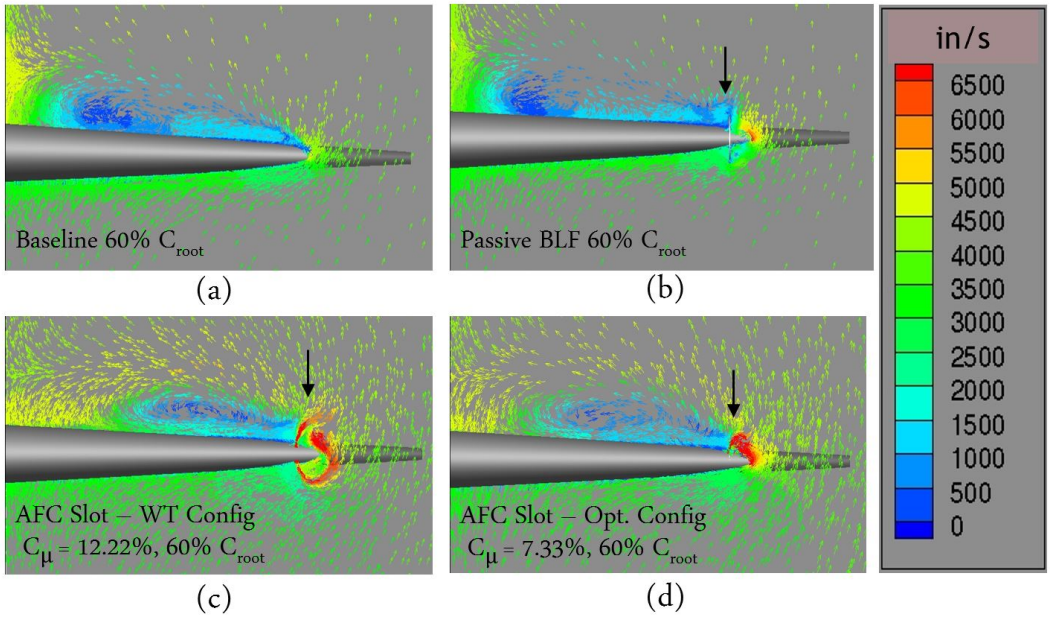

Figure 54. NACA 0012 Cropped Delta-Wing Y-Z Plane Vector Slice Colored by Velocity Magnitude (in/s) 60% Chord, $\alpha = 24°$, Re = 5x10^5: (a) Baseline Configuration, (b) Passive BLF Configuration, (c) AFC Slot Wind Tunnel (WT) Configuration, C_μ = 12.22%, (d) AFC Slot Optimized Configuration, C_μ = 7.33%

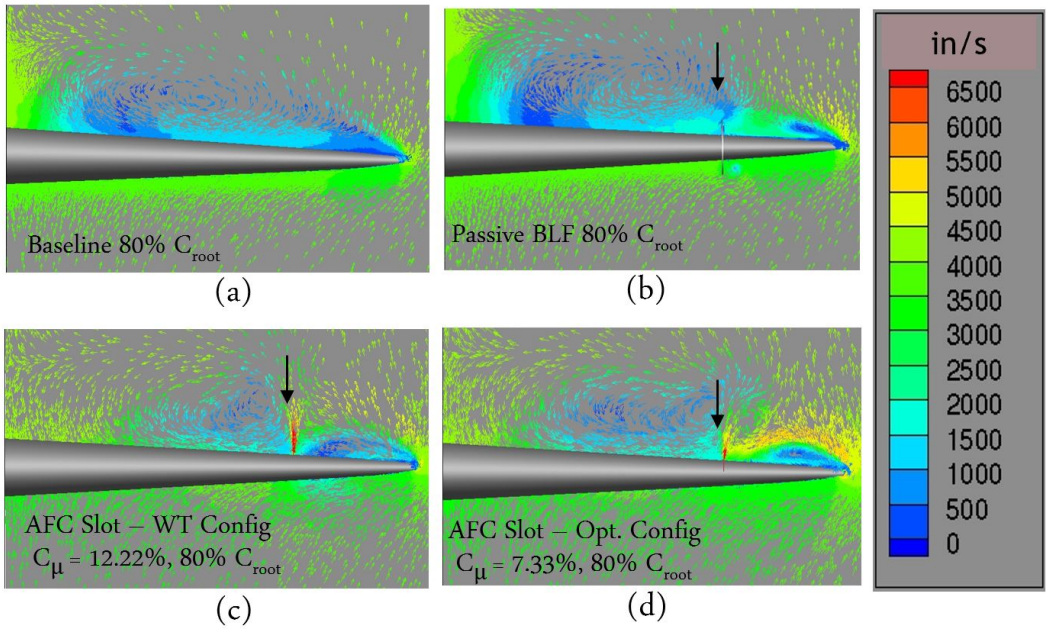

Figure 55. NACA 0012 Cropped Delta-Wing Y-Z Plane Vector Slice Colored by Velocity Magnitude (in/s) 80% Chord, $\alpha = 24°$, Re = 5x10^5: (a) Baseline Configuration, (b) Passive BLF Configuration, (c) AFC Slot Wind Tunnel (WT) Configuration, C_μ = 12.22%, (d) AFC Slot Optimized Configuration, C_μ = 7.33%

by arrows in Figure 56. For the baseline (a) and passive BLF (b) configurations, the low velocity vortex core lifted from the surface of the wing, no longer producing vortex lift. However, the BLF wingtip vortex showed to be intact with strong vector rotation energizing the boundary-layer. The wind tunnel AFC slot configuration (c) primary vortex has also lifted from the surface of the wing. Likewise, the wingtip vortex lifted from the surface indicating no additional performance gains were provided from the flow structure. However, the optimized AFC slot configuration (d) primary vortex continued to show low speed vector rotation near the slot and surface of the wing due to the slot extending to the trailing edge. Continued interaction with the wing tip vortex and AFC slot energized the flow outboard of the flow control mechanism. This allowed for the vortex to stay intact and providing vortex lift between the slot and wingtip. The simultaneous interactions of halting the spanwise flow while also injecting momentum into the primary, leading edge vortex and wingtip vortex are attributes of maximum slot extension to the trailing edge. This analysis coincides with previous visualization analysis of pressure distributions and confirms the vortex-slot viscous entrainment interaction being the primary source of lift performance gains.

Utilizing the quantitative velocity magnitude values of the vortex cores illustrated from the y-z plane slices, 3D iso-surfaces of the vortex cores were generated and shown in Figure 57. All configurations were compared at $\alpha = 24°$. For both the baseline and passive BLF configurations, as determined through analysis of the y-z plane slices, the primary, leading edge vortex extended within close proximity with the root chord (c_{root}) at a steep sweep angle of approximately 75° for the baseline and to 77° for the passive BLF. Furthermore, the leading edge vortex began formation within 1in from the nose of the wing. Vortex interaction with the AFC slot flow entrained the primary vortex of both configurations (c and d) to gravitate toward the source of the injected airflow, reducing the sweep angle of the vortex to 62° for the wind tunnel AFC slot

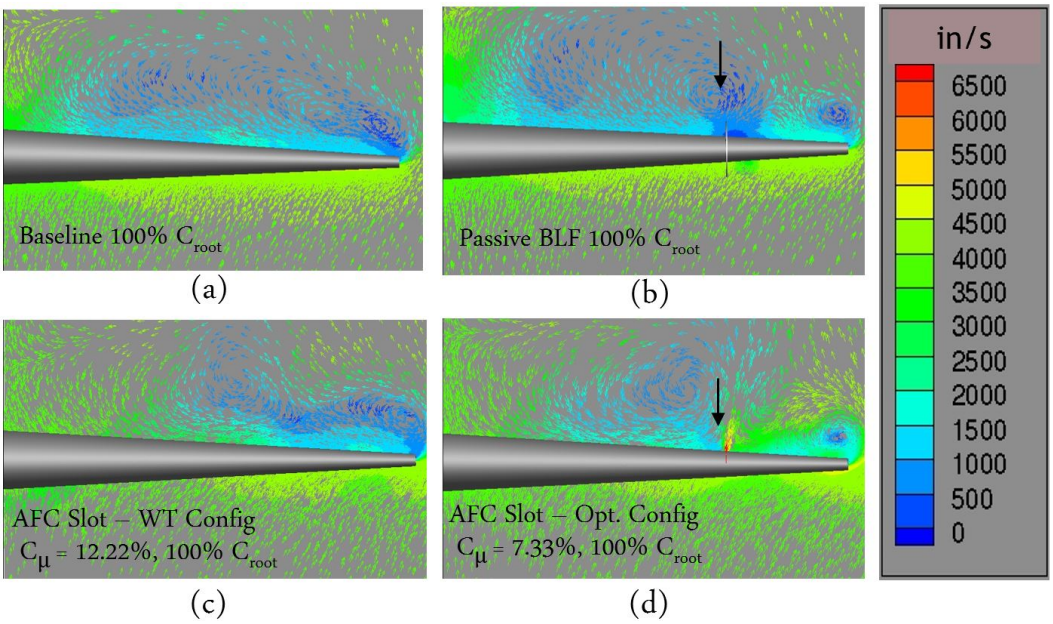

Figure 56. NACA 0012 Cropped Delta-Wing Y-Z Plane Vector Slice Colored by Velocity Magnitude (in/s) 100% Chord, $\alpha = 24°$, Re = 5x10^5: (a) Baseline Configuration, (b) Passive BLF Configuration, (c) AFC Slot Wind Tunnel (WT) Configuration, C_μ = 12.22%, (d) AFC Slot Optimized Configuration, C_μ = 7.33%

configuration and 70° for the optimized AFC slot model. Analysis of the wingtip vortex core indicated the vortex propagated to a position over the wing for all flow control methods and remained intact, while the baseline configuration had separated and broken down. Although the wing tip vortex was present over the wing for the passive BLF, both AFC slot models clearly illustrate the wingtip vortex interacting with the AFC slot injected flow and entrained the vortex to the slot leading edge. This visualization further supports the deduction that the primary, leading edge and wingtip vortices interaction with the AFC slot momentum injection being the primary source of lift performance gains. Furthermore, extension of the slot to the trailing edge allowed the wingtip vortex to be undisturbed and showed a well-defined core structure unlike the AFC slot 0.75 x/c upper slot extent of the best performing wind tunnel configuration.

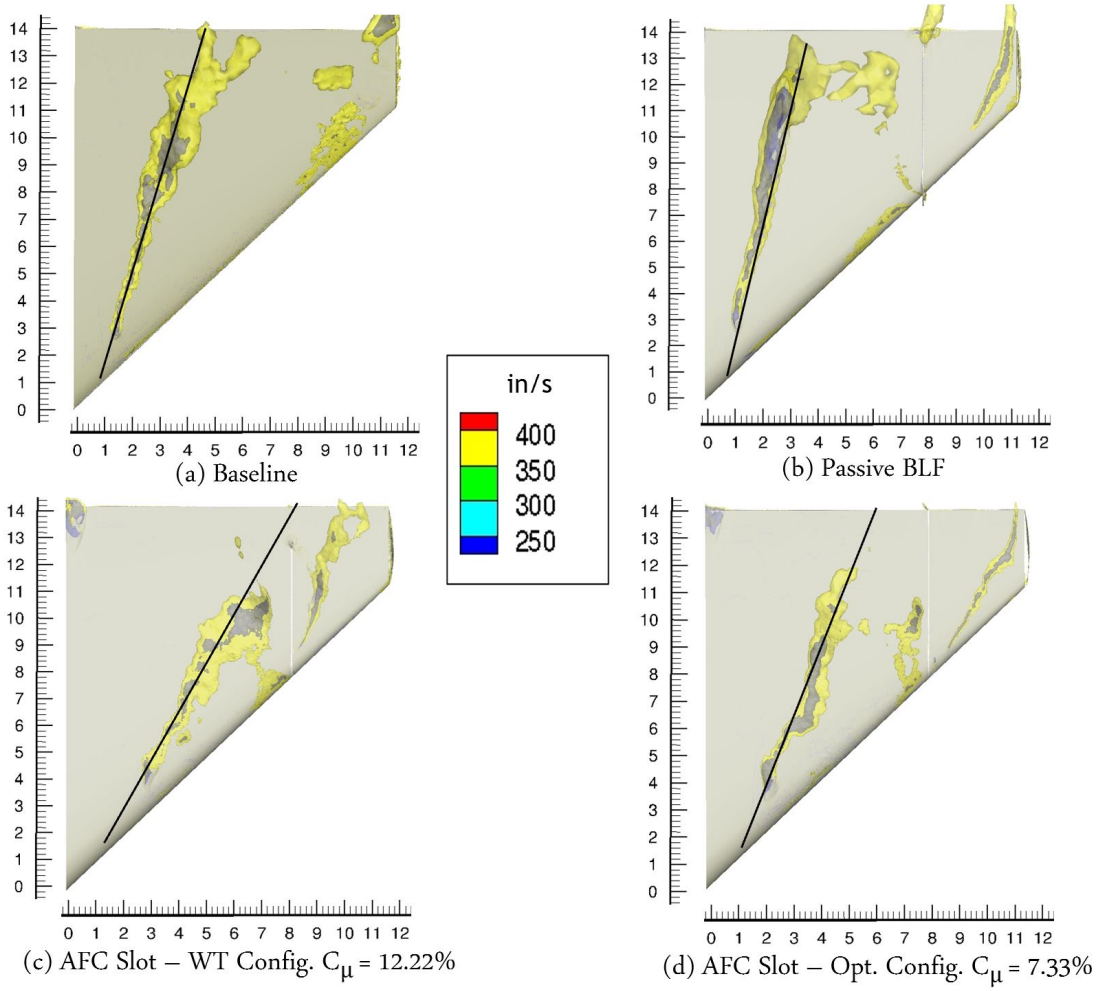

Figure 57. NACA 0012 Cropped Delta-Wing Upper Iso-Surface of Low-Velocity Magnitude (in/s) Vortex Cores, $\alpha = 24°$, Re = 5x10^5: (a) Baseline Configuration, (b) Passive BLF Configuration, (c) AFC Slot Wind Tunnel (WT) Configuration, C_μ = 12.22%, (d) AFC Slot Optimized Configuration, C_μ = 7.33%

4.4 Final Comparison

Utilizing the optimized AFC slot parameters from Sections 4.2.1 and 4.2.2, performance parameters listed in Section 3.4 over a angle-of-attack sweep of 0° to 32° with a $Re = 5\text{x}10^5$ were produced and compared to wind tunnel experimental configurations. Comparison results were compiled in Table 17 for the wind tunnel baseline model, passive BLF model, AFC slot highest performing configuration ($C_\mu = 12.22\%$) and similar producing C_μ model in comparison to the optimized CFD configuration.

The wind tunnel AFC slot $C_\mu = 12.22\%$ was reported by Demoret et al. with a maximum $C_{Lmax,\%Gain} = 61.05\%$. However, with these extraordinary gains produced, the slot dimensions and momentum injected into the system was unrealistic. Reduction and overall optimization of the AFC slot was required. Concluding the optimization study, overall dimensions of the AFC slot were reduced, the slot width by 33.3% and the overall area by 33.3%. According to the coefficient of momentum equation from Section 3.4, momentum reduction scales linearly with area, thus the momentum input was also reduced by 33.3% compared to the wind tunnel's highest input $C_\mu = 12.22\%$. With these reductions in scale and energy injection, the optimized AFC slot for the NACA 0012 cropped delta-wing produced a $C_{Lmax,\%Gain} = 41.09\%$ at $\alpha = 22°$, 6° earlier that the max performing wind tunnel configuration.

Configuration		C_{Lmax}	$\alpha_{C_{Lmax}}$ (deg)	$C_{L,\%Gain}$ vs. $C_{Lmax,CFDBaseline}$	$C\mu$ (%)	$C_{Lmax,\%Gain}$/ $C\mu$	Slot Mach	Slot Width (in)	Slot Extent (x/c)	Area (in^2)
Wind Tunnel	Baseline	0.8021	22	0	NA	NA	NA	NA	NA	NA
	Passive BLF	0.8753	22	9.13	NA	NA	NA	NA	NA	NA
	AFC Slot, Max Performance	1.2918	28	61.05	12.22	5.00	0.8731	0.037	-0.25 - 0.75	0.2535
	AFC Slot, Comparable Performance	1.1246	26	40.21	7.82	5.14	0.6984	0.037	-0.25 - 0.75	0.2535
CFD	Optimal AFC Slot	1.1317	22	41.09	7.33	5.61	0.8731	0.0222	0 to 1.0	0.1521

Table 17. NACA 0012 Cropped Delta-Wing Final Optimization Configuration Vs. Demoret et al. Wind Tunnel Results, Re = 5x10^5

Lift configuration comparisons, via the coefficient of lift (C_L), were plotted in Figure 59. The optimized solution produced increased lift at lower angles-of-attack but does not delay stall of the wing in comparison to AFC slot wind tunnel models. The optimized solution improved upon the lift curve slope which can be attributed to energizing the primary, leading edge vortex, through direct air flow injection, and wingtip vortex, through the production of a counter rotating vortex, via the AFC slot which increased the vortex lift being produced, outlined in Section 4.3.

Drag configuration comparisons, via the coefficient of drag (C_D), were plotted versus angle-of-attack (α) in Figure 59. The plot showed the optimized configuration CFD model trending along the experimental results and producing reduced drag at

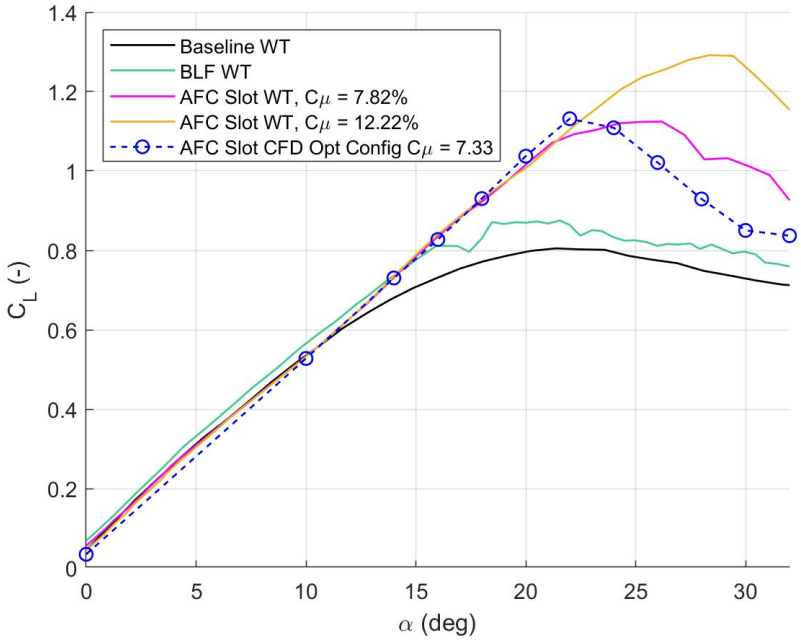

Figure 58. C_L vs α for NACA 0012 Cropped Delta-Wing Configurations, $\alpha = 0°$ to $32°$, Re = 5x10^5

increasing angles-of-attack similar to experimental data. Comparison of drag with respect to lift (C_L vs C_D), also known as the drag polar, showed a more useful representation of the configuration's drag characteristics, given in Figure 60. Also trending with experimental data, the optimized AFC slot does achieve its peak lift with a significantly reduced coefficient of drag, unlike the comparable $C_\mu = 7.82\%$ wind tunnel configuration which almost doubles the drag to achieve the same C_{Lmax}. However, from Figure 58, the comparable $C_\mu = 7.82\%$ wind tunnel configuration achieves its C_{Lmax} an additional 4° after the optimized solution, thus the increased drag associated with achieving the comparable $C_\mu = 7.82\%$ wind tunnel model's C_{Lmax} was the result of the increase angle-of-attack.

Pitching moment configuration comparisons, via the moment coefficient (C_M), were plotted versus angle-of-attack (α) in Figure 61. The plot showed the optimized configuration CFD model trending along the experimental results. For the duration

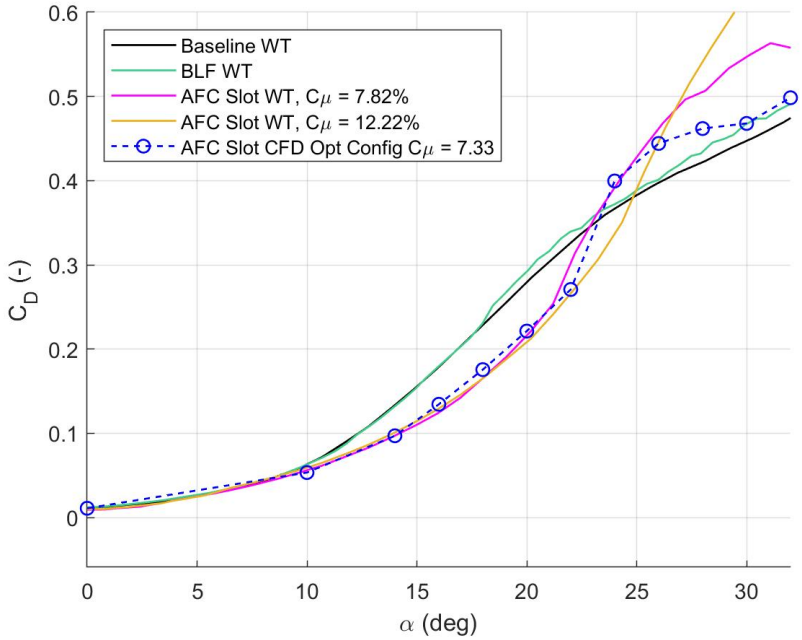

Figure 59. C_D vs. α for NACA 0012 Cropped Delta-Wing Configurations, $\alpha = 0^\circ$ to 32°, Re = 5x10^5

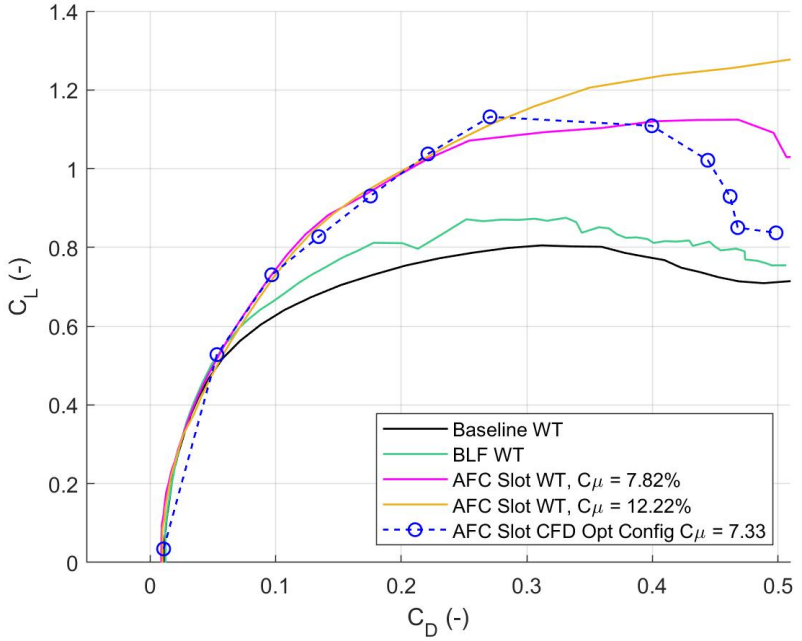

Figure 60. C_L vs. C_D (Drag Polar) for NACA 0012 Cropped Delta-Wing Configurations, $\alpha = 0^\circ$ to 32°, Re = 5x10^5

of the α sweep, the optimized AFC slot produced a continuous negative pitching moment. Furthermore, as indicated by the passive BLF data, a destabilizing pitching moment existed within a delta-wing configuration. However, the optimized AFC slot configuration indicated no destabilizing pitching moment being present, coinciding with the wind tunnel AFC slot models.

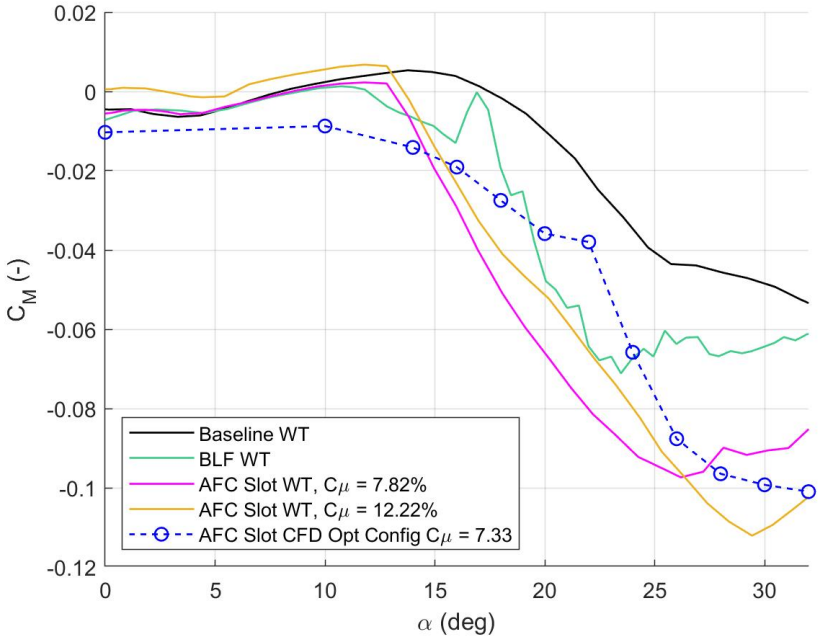

Figure 61. C_M vs. α for NACA 0012 Cropped Delta-Wing Configurations, $\alpha = 0^\circ$ to 32°, Re = 5x10^5

V. Conclusion

5.1 Final Conclusion

Utilizing computational fluid dynamic (CFD) simulations, the presented study was able to further the investigation of replicating and improving upon the performance of a NACA 0012 cropped delta-wing (C_{root} = 14 in, C_{tip} = 2.8 in, $\lambda = 45°$, b = 11.5625 in) at high angles-of-attack with an active flow control (AFC) fluidic fence via wall-normal, steady blowing from an optimized single, chordwise slot located at z/b = 70%, matching that of Demoret's preceding study configuration parameters. The data was generated using CREATE-AV Kestrel v10.1rc5 CFD software on the Department of Defense (DoD) High Performance Computing (HPC) systems. The flight regime was held constant at a Mach numbers of 0.18 and a Reynolds number of 5.0 x 10^5, based on the root chord of 14 in. Computational fluidic performance solutions were successfully compared to previously obtained wind tunnel experimental results of three configurations, baseline, boundary-layer fence and AFC slot of a single momentum coefficients ($C\mu = 0.49\%$), to validate the CFD model prior to slot optimization. Performance parameters compared were coefficients of lift (C_L), drag (C_D) and pitching moment (C_M) at angles-of-attack (α) ranging from 0° to 30°. Optimization parameters included five reduced slot widths, five slot velocities converted to Mach number for use in Kestrel and eight slot length (or extent) configurations. Reduced slot widths were generated in increments of 20% from the original experimental configured slot width. Slot Mach numbers were developed from experimental coefficients of momentum ($C\mu$ = 0.49%, 1.95%, 4.4%, 7.82% and 12.22%) at given volumetric flow rates (200, 400, 600, 800 and 1,000 SLPM). Slot extents varied in length beginning at 0.25 x/c on the lower surface of the wing and continuing around the leading edge to the trailing edge along the upper surface. Performance parameters

used to validate the CFD model, obtained from computationally generated forces and moments, was also used during optimization to capture, compare and assess overall performance gains which also determined the optimal slot parameter configuration. Furthermore, surface flow visualization was assessed with Tecplot 360 in an effort to reveal the unique AFC flow interaction with momentum injecting vortices.

Table 18 shows a summary of the optimization parameters and significant comparative results from experimental results for the present study. Computational results produced accurate comparisons to experimental results, where performance parameter trends and developed fluid structures were analogous with delta-wing characteristics. The optimization produced an overall dimension reduction of the AFC slot, with the slot width reduced by 40%,which likewise reduced the overall area by 40%. With the reduction in area, the momentum input was also decreased by 40% compared to the wind tunnel's highest input $C_{\mu} = 12.22\%$. Removal of the lower 0.25 x/c significantly improved performance due to a negative impact upon the high-pressure region of the lower wing surface. Continuation of the slot on the low-pressure surface from 0.75 x/c to the trailing edge provided an additional performance gain by impeding spanwise flow that translates to stall propagation, injecting added momentum over the lifting surface of the wing and continuing flow interaction with the leading-edge and wingtip vortices. Slot extent analysis indicated that the AFC slot gains were dependent on where the slot interacted chordwise with the flow. Interactions further aft on the wing surface produced higher performance gains compared with interactions near the leading edge. These gain improvements were attributed to the simultaneous interactions of halting the spanwise flow while also injecting momentum into the primary, leading edge vortex and wingtip vortex. With these reductions in scale and energy injection, the optimized AFC slot for the NACA 0012 cropped delta-wing produced a $C_{Lmax,\%Gain} = 41.09\%$ at an $\alpha = 22°$, 6° earlier that the max performing wind

tunnel configuration. Additionally, the optimized AFC slot configuration indicated no destabilizing pitching moment being present, coinciding with experimental wind tunnel results.

Optimized AFC Slot Parameters	
Slot Width (in)	0.0222
Slot Extent (x/c)	0 to 1.0
Mach	0.873
Spanwise Location (z/b)	0.7
Slot Area (in^2)	0.152
Cμ (%)	7.33
C_{Lmax}	1.13
$\alpha_{C_{Lmax}}$	22
$C_{L,\%Gain}$ vs. $C_{Lmax,CFDBaseline}$	41.09
$C_{L,\%Gain}$/ Cμ	5.61
Wind Tunnel AFC Slot Max Performance Comparison	
Momentum Reduction (%)	-40.10
Δ C_L	0.1601
$C_{L,\%Reduction}$ vs. $C_{Lmax,WTMax}$	-12.39
Δ $\alpha_{C_{Lmax}}$ (deg)	7

Table 18. NACA 0012 Cropped Delta-Wing Optimization Parameter Summary, Re = 5x10^5

Visualizations supported the deduction that the primary and wingtip vortices interaction with the AFC slot momentum injection being the primary source of lift performance enhancement. The optimized solution was seen to improve upon total lift which can be attributed to energizing the primary vortex through direct air flow injection and entrainment, and wingtip vortex through the production of a counter rotating vortex, via the AFC slot, increasing the production of vortex lift. The extension of the AFC slot to the trailing edge provided continuous interaction with the primary and wing tip vortices by energizing the flow structures both inboard and outboard of the active flow mechanism. Furthermore, extension of the slot permitted the wingtip vortex to be undisturbed, halting the spanwise flow, allowing the structure to hold a well-defined core across the wing surface. This allowed for the vortices

to stay intact and provided vortex lift across the wing surface at increasing angle-of-attack. Visualization analysis of pressure distributions confirms the vortex-slot viscous entrainment interaction supporting the conclusion of this interaction being the primary source of lift performance gains.

5.2 Future Work

The scope of the current research was the product of previous studies and their results and lessons learned. Reflection of the results produced from the parameters studied revealed additional optimization or reconfiguration of the AFC slot on the NACA 0012 cropped delta-wing was necessary to further reduce momentum, to more realistic thresholds, and improve upon the vortex-slot interaction. Additional areas of interest to be researched include, but are not limited to, a focused investigation on active flow mechanisms physical interaction, including solid slots, sectioned slots, jets, their combination, and steady or pulsed blowing, with a swept wing leading edge vortex, and optimization of the slots spanwise location and sweep angle due to the leading-edge vortex physical characteristics dependence on wing geometry and angle-of-attack. Further investigation also includes effects of multiple spanwise AFC slots on swept wing performance, with the AFC slots capable of being activated and deactivate depending on the leading-edge vortex location during an angle-of-attack sweep, and examination of performance and entrainment effects when applying supersonic slot velocities.

Scheduled continuation of flow control research includes determination of effect of optimal placement of passive vortex generators on a T-38, and flight test of vortex generator configuration with comparison to experimental data, and characterization of wake roll-up utilizing a NACA 0012. Additionally, AFC specific research includes as study of orifice (jet/small slot) geometry, orientation, and location to instigate

lift vortex formation at low angles-of-attack through small perturbation vorticity generation and leading-edge flow separation to enhance lift at low angles-of-attack.

Appendix A. Time-Resolution Plots

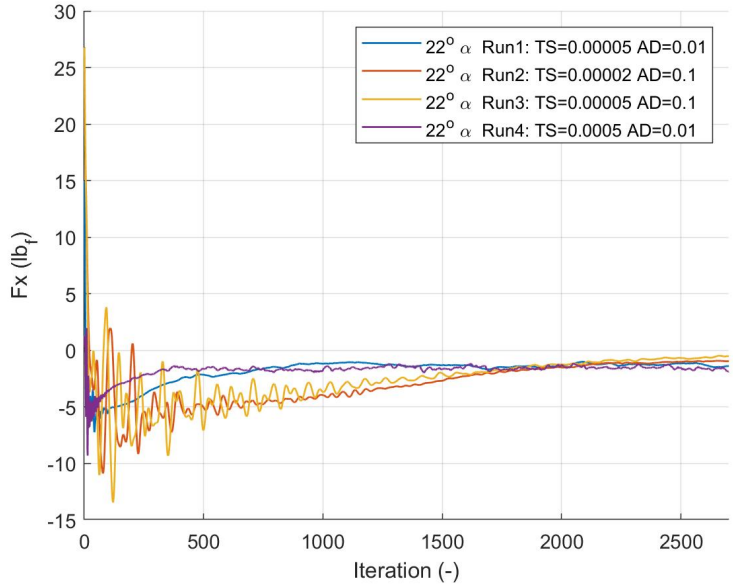

Figure 62. NACA 0012 Cropped Delta-Wing Baseline CFD Model Axial Force (Fx) Time Resolution Results, $\alpha = 22°$, Re = 5x10^5, Time Step (TS) and Advective Damping (AD)

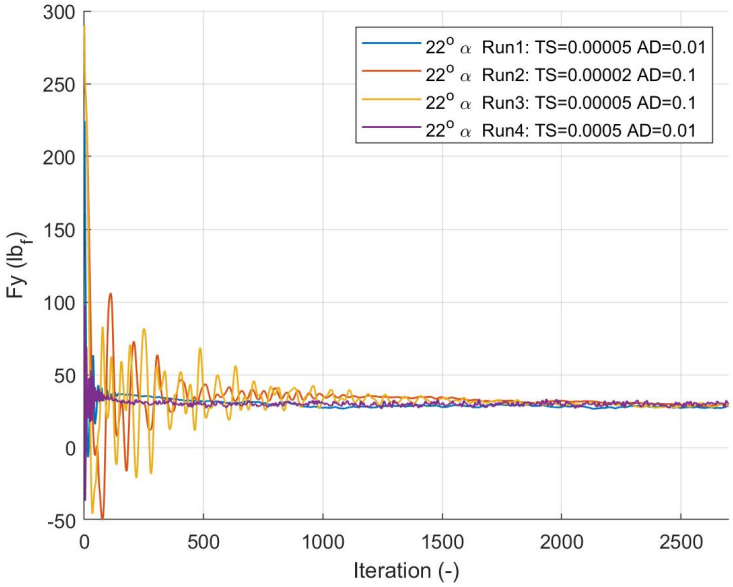

Figure 63. NACA 0012 Cropped Delta-Wing Baseline CFD Model Normal Force (Fy) Time Resolution Results, $\alpha = 22°$, Re = 5x10^5, Time Step (TS) and Advective Damping (AD)

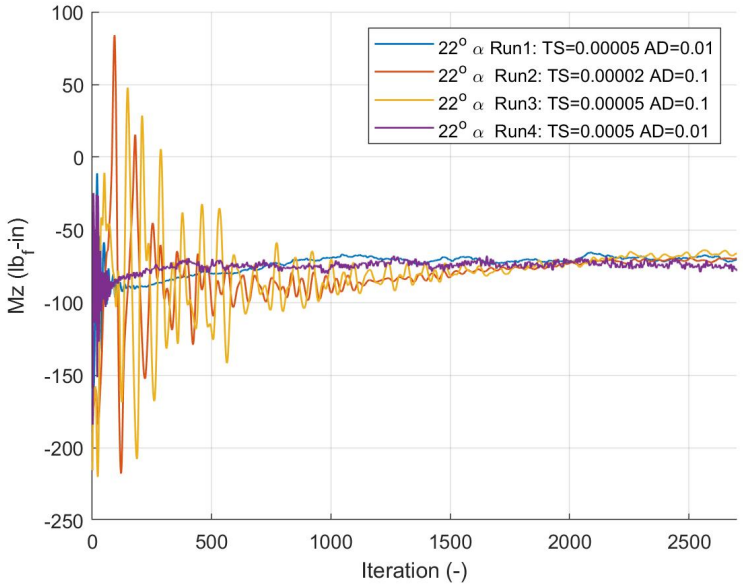

Figure 64. NACA 0012 Cropped Delta-Wing Baseline CFD Model Moment About Z-Axis (Mz) Time Resolution Results, $\alpha = 22^{\circ}$, Re = 5x10^5, Time Step (TS) and Advective Damping (AD)

Appendix B. Mesh Refinement Plots

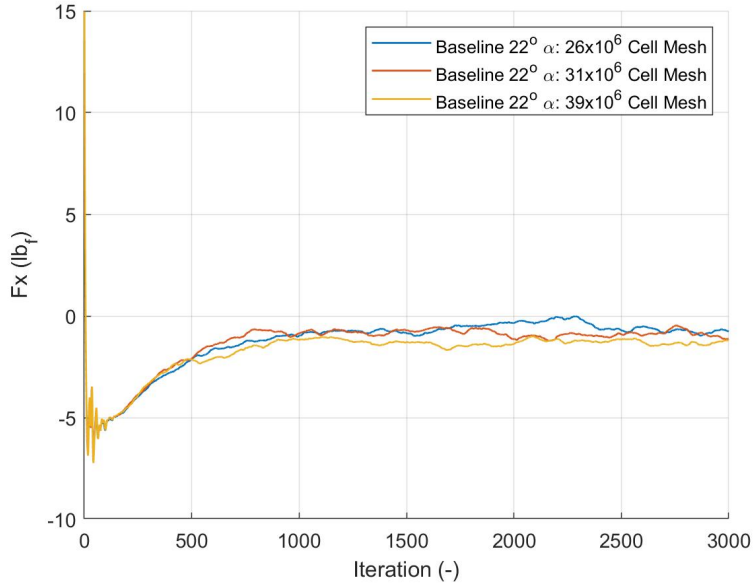

Figure 65. NACA 0012 Cropped Delta-Wing Baseline Axial Force (Fx) Per Iteration CFD Mesh Study Results, $\alpha = 22°$, Re = 5x10^5

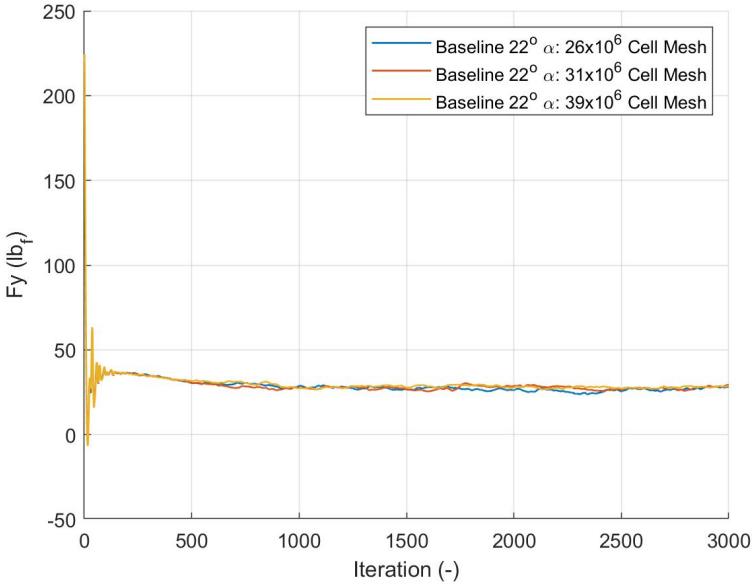

Figure 66. NACA 0012 Cropped Delta-Wing Baseline Normal Force (Fy) Per Iteration CFD Mesh Study Results, $\alpha = 22°$, Re = 5x10^5

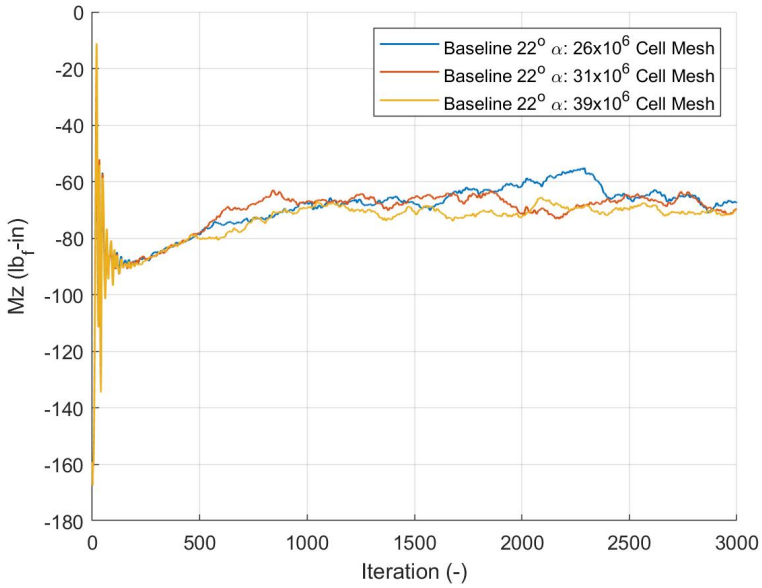

Figure 67. NACA 0012 Cropped Delta-Wing Baseline Moment About Z-Axis (Mz) Per Iteration CFD Mesh Study Results, $\alpha = 22^{\circ}$, Re = 5x10^5

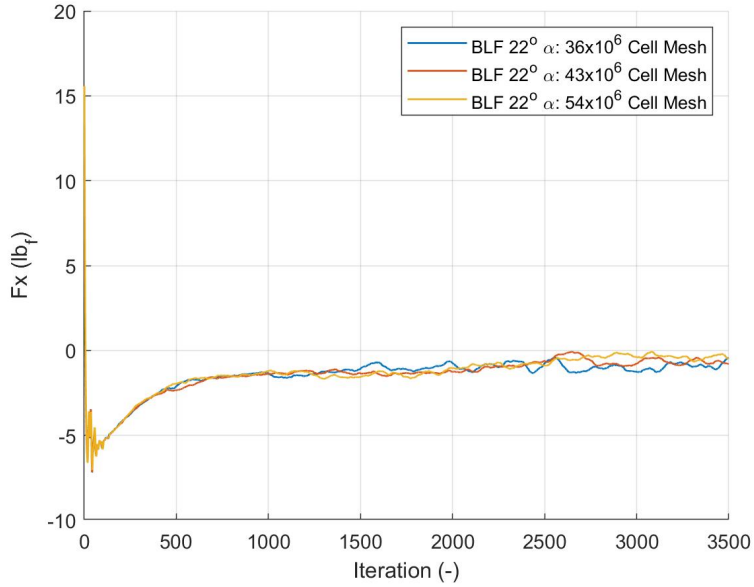

Figure 68. NACA 0012 Cropped Delta-Wing Passive BLF Axial Force (Fx) Per Iteration CFD Mesh Study Results, $\alpha = 22^{\circ}$, Re = 5x10^5

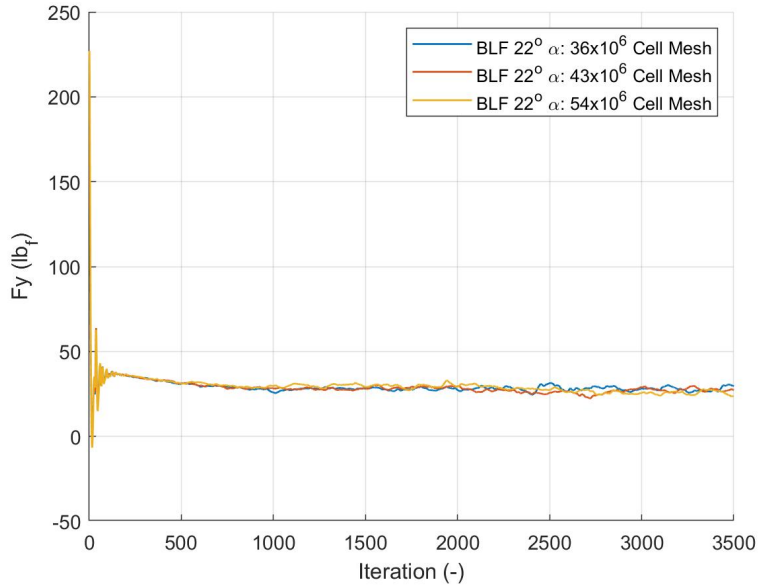

Figure 69. NACA 0012 Cropped Delta-Wing Passive BLF Normal Force (Fy) Per Iteration CFD Mesh Study Results, $\alpha = 22^{\circ}$, Re = 5x10^5

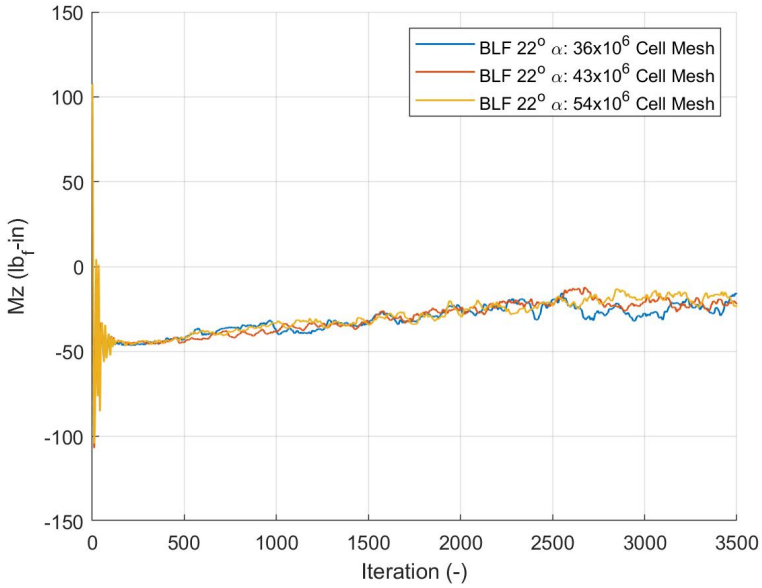

Figure 70. NACA 0012 Cropped Delta-Wing Passive BLF Moment About Z-Axis (Mz) Per Iteration CFD Mesh Study Results, $\alpha = 22^{\circ}$, Re = 5x10^5

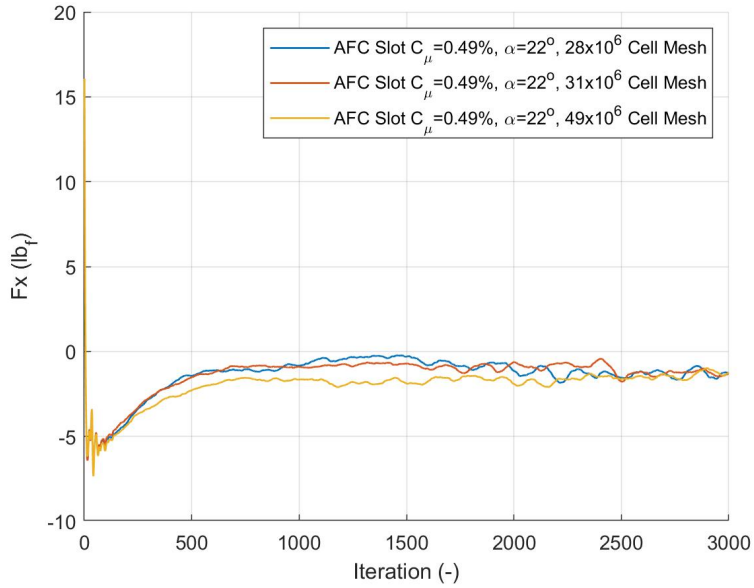

Figure 71. NACA 0012 Cropped Delta-Wing AFC Slot Axial Force (Fx) Per Iteration CFD Mesh Study Results, $\alpha = 22°$, Re = 5x10^5, C_μ= 0.49%

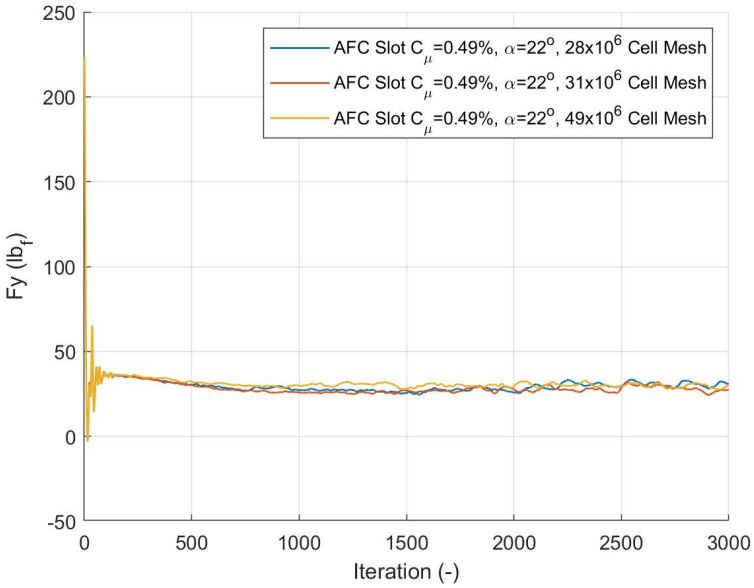

Figure 72. NACA 0012 Cropped Delta-Wing AFC Slot Normal Force (Fy) Per Iteration CFD Mesh Study Results, $\alpha = 22°$, Re = 5x10^5, C_μ= 0.49%

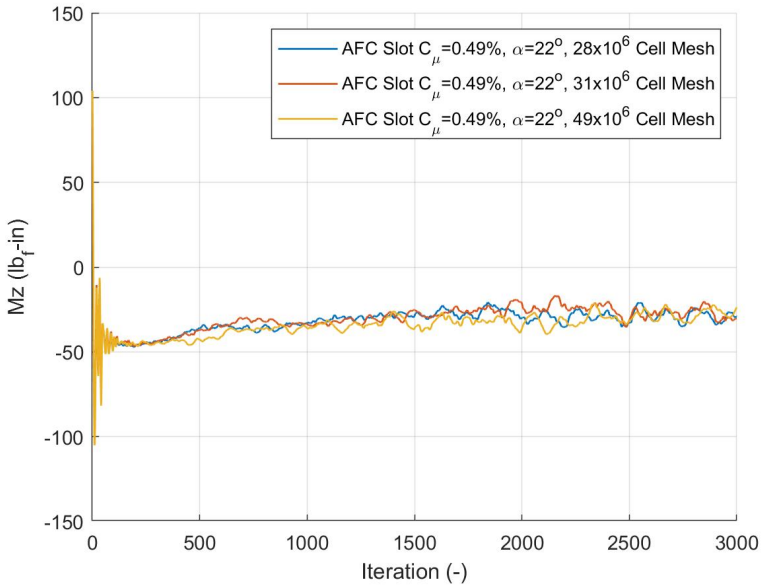

Figure 73. NACA 0012 Cropped Delta-Wing AFC Slot Moment About Z-Axis (Mz) Per Iteration CFD Mesh Study Results, $\alpha = 22^{\circ}$, Re = 5x10^5, C_μ= 0.49%

Appendix C. Flow Visualization Compilation

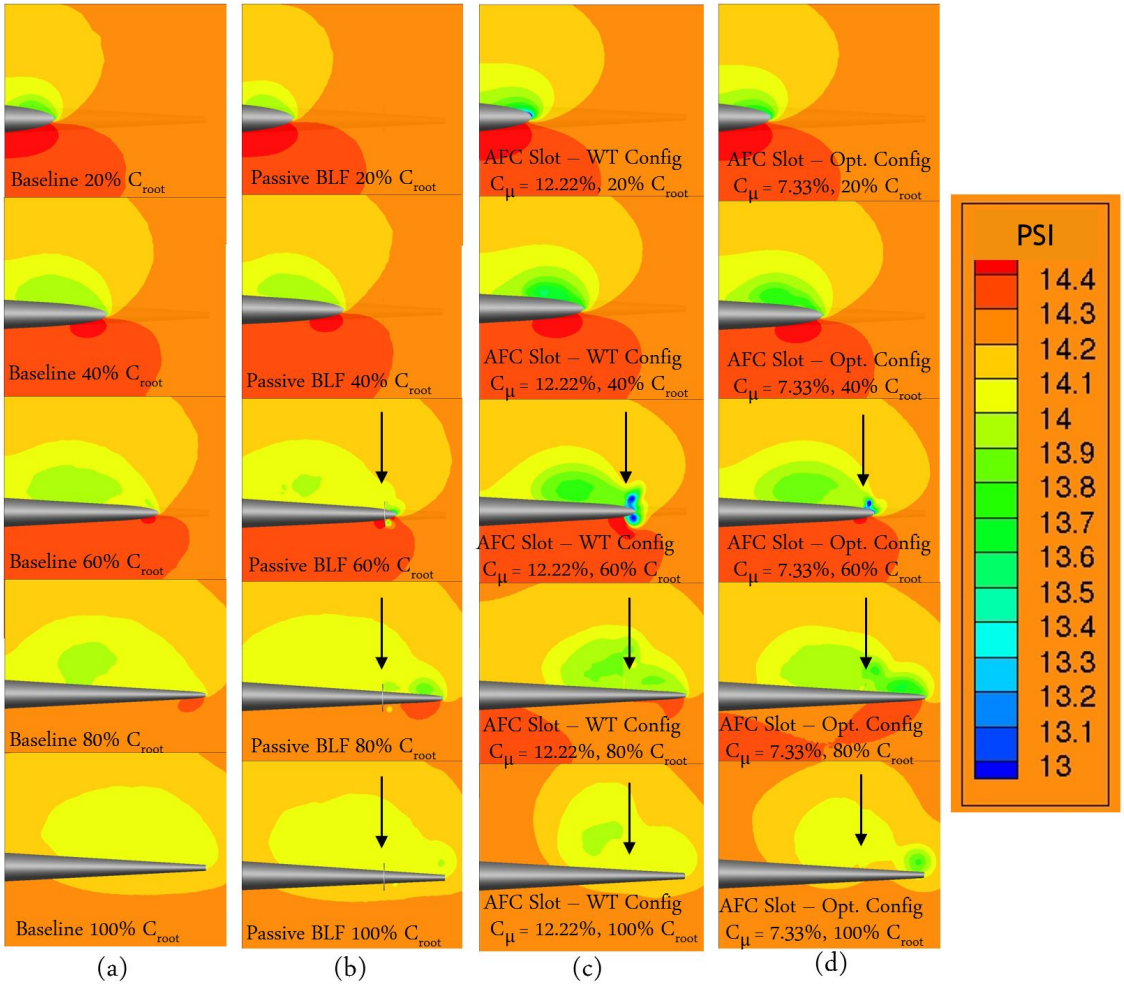

Figure 74. NACA 0012 Cropped Delta-Wing Y-Z Plane Pressure (PSI) Slice Contour Plot, $\alpha = 24°$, Re = 5x10^5: (a) Baseline Configuration, (b) Passive BLF Configuration, (c) AFC Slot Wind Tunnel (WT) Configuration, $C_\mu = 12.22\%$, (d) AFC Slot Optimized Configuration, $C_\mu = 7.33\%$

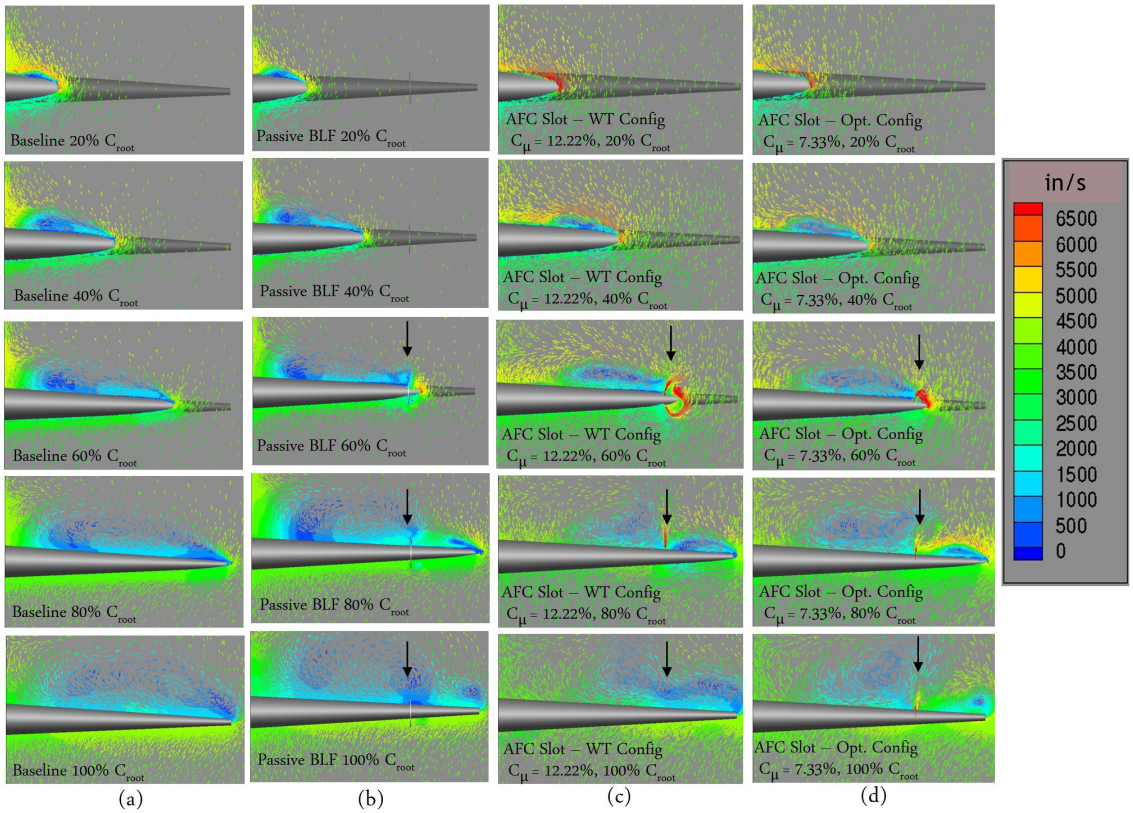

Figure 75. NACA 0012 Cropped Delta-Wing Y-Z Plane Vector Slice Colored by Velocity Magnitude (in/s), $\alpha = 24°$, Re = 5x10^5: (a) Baseline Configuration, (b) Passive BLF Configuration, (c) AFC Slot Wind Tunnel (WT) Configuration, $C_\mu = 12.22\%$, (d) AFC Slot Optimized Configuration, $C_\mu = 7.33\%$

Appendix D. MATLAB Script: Baseline Comparison

```
%% Basic Configuration Data Comparison
clear all; close all; clc; format compact; format short;
%% Basic COnfiguration Wind Tunnel Data (1.5 degree correction applied to all comparison cases)
Alpha_Baseline2=1.5+...
[-8.17894442052277;-7.16850773849801;-6.15464379090849;...
-5.04877209800816;-4.02932120636633;-3.00640352702020;...
-1.98382443346184;-0.870213403716582;0.153319187693818;...
1.17508365277160;2.19900159794485;3.30928370940170;...
4.32751503348324;5.34186930698045;6.44211101586254;...
7.45523765217682;8.46819102061274;9.56920569459411;...
10.6678210098701;11.6756459136262;12.7671846976348;...
13.7663130389622;14.8512817871214;15.9311893169993;...
17.0110707277628;18.0844673115262;19.1538944819053;...
20.2221014158863;21.3721215112022;22.4257937648188;...
23.5698166553147;24.6991922407033;25.7472428560031;...
26.8830239002552;28.0967117595190;29.2310840568254;...
30.4510280084815;31.6729762552610;32.9017417048610;...
34.2275325071614;35.4596797612262;36.7847709966838];...
CD_Base2=...
[0.0326396226315288;0.0273554591561591;0.02320762912...
52264;0.0184655617641355;0.0156734227994947;0.013931...
8232188933;0.0127460003513771;0.0110429698239139;0.0...
115328779992575;0.0132684007837646;0.01594624739861...
14;0.0186260816468254;0.0227511043823911;0.027425377...
8944443;0.0325465190807324;0.0391042044857320;0.0473...
291339011119;0.0578153893612589;0.0714274594986400;0...
.0882968225391222;0.107396801468250;0.12837527862316...
1;0.152008514898266;0.177050724527485;0.203713593209...
787;0.230608840670329;0.257527050009981;0.2850390953...
55441;0.311662701851170;0.335885212499362;0.35962757...
0078000;0.378102215918811;0.393975988177553;0.4094634...
43267234;0.422979456980625;0.438129375146260;0.452553...
360061481;0.469150907399056;0.488570671603892;0.51410...
4483039872;0.536274210618872;0.565069415967284];
CL_Base2=...
[-0.380686716946657,-0.335679522978898,-0.28809803698...
6591,-0.235205472140068,-0.180638051940071,-0.1234544...
23606297,-0.0655693172981972,-0.00446862170388157,0.0...
533671656873325,0.110388299123664,0.169693355141534,...
0.227263490287654,0.279476897333351,0.32863898256204...
2,0.375560539057904,0.422360052709387,0.4700363760260...
67,0.517777718341523,0.561913793013043,0.604151005786...
968,0.641842476206843,0.673795777863523,0.70451924645...
7192,0.729874924214394,0.754142327869694,0.7725926727...
70825,0.786833165496932,0.798718935717348,0.805103685...
529550,0.802634940849533,0.801598645011175,0.78608838...
7524569,0.776596912840933,0.767880111293073,0.7484587...
51498765,0.737187298271561,0.724400980387816,0.713740...
363550526,0.709249314247855,0.715390882106700,0.71448...
6482896382,0.719886109135885]';
CM_Base2=...
[-0.00241933648422381;-0.000994749356042714;0.00052513...
8889181397;0.000531995120895268;-0.000127610521605613;...
-0.00112181497128817;-0.00238738588975404;-0.004014823...
```

```
77348298;-0.00458591893002119;-0.00447507033838957;-0.0...
0570421624022764;-0.00639759228464273;-0.006060593543...
11681;-0.00452373994614179;-0.0025423826386679 5;-0.000...
802608455539601;0.000686585846786974;0.0019224715481...
3012;0.00305034068341110;0.00384085470805589;0.0046514...
9185638424;0.00533251814807207;0.00492217834961218;0.0...
0390892393185356;0.00131507381415635;-0.0018753227054...
2222;-0.00563731602852632;-0.0109907490359497;-0.016914...
9235037892;-0.0248236615415000;-0.0317363120696212;-0.0...
393746528162185;-0.0435606742506112;-0.043896906122957...
7;-0.0457089065451211;-0.0471099572765705;-0.04925656335...
62850;-0.0525805261396649;-0.0556579516727002;-0.0595181...
996791140;-0.0641550435894548;-0.0701361258272115];


%% Import Kestrel Data
[AoA_0] = importdata('0AoA_forces.dat',' ',23);
[AoA_10] = importdata('10AoA_forces.dat',' ',23);
[AoA_14] = importdata('14AoA_forces.dat',' ',23);
[AoA_16] = importdata('16AoA_forces.dat',' ',23);
[AoA_18] = importdata('18AoA_forces.dat',' ',23);
[AoA_20] = importdata('20AoA_forces.dat',' ',23);
[AoA_22] = importdata('22AoA_39Mil_TS-0.00005_AD-0.01_forces.
   dat',' ',23); % Run1: TS=0.00005_AD=0.01
[AoA_24] = importdata('24AoA_forces.dat',' ',23);
[AoA_26] = importdata('26AoA_forces.dat',' ',23);
[AoA_28] = importdata('28AoA_forces.dat',' ',23);
[AoA_30] = importdata('30AoA_forces.dat',' ',23);

[AoA_22_26Mil] = importdata('22AoA_26Mil_forces.dat',' ',23);
[AoA_22_31Mil] = importdata('22AoA_31Mil_forces.dat',' ',23);
[AoA_22_Run2] = importdata('22AoA_TS-0.00002_AD-0.1_forces.dat
   ',' ',23); % Run2: TS=0.00002_AD=0.1
[AoA_22_Run3] = importdata('22AoA_TS-0.00005_AD-0.1_forces.dat
   ',' ',23); % Run3: TS=0.00005_AD=0.1
[AoA_22_Run4] = importdata('22AoA_TS-0.0005_AD-0.01_forces.dat
   ',' ',23); % Run4: TS=0.0005_AD=0.01

%% Axial Forces
Iter = 1000; %Number of iterations to average over

fx_0AoA = mean(AoA_0.data(([length(AoA_0.data)-Iter:end]),3));
fx_10AoA = mean(AoA_10.data(([length(AoA_10.data)-Iter:end])
   ,3));
fx_14AoA = mean(AoA_14.data(([length(AoA_14.data)-Iter:end])
   ,3));
fx_16AoA = mean(AoA_16.data(([length(AoA_16.data)-Iter:end])
   ,3));
fx_18AoA = mean(AoA_18.data(([length(AoA_18.data)-Iter:end])
   ,3));
fx_20AoA = mean(AoA_20.data(([length(AoA_20.data)-Iter:end])
   ,3));
fx_22AoA = mean(AoA_22.data(([length(AoA_22.data)-Iter:end])
   ,3));
fx_24AoA = mean(AoA_24.data(([length(AoA_24.data)-Iter:end])
   ,3));
fx_26AoA = mean(AoA_26.data(([length(AoA_26.data)-Iter:end])
   ,3));
```

```
101 fx_28AoA = mean(AoA_28.data(([length(AoA_28.data)-Iter:end])
      ,3));
102 fx_30AoA = mean(AoA_30.data(([length(AoA_30.data)-Iter:end])
      ,3));
103
104 fx_22AoA_26Mil = mean(AoA_22_26Mil.data(([length(AoA_22_26Mil.
      data)-Iter:end]),3));
105 fx_22AoA_31Mil = mean(AoA_22_31Mil.data(([length(AoA_22_31Mil.
      data)-Iter:end]),3));
106
107 fx_22AoA_Run2 = mean(AoA_22_Run2.data(([length(AoA_22_Run2.
      data)-Iter:end]),3));
108 fx_22AoA_Run3 = mean(AoA_22_Run3.data(([length(AoA_22_Run3.
      data)-Iter:end]),3));
109 fx_22AoA_Run4 = mean(AoA_22_Run4.data(([length(AoA_22_Run4.
      data)-Iter:end]),3));
110
111 %% Vertical Forces
112 fy_0AoA = mean(AoA_0.data(([length(AoA_0.data)-Iter:end]),4));
113 fy_10AoA = mean(AoA_10.data(([length(AoA_10.data)-Iter:end])
      ,4));
114 fy_14AoA = mean(AoA_14.data(([length(AoA_14.data)-Iter:end])
      ,4));
115 fy_16AoA = mean(AoA_16.data(([length(AoA_16.data)-Iter:end])
      ,4));
116 fy_18AoA = mean(AoA_18.data(([length(AoA_18.data)-Iter:end])
      ,4));
117 fy_20AoA = mean(AoA_20.data(([length(AoA_20.data)-Iter:end])
      ,4));
118 fy_22AoA = mean(AoA_22.data(([length(AoA_22.data)-Iter:end])
      ,4));
119 fy_24AoA = mean(AoA_24.data(([length(AoA_24.data)-Iter:end])
      ,4));
120 fy_26AoA = mean(AoA_26.data(([length(AoA_26.data)-Iter:end])
      ,4));
121 fy_28AoA = mean(AoA_28.data(([length(AoA_28.data)-Iter:end])
      ,4));
122 fy_30AoA = mean(AoA_30.data(([length(AoA_30.data)-Iter:end])
      ,4));
123
124 fy_22AoA_26Mil = mean(AoA_22_26Mil.data(([length(AoA_22_26Mil.
      data)-Iter:end]),4));
125 fy_22AoA_31Mil = mean(AoA_22_31Mil.data(([length(AoA_22_31Mil.
      data)-Iter:end]),4));
126
127 fy_22AoA_Run2 = mean(AoA_22_Run2.data(([length(AoA_22_Run2.
      data)-Iter:end]),4));
128 fy_22AoA_Run3 = mean(AoA_22_Run3.data(([length(AoA_22_Run3.
      data)-Iter:end]),4));
129 fy_22AoA_Run4 = mean(AoA_22_Run4.data(([length(AoA_22_Run4.
      data)-Iter:end]),4));
130
131 %% Moment about the z-axis
132 L = -1.75; % Correction for incorrect location of Moment
      Reference point in CFD Settings
133 Mz_0 = mean(AoA_0.data(([length(AoA_0.data)-Iter:end]),8))/L;
134 Mz_10 = mean(AoA_10.data(([length(AoA_10.data)-Iter:end]),8))/
      L;
```

```
135 Mz_14 = mean(AoA_14.data(([length(AoA_14.data)-Iter:end]),8))/
      L;
136 Mz_16 = mean(AoA_16.data(([length(AoA_16.data)-Iter:end]),8))/
      L;
137 Mz_18 = mean(AoA_18.data(([length(AoA_18.data)-Iter:end]),8))/
      L;
138 Mz_20 = mean(AoA_20.data(([length(AoA_20.data)-Iter:end]),8))/
      L;
139 Mz_22 = mean(AoA_22.data(([length(AoA_22.data)-Iter:end]),8))/
      L;
140 Mz_24 = mean(AoA_24.data(([length(AoA_24.data)-Iter:end]),8))/
      L;
141 Mz_26 = mean(AoA_26.data(([length(AoA_26.data)-Iter:end]),8))/
      L;
142 Mz_28 = mean(AoA_28.data(([length(AoA_28.data)-Iter:end]),8))/
      L;
143 Mz_30 = mean(AoA_30.data(([length(AoA_30.data)-Iter:end]),8))/
      L;
144
145 Mz_22AoA_26Mil = mean(AoA_22_26Mil.data(([length(AoA_22_26Mil.
      data)-Iter:end]),8))/L;
146 Mz_22AoA_31Mil = mean(AoA_22_31Mil.data(([length(AoA_22_31Mil.
      data)-Iter:end]),8))/L;
147
148 Mz_22AoA_Run2 = mean(AoA_22_Run2.data(([length(AoA_22_Run2.
      data)-Iter:end]),8))/L;
149 Mz_22AoA_Run3 = mean(AoA_22_Run3.data(([length(AoA_22_Run3.
      data)-Iter:end]),8))/L;
150 Mz_22AoA_Run4 = mean(AoA_22_Run4.data(([length(AoA_22_Run4.
      data)-Iter:end]),8))/L;
151
152 %% Lift
153 AoA = [0 10 14 16 18 20 22 24 26 28 30];
154 L_0 = fy_0AoA*cosd(AoA(:,1))+fx_0AoA*sind(AoA(:,1));
155 L_10 = fy_10AoA*cosd(AoA(:,2))+fx_10AoA*sind(AoA(:,2));
156 L_14 = fy_14AoA*cosd(AoA(:,3))+fx_14AoA*sind(AoA(:,3));
157 L_16 = fy_16AoA*cosd(AoA(:,4))+fx_16AoA*sind(AoA(:,4));
158 L_18 = fy_18AoA*cosd(AoA(:,5))+fx_18AoA*sind(AoA(:,5));
159 L_20 = fy_20AoA*cosd(AoA(:,6))+fx_20AoA*sind(AoA(:,6));
160 L_22 = fy_22AoA*cosd(AoA(:,7))+fx_22AoA*sind(AoA(:,7));
161 L_24 = fy_24AoA*cosd(AoA(:,8))+fx_24AoA*sind(AoA(:,8));
162 L_26 = fy_26AoA*cosd(AoA(:,9))+fx_26AoA*sind(AoA(:,9));
163 L_28 = fy_28AoA*cosd(AoA(:,10))+fx_28AoA*sind(AoA(:,10));
164 L_30 = fy_30AoA*cosd(AoA(:,11))+fx_30AoA*sind(AoA(:,11));
165
166 %% Drag
167
168 D_0 = fx_0AoA*cosd(AoA(:,1))+fy_0AoA*sind(AoA(:,1));
169 D_10 = fx_10AoA*cosd(AoA(:,2))+fy_10AoA*sind(AoA(:,2));
170 D_14 = fx_14AoA*cosd(AoA(:,3))+fy_14AoA*sind(AoA(:,3));
171 D_16 = fx_16AoA*cosd(AoA(:,4))+fy_16AoA*sind(AoA(:,4));
172 D_18 = fx_18AoA*cosd(AoA(:,5))+fy_18AoA*sind(AoA(:,5));
173 D_20 = fx_20AoA*cosd(AoA(:,6))+fy_20AoA*sind(AoA(:,6));
174 D_22 = fx_22AoA*cosd(AoA(:,7))+fy_22AoA*sind(AoA(:,7));
175 D_24 = fx_24AoA*cosd(AoA(:,8))+fy_24AoA*sind(AoA(:,8));
176 D_26 = fx_26AoA*cosd(AoA(:,9))+fy_26AoA*sind(AoA(:,9));
177 D_28 = fx_28AoA*cosd(AoA(:,10))+fy_28AoA*sind(AoA(:,10));
178 D_30 = fx_30AoA*cosd(AoA(:,11))+fy_30AoA*sind(AoA(:,11));
```

```
179
180 %% Pitching Moment
181 x_cm = 1.62; % in - Estimated distance from Aero Center
182 MomRef_L = 1;% in - NA
183
184 PM_0 =  (Mz_0/MomRef_L)-(L_0*cosd(0)*x_cm)+(D_0*-sind(0)*x_cm)
    ;
185 PM_10 = (Mz_10/MomRef_L)-(L_10*cosd(10)*x_cm)+(D_10*-sind(10)*
    x_cm);
186 PM_14 = (Mz_14/MomRef_L)-(L_14*cosd(14)*x_cm)+(D_14*-sind(14)*
    x_cm);
187 PM_16 = (Mz_16/MomRef_L)-(L_16*cosd(16)*x_cm)+(D_16*-sind(16)*
    x_cm);
188 PM_18 = (Mz_18/MomRef_L)-(L_18*cosd(18)*x_cm)+(D_18*-sind(18)*
    x_cm);
189 PM_20 = (Mz_20/MomRef_L)-(L_20*cosd(20)*x_cm)+(D_20*-sind(20)*
    x_cm);
190 PM_22 = (Mz_22/MomRef_L)-(L_22*cosd(22)*x_cm)+(D_22*-sind(22)*
    x_cm);
191 PM_24 = (Mz_24/MomRef_L)-(L_24*cosd(24)*x_cm)+(D_24*-sind(24)*
    x_cm);
192 PM_26 = (Mz_26/MomRef_L)-(L_26*cosd(26)*x_cm)+(D_26*-sind(26)*
    x_cm);
193 PM_28 = (Mz_28/MomRef_L)-(L_28*cosd(28)*x_cm)+(D_28*-sind(28)*
    x_cm);
194 PM_30 = (Mz_30/MomRef_L)-(L_30*cosd(30)*x_cm)+(D_30*-sind(30)*
    x_cm);
195
196 %% Coeffiecient of Lift
197 CL_0 =(L_0*2)/(0.67764*0.0009518*((3751.5/12)^2));
198 CL_10 =(L_10*2)/(0.67764*0.0009518*((3751.5/12)^2));
199 CL_14 =(L_14*2)/(0.67764*0.0009518*((3751.5/12)^2));
200 CL_16 =(L_16*2)/(0.67764*0.0009518*((3751.5/12)^2));
201 CL_18 =(L_18*2)/(0.67764*0.0009518*((3751.5/12)^2));
202 CL_20 =(L_20*2)/(0.67764*0.0009518*((3751.5/12)^2));
203 CL_22 =(L_22*2)/(0.67764*0.0009518*((3751.5/12)^2));
204 CL_24 =(L_24*2)/(0.67764*0.0009518*((3751.5/12)^2));
205 CL_26 =(L_26*2)/(0.67764*0.0009518*((3751.5/12)^2));
206 CL_28 =(L_28*2)/(0.67764*0.0009518*((3751.5/12)^2));
207 CL_30 =(L_30*2)/(0.67764*0.0009518*((3751.5/12)^2));
208
209 CLlist = [CL_0 CL_10 CL_14 CL_16 CL_18 CL_20 CL_22 CL_24 CL_26
     CL_28 CL_30];
210
211 %% Coeffiecient of Drag
212 CD_0 =(D_0*2)/(0.67764*0.0009518*((3751.5/12)^2));
213 CD_10 =(D_10*2)/(0.67764*0.0009518*((3751.5/12)^2));
214 CD_14 =(D_14*2)/(0.67764*0.0009518*((3751.5/12)^2));
215 CD_16 =(D_16*2)/(0.67764*0.0009518*((3751.5/12)^2));
216 CD_18 =(D_18*2)/(0.67764*0.0009518*((3751.5/12)^2));
217 CD_20 =(D_20*2)/(0.67764*0.0009518*((3751.5/12)^2));
218 CD_22 =(D_22*2)/(0.67764*0.0009518*((3751.5/12)^2));
219 CD_24 =(D_24*2)/(0.67764*0.0009518*((3751.5/12)^2));
220 CD_26 =(D_26*2)/(0.67764*0.0009518*((3751.5/12)^2));
221 CD_28 =(D_28*2)/(0.67764*0.0009518*((3751.5/12)^2));
222 CD_30 =(D_30*2)/(0.67764*0.0009518*((3751.5/12)^2));
223
224 CDlist = [CD_0 CD_10 CD_14 CD_16 CD_18 CD_20 CD_22 CD_24 CD_26
```

```
    CD_28 CD_30];

%% Moment Coeffiecient
c_bar = 9.66; % in - Mean Aerodynamic Chord for CFD Model
CM_0 =(PM_0*2)/(0.67764*0.0009518*((3751.5/12)^2)*c_bar);
CM_10 =(PM_10*2)/(0.67764*0.0009518*((3751.5/12)^2)*c_bar);
CM_14 =(PM_14*2)/(0.67764*0.0009518*((3751.5/12)^2)*c_bar);
CM_16 =(PM_16*2)/(0.67764*0.0009518*((3751.5/12)^2)*c_bar);
CM_18 =(PM_18*2)/(0.67764*0.0009518*((3751.5/12)^2)*c_bar);
CM_20 =(PM_20*2)/(0.67764*0.0009518*((3751.5/12)^2)*c_bar);
CM_22 =(PM_22*2)/(0.67764*0.0009518*((3751.5/12)^2)*c_bar);
CM_24 =(PM_24*2)/(0.67764*0.0009518*((3751.5/12)^2)*c_bar);
CM_26 =(PM_26*2)/(0.67764*0.0009518*((3751.5/12)^2)*c_bar);
CM_28 =(PM_28*2)/(0.67764*0.0009518*((3751.5/12)^2)*c_bar);
CM_30 =(PM_30*2)/(0.67764*0.0009518*((3751.5/12)^2)*c_bar);

CMlist = [CM_0 CM_10 CM_14 CM_16 CM_18 CM_20 CM_22 CM_24 CM_26
    CM_28 CM_30];

%% Plot for Baseline Comparison
% figure(1)
% hold on
% plot(Alpha_Baseline2,CD_Base2, 'k',  'LineWidth',0.9)
% plot(AoA,CDlist,'m--o', 'LineWidth',0.9)
% grid on
% xlabel('\alpha (deg)')
% ylabel('C_D (-)')
% xlim([0 30])
% ylim([0 0.5])
% %title('Coefficient of Drag at RE~5e^5')
% legend('Baseline Wind Tunnel Model, Re~5x10^5','Baseline CFD
    Model, Re~5x10^5','Location','northeast')
% hold off

% figure(2)
% hold on
% plot(Alpha_Baseline2,CL_Base2, 'k',  'LineWidth',0.9)
% plot(AoA,CLlist,'b--o',  'LineWidth',0.9)
% grid on
% xlabel('\alpha (deg)')
% ylabel('C_L (-)')
% xlim([0 30])
% ylim([0 1.1])
% %title('Coefficient of Drag at RE~5e^5')
% legend('Baseline Wind Tunnel Model, Re~5x10^5','Baseline CFD
    Model, Re~5x10^5','Location','northeast')
% hold off
%
% figure(3)
% hold on
% plot(Alpha_Baseline2,CM_Base2, 'k',  'LineWidth',0.9)
% plot(AoA,CMlist,'r--o',  'LineWidth',0.9)
% grid on
% xlabel('\alpha (deg)')
% ylabel('C_M (-)')
% xlim([0 30])
% ylim([-0.05 0.025])
% %title('Pitch Moment Coefficient at RE~5e^5')
```

```
279 % legend('Baseline Wind Tunnel Model, Re~5x10^5','Baseline CFD
        Model, Re~5x10^5','Location','northeast')
280 % hold off
281
282 %% Grid Study Plots
283
284 figure (4) % Iterations vs fx
285 hold on
286 plot (AoA_22_26Mil.data(:,1),AoA_22_26Mil.data(:,3), '
      LineWidth',.9)
287 plot (AoA_22_31Mil.data(:,1),AoA_22_31Mil.data(:,3), '
      LineWidth',.9)
288 plot (AoA_22.data(:,1),AoA_22.data(:,3), 'LineWidth',.9)
289 grid on
290 legend('Baseline 22^o \alpha: 26x10^6 Cell Mesh','Baseline 22^
      o \alpha: 31x10^6 Cell Mesh','Baseline 22^o \alpha: 39x10^6
       Cell Mesh')
291 xlabel('Iteration (-)')
292 ylabel('Fx (lb_f)')
293 hold off
294
295 % figure (5) % Iterations vs fy
296 % hold on
297 % plot (AoA_22_26Mil.data(:,1),AoA_22_26Mil.data(:,4), '
      LineWidth',.9)
298 % plot (AoA_22_31Mil.data(:,1),AoA_22_31Mil.data(:,4), '
      LineWidth',.9)
299 % plot (AoA_22.data(:,1),AoA_22.data(:,4), 'LineWidth',.9)
300 % grid on
301 % legend('Baseline 22^o \alpha: 26x10^6 Cell Mesh','Baseline
      22^o \alpha: 31x10^6 Cell Mesh','Baseline 22^o \alpha: 39
      x10^6 Cell Mesh')
302 % xlabel('Iteration (-)')
303 % ylabel('Fy (lb_f)')
304 % hold off
305 %
306 % figure (7) % Iterations vs Mz
307 % hold on
308 % plot (AoA_22_26Mil.data(:,1),AoA_22_26Mil.data(:,8), '
      LineWidth',.9)
309 % plot (AoA_22_31Mil.data(:,1),AoA_22_31Mil.data(:,8), '
      LineWidth',.9)
310 % plot (AoA_22.data(:,1),AoA_22.data(:,8), 'LineWidth',.9)
311 % grid on
312 % legend('Baseline 22^o \alpha: 26x10^6 Cell Mesh','Baseline
      22^o \alpha: 31x10^6 Cell Mesh','Baseline 22^o \alpha: 39
      x10^6 Cell Mesh')
313 % xlabel('Iteration (-)')
314 % ylabel('Mz (lb_f-in)')
315 % hold off
316
317 %% Settings Plots
318 % figure (8) % Iterations vs fx, TS = Time Step, AD = Temporal
       Advective Damping
319 % hold on
320 % plot (AoA_22.data(:,1),AoA_22.data(:,3), 'LineWidth',.9)
321 % plot (AoA_22_Run2.data(:,1),AoA_22_Run2.data(:,3),'LineWidth
      ',.9)
```

```
322 % plot (AoA_22_Run3.data(:,1),AoA_22_Run3.data(:,3),'LineWidth
      ',.9)
323 % plot (AoA_22_Run4.data(:,1),AoA_22_Run4.data(:,3),'LineWidth
      ',.9)
324 % xlim([0 2700])
325 % grid on
326 % legend('22^o \alpha  Run1: TS=0.00005 AD=0.01','22^o \alpha
      Run2: TS=0.00002 AD=0.1','22^o \alpha  Run3: TS=0.00005 AD
     =0.1','22^o \alpha  Run4: TS=0.0005 AD=0.01')
327 % xlabel('Iteration (-)')
328 % ylabel('Fx (lb_f)')
329 % hold off
330 %
331 % figure (9) % Iterations vs fy
332 % hold on
333 % plot (AoA_22.data(:,1),AoA_22.data(:,4),'LineWidth',.9)
334 % plot (AoA_22_Run2.data(:,1),AoA_22_Run2.data(:,4),'LineWidth
      ',.9)
335 % plot (AoA_22_Run3.data(:,1),AoA_22_Run3.data(:,4),'LineWidth
      ',.9)
336 % plot (AoA_22_Run4.data(:,1),AoA_22_Run4.data(:,4),'LineWidth
      ',.9)
337 % xlim([0 2700])
338 % grid on
339 % legend('22^o \alpha  Run1: TS=0.00005 AD=0.01','22^o \alpha
      Run2: TS=0.00002 AD=0.1','22^o \alpha  Run3: TS=0.00005 AD
     =0.1','22^o \alpha  Run4: TS=0.0005 AD=0.01')
340 % xlabel('Iteration (-)')
341 % ylabel('Fy (lb_f)')
342 % hold off
343 %
344 % figure (10) % Iterations vs Mz
345 % hold on
346 % plot (AoA_22.data(:,1),AoA_22.data(:,8),'LineWidth',.9)
347 % plot (AoA_22_Run2.data(:,1),AoA_22_Run2.data(:,8),'LineWidth
      ',.9)
348 % plot (AoA_22_Run3.data(:,1),AoA_22_Run3.data(:,8),'LineWidth
      ',.9)
349 % plot (AoA_22_Run4.data(:,1),AoA_22_Run4.data(:,8),'LineWidth
      ',.9)
350 % xlim([0 2700])
351 % grid on
352 % legend('22^o \alpha Run1: TS=0.00005 AD=0.01','22^o \alpha
     Run2: TS=0.00002 AD=0.1','22^o \alpha  Run3: TS=0.00005 AD
     =0.1','22^o \alpha  Run4: TS=0.0005 AD=0.01')
353 % xlabel('Iteration (-)')
354 % ylabel('Mz (lb_f-in)')
355 % hold off
```

Appendix E. MATLAB Script: Passive BLF Comparison

```
%% Passive BLF Configuration Data Comparison
clear all; close all; clc; format compact; format short;
%% Passive BLF Wind Tunnel Data (1.5 degree correction applied to all comparison cases)
Alpha_BLF_1=1.5+...
[-8.06594564259070;-7.14241231732519;-6.03905594741620;...
-5.01406378048430;-3.98721923601549;-2.87195351727540;...
-1.85058803650554;-0.831110322743736;0.275151806711067;...
1.29346471552093;2.31597900276951;3.42813304789199;...
4.45108375100950;5.55684707512697;6.57167414343638;...
7.58705903612775;8.69009006482263;9.70504580065541;...
10.7161174843277;11.2642436005670;11.8166774071110;...
12.2766843085277;12.8266085308312;13.3790159996166;...
13.8375751427264;14.3856475805125;14.9354617926899;...
15.3929723623862;15.9414105042531;16.4688861494385;...
16.9094889255359;17.4240418013865;17.9837233404080;...
18.4646453036484;18.9881016785306;19.5209239626320;...
20.0480920643511;20.4921008071506;21.0161537952655;...
21.5513155912465;21.9819661259102;22.4844514540255;...
23.0266031504895;23.4649469590941;23.9788010755111;...
24.4993216153161;24.9404098936923;25.4654301290090;...
25.9851110721517;26.4294113964856;26.9572368515206;...
27.4879036272060;27.9159749086103;28.4552397489093;...
28.9719941570135;29.4032901602970;29.9353877441201;...
30.4579590792370;30.8794429116547;31.4044874140582;...
31.9278672633083;32.3622515736385;32.8915967016012];
 CD_BLF_1=...
 [0.0331859562592513;0.0285589439023825;0.0225065331772370;...
 0.0189468223940387;0.0158403087605802;0.0131311169034887;...
 0.0122527914619488;0.0124686038531358;0.0121007596222725;...
 0.0139941157444537;0.0168024120917713;0.0202655564151916;...
 0.0245968486909978;0.0291105237603469;0.0348275369759939;...
 0.0415565640185381;0.0491966039352059;0.0596374268695133;...
 0.0712235463740903;0.0783859677428014;0.0880240892437888;...
 0.0983355252004903;0.108101954523449;0.118749897647422;...
 0.128576970063239;0.140223144052195;0.152845063683076;...
 0.165098099722719;0.178263738604623;0.190669762413875;...
 0.200917116172463;0.213283639422009;0.230302422336980;...
 0.251856410673102;0.265348318598858;0.280169649171469;...
 0.293079995746426;0.306468524342820;0.316087744265308;...
 0.331153701240424;0.339352993468659;0.343805149187245;...
 0.357367274638073;0.365487071651346;0.371746744842184;...
 0.378965080879246;0.387348160309275;0.396148794017582;...
 0.400919634435716;0.410355844881111;0.418992542285874;...
 0.429377784632715;0.432161428908286;0.445358004857721;...
 0.449511061662298;0.454432235165533;0.466615637205070;...
 0.473488130419345;0.473825618553497;0.483262801297828;...
 0.490134615871489;0.495193519187196;0.506592291154017];
 CL_BLF_1=...
 [-0.354173691100548,-0.309063999932849,-0.259899691306692,...
 -0.201576490582196,-0.140228135605584,-0.0784330946201286,...
 -0.0228956859968763,0.0306396081385506,0.0818251136500848,...
 0.134125047245865,0.190880848861979,0.249375733204867,...
 0.306594385654906,0.357250871754507,0.405853817460111,...
 0.455048376575644,0.503867637134175,0.552607044125295,...
```

```
0.596166557862589,0.617511770875898,0.642365030513726,...
0.663583807519691,0.685775470178208,0.710600796703577,...
0.730284120516020,0.750511830740319,0.773647392520254,...
0.791158054932682,0.811773620986288,0.811217504491707,...
0.810796219594365,0.796534564440700,0.829074572567749,...
0.871414723998235,0.866595878432624,0.870649689280734,...
0.869767400527153,0.872958391535774,0.867711724905650,...
0.875307331477488,0.864330969244883,0.837270800264997,...
0.851219132828200,0.848402048276708,0.833399307819857,...
0.824406222320952,0.825560420849990,0.821339590367901,...
0.811456051420846,0.816016858774003,0.814771168240697,...
0.817599478203143,0.803887629919240,0.814774241132624,...
0.802847471376179,0.792555675655018,0.796901461921134,...
0.790083394307436,0.769385076296350,0.766250555705866,...
0.760289976252899,0.754334128100513,0.754700161457019]';
CM_BLF_1=...
[-0.00645565729432271;-0.00543366737074639;-0.00497230375830425;...

-0.00626840903527524;-0.00812639164827980;-0.00967798053293440;...

-0.00945309222782101;-0.00865038220961338;-0.00670502210461011;...

-0.00488751112138329;-0.00454480696604581;-0.00481732423437155;...

-0.00548800757156123;-0.00442664971617944;-0.00282825806744191;...

-0.00138620542503159;-0.000204421890390911;...
0.000817753587349030;0.00130240859034837;0.00109615288671430;
0.000464851194557061;-0.00149193626706634;-0.00380972808029311;...

-0.00533306500332433;-0.00620595983241655;-0.00759321564382312;...

-0.00870105692850148;-0.0108249745414312;-0.0129892457825265;...

-0.00516853422314401;-0.000189350755310846;-0.00462159855872107;...

-0.0191437591914945;-0.0261932152732147;-0.0251904959472022;...

-0.0378876638882588;-0.0478485428343769;-0.0499899927653833;...

-0.0545965073248441;-0.0540169594750646;-0.0642403701311685;...

-0.0678397210048976;-0.0669126861227226;-0.0711347448349583;...

-0.0673556117123620;-0.0649522888342130;-0.0668780318358190;...

-0.0603695865129550;-0.0637109281367164;-0.0621148519578112;...

-0.0619758111857658;-0.0662567712765227;-0.0668173655521368;...

-0.0655033106457927;-0.0660623006320958;-0.0655506777401585;...

-0.0645042350127906;-0.0634239194747829;-0.0619745103601840;...

-0.0628071667857057;-0.0612590184216668;-0.0608586271989955;...

-0.0620809601781004]+0.01;

```

```
94
95  %% Import Kestrel Data
96  [AoA_0] = importdata('0AoA_forces.dat',' ',23);
97  [AoA_10] = importdata('10AoA_forces.dat',' ',23);
98  [AoA_14] = importdata('14AoA_forces.dat',' ',23);
99  [AoA_16] = importdata('16AoA_forces.dat',' ',23);
100 [AoA_18] = importdata('18AoA_forces.dat',' ',23);
101 [AoA_20] = importdata('20AoA_forces.dat',' ',23);
102 [AoA_22] = importdata('22AoA_36Mil_forces.dat',' ',23);
103 [AoA_24] = importdata('24AoA_forces.dat',' ',23);
104 [AoA_26] = importdata('26AoA_forces.dat',' ',23);
105 [AoA_28] = importdata('28AoA_forces.dat',' ',23);
106 [AoA_30] = importdata('30AoA_forces.dat',' ',23);
107
108 [AoA_22_36Mil] = importdata('22AoA_36Mil_forces.dat',' ',23);
109 [AoA_22_43Mil] = importdata('22AoA_43Mil_forces.dat',' ',23);
110 [AoA_22_54Mil] = importdata('22AoA_54Mil_forces.dat',' ',23);
111
112 %% Axial Forces
113 Iter = 1000; %Number of iterations to average overe
114
115 fx_0AoA = mean(AoA_0.data(([length(AoA_0.data)-Iter:end]),3));
116 fx_10AoA = mean(AoA_10.data(([length(AoA_10.data)-Iter:end])
        ,3));
117 fx_14AoA = mean(AoA_14.data(([length(AoA_14.data)-Iter:end])
        ,3));
118 fx_16AoA = mean(AoA_16.data(([length(AoA_16.data)-Iter:end])
        ,3));
119 fx_18AoA = mean(AoA_18.data(([length(AoA_18.data)-Iter:end])
        ,3));
120 fx_20AoA = mean(AoA_20.data(([length(AoA_20.data)-Iter:end])
        ,3));
121 fx_22AoA = mean(AoA_22.data(([length(AoA_22.data)-Iter:end])
        ,3));
122 fx_24AoA = mean(AoA_24.data(([length(AoA_24.data)-Iter:end])
        ,3));
123 fx_26AoA = mean(AoA_26.data(([length(AoA_26.data)-Iter:end])
        ,3));
124 fx_28AoA = mean(AoA_28.data(([length(AoA_28.data)-Iter:end])
        ,3));
125 fx_30AoA = mean(AoA_30.data(([length(AoA_30.data)-Iter:end])
        ,3));
126
127 fx_22AoA_36Mil = mean(AoA_22_36Mil.data(([length(AoA_22_36Mil.
      data)-Iter:end]),3));
128 fx_22AoA_43Mil = mean(AoA_22_43Mil.data(([length(AoA_22_43Mil.
      data)-Iter:end]),3));
129 fx_22AoA_54Mil = mean(AoA_22_54Mil.data(([length(AoA_22_54Mil.
      data)-Iter:end]),3));
130 %% Vertical Forces
131 fy_0AoA = mean(AoA_0.data(([length(AoA_0.data)-Iter:end]),4));
132 fy_10AoA = mean(AoA_10.data(([length(AoA_10.data)-Iter:end])
        ,4));
133 fy_14AoA = mean(AoA_14.data(([length(AoA_14.data)-Iter:end])
        ,4));
134 fy_16AoA = mean(AoA_16.data(([length(AoA_16.data)-Iter:end])
        ,4));
135 fy_18AoA = mean(AoA_18.data(([length(AoA_18.data)-Iter:end])
```

```
    ,4));
136 fy_20AoA = mean(AoA_20.data(([length(AoA_20.data)-Iter:end])
    ,4));
137 fy_22AoA = mean(AoA_22.data(([length(AoA_22.data)-Iter:end])
    ,4));
138 fy_24AoA = mean(AoA_24.data(([length(AoA_24.data)-Iter:end])
    ,4));
139 fy_26AoA = mean(AoA_26.data(([length(AoA_26.data)-Iter:end])
    ,4));
140 fy_28AoA = mean(AoA_28.data(([length(AoA_28.data)-Iter:end])
    ,4));
141 fy_30AoA = mean(AoA_30.data(([length(AoA_30.data)-Iter:end])
    ,4));
142
143 fy_22AoA_36Mil = mean(AoA_22_36Mil.data(([length(AoA_22_36Mil.
    data)-Iter:end]),4));
144 fy_22AoA_43Mil = mean(AoA_22_43Mil.data(([length(AoA_22_43Mil.
    data)-Iter:end]),4));
145 fy_22AoA_54Mil = mean(AoA_22_54Mil.data(([length(AoA_22_54Mil.
    data)-Iter:end]),4));
146 %% Moment about the z-axis
147 L = -2.7; % Correction for incorrect location of Moment
    Reference point in CFD Settings
148 Mz_0 = mean(AoA_0.data(([length(AoA_0.data)-Iter:end]),8))/L;
149 Mz_10 = mean(AoA_10.data(([length(AoA_10.data)-Iter:end]),8))/
    L;
150 Mz_14 = mean(AoA_14.data(([length(AoA_14.data)-Iter:end]),8))/
    L;
151 Mz_16 = mean(AoA_16.data(([length(AoA_16.data)-Iter:end]),8))/
    L;
152 Mz_18 = mean(AoA_18.data(([length(AoA_18.data)-Iter:end]),8))/
    L;
153 Mz_20 = mean(AoA_20.data(([length(AoA_20.data)-Iter:end]),8))/
    L;
154 Mz_22 = mean(AoA_22.data(([length(AoA_22.data)-Iter:end]),8))/
    L;
155 Mz_24 = mean(AoA_24.data(([length(AoA_24.data)-Iter:end]),8))/
    L;
156 Mz_26 = mean(AoA_26.data(([length(AoA_26.data)-Iter:end]),8))/
    L;
157 Mz_28 = mean(AoA_30.data(([length(AoA_30.data)-Iter:end]),8))/
    L;
158 Mz_30 = mean(AoA_30.data(([length(AoA_30.data)-Iter:end]),8))/
    L;
159
160 Mz_22AoA_36Mil = mean(AoA_22_36Mil.data(([length(AoA_22_36Mil.
    data)-Iter:end]),8))/L;
161 Mz_22AoA_43Mil = mean(AoA_22_43Mil.data(([length(AoA_22_43Mil.
    data)-Iter:end]),8))/L;
162 Mz_22AoA_54Mil = mean(AoA_22_54Mil.data(([length(AoA_22_54Mil.
    data)-Iter:end]),8))/L;
163
164 %% Lift
165 AoA = [0 10 14 16 18 20 22 24 26 28 30];
166
167 L_0 = fy_0AoA*cosd(AoA(:,1))+fx_0AoA*sind(AoA(:,1));
168 L_10 = fy_10AoA*cosd(AoA(:,2))+fx_10AoA*sind(AoA(:,2));
169 L_14 = fy_14AoA*cosd(AoA(:,3))+fx_14AoA*sind(AoA(:,3));
```

```
L_16 = fy_16AoA*cosd(AoA(:,4))+fx_16AoA*sind(AoA(:,4));
L_18 = fy_18AoA*cosd(AoA(:,5))+fx_18AoA*sind(AoA(:,5));
L_20 = fy_20AoA*cosd(AoA(:,6))+fx_20AoA*sind(AoA(:,6));
L_22 = fy_22AoA*cosd(AoA(:,7))+fx_22AoA*sind(AoA(:,7));
L_24 = fy_24AoA*cosd(AoA(:,8))+fx_24AoA*sind(AoA(:,8));
L_26 = fy_26AoA*cosd(AoA(:,9))+fx_26AoA*sind(AoA(:,9));
L_28 = fy_28AoA*cosd(AoA(:,10))+fx_28AoA*sind(AoA(:,10));
L_30 = fy_30AoA*cosd(AoA(:,11))+fx_30AoA*sind(AoA(:,11));

%% Drag

D_0 = fx_0AoA*cosd(AoA(:,1))+fy_0AoA*sind(AoA(:,1));
D_10 = fx_10AoA*cosd(AoA(:,2))+fy_10AoA*sind(AoA(:,2));
D_14 = fx_14AoA*cosd(AoA(:,3))+fy_14AoA*sind(AoA(:,3));
D_16 = fx_16AoA*cosd(AoA(:,4))+fy_16AoA*sind(AoA(:,4));
D_18 = fx_18AoA*cosd(AoA(:,5))+fy_18AoA*sind(AoA(:,5));
D_20 = fx_20AoA*cosd(AoA(:,6))+fy_20AoA*sind(AoA(:,6));
D_22 = fx_22AoA*cosd(AoA(:,7))+fy_22AoA*sind(AoA(:,7));
D_24 = fx_24AoA*cosd(AoA(:,8))+fy_24AoA*sind(AoA(:,8));
D_26 = fx_26AoA*cosd(AoA(:,9))+fy_26AoA*sind(AoA(:,9));
D_28 = fx_28AoA*cosd(AoA(:,10))+fy_28AoA*sind(AoA(:,10));
D_30 = fx_30AoA*cosd(AoA(:,11))+fy_30AoA*sind(AoA(:,11));

%% Pitching Moment
x_cm = 0.9; % in - Estimated distance from Aero Center
MomRef_L = 1;% in - NA

PM_0 =  (Mz_0/MomRef_L)-(L_0*cosd(0)*x_cm)+(D_0*-sind(0)*x_cm)
    ;
PM_10 = (Mz_10/MomRef_L)-(L_10*cosd(10)*x_cm)+(D_10*-sind(10)*
    x_cm);
PM_14 = (Mz_14/MomRef_L)-(L_14*cosd(14)*x_cm)+(D_14*-sind(14)*
    x_cm);
PM_16 = (Mz_16/MomRef_L)-(L_16*cosd(16)*x_cm)+(D_16*-sind(16)*
    x_cm);
PM_18 = (Mz_18/MomRef_L)-(L_18*cosd(18)*x_cm)+(D_18*-sind(18)*
    x_cm);
PM_20 = (Mz_20/MomRef_L)-(L_20*cosd(20)*x_cm)+(D_20*-sind(20)*
    x_cm);
PM_22 = (Mz_22/MomRef_L)-(L_22*cosd(22)*x_cm)+(D_22*-sind(22)*
    x_cm);
PM_24 = (Mz_24/MomRef_L)-(L_24*cosd(24)*x_cm)+(D_24*-sind(24)*
    x_cm);
PM_26 = (Mz_26/MomRef_L)-(L_26*cosd(26)*x_cm)+(D_26*-sind(26)*
    x_cm);
PM_28 = (Mz_28/MomRef_L)-(L_28*cosd(28)*x_cm)+(D_28*-sind(28)*
    x_cm);
PM_30 = (Mz_30/MomRef_L)-(L_30*cosd(30)*x_cm)+(D_30*-sind(30)*
    x_cm);

%% Coeffiecient of Lift
CL_0 =(L_0*2)/(0.67764*0.0009518*((3751.5/12)^2));
CL_10 =(L_10*2)/(0.67764*0.0009518*((3751.5/12)^2));
CL_14 =(L_14*2)/(0.67764*0.0009518*((3751.5/12)^2));
CL_16 =(L_16*2)/(0.67764*0.0009518*((3751.5/12)^2));
CL_18 =(L_18*2)/(0.67764*0.0009518*((3751.5/12)^2));
CL_20 =(L_20*2)/(0.67764*0.0009518*((3751.5/12)^2));
CL_22 =(L_22*2)/(0.67764*0.0009518*((3751.5/12)^2));
```

```
217 CL_24 =(L_24*2)/(0.67764*0.0009518*((3751.5/12)^2));
218 CL_26 =(L_26*2)/(0.67764*0.0009518*((3751.5/12)^2));
219 CL_28 =(L_28*2)/(0.67764*0.0009518*((3751.5/12)^2));
220 CL_30 =(L_30*2)/(0.67764*0.0009518*((3751.5/12)^2));
221
222 CLlist = [CL_0 CL_10 CL_14 CL_16 CL_18 CL_20 CL_22 CL_24 CL_26
        CL_28 CL_30];
223
224 %% Coeffiecient of Drag
225 CD_0 =(D_0*2)/(0.67764*0.0009518*((3751.5/12)^2));
226 CD_10 =(D_10*2)/(0.67764*0.0009518*((3751.5/12)^2));
227 CD_14 =(D_14*2)/(0.67764*0.0009518*((3751.5/12)^2));
228 CD_16 =(D_16*2)/(0.67764*0.0009518*((3751.5/12)^2));
229 CD_18 =(D_18*2)/(0.67764*0.0009518*((3751.5/12)^2));
230 CD_20 =(D_20*2)/(0.67764*0.0009518*((3751.5/12)^2));
231 CD_22 =(D_22*2)/(0.67764*0.0009518*((3751.5/12)^2));
232 CD_24 =(D_24*2)/(0.67764*0.0009518*((3751.5/12)^2));
233 CD_26 =(D_26*2)/(0.67764*0.0009518*((3751.5/12)^2));
234 CD_28 =(D_28*2)/(0.67764*0.0009518*((3751.5/12)^2));
235 CD_30 =(D_30*2)/(0.67764*0.0009518*((3751.5/12)^2));
236
237 CDlist = [CD_0 CD_10 CD_14 CD_16 CD_18 CD_20 CD_22 CD_24 CD_26
        CD_28 CD_30];
238
239 %% Moment Coeffiecient
240 c_bar = 9.66;
241 CM_0 =(PM_0*2)/(0.67764*0.0009518*((3751.5/12)^2)*c_bar);
242 CM_10 =(PM_10*2)/(0.67764*0.0009518*((3751.5/12)^2)*c_bar);
243 CM_14 =(PM_14*2)/(0.67764*0.0009518*((3751.5/12)^2)*c_bar);
244 CM_16 =(PM_16*2)/(0.67764*0.0009518*((3751.5/12)^2)*c_bar);
245 CM_18 =(PM_18*2)/(0.67764*0.0009518*((3751.5/12)^2)*c_bar);
246 CM_20 =(PM_20*2)/(0.67764*0.0009518*((3751.5/12)^2)*c_bar);
247 CM_22 =(PM_22*2)/(0.67764*0.0009518*((3751.5/12)^2)*c_bar);
248 CM_24 =(PM_24*2)/(0.67764*0.0009518*((3751.5/12)^2)*c_bar);
249 CM_26 =(PM_26*2)/(0.67764*0.0009518*((3751.5/12)^2)*c_bar);
250 CM_28 =(PM_28*2)/(0.67764*0.0009518*((3751.5/12)^2)*c_bar);
251 CM_30 =(PM_30*2)/(0.67764*0.0009518*((3751.5/12)^2)*c_bar);
252
253 CMlist = [CM_0 CM_10 CM_14 CM_16 CM_18 CM_20 CM_22 CM_24 CM_26
        CM_28 CM_30];
254
255 %% Plot
256 % figure(1)
257 % hold on
258 % plot(Alpha_BLF_1,CD_BLF_1, 'k',   'LineWidth',0.9)
259 % plot(AoA,CDlist,'m--o', 'LineWidth',0.9)
260 % grid on
261 % xlabel('\alpha (deg)')
262 % ylabel('C_D (-)')
263 % xlim([0 30])
264 % ylim([0 0.55])
265 % %title('Coefficient of Drag at RE~5e^5')
266 % legend('BLF Wind Tunnel Model, Re~5x10^5','BLF CFD Model, Re
        ~5x10^5','Location','northeast')
267 % hold off
268
269 % figure(2)
270 % hold on
```

```
271 % plot(Alpha_BLF_1,CL_BLF_1, 'k',  'LineWidth',0.9)
272 % plot(AoA,CLlist,'b--o',  'LineWidth',0.9)
273 % grid on
274 % xlabel('\alpha (deg)')
275 % ylabel('C_L (-)')
276 % xlim([0 30])
277 % ylim([0 1.1])
278 % %title('Coefficient of Drag at RE~5e^5')
279 % legend('BLF Wind Tunnel Model, Re~5x10^5','BLF CFD Model, Re
      ~5x10^5','Location','northeast')
280 % hold off
281 %
282 figure(3)
283 hold on
284 plot(Alpha_BLF_1,CM_BLF_1, 'k', 'LineWidth',0.9)
285 plot(AoA,CMlist,'r--o',  'LineWidth',0.9)
286 grid on
287 xlabel('\alpha (deg)')
288 ylabel('C_M (-)')
289 xlim([0 30])
290 ylim([-0.07 0.03])
291 %title('Coefficient of Drag at RE~5e^5')
292 legend('BLF Wind Tunnel Model, Re~5x10^5','BLF CFD Model, Re~5
      x10^5','Location','northeast')
293 hold off
294
295 %% Grid Study Plots
296
297 % figure (4) % Iterations vs fx
298 % hold on
299 % plot (AoA_22_36Mil.data(:,1),AoA_22_36Mil.data(:,3), '
      LineWidth',.9)
300 % plot (AoA_22_43Mil.data(:,1),AoA_22_43Mil.data(:,3), '
      LineWidth',.9)
301 % plot (AoA_22_54Mil.data(:,1),AoA_22_54Mil.data(:,3), '
      LineWidth',.9)
302 % grid on
303 % legend('BLF 22^o \alpha: 36x10^6 Cell Mesh','BLF 22^o \alpha
      : 43x10^6 Cell Mesh','BLF 22^o \alpha: 54x10^6 Cell Mesh')
304 % xlabel('Iteration (-)')
305 % ylabel('Fx (lb_f)')
306 % xlim([0 3500])
307 % hold off
308 %
309 % figure (5) % Iterations vs fy
310 % hold on
311 % plot (AoA_22_36Mil.data(:,1),AoA_22_36Mil.data(:,4), '
      LineWidth',.9)
312 % plot (AoA_22_43Mil.data(:,1),AoA_22_43Mil.data(:,4), '
      LineWidth',.9)
313 % plot (AoA_22_54Mil.data(:,1),AoA_22_54Mil.data(:,4), '
      LineWidth',.9)
314 % grid on
315 % legend('BLF 22^o \alpha: 36x10^6 Cell Mesh','BLF 22^o \alpha
      : 43x10^6 Cell Mesh','BLF 22^o \alpha: 54x10^6 Cell Mesh')
316 % xlabel('Iteration (-)')
317 % ylabel('Fy (lb_f)')
318 % xlim([0 3500])
```

```
319 % hold off
320 %
321 % figure (7) % Iterations vs Mz
322 % hold on
323 % plot (AoA_22_36Mil.data(:,1),AoA_22_36Mil.data(:,8), '
      LineWidth',.9)
324 % plot (AoA_22_43Mil.data(:,1),AoA_22_43Mil.data(:,8), '
      LineWidth',.9)
325 % plot (AoA_22_54Mil.data(:,1),AoA_22_54Mil.data(:,8), '
      LineWidth',.9)
326 % grid on
327 % legend('BLF 22^o \alpha: 36x10^6 Cell Mesh','BLF 22^o \alpha
      : 43x10^6 Cell Mesh','BLF 22^o \alpha: 54x10^6 Cell Mesh')
328 % xlabel('Iteration (-)')
329 % ylabel('Mz (lb_f-in)')
330 % xlim([0 3500])
331 % hold off
332 %
```

Appendix F. MATLAB Script: AFC Slot Comparison

```
%% AFC Windtunnel Configuration at Slot 200 SLPM Equvalent Mach Comparison
clear all; close all; clc; format compact; format short;
%% AFC 200 SLPM Wind Tunnel Data (Used Data Corrected for Slot Forces)
% (1.5 degree correction applied to all comparison cases)
%Corrected - Includes Slot Forces (Used because slot force accounting was
% not used on CFD Model
Alpha_Slot_200=1.5+...
[-7.32536000000000;-7.12619691322077;-6.01826819591974;...
-4.99732769885743;-3.97582237402429;-2.86342706392424;...
-1.84094117227809;-0.728418723321121;0.294384067844568;...
1.31593289300810;2.33851440655027;3.45016976776966;...
4.47206617206829;5.49070656871355;6.59454368653200;...
7.61119362226182;8.71646655625306;9.73406169439868;...
10.7501841133734;11.8546234227027;12.8685771271328;...
13.8843050386178;14.9877156184099;15.9766275933576;...
16.9667764697981;18.0387374621311;19.0188898729756;...
20.0827728221427;21.0581188095630;22.0214926072595;...
23.0756100723189;24.0351895977165;25.0254177062543;...
26.0886845757370;27.0624075174387;28.0010985196644;...
29.0358902266110;30.0067726241810;30.9823507347488;...
32.0290971475978;32.9765237666068];
CD_Slot_200=...
[0.0320851692367218;0.0273815158308049;0.022028068283...
1334;0.0189948756536030;0.0167746691423112;0.01383175...
73836602;0.0130883781625435;0.0132404288164375;0.01360...
89776067175;0.0151711588370946;0.0170179100405769;0.02...
08589907757831;0.0251307316165439;0.0292991820534647;...
0.0343779160466618;0.0399904833734356;0.04714885833623...
37;0.0548359613605498;0.0646154741009459;0.080281580552...
7789;0.0987049411330914;0.119516801309473;0.147431051406...
686;0.176492397770010;0.203682297126652;0.2342171005386...
91;0.262088029070669;0.291016585238808;0.3114467560713...
94;0.330436992680708;0.350846091507866;0.3712437809582...
23;0.389332297209873;0.405519824046928;0.4295591767327...
85;0.443403369553939;0.460859536482907;0.4769916770151...
77;0.488632311142265;0.510383332757284;0.521800095686450];
CL_Slot_200=...
[-0.335479659988982;-0.289723542352643;-0.2383758075032...
50;-0.185735224621090;-0.131647542404540;-0.07400863802...
58560;-0.0179183018172943;0.0357991832424506;0.0877594...
908739248;0.139620538444450;0.192033665532018;0.247965...
668019429;0.300433823974841;0.344503558646343;0.392427...
083770628;0.436480378822970;0.485037273214251;0.530485...
368755756;0.576947549000008;0.624408759142942;0.671359...
983759139;0.733289050863228;0.793372641556728;0.833976...
884518732;0.875995042630878;0.881499492606525;0.888641...
572961824;0.883404282806119;0.872417014112908;0.857981...
275529303;0.857459131143811;0.852351843832441;0.848668...
821163629;0.847173246376986;0.858961211546805;0.839120...
243942654;0.830986259074614;0.828885307451839;0.800747...
889683352;0.814787518311700;0.795533401163343];
CM_Slot_200=...
```

```
[-0.00889959111869580;-0.00778045651020314;-0.007310345...
19728563;-0.00768453754214641;-0.00878640412371663;-0.0...
101995079971602;-0.0106242428121077;-0.010620921998711...
2;-0.00912260756273299;-0.00794144387024076;-0.00724631...
706996894;-0.00799818316211891;-0.00742068458948495;-0....
00588142736053394;-0.00387951969514295;-0.002152077560...
13230;-0.000813989534200628;7.53100690620058e
   -05;0.000576047750594334;-0.00334800935435651;-0.0145503...
535703555;-0.027429069408750 0;-0.0405778396192745;-0.05...
08147274565507;-0.0600713073812277;-0.0623202507925946...
;-0.0649580225354113;-0.0675484100666562;-0.06971550741...
67166;-0.0713675481322402;-0.0752711253271166;-0.075739...
2784226241;-0.0768935292888157;-0.0782355024377671;-0.0...
783986741164982;-0.0765276274596814;-0.075983837650995...
9;-0.0754625886066138;-0.0737799892519261;-0.0730929027...
786348;-0.0745404094970535]+0.01;

% Uncorrected Data
% Alpha_Slot_200_UN=1.5+...
[-8.13930569650318;-7.12694507515062;-6.02140811853273;...
-5.00170105594408;-3.98198111516462;-2.87036265170578;...
-1.84851324989122;-0.829147376904798;0.278405572171361;...
0.830926257583539;1.29568572893127;1.84718260035369;...
2.40197787987524;2.86990616314340;3.42386719604621;...
3.89045100146877;4.44232258507587;5.45367108933443;...
6.55597231268537;7.56639951144478;8.66928705589410;...
9.68113243597496;10.6947912580051;11.7961467191067;...
12.8093111578703;13.8364110334608;14.9500955001699;...
15.9579723471582;16.9664225058238;18.0282886988279;...
19.0036122250817;20.0556137860657;21.0148460077832;...
21.9702533986755;22.9384955211547;23.9902030711724;...
24.9551128961650;25.9233516796538;26.9910982455396;...
27.9409309963523;28.9897676706375;29.9562597573613;...
30.8989470972295;31.9683622607734;32.9188182156738];...
% CD_Slot_200_UN=...
[0.0249842840892673;0.0195604134915005;0.0143834216638...
751;0.0108549143990608;0.00816881835012328;0.004879311...
46539239;0.00395781966804512;0.00365483992792561;0.004...
28241322482735;0.00474407790921938;0.0057582558648709...
8;0.00645273970293498;0.00751031094048318;0.0094122348...
9896528;0.0110575635340329;0.0132817317745282;0.015133...
5148856012;0.0188803112856184;0.0240003722774144;0.029...
4918706354342;0.0366716976789302;0.0443669347927839;0....
0532532582951283;0.0695916787031502;0.088008587337434...
5;0.108464773625040;0.136824436503663;0.16582820991150...
7;0.192436036579450;0.223461254556216;0.25112573246278...
7;0.280867767929434;0.301227165976154;0.32037888054629...
5;0.341135419249444;0.360932278333196;0.37833276340675...
3;0.395976505144352;0.419017614622716;0.43261089695018...
3;0.450796231404737;0.466349160853958;0.47795232912708...
8;0.500123088459546;0.510802744409361];
% CL_Slot_200_UN
   =[-0.338646961351646,-0.292659862392328,-0.2411828826456...
14,-0.188464920242479,-0.134672726701926,-0.07674586574...
51916,-0.0206952235870607,0.0327214552553833,0.0852759...
690471117,0.111281942933680,0.136480593829496,0.161400...
738366892,0.188758512195716,0.217317919068340,0.244851...
486437686,0.271984976572820,0.297302530690163,0.341155...
```

```
632833166,0.389200881638037,0.433137445034258,0.481804...
530093597,0.527245178134752,0.573548540644765,0.620590...
739659397,0.667430345563330,0.729049497802401,0.789167...
505771261,0.829338662373363,0.871178430668242,0.876339...
382985236,0.883045943420430,0.877744734569981,0.866324...
720972384,0.851908768417901,0.851104984074884,0.845491...
955167970,0.841154026490747,0.839286128027530,0.850683...
644332506,0.830355379707657,0.821697577864173,0.819037...
753064181,0.790070686515306,0.803237872240048,0.783570...
560967676]';
% CM_Slot_200_UN=...
[-0.00834979338577161;-0.00715681206848110;-0.0065466537...
4145752;-0.00688203234423188;-0.00779458060051240;-0.009...
27762017151896;-0.00966528705279758;-0.0095679478086160...
9;-0.00825205444560790;-0.00753024158239537;-0.006931591...
21437764;-0.00624167419865799;-0.00627780524635620;-0.00...
677685305657774;-0.00714047929698264;-0.00719647138574...
427;-0.00666526788181024;-0.00520675806074079;-0.0033756...
8081036960;-0.00182896399677014;-0.000752203860571932;...
-8.69837691748233e
   -05;0.000220931046794505;-0.00394263893098121;-0.01545796...

10548854;-0.0286247777470567;-0.0421161886578441;-0.0526...
581066968622;-0.0622903713117134;-0.0649164366029284;-0....
0679676602655533;-0.0710301613427541;-0.073605044751386...
5;-0.0757827756531143;-0.0801753059813129;-0.08113066871...
99231;-0.0827144357251951;-0.0846946079541785;-0.0854294...
231628424;-0.0841215861740769;-0.0841665989358836;-0.084...
2169756662313;-0.0831993253281970;-0.0831674320221782;...
-0.0852008474669002];


%% Import Kestrel Data
[AoA_0] = importdata('0AoA_forces.dat',' ',23);
[AoA_10] = importdata('10AoA_forces.dat',' ',23);
[AoA_14] = importdata('14AoA_forces.dat',' ',23);
[AoA_16] = importdata('16AoA_forces.dat',' ',23);
[AoA_18] = importdata('18AoA_forces.dat',' ',23);
[AoA_20] = importdata('20AoA_forces.dat',' ',23);
[AoA_22] = importdata('22AoA_49Mil_forces.dat',' ',23);
[AoA_24] = importdata('24AoA_forces.dat',' ',23);
[AoA_26] = importdata('26AoA_forces.dat',' ',23);
[AoA_28] = importdata('28AoA_forces.dat',' ',23);
[AoA_30] = importdata('30AoA_forces.dat',' ',23);

[AoA_22_28Mil] = importdata('22AoA_28Mil_forces.dat',' ',23);
[AoA_22_31Mil] = importdata('22AoA_31Mil_forces.dat',' ',23);

%% Axial Forces
Iter = 1000; %Number of iterations to average over

fx_0AoA = mean(AoA_0.data(([length(AoA_0.data)-Iter:end]),33))
   ;
fx_10AoA = mean(AoA_10.data(([length(AoA_10.data)-Iter:end])
   ,33));
fx_14AoA = mean(AoA_14.data(([length(AoA_14.data)-Iter:end])
   ,33));
fx_16AoA = mean(AoA_16.data(([length(AoA_16.data)-Iter:end])
```

```
    ,33));
fx_18AoA = mean(AoA_18.data(([length(AoA_18.data)-Iter:end])
    ,33));
fx_20AoA = mean(AoA_20.data(([length(AoA_20.data)-Iter:end])
    ,33));
fx_22AoA = mean(AoA_22.data(([length(AoA_22.data)-Iter:end])
    ,33));
fx_24AoA = mean(AoA_24.data(([length(AoA_24.data)-Iter:end])
    ,33));
fx_26AoA = mean(AoA_26.data(([length(AoA_26.data)-Iter:end])
    ,33));
fx_28AoA = mean(AoA_28.data(([length(AoA_28.data)-Iter:end])
    ,33));
fx_30AoA = mean(AoA_30.data(([length(AoA_30.data)-Iter:end])
    ,33));

fx_22AoA_28Mil = mean(AoA_22_28Mil.data(([length(AoA_22_28Mil.
    data)-Iter:end]),33));
fx_22AoA_31Mil = mean(AoA_22_31Mil.data(([length(AoA_22_31Mil.
    data)-Iter:end]),33));

%% Vertical Forces
fy_0AoA = mean(AoA_0.data(([length(AoA_0.data)-Iter:end]),34))
    ;
fy_10AoA = mean(AoA_10.data(([length(AoA_10.data)-Iter:end])
    ,34));
fy_14AoA = mean(AoA_14.data(([length(AoA_14.data)-Iter:end])
    ,34));
fy_16AoA = mean(AoA_16.data(([length(AoA_16.data)-Iter:end])
    ,34));
fy_18AoA = mean(AoA_18.data(([length(AoA_18.data)-Iter:end])
    ,34));
fy_20AoA = mean(AoA_20.data(([length(AoA_20.data)-Iter:end])
    ,34));
fy_22AoA = mean(AoA_22.data(([length(AoA_22.data)-Iter:end])
    ,34));
fy_24AoA = mean(AoA_24.data(([length(AoA_24.data)-Iter:end])
    ,34));
fy_26AoA = mean(AoA_26.data(([length(AoA_26.data)-Iter:end])
    ,34));
fy_28AoA = mean(AoA_28.data(([length(AoA_28.data)-Iter:end])
    ,34));
fy_30AoA = mean(AoA_30.data(([length(AoA_30.data)-Iter:end])
    ,34));

fy_22AoA_28Mil = mean(AoA_22_28Mil.data(([length(AoA_22_28Mil.
    data)-Iter:end]),34));
fy_22AoA_31Mil = mean(AoA_22_31Mil.data(([length(AoA_22_31Mil.
    data)-Iter:end]),34));

%% Moment about the z-axis
L = -1.28; % Correction for incorrect location of Moment
    Reference point in CFD Settings
Mz_0 = mean(AoA_0.data(([length(AoA_0.data)-Iter:end]),38))/L;
Mz_10 = mean(AoA_10.data(([length(AoA_10.data)-Iter:end]),38))
    /L;
Mz_14 = mean(AoA_14.data(([length(AoA_14.data)-Iter:end]),38))
    /L;
```

```
194 Mz_16 = mean(AoA_16.data(([length(AoA_16.data)-Iter:end]),38))
    /L;
195 Mz_18 = mean(AoA_18.data(([length(AoA_18.data)-Iter:end]),38))
    /L;
196 Mz_20 = mean(AoA_20.data(([length(AoA_20.data)-Iter:end]),38))
    /L;
197 Mz_22 = mean(AoA_22.data(([length(AoA_22.data)-Iter:end]),38))
    /L;
198 Mz_24 = mean(AoA_24.data(([length(AoA_24.data)-Iter:end]),38))
    /L;
199 Mz_26 = mean(AoA_26.data(([length(AoA_26.data)-Iter:end]),38))
    /L;
200 Mz_28 = mean(AoA_28.data(([length(AoA_28.data)-Iter:end]),38))
    /L;
201 Mz_30 = mean(AoA_30.data(([length(AoA_30.data)-Iter:end]),38))
    /L;
202
203 Mz_22AoA_28Mil = mean(AoA_22_28Mil.data(([length(AoA_22_28Mil.
    data)-Iter:end]),38))/L;
204 Mz_22AoA_31Mil = mean(AoA_22_31Mil.data(([length(AoA_22_31Mil.
    data)-Iter:end]),38))/L;
205
206 %% Lift
207 AoA = [0 10 14 16 18 20 22 24 26 28 30];
208
209 L_0 = fy_0AoA*cosd(AoA(:,1))+fx_0AoA*sind(AoA(:,1));
210 L_10 = fy_10AoA*cosd(AoA(:,2))+fx_10AoA*sind(AoA(:,2));
211 L_14 = fy_14AoA*cosd(AoA(:,3))+fx_14AoA*sind(AoA(:,3));
212 L_16 = fy_16AoA*cosd(AoA(:,4))+fx_16AoA*sind(AoA(:,4));
213 L_18 = fy_18AoA*cosd(AoA(:,5))+fx_18AoA*sind(AoA(:,5));
214 L_20 = fy_20AoA*cosd(AoA(:,6))+fx_20AoA*sind(AoA(:,6));
215 L_22 = fy_22AoA*cosd(AoA(:,7))+fx_22AoA*sind(AoA(:,7));
216 L_24 = fy_24AoA*cosd(AoA(:,8))+fx_24AoA*sind(AoA(:,8));
217 L_26 = fy_26AoA*cosd(AoA(:,9))+fx_26AoA*sind(AoA(:,9));
218 L_28 = fy_28AoA*cosd(AoA(:,10))+fx_28AoA*sind(AoA(:,10));
219 L_30 = fy_30AoA*cosd(AoA(:,11))+fx_30AoA*sind(AoA(:,11));
220
221 %% Drag
222
223 D_0 = fx_0AoA*cosd(AoA(:,1))+fy_0AoA*sind(AoA(:,1));
224 D_10 = fx_10AoA*cosd(AoA(:,2))+fy_10AoA*sind(AoA(:,2));
225 D_14 = fx_14AoA*cosd(AoA(:,3))+fy_14AoA*sind(AoA(:,3));
226 D_16 = fx_16AoA*cosd(AoA(:,4))+fy_16AoA*sind(AoA(:,4));
227 D_18 = fx_18AoA*cosd(AoA(:,5))+fy_18AoA*sind(AoA(:,5));
228 D_20 = fx_20AoA*cosd(AoA(:,6))+fy_20AoA*sind(AoA(:,6));
229 D_22 = fx_22AoA*cosd(AoA(:,7))+fy_22AoA*sind(AoA(:,7));
230 D_24 = fx_24AoA*cosd(AoA(:,8))+fy_24AoA*sind(AoA(:,8));
231 D_26 = fx_26AoA*cosd(AoA(:,9))+fy_26AoA*sind(AoA(:,9));
232 D_28 = fx_28AoA*cosd(AoA(:,10))+fy_28AoA*sind(AoA(:,10));
233 D_30 = fx_30AoA*cosd(AoA(:,11))+fy_30AoA*sind(AoA(:,11));
234
235 %% Pitching Moment
236 x_cm = 1.3; % in - Estimated distance from Aero Center
237 MomRef_L = 1; % in - NA
238
239 PM_0 =  (Mz_0/MomRef_L)-(L_0*cosd(0)*x_cm)+(D_0*-sind(0)*x_cm)
    ;
240 PM_10 = (Mz_10/MomRef_L)-(L_10*cosd(10)*x_cm)+(D_10*-sind(10)*
```

```
    x_cm);
241 PM_14 = (Mz_14/MomRef_L)-(L_14*cosd(14)*x_cm)+(D_14*-sind(14)*
    x_cm);
242 PM_16 = (Mz_16/MomRef_L)-(L_16*cosd(16)*x_cm)+(D_16*-sind(16)*
    x_cm);
243 PM_18 = (Mz_18/MomRef_L)-(L_18*cosd(18)*x_cm)+(D_18*-sind(18)*
    x_cm);
244 PM_20 = (Mz_20/MomRef_L)-(L_20*cosd(20)*x_cm)+(D_20*-sind(20)*
    x_cm);
245 PM_22 = (Mz_22/MomRef_L)-(L_22*cosd(22)*x_cm)+(D_22*-sind(22)*
    x_cm);
246 PM_24 = (Mz_24/MomRef_L)-(L_24*cosd(24)*x_cm)+(D_24*-sind(24)*
    x_cm);
247 PM_26 = (Mz_26/MomRef_L)-(L_26*cosd(26)*x_cm)+(D_26*-sind(26)*
    x_cm);
248 PM_28 = (Mz_28/MomRef_L)-(L_28*cosd(28)*x_cm)+(D_28*-sind(28)*
    x_cm);
249 PM_30 = (Mz_30/MomRef_L)-(L_30*cosd(30)*x_cm)+(D_30*-sind(30)*
    x_cm);
250
251 %% Coeffiecient of Lift
252 CL_0 =(L_0*2)/(0.67764*0.0009518*((3751.5/12)^2));
253 CL_10 =(L_10*2)/(0.67764*0.0009518*((3751.5/12)^2));
254 CL_14 =(L_14*2)/(0.67764*0.0009518*((3751.5/12)^2));
255 CL_16 =(L_16*2)/(0.67764*0.0009518*((3751.5/12)^2));
256 CL_18 =(L_18*2)/(0.67764*0.0009518*((3751.5/12)^2));
257 CL_20 =(L_20*2)/(0.67764*0.0009518*((3751.5/12)^2));
258 CL_22 =(L_22*2)/(0.67764*0.0009518*((3751.5/12)^2));
259 CL_24 =(L_24*2)/(0.67764*0.0009518*((3751.5/12)^2));
260 CL_26 =(L_26*2)/(0.67764*0.0009518*((3751.5/12)^2));
261 CL_28 =(L_28*2)/(0.67764*0.0009518*((3751.5/12)^2));
262 CL_30 =(L_30*2)/(0.67764*0.0009518*((3751.5/12)^2));
263
264 CLlist = [CL_0 CL_10 CL_14 CL_16 CL_18 CL_20 CL_22 CL_24 CL_26
     CL_28 CL_30];
265
266 %% Coeffiecient of Drag
267 CD_0 =(D_0*2)/(0.67764*0.0009518*((3751.5/12)^2));
268 CD_10 =(D_10*2)/(0.67764*0.0009518*((3751.5/12)^2));
269 CD_14 =(D_14*2)/(0.67764*0.0009518*((3751.5/12)^2));
270 CD_16 =(D_16*2)/(0.67764*0.0009518*((3751.5/12)^2));
271 CD_18 =(D_18*2)/(0.67764*0.0009518*((3751.5/12)^2));
272 CD_20 =(D_20*2)/(0.67764*0.0009518*((3751.5/12)^2));
273 CD_22 =(D_22*2)/(0.67764*0.0009518*((3751.5/12)^2));
274 CD_24 =(D_24*2)/(0.67764*0.0009518*((3751.5/12)^2));
275 CD_26 =(D_26*2)/(0.67764*0.0009518*((3751.5/12)^2));
276 CD_28 =(D_28*2)/(0.67764*0.0009518*((3751.5/12)^2));
277 CD_30 =(D_30*2)/(0.67764*0.0009518*((3751.5/12)^2));
278
279 CDlist = [CD_0 CD_10 CD_14 CD_16 CD_18 CD_20 CD_22 CD_24 CD_26
     CD_28 CD_30];
280
281 %% Moment Coeffiecient
282 c_bar = 9.66;
283 CM_0 =(PM_0*2)/(0.67764*0.0009518*((3751.5/12)^2)*c_bar);
284 CM_10 =(PM_10*2)/(0.67764*0.0009518*((3751.5/12)^2)*c_bar);
285 CM_14 =(PM_14*2)/(0.67764*0.0009518*((3751.5/12)^2)*c_bar);
286 CM_16 =(PM_16*2)/(0.67764*0.0009518*((3751.5/12)^2)*c_bar);
```

```
287 CM_18 =(PM_18*2)/(0.67764*0.0009518*((3751.5/12)^2)*c_bar);
288 CM_20 =(PM_20*2)/(0.67764*0.0009518*((3751.5/12)^2)*c_bar);
289 CM_22 =(PM_22*2)/(0.67764*0.0009518*((3751.5/12)^2)*c_bar);
290 CM_24 =(PM_24*2)/(0.67764*0.0009518*((3751.5/12)^2)*c_bar);
291 CM_26 =(PM_26*2)/(0.67764*0.0009518*((3751.5/12)^2)*c_bar);
292 CM_28 =(PM_28*2)/(0.67764*0.0009518*((3751.5/12)^2)*c_bar);
293 CM_30 =(PM_30*2)/(0.67764*0.0009518*((3751.5/12)^2)*c_bar);
294
295 CMlist = [CM_0 CM_10 CM_14 CM_16 CM_18 CM_20 CM_22 CM_24 CM_26
        CM_28 CM_30];
296
297
298 %% Plot
299 % figure(1)
300 % hold on
301 % plot(Alpha_Slot_200,CD_Slot_200, 'k',   'LineWidth',0.9)
302 % %plot(Alpha_Slot_200_UN,CD_Slot_200_UN, 'g',   'LineWidth
        ',0.9)
303 % plot(AoA,CDlist,'m--o', 'LineWidth',0.9)
304 % grid on
305 % xlabel('\alpha (deg)')
306 % ylabel('C_D (-)')
307 % xlim([0 30])
308 % ylim([0 0.55])
309 % legend('AFC C_{\mu}=0.49% Wind Tunnel Model, Re~5x10^5','AFC
        C_{\mu}=0.49% CFD Model, Re~5x10^5','Location','northeast
       ')
310 % hold off
311
312 % figure(2)
313 % hold on
314 % plot(Alpha_Slot_200,CL_Slot_200, 'k',  'LineWidth',0.9)
315 % %plot(Alpha_Slot_200_UN,CL_Slot_200_UN, 'g',  'LineWidth
        ',0.9)
316 % plot(AoA,CLlist,'b--o',  'LineWidth',0.9)
317 % grid on
318 % xlabel('\alpha (deg)')
319 % ylabel('C_L (-)')
320 % xlim([0 30])
321 % ylim([0 1.15])
322 % legend('AFC C_{\mu}=0.49% Wind Tunnel Model, Re~5x10^5','AFC
        C_{\mu}=0.49% CFD Model, Re~5x10^5','Location','northeast
       ')
323 % hold off
324 %
325 % figure(3)
326 % hold on
327 % plot(Alpha_Slot_200,CM_Slot_200, 'k', 'LineWidth',0.9)
328 % %plot(Alpha_Slot_200_UN,CM_Slot_200_UN, 'g',   'LineWidth
        ',0.9)
329 % plot(AoA,CMlist,'r--o',  'LineWidth',0.9)
330 % grid on
331 % xlabel('\alpha (deg)')
332 % ylabel('C_M (-)')
333 % xlim([0 30])
334 % ylim([-0.08 0.035])
335 % legend('AFC C_{\mu}=0.49% Wind Tunnel Model, Re~5x10^5','AFC
        C_{\mu}=0.49% CFD Model, Re~5x10^5','Location','northeast
```

```
    ')
% hold off

%% Grid Study Plots

% figure (4) % Iterations vs fx
% hold on
% plot (AoA_22_28Mil.data(:,1),AoA_22_28Mil.data(:,3), '
    LineWidth',.9)
% plot (AoA_22_31Mil.data(:,1),AoA_22_31Mil.data(:,3), '
    LineWidth',.9)
% plot (AoA_22.data(:,1),AoA_22.data(:,3), 'LineWidth',.9)
% grid on
% legend('AFC Slot C_{\mu}=0.49%, \alpha=22^o, 28x10^6 Cell
    Mesh','AFC Slot C_{\mu}=0.49%, \alpha=22^o, 31x10^6 Cell
    Mesh','AFC Slot C_{\mu}=0.49%, \alpha=22^o, 49x10^6 Cell
    Mesh')
% xlabel('Iteration (-)')
% ylabel('Fx (lb_f)')
% xlim([0 3000])
% hold off
%
% figure (5) % Iterations vs fy
% hold on
% plot (AoA_22_28Mil.data(:,1),AoA_22_28Mil.data(:,4), '
    LineWidth',.9)
% plot (AoA_22_31Mil.data(:,1),AoA_22_31Mil.data(:,4), '
    LineWidth',.9)
% plot (AoA_22.data(:,1),AoA_22.data(:,4), 'LineWidth',.9)
% grid on
% legend('AFC Slot C_{\mu}=0.49%, \alpha=22^o, 28x10^6 Cell
    Mesh','AFC Slot C_{\mu}=0.49%, \alpha=22^o, 31x10^6 Cell
    Mesh','AFC Slot C_{\mu}=0.49%, \alpha=22^o, 49x10^6 Cell
    Mesh')
% xlabel('Iteration (-)')
% ylabel('Fy (lb_f)')
% xlim([0 3000])
% hold off
%
figure (7) % Iterations vs Mz
hold on
plot (AoA_22_28Mil.data(:,1),AoA_22_28Mil.data(:,8), '
    LineWidth',.9)
plot (AoA_22_31Mil.data(:,1),AoA_22_31Mil.data(:,8), '
    LineWidth',.9)
plot (AoA_22.data(:,1),AoA_22.data(:,8), 'LineWidth',.9)
grid on
legend('AFC Slot C_{\mu}=0.49%, \alpha=22^o, 28x10^6 Cell Mesh
    ','AFC Slot C_{\mu}=0.49%, \alpha=22^o, 31x10^6 Cell Mesh',
    'AFC Slot C_{\mu}=0.49%, \alpha=22^o, 49x10^6 Cell Mesh')
xlabel('Iteration (-)')
ylabel('Mz (lb_f-in)')
xlim([0 3000])
hold off
```

Appendix G. MATLAB Script: AFC Slot Width Optimization

```
%% AFC Slot Width Optimization
%clear all; close all; clc; format compact; format short;
%% Baseline, Passive BLF and AFC Slot, Freestream M = 0.059,
   SW1, M1-M5 Wind Tunnel Uncorrected Data
alpha = 1;
Alpha_Baseline2=alpha+...
[-8.17894442052277;-7.16850773849801;-6.15464379090849;...
-5.04877209800816;-4.02932120636633;-3.00640352702020;...
-1.98382443346184;-0.870213403716582;0.153319187693818;...
1.17508365277160;2.19900159794485;3.30928370940170;...
4.32751503348324;5.34186930698045;6.44211101586254;...
7.45523765217682;8.46819102061274;9.56920569459411;...
10.6678210098701;11.6756459136262;12.7671846976348;...
13.7663130389622;14.8512817871214;15.9311893169993;...
17.0110707277628;18.0844673115262;19.1538944819053;...
20.2221014158863;21.3721215112022;22.4257937648188;...
23.5698166553147;24.6991922407033;25.7472428560031;...
26.8830239002552;28.0967117595190;29.2310840568254;...
30.4510280084815;31.6729762552610;32.9017417048610;...
34.2275325071614;35.4596797612262;36.7847709966838];...
CD_Base2=...
[0.0326396226315288;0.0273554591561591;0.02320762912...
52264;0.0184655617641355;0.0156734227994947;0.013931...
8232188933;0.0127460003513771;0.0110429698239139;0.0...
115328779992575;0.0132684007837646;0.01594624739861...
14;0.0186260816468254;0.0227511043823911;0.027425377...
8944443;0.0325465190807324;0.0391042044857320;0.0473...
291339011119;0.0578153893612589;0.0714274594986400;0...
.0882968225391222;0.107396801468250;0.12837527862316...
1;0.152008514898266;0.177050724527485;0.203713593209...
787;0.230608840670329;0.257527050009981;0.2850390953...
55441;0.311662701851170;0.335885212499362;0.35962757...
0078000;0.378102215918811;0.393975988177553;0.4094634...
43267234;0.422979456980625;0.438129375146260;0.452553...
360061481;0.469150907399056;0.488570671603892;0.51410...
4483039872;0.536274210618872;0.565069415967284];
CL_Base2=...
[-0.380686716946657,-0.335679522978898,-0.28809803698...
6591,-0.235205472140068,-0.180638051940071,-0.1234544...
23606297,-0.0655693172981972,-0.00446862170388157,0.0...
533671656873325,0.110388299123664,0.169693355141534,...
0.227263490287654,0.279476897333351,0.32863898256204...
2,0.375560539057904,0.422360052709387,0.4700363760260...
67,0.517777718341523,0.561913793013043,0.604151005786...
968,0.641842476206843,0.673795777863523,0.70451924645...
7192,0.729874924214394,0.754142327869694,0.7725926727...
70825,0.786833165496932,0.798718935717348,0.805103685...
529550,0.802634940849533,0.801598645011175,0.78608838...
7524569,0.776596912840933,0.767880111293073,0.7484587...
51498765,0.737187298271561,0.724400980387816,0.713740...
363550526,0.709249314247855,0.715390882106700,0.71448...
6482896382,0.719886109135885]';
CM_Base2=...
[-0.00241933648422381;-0.000994749356042714;0.00052513...
```

```
8889181397;0.000531995120895268;-0.000127610521605613;...
-0.00112181497128817;-0.00238738588975404;-0.004014823...
77348298;-0.00458591893002119;-0.00447507033838957;-0.0...
0570421624022764;-0.0063975922846427 3;-0.006060593543...
11681;-0.00452373994614179;-0.00254238263866779;-0.000...
802608455539601;0.000686585846786974;0.0019224715481...
3012;0.00305034068341110;0.00384085470805589;0.0046514...
9185638424;0.00533251814807207;0.00492217834961218;0.0...
0390892393185356;0.00131507381415635;-0.0018753227054...
2222;-0.00563731602852632;-0.0109907490359497;-0.016914...
9235037892;-0.0248236615415000;-0.0317363120696212;-0.0...
393746528162185;-0.0435606742506112;-0.043896906122957...
7;-0.0457089065451211;-0.0471099572765705;-0.04925656335...
62850;-0.0525805261396649;-0.0556579516727002;-0.0595181...
996791140;-0.0641550435894548;-0.0701361258272115];


Alpha_BLF_1=alpha+...
[-8.06594564259070;-7.14241231732519;-6.03905594741620;...
-5.01406378048430;-3.98721923601549;-2.87195351727540;...
-1.85058803650554;-0.831110322743736;0.275151806711067;...
1.29346471552093;2.31597900276951;3.42813304789199;...
4.45108375100950;5.55684707512697;6.57167414343638;...
7.58705903612775;8.69009006482263;9.70504580065541;...
10.7161174843277;11.2642436005670;11.8166774071110;...
12.2766843085277;12.8266085308312;13.3790159996166;...
13.8375751427264;14.3856475805125;14.9354617926899;...
15.3929723623862;15.9414105042531;16.4688861494385;...
16.9094889255359;17.4240418013865;17.9837233404080;...
18.4646453036484;18.9881016785306;19.5209239626320;...
20.0480920643511;20.4921008071506;21.0161537952655;...
21.5513155912465;21.9819661259102;22.4844514540255;...
23.0266031504895;23.4649469590941;23.9788010755111;...
24.4993216153161;24.9404098936923;25.4654301290090;...
25.9851110721517;26.4294113964856;26.9572368515206;...
27.4879036272060;27.9159749086103;28.4552397489093;...
28.9719941570135;29.4032901602970;29.9353877441201;...
30.4579590792370;30.8794429116547;31.4044874140582;...
31.9278672633083;32.3622515736385;32.8915967016012];
 CD_BLF_1=...
 [0.0331859562592513;0.0285589439023825;0.0225065331772370;...
 0.0189468223940387;0.0158403087605802;0.0131311169034887;...
 0.0122527914619488;0.0124686038531358;0.0121007596222725;...
 0.0139941157444537;0.0168024120917713;0.0202655564151916;...
 0.0245968486909978;0.0291105237603469;0.0348275369759939;...
 0.0415565640185381;0.0491966039352059;0.0596374268695133;...
 0.0712235463740903;0.0783859677428014;0.0880240892437888;...
 0.0983355252004903;0.108101954523449;0.118749897647422;...
 0.128576970063239;0.140223144052195;0.152845063683076;...
 0.165098099722719;0.178263738604623;0.190669762413875;...
 0.200917116172463;0.213283639422009;0.230302422336980;...
 0.251856410673102;0.265348318598858;0.280169649171469;...
 0.293079995746426;0.306468524342820;0.316087744265308;...
 0.331153701240424;0.339352993468659;0.343805149187245;...
 0.357367274638073;0.365487071651346;0.371746744842184;...
 0.378965080879246;0.387348160309275;0.396148794017582;...
 0.400919634435716;0.410355844881111;0.418992542285874;...
 0.429377784632715;0.432161428908286;0.445358004857721;...
```

```
0.449511061662298;0.454432235165533;0.466615637205070;...
0.473488130419345;0.473825618553497;0.483262801297828;...
0.490134615871489;0.495193519187196;0.506592291154017];
CL_BLF_1=...
[-0.354173691100548,-0.309063999932849,-0.259899691306692,...
-0.201576490582196,-0.140228135605584,-0.0784330946201286,...
-0.0228956859968763,0.0306396081385506,0.0818251136500848,...
0.134125047245865,0.190880848861979,0.249375733204867,...
0.306594385654906,0.357250871754507,0.405853817460111,...
0.455048376575644,0.503867637134175,0.552607044125295,...
0.596166557862589,0.617511770875898,0.642365030513726,...
0.663583807519691,0.685775470178208,0.710600796703577,...
0.730284120516020,0.750511830740319,0.773647392520254,...
0.791158054932682,0.811773620986288,0.811217504491707,...
0.810796219594365,0.796534564440700,0.829074572567749,...
0.871414723998235,0.866595878432624,0.870649689280734,...
0.869767400527153,0.872958391535774,0.867711724905650,...
0.875307331477488,0.864330969244883,0.837270800264997,...
0.851219132828200,0.848402048276708,0.833399307819857,...
0.824406222320952,0.825560420849990,0.821339590367901,...
0.811456051420846,0.816016858774003,0.814771168240697,...
0.817599478203143,0.803887629919240,0.814774241132624,...
0.802847471376179,0.792555675655018,0.796901461921134,...
0.790083394307436,0.769385076296350,0.766250555705866,...
0.760289976252899,0.754334128100513,0.754700161457019]';
CM_BLF_1=...
[-0.00645565729432271;-0.00543366737074639;-0.00497230375830425;...

-0.00626840903527524;-0.00812639164827980;-0.00967798053293440;...

-0.00945309222782101;-0.00865038220961338;-0.00670502210461011;...

-0.00488751112138329;-0.00454480696604581;-0.00481732423437155;...

-0.00548800757156123;-0.00442664971617944;-0.00282825806744191;...

-0.00138620542503159;-0.000204421890390911;...
0.000817753587349030;0.00130240859034837;0.00109615288671430;
0.000464851194557061;-0.00149193626706634;-0.00380972808029311;...

-0.00533306500332433;-0.00620595983241655;-0.00759321564382312;...

-0.00870105692850148;-0.0108249745414312;-0.0129892457825265;...

-0.00516853422314401;-0.000189350755310846;-0.00462159855872107;...

-0.0191437591914945;-0.0261932152732147;-0.0251904959472022;...

-0.0378876638882588;-0.0478485428343769;-0.0499899927653833;...

-0.0545965073248441;-0.0540169594750646;-0.0642403701311685;...

-0.0678397210048976;-0.0669126861227226;-0.0711347448349583;...

-0.0673556117123620;-0.0649522888342130;-0.0668780318358190;...

-0.0603695865129550;-0.0637109281367164;-0.0621148519578112;...
```

```
  -0.0619758111857658;-0.0662567712765227;-0.0668173655521368;...
  -0.0655033106457927;-0.0660623006320958;-0.0655506777401585;...
  -0.0645042350127906;-0.0634239194747829;-0.0619745103601840;...
  -0.0628071667857057;-0.0612590184216668;-0.0608586271989955;...
  -0.0620809601781004]+0.01;

Alpha_Slot_200_JD=alpha+...
[-8.13930569650318;-7.12694507515062;-6.02140811853273;...
-5.00170105594408;-3.98198111516462;-2.87036265170578;...
-1.84851324989122;-0.829147376904798;0.278405572171361;...
0.830926257583539;1.29568572893127;1.84718260035369;...
2.40197787987524;2.86990616314340;3.42386719604621;...
3.89045100146877;4.44232258507587;5.45367108933443;...
6.55597231268537;7.56639951144478;8.66928705589410;...
9.68113243597496;10.6947912580051;11.7961467191067;...
12.8093111578703;13.8364110334608;14.9500955001699;...
15.9579723471582;16.9664225058238;18.0282886988279;...
19.0036122250817;20.0556137860657;21.0148460077832;...
21.9702533986755;22.9384955211547;23.9902030711724;...
24.9551128961650;25.9233516796538;26.9910982455396;...
27.9409309963523;28.9897676706375;29.9562597573613;...
30.8989470972295;31.9683622607734;32.9188182156738];...
CD_Slot_200_JD=...
[0.0249842840892673;0.0195604134915005;0.0143834216638...
751;0.0108549143990608;0.00816881835012328;0.004879311...
46539239;0.00395781966804512;0.00365483992792561;0.004...
28241322482735;0.00474407790921938;0.0057582558648709...
8;0.00645273970293498;0.00751031094048318;0.0094122348...
9896528;0.0110575635340329;0.0132817317745282;0.015133...
5148856012;0.0188803112856184;0.0240003722774144;0.029...
4918706354342;0.0366716976789302;0.0443669347927839;0....
0532532582951283;0.0695916787031502;0.088008587337434...
5;0.108464773625040;0.136824436503663;0.16582820991150...
7;0.192436036579450;0.223461254556216;0.25112573246278...
7;0.280867767929434;0.301227165976154;0.32037888054629...
5;0.341135419249444;0.360932278333196;0.37833276340675...
3;0.395976505144352;0.419017614622716;0.43261089695018...
3;0.450796231404737;0.466349160853958;0.47795232912708...
8;0.500123088459546;0.510802744409361];
CL_Slot_200_JD=...
[-0.338646961351646,-0.292659862392328,-0.2411828826456...
14,-0.188464920242479,-0.134672726701926,-0.07674586574...
51916,-0.0206952235870607,0.0327214552553833,0.0852759...
690471117,0.111281942933680,0.136480593829496,0.161400...
738366892,0.188758512195716,0.217317919068340,0.244851...
486437686,0.271984976572820,0.297302530690163,0.341155...
632833166,0.389200881638037,0.433137445034258,0.481804...
530093597,0.527245178134752,0.573548540644765,0.620590...
739659397,0.667430345563330,0.729049497802401,0.789167...
505771261,0.829338662373363,0.871178430668242,0.876339...
382985236,0.883045943420430,0.877744734569981,0.866324...
720972384,0.851908768417901,0.851104984074884,0.845491...
955167970,0.841154026490747,0.839286128027530,0.850683...
644332506,0.830355379707657,0.821697577864173,0.819037...
```

```
753064181,0.790070686515306,0.803237872240048,0.783570...
560967676]';
CM_Slot_200_JD=...
[-0.0083497933857716 1;-0.00715681206848110;-0.0065466537...
4145752;-0.00688203234423188;-0.00779458060051240;-0.009...
27762017151896;-0.00966528705279758;-0.009567947808616 0...
9;-0.00825205444560790;-0.00753024158239537;-0.006931591...
21437764;-0.00624167419865799;-0.00627780524635620;-0.00...
677685305657774;-0.00714047929698264;-0.00719647138574...
427;-0.00666526788181024;-0.00520675806074079;-0.0033756...
8081036960;-0.00182896399677014;-0.000752203860571932;...
-8.69837691748233e
   -05;0.000220931046794505;-0.00394263893098121;-0.01545796...

10548854;-0.0286247777470567;-0.0421161886578441;-0.0526...
581066968622;-0.0622903713117134;-0.0649164366029284;-0....
0679676602655533;-0.0710301613427541;-0.073605044751386...
5;-0.0757827756531143;-0.0801753059813129;-0.08113066871...
99231;-0.0827144357251951;-0.0846946079541785;-0.0854294...
231628424;-0.0841215861740769;-0.0841665989358836;-0.084...
2169756662313;-0.0831993253281970;-0.0831674320221782;...
-0.0852008474669002];

Alpha_Slot_400_JD=alpha+...
[-8.14107995734776;-7.12810380397329;-6.02294002587198;...
-5.00100829505852;-3.98065584668460;-2.87139441735438;...
-1.84952770602303;-0.829170803599483;0.280451313638561;...
0.832112928356729;1.29695570220239;1.84800350937919;...
2.40181187810453;2.86816341968855;3.42161042868440;...
3.88872287648642;4.43966731528486;5.45162906889796;...
6.55437032751475;7.56363601108004;8.66657245565575;...
9.67845705484742;10.6909516992006;11.7958743891732;...
12.8114141249747;13.8346778549107;14.9378776008161;...
15.9387749238412;16.9346122624383;18.0179820522858;...
18.9964023200859;20.0620812411592;21.0303959822269;...
22.0041179249296;22.9715615402812;24.0260517121405;...
24.9988278640787;25.9736340670725;27.0422333311487;...
27.9946973069450;29.0418733935211;29.9959334967865;...
30.9671914337833;32.0001766548288;32.9663708286242];...
CD_Slot_400_JD=...
[0.00569768908582134;0.000653616631782971;-0.0040173...
3492747906;-0.00742990193772587;-0.0102174497790087;...
-0.0133023270693763;-0.0142207914583933;-0.014594291...
7647373;-0.0142093229799219;-0.0138959193545874;-0.01...
26582858300000;-0.0117907234379582;-0.01058897412493...
04;-0.00846719539239434;-0.00710909653460416;-0.00465...
318894119242;-0.00296639088322539;0.001052522621462...
43;0.00651350808441484;0.0117933998076995;0.01891820...
08004069;0.0261482628131217;0.0342962335695831;0.043...
8656700474776;0.0552077756509481;0.0693740477420460;...
0.105172507392724;0.139528921009682;0.1679357319248...
90;0.199834155989705;0.226344669145139;0.25453057310...
9369;0.277085828367057;0.300568277707328;0.322077310...
429307;0.346829752414292;0.367124558895408;0.3862760...
86830406;0.412179568299533;0.427395948086337;0.44643...
3916573160;0.462425886927703;0.482117157303679;0.493...
772336860829;0.513431234800692];
CL_Slot_400_JD=...
```

```
[-0.340528694281068,-0.293888778754073,-0.242807582020...
513,-0.187730196836646,-0.133267182896577,-0.077840128...
4080720,-0.0217711282459079,0.0326966095383901,0.08744...
56269616597,0.112540493770281,0.137827493036031,0.162...
271372214259,0.188582455220084,0.215469612627635,0.242...
458020182855,0.270152174087562,0.294486423567305,0.338...
989921342888,0.387501859615882,0.430206551500381,0.478...
925498707463,0.524407741473837,0.569476408715038,0.620...
301913918239,0.669660695436623,0.727211335640237,0.776...
209533096261,0.808978395884902,0.837441349306045,0.865...
408433204394,0.875399313732268,0.884603942028837,0.882...
816602113635,0.887824566473365,0.886173907128255,0.883...
512051474941,0.887516935802066,0.892614264341189,0.904...
916129219707,0.887378470447064,0.876959494318545,0.861...
114645048685,0.862448778909116,0.836979355690106,0.834...
003572518458]';
CM_Slot_400_JD=...
[-0.0095985070030111;-0.00874982906994464;-0.007907456...
16336122;-0.00881500204053227;-0.00980820493121330;-0.0...
110651682189337;-0.0113239431035566;-0.011840219262665...
1;-0.0108308275197412;-0.0103000706859604;-0.0095246466...
1322938;-0.0085719019079036 5;-0.00834770619569028;-0.00...
849964062857796;-0.00863106772547918;-0.00879291315863...
069;-0.00837630719200007;-0.00694002271937745;-0.005296...
62406811701;-0.00331477093293976;-0.00212958191237636;...
-0.00145238375830875;-0.000726417246053755;-0.00025042...
8208528577;-0.00158101230521345;-0.0119384093858803;-0...
.0278569646668860;-0.0391783362526073;-0.0469237967756...
573;-0.0566692689865733;-0.0616690489485235;-0.06525804...
91857559;-0.0682765276124359;-0.0731923881907869;-0.075...
6053897214873;-0.0829084605615219;-0.0854438243424612;...
-0.0882944149254450;-0.0890506385715564;-0.08978128770...
85074;-0.0915346082694105;-0.0921384186320555;-0.092891...
1886500812;-0.0935403064400923;-0.0928891979397311];...

Alpha_Slot_600_JD=alpha+...
[-8.15250305008806;-7.13851290714992;-6.03051364430308;...
-5.01117589838906;-3.99037918445528;-2.87932753037828;...
-1.85626236599775;-0.834814878555532;0.274142141001341;...
0.826066351573143;1.29116820600337;1.84275410005435;...
2.39770025991947;2.86382014537051;3.41749994600344;...
3.88381537566056;4.43571125667504;5.44782988317605;...
6.55176145418855;7.56357115087161;8.66644528646187;...
9.67834967266616;10.6916630962418;11.7982876029726;...
12.8131855970119;13.8340664829350;14.9467350593083;...
15.9674637590202;16.9845101257540;18.0875632637920;...
19.0966204643189;20.1633774635334;21.1396071845055;...
22.1110566367845;23.0677525891127;24.1201163602511;...
25.0488677017462;25.9941081509589;27.0518668176482;...
28.0270018230895;29.0770736345079;30.0501514516892;...
31.0001085712215;32.0467826847915;33.0096335195687];...
CD_Slot_600_JD=...
[-0.0130658913688246;-0.0180842416071628;-0.022456305...
0802255;-0.0257976158492426;-0.0287702976700154;-0.03...
20076226532163;-0.0324107936394564;-0.03261643771122...
30;-0.0319837811121743;-0.0315085156292136;-0.0299661...
090276477;-0.0291775542254593;-0.0280246271852704;-0....
0256038813179883;-0.0238580183687156;-0.021228450678...
```

```
7270;-0.0191196323640248;-0.0149694630879372;-0.009078...
06619669437;-0.00304101045471653;0.00383001613165229...
;0.0113398715173390;0.019705816947943 0;0.030249908478...
1012;0.0403212498678895;0.0524337189708148;0.06698199...
27082439;0.0825577218736728;0.103000268644405;0.13377...
6722358127;0.185679142766743;0.238490168158967;0.2693...
60459893327;0.299375454581163;0.324196829528256;0.351...
115142779436;0.367985743075838;0.376515906340747;0.39...
9577001851152;0.422730003720431;0.444102434599543;0.4...
65101086216071;0.483472381511884;0.501379222405195;...
0.518553198817997];
CL_Slot_600_JD=...
[-0.352643716618924,-0.304928391262603,-0.250839956313...
286,-0.198513681158485,-0.143579491215208,-0.086253772...
9155831,-0.0289137259544743,0.0267106567212663,0.08075...
42895829787,0.106127658431716,0.131689431538560,0.156...
703991061284,0.184221784490254,0.210863253686253,0.23...
8098553737877,0.264947411815210,0.290290735103814,0.3...
34960608009534,0.384734959325207,0.430137762522489,0....
478790626509576,0.524293854844864,0.570230897122041,0...
.622861303021514,0.671539470632569,0.726562931104796,0...
.785603513336904,0.839404996363596,0.890361669785317,0...
.939204378913497,0.981687959342012,0.992035968075043,0...
.998643041172583,1.00124086382455,0.988191524579992,0....
983274465995295,0.940587830428161,0.914328522403276,0....
915133143717022,0.921639764091660,0.914291915191565,0....
918616737493617,0.897359802082030,0.886408446997923,0....
879886809143175]';
CM_Slot_600_JD=...
[-0.00723738933360987;-0.00620776301636090;-0.00619294...
458505423;-0.00651444951696916;-0.00743876910006222;-0...
.00861584790279979;-0.00966118845439566;-0.0105746532...
004899;-0.00980569395259948;-0.00916198942512294;-0.00...
848389612122977;-0.00782406485606092;-0.0076584206531...
9508;-0.00782905371730899;-0.00814129622862258;-0.0082...
4703629731736;-0.00807708135388103;-0.006707450540029...
11;-0.00524683155342631;-0.00386734839632959;-0.002368...
46368680112;-0.00158201749017828;-0.00111774076086887...
;-0.000634937187145405;-0.00138717124650150;-0.0105812...
981760175;-0.0222199752206172;-0.0342678895374102;-0.0...
456083761608960;-0.0577344485022751;-0.06970409688556...
46;-0.0754547156471550;-0.0791776508059520;-0.08150487...
85559114;-0.0829557505717916;-0.0847154169596503;-0.08...
23035973940487;-0.0858402438505193;-0.084752948869612...
3;-0.0857334788596333;-0.0837092498012970;-0.085689331...
5450340;-0.0917963917474111;-0.0940930991685665;-0.097...
4335038708480];

Alpha_Slot_800_JD=alpha+...
[-8.16532994130786;-7.15071579092200;-6.04244860884083;...
-5.02099510922208;-4.00074350475546;-2.89013300970893;...
-1.86673672339860;-0.845557601359153;0.262744376454180;...
0.815668234712962;1.28098830005780;1.83392968241970;...
2.38963009158842;2.85600354947695;3.41124262157922;...
3.87728372488066;4.42928798070192;5.44207749788951;...
6.54701850023257;7.55851760590759;8.66181167361823;...
9.67231113504006;10.6858135558792;11.7945702669411;...
12.8095448979892;13.8303756931133;14.9434105377481;...
```

```
15.9616233762802;16.9770125159476;18.0751112575024;...
19.0870816918115;20.1944651800602;21.2080328942639;...
22.1973387095223;23.1762140686440;24.2493579805815;...
25.2214289083073;26.1923382924692;27.2178579547376;...
28.1285669372076;29.1882477121527;30.1384264568971;...
31.0873604704253;32.0796152955456;33.0318609966642];...
CD_Slot_800_JD=...
[-0.00681050693390072;-0.0126543294087441;-0.0182495...
693770797;-0.0214166231427484;-0.0251674028323114;-0...
.0284813491243448;-0.0295284521703782;-0.0300352983...
439126;-0.0297999387101721;-0.0295720385414848;-0.02...
82132488021699;-0.0273310852132612;-0.026210383664...
1072;-0.0240278454672732;-0.0220435932508557;-0.0190...
684670650371;-0.0168993698727356;-0.01216566243845...
81;-0.00643704479454368;-0.000469991253904901;0.0068...
1634235048144;0.0143941708545328;0.022555795883598...
0;0.0335793770283875;0.0439463538650867;0.0560009143...
510980;0.0702808537518199;0.0848501778814416;0.10300...
2466782877;0.128061227791715;0.152144243602451;0.182...
336909797974;0.215148357201335;0.275067267157616;0.3...
20558261523750;0.362479685381631;0.396531037918776;...
0.429234176477427;0.457465813635064;0.4677768042418...
04;0.494369876697358;0.510196123102673;0.52428205263...
3874;0.518416110561748;0.533085621458722];
CL_Slot_800_JD=...
[-0.366247569549657,-0.317870438818895,-0.2634978559...
96289,-0.208927669846718,-0.154571608219602,-0.09771...
37712223667,-0.0400225453233562,0.0153172162849387,...
0.0686661296398034,0.0950996977124353,0.1208928993...
96894,0.147345053057996,0.175662782841257,0.2025731...
84086938,0.231462205167657,0.258020120152550,0.2834...
78382821840,0.328859784193542,0.379704711000120,0.4...
24778109798272,0.473876342402648,0.517889545618680...
,0.564027033267523,0.618918797249851,0.667678243993...
874,0.722648579523156,0.782077615939359,0.833210844...
835199,0.882409908178346,0.925998118771882,0.971571...
395935769,1.02500675704765,1.07121349306802,1.09274...
928998711,1.10322282802753,1.12034462316562,1.12360...
156582039,1.12456603399776,1.09117884162421,1.02935...
696942839,1.03220012662585,1.01223881378076,0.98989...
6799890378,0.921229823462180,0.903460668486540]';
CM_Slot_800_JD=...
[-0.00271428206765456;-0.00189706750827400;-0.001585...
10093408801;-0.00257006623435670;-0.003639827594117...
15;-0.00377285117644621;-0.00528002084311486;-0.0060...
4783914821188;-0.00542639016919631;-0.0048547859236...
7664;-0.00467522918668672;-0.00464200994639661;-0.00...
484881943788308;-0.00517612644732052;-0.00576129489...
607823;-0.00558567933442236;-0.00544667475420462;-0....
00388856835124193;-0.00257735756993069;-0.001209129...
76751777;0.000188843218942158;0.00126966991609235;0...
.00194730019213918;0.00226867902786383;0.0020075243...
3835763;-0.00655633847238418;-0.0191938207372223;-0.0...
288876484116350;-0.0402225780133489;-0.0509736602055...
526;-0.0593875338193712;-0.0673592849128238;-0.074871...
3020188131;-0.0814793195538752;-0.0864569567583774;-0...
.0922018627535162;-0.0947708467128809;-0.09736442547...
76938;-0.0959300891773638;-0.0898902740886361;-0.0917...
```

```
042960490281;-0.0905853919434668;-0.089976876926054...
0;-0.0848269056017114;-0.0859492228960141];

Alpha_Slot_1000_JD=alpha+...
[-8.19296176515518;-7.17933574587292;-6.07141593961330;...
-5.05068766637736;-4.01478390175705;-2.90376884270189;...
-1.88070289398938;-0.858610138673839;0.251892829170128;...
0.805045079373169;1.27096880298182;1.82550033419823;...
2.29328670403366;2.84752853218911;3.40257829519855;...
3.86968238230243;4.42287620882581;5.43862308343971;...
6.54573182715474;7.55713986284914;8.66098722550410;...
9.67236449623901;10.6852903591628;11.7936837267243;...
12.8112788281600;13.8329825727792;14.9471087553110;1...
5.9664578225023;16.9791398538928;18.0817616704432;...
19.0886948118036;20.1847033352771;21.2029090750168;...
22.2183661266420;23.2279674798223;24.3299915044846;...
25.3283955867359;26.3157875287581;27.3957186622302;...
28.3760532549829;29.4314555943111;30.3576518649962;...
31.2810950601421;32.2836331725416;33.2135410784349];
CD_Slot_1000_JD=...
[-0.0193797893655357;-0.0259114877416335;-0.03258667...
37823424;-0.0372877316448054;-0.0409895595179842;-0.0...
451211540031038;-0.0465323825799716;-0.046985848615...
9102;-0.0470235007266426;-0.0471019968699758;-0.04558...
46122476344;-0.0447892744155420;-0.0432186377043500;...
-0.0416831615990399;-0.0400375162366334;-0.037384285...
6392081;-0.0350786936687696;-0.0303777956122959;-0.02...
17416728583107;-0.0157560312384841;-0.00811648099009...
559;-0.000582397437687672;0.00780414749527014;0.0186...
951181907445;0.0294869235072628;0.0417640755961384;...
0.0566192455906378;0.0718139381421382;0.08864026042...
94024;0.109696609944029;0.131368096438492;0.15524846...
0024663;0.184343329546123;0.215847194077492;0.248784...
760521435;0.293162365698196;0.352499161384842;0.4063...
87379826736;0.458282454622353;0.500207681789809;0.54...
2355888075449;0.570273045623037;0.586548858269573;...
0.595084080898688;0.601632791661711];
CL_Slot_1000_JD=...
[-0.395553132478767,-0.348223986795931,-0.29421982134...
7971,-0.240418790630072,-0.169462472469212,-0.1121755...
65857211,-0.0548346870548746,0.00147404922605309,0.05...
71572729111181,0.0838330672852779,0.110266492551626,...
0.138405114959061,0.166814012293967,0.19358481061487...
2,0.222273055606256,0.249958342381286,0.2766782314731...
33,0.325196125920342,0.378340100431535,0.423316912878...
281,0.473001955093872,0.517946139059006,0.56347214502...
0504,0.617978556741035,0.669517203304557,0.7254133653...
91840,0.785999845181785,0.838338127376218,0.884666105...
104343,0.933051366361309,0.973282227247636,1.01465360...
923606,1.06577930934517,1.11505039826875,1.1581110922...
4280,1.20586235163683,1.23704752376115,1.255492945757...
42,1.27981308396896,1.29183424562026,1.29013981004425...
1.24474333567583,1.19536645118314,1.13760565033506,1.0...
9614563559966]';
CM_Slot_1000_JD=...
[0.00507017714348937;0.00614418826676139;0.006842971...
85030537;0.00699513112022954;0.00437741572681731;0.0...
0282945856269266;0.00113340818135327;0.000333189608...
```

```
933874;0.000586231571137447;0.000924799225952278;0.0...
00824185731205280;0.000767407000762050;0.0003493200...
57341334;-0.000162324801487116;-0.00074296932765326...
5;-0.00125212658580521;-0.00147376228469160;-0.001264...
98499510802;0.00179972763032268;0.00314076315957652...
;0.00435342405830659;0.00526227344420236;0.006221210...
03062758;0.00675959969365219;0.00639421820758831;-0....
00220469951161398;-0.0136034339227159;-0.0230183035...
253696;-0.0325897625335028;-0.0410750732024380;-0.046...
7011262564439;-0.0522773449139122;-0.05960919917759...
88;-0.0671714951745267;-0.0740194214401699;-0.0823273...
039146220;-0.0909191500060944;-0.0970089485628756;...
-0.103913781913880;-0.108509186502984;-0.11207993050...
2852;-0.109408392847778;-0.105477991507032;-0.101058...
260651483;-0.0975542197429547];

%% Import Kestrel Data

[SW1_M1] = importdata('SW1/OptimizationData/M1_Run1_forces.dat
    ',' ',23);
[SW1_M2] = importdata('SW1/OptimizationData/M2_forces.dat',' '
    ,23);
[SW1_M3] = importdata('SW1/OptimizationData/M3_forces.dat',' '
    ,23);
[SW1_M4] = importdata('SW1/OptimizationData/M4_forces.dat',' '
    ,23);
[SW1_M5] = importdata('SW1/OptimizationData/M5_forces.dat',' '
    ,23);

[SW2_M1] = importdata('SW2/OptimizationData/M1_forces.dat',' '
    ,23);
[SW2_M2] = importdata('SW2/OptimizationData/M2_forces.dat',' '
    ,23);
[SW2_M3] = importdata('SW2/OptimizationData/M3_forces.dat',' '
    ,23);
[SW2_M4] = importdata('SW2/OptimizationData/M4_forces.dat',' '
    ,23);
[SW2_M5] = importdata('SW2/OptimizationData/M5_forces.dat',' '
    ,23);

[SW3_M1] = importdata('SW3/OptimizationData/M1_forces.dat',' '
    ,23);
[SW3_M2] = importdata('SW3/OptimizationData/M2_forces.dat',' '
    ,23);
[SW3_M3] = importdata('SW3/OptimizationData/M3_forces.dat',' '
    ,23);
[SW3_M4] = importdata('SW3/OptimizationData/M4_forces.dat',' '
    ,23);
[SW3_M5] = importdata('SW3/OptimizationData/M5_forces.dat',' '
    ,23);

[SW4_M1] = importdata('SW4/OptimizationData/M1_forces.dat',' '
    ,23);
[SW4_M2] = importdata('SW4/OptimizationData/M2_forces.dat',' '
    ,23);
[SW4_M3] = importdata('SW4/OptimizationData/M3_forces.dat',' '
    ,23);
[SW4_M4] = importdata('SW4/OptimizationData/M4_forces.dat',' '
```

```
    ,23);
[SW4_M5] = importdata('SW4/OptimizationData/M5_forces.dat',' '
    ,23);

[SW5_M1] = importdata('SW5/OptimizationData/M1_forces.dat',' '
    ,23);
[SW5_M2] = importdata('SW5/OptimizationData/M2_forces.dat',' '
    ,23);
[SW5_M3] = importdata('SW5/OptimizationData/M3_forces.dat',' '
    ,23);
[SW5_M4] = importdata('SW5/OptimizationData/M4_forces.dat',' '
    ,23);
[SW5_M5] = importdata('SW5/OptimizationData/M5_forces.dat',' '
    ,23);

SW_M = {SW1_M1, SW1_M2, SW1_M3, SW1_M4, SW1_M5, SW2_M1, SW2_M2
    , SW2_M3, SW2_M4, SW2_M5, SW3_M1, SW3_M2, SW3_M3, SW3_M4,
    SW3_M5, SW4_M1, SW4_M2, SW4_M3, SW4_M4, SW4_M5, SW5_M1,
    SW5_M2, SW5_M3, SW5_M4, SW5_M5};

%% Axial Forces
Iter = 1000; %Number of iterations to average over
k = 0;
for i = 1:length(SW_M)
    I = SW_M{i};
    k=k+1;
    fx_I = mean(I.data(([length(I.data)-Iter:end]),33)); %
        Time Avg at 33
    fx(:,k) = fx_I;
end
fx_3_check = mean(SW1_M3.data(([length(SW1_M3.data)-Iter:end])
    ,33));

%% Vertical Forces
k = 0;
for j = 1:length(SW_M)
    J = SW_M{j};
    k=k+1;
    fy_J = mean(J.data(([length(J.data)-Iter:end]),34)); %
        Time Avg at 34
    fy(:,k) = fy_J;
end
fy_3_Check = mean(SW1_M3.data(([length(SW1_M3.data)-Iter:end])
    ,34));

%% Moment about the z-axis
x_cor = -1.28; % Correction for incorrect location of Moment
    Reference point in CFD Settings
k = 0;
for e = 1:length(SW_M)
    E = SW_M{e};
    k=k+1;
    Mz_E = mean(E.data(([length(E.data)-Iter:end]),38))/x_cor;
        % Time Avg at 38
    Mz(:,k) = Mz_E;
end
 Mz_3_Check = mean(SW1_M3.data(([length(SW1_M3.data)-Iter:end
    ]),38))/x_cor;
```

```
578
579 %% Lift
580 AoA = 24;
581 k = 0;
582 for p = 1:length(SW_M)
583     FX_L = fx(p);
584     FY_L = fy(p);
585     k=k+1;
586     L_P = FY_L*cosd(AoA)-FX_L*sind(AoA);
587     L(:,k) = L_P;
588 end
589 L_3_Check = fy(:,3)*cosd(AoA)+fx(:,3)*sind(AoA);
590
591 %% Drag
592 k = 0;
593 for q = 1:length(SW_M)
594     FX_D = fx(q);
595     FY_D = fy(q);
596     k=k+1;
597     D_P = FX_D*cosd(AoA)+FY_D*sind(AoA);
598     D(:,k) = D_P;
599 end
600 D_3_Check = fx(:,3)*cosd(AoA)+fy(:,3)*sind(AoA);
601
602 %% Pitching Moment
603 x_cm = 1.3; % in - Estimated distance from Aero Center
604 MomRef_L = 1; % in - NA
605 % PM_0 =  (Mz_0/MomRef_L)-(L_0*cosd(0)*x_cm)+(D_0*-sind(0)*
       x_cm);
606 k = 0;
607 for z = 1:length(SW_M)
608     L_PM = L(z);
609     D_PM = D(z);
610     Mz_PM = Mz(z);
611     k=k+1;
612     PM_Z = (Mz_PM/MomRef_L)-(L_PM*cosd(AoA)*x_cm)+(D_PM*-sind(
          AoA)*x_cm);
613     PM(:,k) = PM_Z;
614 end
615 PM_3_Check = (Mz(:,3)/MomRef_L)-(L(:,3)*cosd(AoA)*x_cm)+(D
       (:,3)*-sind(AoA)*x_cm);
616
617 %% Coeffiecient of Lift
618 k = 0;
619 for v = 1:length(SW_M)
620     L_CL = L(v);
621     k=k+1;
622     CL_V = (L_CL*2)/(0.67764*0.0009518*((3751.5/12)^2));
623     CL(:,k) = CL_V;
624 end
625 CL_3_Check = (L(:,3)*2)/(0.67764*0.0009518*((3751.5/12)^2));
626
627 %% Coeffiecient of Drag
628 % CD_0 =(D_0*2)/(0.67764*0.0009518*((3751.5/12)^2));
629 k = 0;
630 for w = 1:length(SW_M)
631     D_CD = D(w);
632     k=k+1;
```

```
633         CD_W = (D_CD*2)/(0.67764*0.0009518*((3751.5/12)^2));
634         CD(:,k) = CD_W;
635     end
636     CD_3_Check = (D(:,3)*2)/(0.67764*0.0009518*((3751.5/12)^2));
637
638     %% Moment Coeffiecient
639     c_bar = 9.66;
640     % CM_0 =(PM_0*2)/(0.67764*0.0009518*((3751.5/12)^2)*c_bar);
641     k = 0;
642     for x = 1:length(SW_M)
643         PM_CM = PM(x);
644         k=k+1;
645         CM_X = (PM_CM*2)/(0.67764*0.0009518*((3751.5/12)^2)*c_bar)
                ;
646         CM(:,k) = CM_X;
647     end
648     CM_3_Check =(PM(:,3)*2)/(0.67764*0.0009518*((3751.5/12)^2)*
        c_bar);
649
650     %% Momentum Cefficient (C_mu) and Blowing Ratio (BR)
        Calcualtion
651     V_inf = 3751.5; % in/s
652     C_mu = [0.49, 1.95, 4.4, 7.82, 12.22, 0.392, 1.56, 3.52,
        6.256, 9.776, 0.294, 1.17, 2.64, 4.692, 7.332, 0.196, 0.78,
         1.76, 3.128, 4.888, 0.098, 0.39, 0.88, 1.564, 2.444];
653     V_slot = [3643.67, 7268.72, 10918.61, 14556.07, 18196.02];
654
655     BR = V_slot/V_inf;
656
657     %% Percent Gain/Reduction CL/CD/CM
658     CL_Base_24AoA = 0.8021; % <--CFD, WT =0.8021
659     CD_Base_24AoA = 0.3503; % <--CFD, WT =0.3478
660     CM_Base_24AoA = -0.03129; % <--CFD, WT =-0.028291
661
662     CL_BLF_24AoA = 0.8505; %WT
663     CD_BLF_24AoA = 0.3567;  %WT
664     CM_BLF_24AoA = -0.06696; %WT
665
666     CL_AFC_WT = [0.8508, 0.8861, 0.98912, 1.10134, 1.14839,]; % 24
        AoA Wind tunnel values in order of Cmu (M1, M2, M3, M4, M5)
667     CD_AFC_WT = [0.3423, 0.32275, 0.32244, 0.31237, 0.24135,]; %
        24AoA Wind tunnel values in order of Cmu (M1, M2, M3, M4,
        M5)
668     CM_AFC_WT = [-0.08023, -0.0758, -0.08285, -0.08556,
        -0.07247,]; % 24AoA Wind tunnel values in order of Cmu (M1,
         M2, M3, M4, M5)
669
670     CL_Combine = [CL, CL_Base_24AoA, CL_BLF_24AoA, CL_AFC_WT];
671     CD_Combine = [CD, CD_Base_24AoA, CD_BLF_24AoA, CD_AFC_WT];
672     CM_Combine = [CM, CM_Base_24AoA, CM_BLF_24AoA, CM_AFC_WT];
673
674     CL_PerGain = 100*((CL_Combine-CL_Base_24AoA)/abs(CL_Base_24AoA
        ));
675
676     CD_PerRed = 100*((CD_Combine-CD_Base_24AoA)/abs(CD_Base_24AoA)
        );
677
678     CM_PerRed = 100*((CM_Combine-CM_Base_24AoA)/abs(CM_Base_24AoA)
```

```
    );
679
680 %% CD, CL, CM vs Alpha Plots
681 % figure()
682 % hold on
683 % plot(Alpha_Baseline2,CD_Base2, 'k--*',  'LineWidth',0.9)
684 % plot(Alpha_BLF_1,CD_BLF_1,'--p','Color', [0.25 0.80 0.54],
      'LineWidth',0.9)
685 % plot(Alpha_Slot_200_JD,CD_Slot_200_JD, 'r--v',  'LineWidth
      ',0.9)
686 % plot(Alpha_Slot_400_JD,CD_Slot_400_JD, 'g--^',  'LineWidth
      ',0.9)
687 % plot(Alpha_Slot_600_JD,CD_Slot_600_JD, 'b-->',  'LineWidth
      ',0.9)
688 % plot(Alpha_Slot_800_JD,CD_Slot_800_JD, 'm--<',  'LineWidth
      ',0.9)
689 % plot(Alpha_Slot_1000_JD,CD_Slot_1000_JD, '--s',  'LineWidth
      ',0.9)
690 % plot(AoA,CD(:,1),'ro',AoA,CD(:,2),'go',AoA,CD(:,3),'bo',AoA,
      CD(:,4),'mo',AoA,CD(:,5),'o','LineWidth',0.9)
691 % grid on
692 % colororder([0.9290 0.6940 0.1250]) % Marker with no color
      assigned is Orange (M5)
693 % xlim([23 25])
694 % xlabel('\alpha (deg)')
695 % ylabel('Uncorrected C_D (-)')
696 % hold off
697 % %title('Coefficient of Drag at 45 mph')
698 % legend('Baseline Model','BLF Model','Slot Model, C\mu
      =0.49%','Slot Model, C\mu=1.95%','Slot Model, C\mu=4.40%'
      ,'Slot Model, C\mu=7.82%','Slot Model, C\mu=12.22%','SW1 M1
      ','SW1 M2','SW1 M3','SW1 M4','SW1 M5','Location','best')
699 % %legend('Windtunnel Basic Model','Fence Model','Slot Model,
      600 SLPM%')
700 % %legend('Windtunnel Basic Model','CFD Basic Model','Location
      ','best')
701 %
702 % figure()
703 % hold on
704 % plot(Alpha_Baseline2,CL_Base2, 'k--*',  'LineWidth',0.9)
705 % plot(Alpha_BLF_1,CL_BLF_1,'--p','Color', [0.25 0.80 0.54],
      'LineWidth',0.9)
706 % plot(Alpha_Slot_200_JD,CL_Slot_200_JD, 'r--v',  'LineWidth
      ',0.9)
707 % plot(Alpha_Slot_400_JD,CL_Slot_400_JD, 'g--^',  'LineWidth
      ',0.9)
708 % plot(Alpha_Slot_600_JD,CL_Slot_600_JD, 'b-->',  'LineWidth
      ',0.9)
709 % plot(Alpha_Slot_800_JD,CL_Slot_800_JD, 'm--<',  'LineWidth
      ',0.9)
710 % plot(Alpha_Slot_1000_JD,CL_Slot_1000_JD, '--s','LineWidth
      ',0.9)
711 % plot(AoA,CL(:,1),'ro',AoA,CL(:,2),'go',AoA,CL(:,3),'bo',AoA,
      CL(:,4),'mo',AoA,CL(:,5),'o','LineWidth',0.9)
712 % grid on
713 % colororder([0.9290 0.6940 0.1250]) % Marker with no color
      assigned is Orange (M5)
714 % xlim([23 25])
```

```
715 % xlabel('\alpha  (deg)')
716 % ylabel('Uncorrected C_L (-)')
717 % hold off
718 % legend('Baseline Model','Fence Model','Slot Model, C\mu
      =0.49%','Slot Model, C\mu=1.95%','Slot Model, C\mu=4.40%'
      ,'Slot Model, C\mu=7.82%','Slot Model, C\mu=12.22%','SW1 M1
      ','SW1 M2','SW1 M3','SW1 M4','SW1 M5','Location','best')
719 % %title('Coefficient of Lift at 45 mph')
720 % %legend('Windtunnel Basic Model','CFD Basic Model','Location
      ','best')
721 %
722 % figure()
723 % hold on
724 % plot(Alpha_Baseline2,CM_Base2, 'k--*',  'LineWidth',0.9)
725 % plot(Alpha_BLF_1,CM_BLF_1,'--p','Color', [0.25 0.80 0.54], '
      LineWidth',0.9)
726 % plot(Alpha_Slot_200_JD,CM_Slot_200_JD, 'r--v',  'LineWidth
      ',0.9)
727 % plot(Alpha_Slot_400_JD,CM_Slot_400_JD, 'g--^',  'LineWidth
      ',0.9)
728 % plot(Alpha_Slot_600_JD,CM_Slot_600_JD, 'b-->',  'LineWidth
      ',0.9)
729 % plot(Alpha_Slot_800_JD,CM_Slot_800_JD, 'm--<',  'LineWidth
      ',0.9)
730 % plot(Alpha_Slot_1000_JD,CM_Slot_1000_JD, '--s', 'LineWidth
      ',0.9)
731 % plot(AoA,CM(:,1),'ro',AoA,CM(:,2),'go',AoA,CM(:,3),'bo',AoA,
      CM(:,4),'mo',AoA,CM(:,5),'o','LineWidth',0.9)
732 % grid on
733 % colororder([0.9290 0.6940 0.1250]) % Marker with no color
      assigned is Orange (M5)
734 % xlim([23 25])
735 % xlabel('\alpha (deg)')
736 % ylabel('Uncorrected C_M (-)')
737 % hold off
738 % legend('Baseline Model','Fence Model','Slot Model, C\mu
      =0.49%','Slot Model, C\mu=1.95%','Slot Model, C\mu=4.40%'
      ,'Slot Model, C\mu=7.82%','Slot Model, C\mu=12.22%','SW1 M1
      ','SW1 M2','SW1 M3','SW1 M4','SW1 M5','Location','best')
739 % %title('Pitch Moment Coefficient at 45 mph')
740 % %The coeffcient curves are superimposed, providng evidence
      that the data is good
741
742 %% Same Plots as above w/different markers
743 % figure()
744 % hold on
745 % plot(Alpha_Baseline2,CD_Base2, 'k:.',  'LineWidth',1.5)
746 % plot(Alpha_BLF_1,CD_BLF_1,':.','Color', [0.25 0.80 0.54],  '
      LineWidth',1.5)
747 % plot(Alpha_Slot_200_JD,CD_Slot_200_JD, 'r:.',  'LineWidth
      ',1.5)
748 % plot(Alpha_Slot_400_JD,CD_Slot_400_JD, 'g:.',  'LineWidth
      ',1.5)
749 % plot(Alpha_Slot_600_JD,CD_Slot_600_JD, 'b:.',  'LineWidth
      ',1.5)
750 % plot(Alpha_Slot_800_JD,CD_Slot_800_JD, 'm:.',  'LineWidth
      ',1.5)
751 % plot(Alpha_Slot_1000_JD,CD_Slot_1000_JD, ':.', 'LineWidth
```

```
      ',1.5)
752 % plot(AoA,CD(:,1),'ro',AoA,CD(:,2),'go',AoA,CD(:,3),'bo',AoA,
      CD(:,4),'mo',AoA,CD(:,5),'o','LineWidth',1.1)
753 % grid on
754 % colororder([0.9290 0.6940 0.1250]) % Marker with no color
      assigned is Orange (M5)
755 % xlim([23 26.5])
756 % ylim([0.23 0.39])
757 % xlabel('\alpha (deg)')
758 % ylabel('C_D (-)')
759 % hold off
760 % %title('Coefficient of Drag at 45 mph')
761 % legend('Baseline WT','BLF WT','AFC WT, C\mu=0.49%','AFC WT,
      C\mu=1.95%','AFC WT, C\mu=4.40%' ,'AFC WT, C\mu=7.82%','AFC
       WT, C\mu=12.22%','AFC CFD, C\mu=0.49%','AFC CFD, C\mu
      =1.95%','AFC CFD, C\mu=4.40%','AFC CFD, C\mu=7.82%','AFC
      CFD, C\mu=12.22%','Location','east')
762 % %legend('Windtunnel Basic Model','Fence Model','Slot Model,
      600 SLPM%')
763 % %legend('Windtunnel Basic Model','CFD Basic Model','Location
      ','best')
764 %
765 % figure()
766 % hold on
767 % plot(Alpha_Baseline2,CL_Base2, 'k:.',  'LineWidth',1.5)
768 % plot(Alpha_BLF_1,CL_BLF_1,':.','Color', [0.25 0.80 0.54],  '
      LineWidth',1.5)
769 % plot(Alpha_Slot_200_JD,CL_Slot_200_JD, 'r:.',  'LineWidth
      ',1.5)
770 % plot(Alpha_Slot_400_JD,CL_Slot_400_JD, 'g:.',  'LineWidth
      ',1.5)
771 % plot(Alpha_Slot_600_JD,CL_Slot_600_JD, 'b:.',  'LineWidth
      ',1.5)
772 % plot(Alpha_Slot_800_JD,CL_Slot_800_JD, 'm:.',  'LineWidth
      ',1.5)
773 % plot(Alpha_Slot_1000_JD,CL_Slot_1000_JD, ':.','LineWidth
      ',1.5)
774 % plot(AoA,CL(:,1),'ro',AoA,CL(:,2),'go',AoA,CL(:,3),'bo',AoA,
      CL(:,4),'mo',AoA,CL(:,5),'o','LineWidth',1.1)
775 % grid on
776 % colororder([0.9290 0.6940 0.1250]) % Marker with no color
      assigned is Orange (M5)
777 % xlim([23 26.5])
778 % xlabel('\alpha  (deg)')
779 % ylabel('C_L (-)')
780 % hold off
781 % legend('Baseline WT','BLF WT','AFC WT, C\mu=0.49%','AFC WT,
      C\mu=1.95%','AFC WT, C\mu=4.40%' ,'AFC WT, C\mu=7.82%','AFC
       WT, C\mu=12.22%','AFC CFD, C\mu=0.49%','AFC CFD, C\mu
      =1.95%','AFC CFD, C\mu=4.40%','AFC CFD, C\mu=7.82%','AFC
      CFD, C\mu=12.22%','Location','east')
782 % %title('Coefficient of Lift at 45 mph')
783 % %legend('Windtunnel Basic Model','CFD Basic Model','Location
      ','best')
784 %
785 % figure()
786 % hold on
787 % plot(Alpha_Baseline2,CM_Base2, 'k:.',  'LineWidth',1.5)
```

```
788 % plot(Alpha_BLF_1,CM_BLF_1,':.','Color', [0.25 0.80 0.54], '
      LineWidth',1.5)
789 % plot(Alpha_Slot_200_JD,CM_Slot_200_JD, 'r:.',  'LineWidth
      ',1.5)
790 % plot(Alpha_Slot_400_JD,CM_Slot_400_JD, 'g:.',  'LineWidth
      ',1.5)
791 % plot(Alpha_Slot_600_JD,CM_Slot_600_JD, 'b:.',  'LineWidth
      ',1.5)
792 % plot(Alpha_Slot_800_JD,CM_Slot_800_JD, 'm:.',  'LineWidth
      ',1.5)
793 % plot(Alpha_Slot_1000_JD,CM_Slot_1000_JD,':.', 'LineWidth
      ',1.5)
794 % plot(AoA,CM(:,1),'ro',AoA,CM(:,2),'go',AoA,CM(:,3),'bo',AoA,
      CM(:,4),'mo',AoA,CM(:,5),'o','LineWidth',1.1)
795 % grid on
796 % colororder([0.9290 0.6940 0.1250]) % Marker with no color
      assigned is Orange (M5)
797 % xlim([23 26.5])
798 % xlabel('\alpha (deg)')
799 % ylabel('C_M (-)')
800 % hold off
801 % legend('Baseline WT','BLF WT','AFC WT, C\mu=0.49%','AFC WT,
      C\mu=1.95%','AFC WT, C\mu=4.40%' ,'AFC WT, C\mu=7.82%','AFC
       WT, C\mu=12.22%','AFC CFD, C\mu=0.49%','AFC CFD, C\mu
      =1.95%','AFC CFD, C\mu=4.40%','AFC CFD, C\mu=7.82%','AFC
      CFD, C\mu=12.22%','Location','east')
802 % %title('Pitch Moment Coefficient at 45 mph')
803 % %The coeffcient curves are superimposed, providng evidence
      that the data is good
804
805 %% Slot Comparison All CL,CD,CM
806 % figure ()
807 % hold on
808 % yline(CL_Base_24AoA, '--k')
809 % plot(AoA,CL(:,1),'ro',AoA,CL(:,2),'go',AoA,CL(:,3),'bo',AoA,
      CL(:,4),'mo',AoA,CL(:,5),'o','LineWidth',0.9) % SW1 - M1,M2
      ,M3,M4,M5
810 % plot(AoA,CL(:,6),'rv',AoA,CL(:,7),'gv',AoA,CL(:,8),'bv',AoA,
      CL(:,9),'mv',AoA,CL(:,10),'v','LineWidth',0.9) % SW2 - M1,
      M2,M3,M4,M5
811 % plot(AoA,CL(:,11),'r^',AoA,CL(:,12),'g^',AoA,CL(:,13),'b^',
      AoA,CL(:,14),'m^',AoA,CL(:,15),'^','LineWidth',0.9) % SW3 -
       M1,M2,M3,M4,M5
812 % plot(AoA,CL(:,16),'rs',AoA,CL(:,17),'gs',AoA,CL(:,18),'bs',
      AoA,CL(:,19),'ms',AoA,CL(:,20),'s','LineWidth',0.9) % SW4 -
       M1,M2,M3,M4,M5
813 % plot(AoA,CL(:,21),'rd',AoA,CL(:,22),'gd',AoA,CL(:,23),'bd',
      AoA,CL(:,24),'md',AoA,CL(:,25),'d','LineWidth',0.9) % SW5 -
       M1,M2,M3,M4,M5
814 % colororder([0.9290 0.6940 0.1250]) % Marker with no color
      assigned is Orange (M5)
815 % grid on
816 % legend('Baseline','SW1 M1','SW1 M2','SW1 M3','SW1 M4','SW1
      M5','SW2 M1','SW2 M2','SW2 M3','SW2 M4','SW2 M5','SW3 M1','
      SW3 M2','SW3 M3','SW3 M4','SW3 M5','SW4 M1','SW4 M2','SW4
      M3','SW4 M4','SW4 M5','SW5 M1','SW5 M2','SW5 M3','SW5 M4','
      SW5 M5','Location','best')
817 % xlabel('\alpha (deg)')
```

```
818 % ylabel('C_{L Uncorrected} (-)')
819 % hold off
820 %
821 % figure ()
822 % hold on
823 % yline(CD_Base_24AoA, '--k')
824 % plot(AoA,CD(:,1),'ro',AoA,CD(:,2),'go',AoA,CD(:,3),'bo',AoA,
      CD(:,4),'mo',AoA,CD(:,5),'o','LineWidth',0.9) % SW1 - M1,M2
      ,M3,M4,M5
825 % plot(AoA,CD(:,6),'rv',AoA,CD(:,7),'gv',AoA,CD(:,8),'bv',AoA,
      CD(:,9),'mv',AoA,CD(:,10),'v','LineWidth',0.9) % SW2 - M1,
      M2,M3,M4,M5
826 % plot(AoA,CD(:,11),'r^',AoA,CD(:,12),'g^',AoA,CD(:,13),'b^',
      AoA,CD(:,14),'m^',AoA,CD(:,15),'^','LineWidth',0.9) % SW3 -
       M1,M2,M3,M4,M5
827 % plot(AoA,CD(:,16),'rs',AoA,CD(:,17),'gs',AoA,CD(:,18),'bs',
      AoA,CD(:,19),'ms',AoA,CD(:,20),'s','LineWidth',0.9) % SW4 -
       M1,M2,M3,M4,M5
828 % plot(AoA,CD(:,21),'rd',AoA,CD(:,22),'gd',AoA,CD(:,23),'bd',
      AoA,CD(:,24),'md',AoA,CD(:,25),'d','LineWidth',0.9) % SW5 -
       M1,M2,M3,M4,M5
829 % colororder([0.9290 0.6940 0.1250]) % Marker with no color
      assigned is Orange (M5)
830 % grid on
831 % legend('Baseline','SW1 M1','SW1 M2','SW1 M3','SW1 M4','SW1
      M5','SW2 M1','SW2 M2','SW2 M3','SW2 M4','SW2 M5','SW3 M1','
      SW3 M2','SW3 M3','SW3 M4','SW3 M5','SW4 M1','SW4 M2','SW4
      M3','SW4 M4','SW4 M5','SW5 M1','SW5 M2','SW5 M3','SW5 M4','
      SW5 M5','Location','best')
832 % xlabel('\alpha (deg)')
833 % ylabel('C_{D Uncorrected} (-)')
834 % hold off
835 %
836 % figure ()
837 % hold on
838 % yline(CM_Base_24AoA, '--k')
839 % plot(AoA,CM(:,1),'ro',AoA,CM(:,2),'go',AoA,CM(:,3),'bo',AoA,
      CM(:,4),'mo',AoA,CM(:,5),'o','LineWidth',0.9) % SW1 - M1,M2
      ,M3,M4,M5
840 % plot(AoA,CM(:,6),'rv',AoA,CM(:,7),'gv',AoA,CM(:,8),'bv',AoA,
      CM(:,9),'mv',AoA,CM(:,10),'v','LineWidth',0.9) % SW2 - M1,
      M2,M3,M4,M5
841 % plot(AoA,CM(:,11),'r^',AoA,CM(:,12),'g^',AoA,CM(:,13),'b^',
      AoA,CM(:,14),'m^',AoA,CM(:,15),'^','LineWidth',0.9) % SW3 -
       M1,M2,M3,M4,M5
842 % plot(AoA,CM(:,16),'rs',AoA,CM(:,17),'gs',AoA,CM(:,18),'bs',
      AoA,CM(:,19),'ms',AoA,CM(:,20),'s','LineWidth',0.9) % SW4 -
       M1,M2,M3,M4,M5
843 % plot(AoA,CM(:,21),'rd',AoA,CM(:,22),'gd',AoA,CM(:,23),'bd',
      AoA,CM(:,24),'md',AoA,CM(:,25),'d','LineWidth',0.9) % SW5 -
       M1,M2,M3,M4,M5
844 % colororder([0.9290 0.6940 0.1250]) % Marker with no color
      assigned is Orange (M5)
845 % grid on
846 % legend('Baseline','SW1 M1','SW1 M2','SW1 M3','SW1 M4','SW1
      M5','SW2 M1','SW2 M2','SW2 M3','SW2 M4','SW2 M5','SW3 M1','
      SW3 M2','SW3 M3','SW3 M4','SW3 M5','SW4 M1','SW4 M2','SW4
      M3','SW4 M4','SW4 M5','SW5 M1','SW5 M2','SW5 M3','SW5 M4','
```

```
    SW5 M5','Location','best')
% xlabel('\alpha (deg)')
% ylabel('C_{M Uncorrected} (-) (-)')
% hold off

%% Compare each Mach at each slot widths
% figure ()
% hold on
% subplot(1,5,1)
% yline(CL_Base_24AoA, '--k')
% plot(AoA,CL(:,1),'ro',AoA,CL(:,6),'r+',AoA,CL(:,11),'r*',AoA
    ,CL(:,16),'rs',AoA,CL(:,21),'rd','LineWidth',0.9)
% legend('Baseline','SW1 M1','SW2 M1','SW3 M1','SW4 M1','SW5
    M1','Location','northoutside')
% xlim([23 25])
% ylim([min(CL)-0.02 max(CL)+0.02])
% ylabel('Coeffiecient of Lift')
%
% subplot(1,5,2)
% yline(CL_Base_24AoA, '--k')
% plot(AoA,CL(:,2),'go',AoA,CL(:,7),'g+',AoA,CL(:,12),'g*',AoA
    ,CL(:,17),'gs',AoA,CL(:,22),'gd','LineWidth',0.9)
% legend('Baseline','SW1 M2','SW2 M2','SW3 M2','SW4 M2','SW5
    M2','Location','northoutside')
% xlim([23 25])
% ylim([min(CL)-0.02 max(CL)+0.02])
%
% subplot(1,5,3)
% yline(CL_Base_24AoA, '--k')
% plot(AoA,CL(:,3),'bo',AoA,CL(:,8),'b+',AoA,CL(:,13),'b*',AoA
    ,CL(:,18),'bs',AoA,CL(:,23),'bd','LineWidth',0.9)
% legend('Baseline','SW1 M3','SW2 M3','SW3 M3','SW4 M3','SW5
    M3','Location','northoutside')
% xlim([23 25])
% ylim([min(CL)-0.02 max(CL)+0.02])
% xlabel('Angle of Attack (deg)')
%
%
% subplot(1,5,4)
% yline(CL_Base_24AoA, '--k')
% plot(AoA,CL(:,4),'mo',AoA,CL(:,9),'m+',AoA,CL(:,14),'m*',AoA
    ,CL(:,19),'ms',AoA,CL(:,24),'md','LineWidth',0.9)
% legend('Baseline','SW1 M4','SW2 M4','SW3 M4','SW4 M4','SW5
    M4','Location','northoutside')
% xlim([23 25])
% ylim([min(CL)-0.02 max(CL)+0.02])
%
% subplot(1,5,5)
% yline(CL_Base_24AoA, '--k')
% plot(AoA,CL(:,5),'o',AoA,CL(:,10),'+',AoA,CL(:,15),'*',AoA,
    CL(:,20),'s',AoA,CL(:,25),'d','LineWidth',0.9,'Color
    ',[0.9290 0.6940 0.1250])
% legend('Baseline','SW1 M5','SW2 M5','SW3 M5','SW4 M5','SW5
    M5','Location','northoutside')
% xlim([23 25])
% ylim([min(CL)-0.02 max(CL)+0.02])
% hold off

```

```
893 %% CL/CD/CM vs Cmu - Individual Points
894 % figure ()
895 % hold on
896 % yline(CL_Base_24AoA, '--k')
897 % plot(C_mu(:,1),CL(:,1),'ro',C_mu(:,2),CL(:,2),'go',C_mu(:,3)
      ,CL(:,3),'bo',C_mu(:,4),CL(:,4),'mo',C_mu(:,5),CL(:,5),'o
      ','LineWidth',0.9)
898 % plot(C_mu(:,6),CL(:,6),'r+',C_mu(:,7),CL(:,7),'g+',C_mu(:,8)
      ,CL(:,8),'b+',C_mu(:,9),CL(:,9),'m+',C_mu(:,10),CL(:,10)
      ,'+','LineWidth',0.9)
899 % plot(C_mu(:,11),CL(:,11),'r*',C_mu(:,12),CL(:,12),'g*',C_mu
      (:,13),CL(:,13),'b*',C_mu(:,14),CL(:,14),'m*',C_mu(:,15),CL
      (:,15),'*','LineWidth',0.9)
900 % plot(C_mu(:,16),CL(:,16),'rs',C_mu(:,17),CL(:,17),'gs',C_mu
      (:,18),CL(:,18),'bs',C_mu(:,19),CL(:,19),'ms',C_mu(:,20),CL
      (:,20),'s','LineWidth',0.9)
901 % plot(C_mu(:,21),CL(:,21),'rd',C_mu(:,22),CL(:,22),'gd',C_mu
      (:,23),CL(:,23),'bd',C_mu(:,24),CL(:,24),'md',C_mu(:,25),CL
      (:,25),'d','LineWidth',0.9)
902 % colororder([0.9290 0.6940 0.1250]) % Marker with no color
      assigned is Orange (M5)
903 % legend({'Baseline','SW1 M1','SW1 M2','SW1 M3','SW1 M4','SW1
      M5','SW2 M1','SW2 M2','SW2 M3','SW2 M4','SW2 M5','SW3 M1','
      SW3 M2','SW3 M3','SW3 M4','SW3 M5','SW4 M1','SW4 M2','SW4
      M3','SW4 M4','SW4 M5','SW5 M1','SW5 M2','SW5 M3','SW5 M4','
      SW5 M5'},'Location','southeast')
904 % ylabel('Coeffiecient of Lift')
905 % xlabel('Momentum Coefficient')
906 % hold off
907
908 %% CL/CD/CM vs Cmu - Lines of Constant Slot Width
909 % figure ()
910 % hold on
911 % yline(CL_Base_24AoA, '--k')
912 % plot(C_mu(:,[1 2 4 5]),CL(:,[1 2 4 5]),'r','LineWidth',0.9)
913 % plot(C_mu(:,[6 8 9 10]),CL(:,[6 8 9 10]),'g','LineWidth
      ',0.9)
914 % plot(C_mu(:,[11 12 14 15]),CL(:,[11 12 14 15]),'b','
      LineWidth',0.9)
915 % plot(C_mu(:,[16 17 18 19 20]),CL(:,[16 17 18 19 20]),'m','
      LineWidth',0.9)
916 % plot(C_mu(:,[21 22 24 25]),CL(:,[21 22 24 25]),'LineWidth
      ',0.9,'Color',[0.9290 0.6940 0.1250])
917 % % plot(fit(C_mu(:,[1 2 3 4 5])',CL(:,[1 2 3 4 5])','
      smoothingspline','SmoothingParam',[0.1]),'r--') %
      smoothingspline
918 % % plot(fit(C_mu(:,[6 7 8 9 10])',CL(:,[6 7 8 9 10])','
      smoothingspline','SmoothingParam',[0.5]),'g--')
919 % % plot(fit(C_mu(:,[11 12 13 14 15])',CL(:,[11 12 13 14 15])
      ','smoothingspline','SmoothingParam',[0.5]),'b--')
920 % % plot(fit(C_mu(:,[16 17 18 19 20])',CL(:,[16 17 18 19 20])
      ','smoothingspline','SmoothingParam',[0.5]),'m--')
921 % % plot(fit(C_mu(:,[21 22 24 25])',CL(:,[21 22 24 25])','
      smoothingspline','SmoothingParam',[0.5]),'--')
922 % ylim([min(CL)-0.01 max(CL)+0.02])
923 % colororder([0.9290 0.6940 0.1250]) % Marker with no color
      assigned is Orange (M5)
924 % legend('Baseline','24^o \alpha: SW1','24^o \alpha SW2','24^o
```

```
       \alpha SW3','24^o \alpha SW4','24^o \alpha SW5','SW1 Fit
      ','SW2 Fit','SW3 Fit','SW4 Fit','SW5 Fit','Location','
      southeast')
925 % ylabel('Coeffiecient of Lift')
926 % xlabel('Momentum Coefficient')
927 % hold off
928 %
929 % figure ()
930 % hold on
931 % yline(CD_Base_24AoA, '--k')
932 % plot(C_mu(:,[1 2 4 5]),CD(:,[1 2 4 5]),'r','LineWidth',0.9)
933 % plot(C_mu(:,[6 8 9 10]),CD(:,[6 8 9 10]),'g','LineWidth
      ',0.9)
934 % plot(C_mu(:,[11 12 14 15]),CD(:,[11 12 14 15]),'b','
      LineWidth',0.9)
935 % plot(C_mu(:,[16 17 18 19 20]),CD(:,[16 17 18 19 20]),'m','
      LineWidth',0.9)
936 % plot(C_mu(:,[21 22 24 25]),CD(:,[21 22 24 25]),'LineWidth
      ',0.9,'Color',[0.9290 0.6940 0.1250])
937 % legend('Baseline','24^o \alpha: SW1','24^o \alpha SW2','24^o
       \alpha SW3','24^o \alpha SW4','24^o \alpha SW5','SW1 Fit
      ','SW2 Fit','SW3 Fit','SW4 Fit','SW5 Fit','Location','
      southeast')
938 % ylabel('Coeffiecient of Drag')
939 % xlabel('Momentum Coefficient')
940 % hold off
941 %
942 % figure ()
943 % hold on
944 % yline(CM_Base_24AoA, '--k')
945 % plot(C_mu(:,[1 2 4 5]),CM(:,[1 2 4 5]),'r','LineWidth',0.9)
946 % plot(C_mu(:,[6 8 9 10]),CM(:,[6 8 9 10]),'g','LineWidth
      ',0.9)
947 % plot(C_mu(:,[11 12 14 15]),CM(:,[11 12 14 15]),'b','
      LineWidth',0.9)
948 % plot(C_mu(:,[16 17 18 19 20]),CM(:,[16 17 18 19 20]),'m','
      LineWidth',0.9)
949 % plot(C_mu(:,[21 22 24 25]),CM(:,[21 22 24 25]),'LineWidth
      ',0.9,'Color',[0.9290 0.6940 0.1250])
950 % legend('Baseline','24^o \alpha: SW1','24^o \alpha SW2','24^o
       \alpha SW3','24^o \alpha SW4','24^o \alpha SW5','SW1 Fit
      ','SW2 Fit','SW3 Fit','SW4 Fit','SW5 Fit','Location','
      southeast')
951 % ylabel('Pitching Moment Coeffiecient')
952 % xlabel('Momentum Coefficient')
953 % hold off
954
955
956 %% CL/CD/CM vs BR - Lines of Constant Slot Width
957 %
958 % figure ()
959 % hold on
960 % yline(CL_Base_24AoA, '--k')
961 % plot(BR(:,[1 2 4 5]),CL(:,[1 2 4 5]),'r','LineWidth',0.9)
962 % plot(BR(:,[1 3 4 5]),CL(:,[6 8 9 10]),'g','LineWidth',0.9)
963 % plot(BR(:,[1 2 4 5]),CL(:,[11 12 14 15]),'b','LineWidth
      ',0.9)
964 % plot(BR(:,[1 2 3 4 5]),CL(:,[16 17 18 19 20]),'m','LineWidth
```

```
    ',0.9)
965 % plot(BR(:,[1 2 4 5]),CL(:,[21 22 24 25]),'LineWidth',0.9,'
    Color',[0.9290 0.6940 0.1250])
966 % legend('Baseline','24^o \alpha: SW1','24^o \alpha SW2','24^o
    \alpha SW3','24^o \alpha SW4','24^o \alpha SW5','SW1 Fit
    ','SW2 Fit','SW3 Fit','SW4 Fit','SW5 Fit','Location','
    northwest')
967 % ylabel('Coeffiecient of Lift')
968 % xlabel('Blowing Ratio (V_{slot}/V_{\infty})')
969 % hold off
970 %
971 % figure ()
972 % hold on
973 % yline(CD_Base_24AoA, '--k')
974 % plot(BR(:,[1 2 4 5]),CD(:,[1 2 4 5]),'r','LineWidth',0.9)
975 % plot(BR(:,[1 3 4 5]),CD(:,[6 8 9 10]),'g','LineWidth',0.9)
976 % plot(BR(:,[1 2 4 5]),CD(:,[11 12 14 15]),'b','LineWidth
    ',0.9)
977 % plot(BR(:,[1 2 3 4 5]),CD(:,[16 17 18 19 20]),'m','LineWidth
    ',0.9)
978 % plot(BR(:,[1 2 4 5]),CD(:,[21 22 24 25]),'LineWidth',0.9,'
    Color',[0.9290 0.6940 0.1250])
979 % legend('Baseline','24^o \alpha: SW1','24^o \alpha SW2','24^o
    \alpha SW3','24^o \alpha SW4','24^o \alpha SW5','SW1 Fit
    ','SW2 Fit','SW3 Fit','SW4 Fit','SW5 Fit','Location','
    southeast')
980 % ylabel('Coeffiecient of Drag')
981 % xlabel('Blowing Ratio (V_{slot}/V_{\infty})')
982 % hold off
983 %
984 % figure ()
985 % hold on
986 % yline(CM_Base_24AoA, '--k')
987 % plot(BR(:,[1 2 4 5]),CM(:,[1 2 4 5]),'r','LineWidth',0.9)
988 % plot(BR(:,[1 3 4 5]),CM(:,[6 8 9 10]),'g','LineWidth',0.9)
989 % plot(BR(:,[1 2 4 5]),CM(:,[11 12 14 15]),'b','LineWidth
    ',0.9)
990 % plot(BR(:,[1 2 3 4 5]),CM(:,[16 17 18 19 20]),'m','LineWidth
    ',0.9)
991 % plot(BR(:,[1 2 4 5]),CM(:,[21 22 24 25]),'LineWidth',0.9,'
    Color',[0.9290 0.6940 0.1250])
992 % legend('Baseline','24^o \alpha: SW1','24^o \alpha SW2','24^o
    \alpha SW3','24^o \alpha SW4','24^o \alpha SW5','SW1 Fit
    ','SW2 Fit','SW3 Fit','SW4 Fit','SW5 Fit','Location','north
    ')
993 % ylabel('Pitching Moment Coeffiecient')
994 % xlabel('Blowing Ratio (V_{slot}/V_{\infty})')
995 % hold off
996
997 %% Cmu VS Percent Gain with lines of Constant Slot Width
998
999 figure ()
1000 hold on
1001 %plot(0,CL_PerGain(:,[26]),'ko','LineWidth',2)
1002 % plot(0,CL_PerGain(:,[27]),'ks','Color', [0.25 0.80 0.54],'
    LineWidth',1.7) % BLF WT Gains
1003 %plot(C_mu(:,[1 2 3 4 5]),CL_PerGain(:,[28 29 30 31 32]),'k--h
    ','LineWidth',0.9) %AFC WT Percent Gains
```

```
plot(C_mu(:,[1 2 4 5]),CL_PerGain(:,[1 2 4 5]),'r--o','LineWidth',0.9)
plot(C_mu(:,[6 8 9 10]),CL_PerGain(:,[6 8 9 10]),'g--v','LineWidth',0.9)
plot(C_mu(:,[11 12 14 15]),CL_PerGain(:,[11 12 14 15]),'b--^','LineWidth',0.9)
plot(C_mu(:,[16 17 18 19 20]),CL_PerGain(:,[16 17 18 19 20]),'m--s','LineWidth',0.9)
plot(C_mu(:,[21 22 24 25]),CL_PerGain(:,[21 22 24 25]),'--d','LineWidth',0.9,'Color',[0.9290 0.6940 0.1250])
grid on
%legend('24^o \alpha: Baseline CFD','24^o \alpha: BLF CFD','24^o \alpha: AFC WT','24^o \alpha: AFC CFD SW1','24^o \alpha: AFC CFD SW2','24^o \alpha: AFC CFD SW3','24^o \alpha: AFC CFD SW4','24^o \alpha: AFC CFD SW5','Location','east')
legend('AFC CFD SW1(0.037in), \alpha = 24^o','AFC CFD SW2(0.0296in), \alpha = 24^o','AFC CFD SW3(0.0222in), \alpha = 24^o','AFC CFD SW4(0.0148in), \alpha = 24^o','AFC CFD SW5(0.0074in), \alpha = 24^o','Location','southeast')
ylabel('C_L (% Gain)')
xlabel('C_\mu (%)')
xlim([0 14])
ylim([0 40])
hold off

% figure ()
% hold on
% plot(0,CD_PerRed(:,[26]),'k*','LineWidth',1.5)
% plot(0,CD_PerRed(:,[27]),'p','Color', [0.25 0.80 0.54],'LineWidth',0.9)
% plot(C_mu(:,[1 2 3 4 5]),CD_PerRed(:,[28 29 30 31 32]),'k--h','LineWidth',0.9)
% plot(C_mu(:,[1 2 4 5]),CD_PerRed(:,[1 2 4 5]),'r--o','LineWidth',0.9)
% plot(C_mu(:,[6 8 9 10]),CD_PerRed(:,[6 8 9 10]),'g--v','LineWidth',0.9)
% plot(C_mu(:,[11 12 14 15]),CD_PerRed(:,[11 12 14 15]),'b--^','LineWidth',0.9)
% plot(C_mu(:,[16 17 18 19 20]),CD_PerRed(:,[16 17 18 19 20]),'m--s','LineWidth',0.9)
% plot(C_mu(:,[21 22 24 25]),CD_PerRed(:,[21 22 24 25]),'--d','LineWidth',0.9,'Color',[0.9290 0.6940 0.1250])
% grid on
% legend('24^o \alpha: Baseline WT','24^o \alpha: BLF WT','24^o \alpha: AFC WT','24^o \alpha: AFC CFD SW1','24^o \alpha: AFC CFD SW2','24^o \alpha: AFC CFD SW3','24^o \alpha: AFC CFD SW4','24^o \alpha: AFC CFD SW5','Location','east')
% ylabel('C_D (% Reduction)')
% xlabel('C_\mu (%)')
% xlim([0 19])
% hold off
%
% figure ()
% hold on
% plot(0,CM_PerRed(:,[26]),'k*','LineWidth',1.5)
% plot(0,CM_PerRed(:,[27]),'p','Color', [0.25 0.80 0.54],'LineWidth',0.9)
```

```
% plot(C_mu(:,[1 2 3 4 5]),CM_PerRed(:,[28 29 30 31 32]),'k--h
  ','LineWidth',0.9)
% plot(C_mu(:,[1 2 4 5]),CM_PerRed(:,[1 2 4 5]),'r--o','
  LineWidth',0.9)
% plot(C_mu(:,[6 8 9 10]),CM_PerRed(:,[6 8 9 10]),'g--v','
  LineWidth',0.9)
% plot(C_mu(:,[11 12 14 15]),CM_PerRed(:,[11 12 14 15]),'b
  --^','LineWidth',0.9)
% plot(C_mu(:,[16 17 18 19 20]),CM_PerRed(:,[16 17 18 19 20])
  ,'m--s','LineWidth',0.9)
% plot(C_mu(:,[21 22 24 25]),CM_PerRed(:,[21 22 24 25]),'--d
  ','LineWidth',0.9,'Color',[0.9290 0.6940 0.1250])
% grid on
% legend('24^o \alpha: Baseline WT','24^o \alpha: BLF WT','24^
  o \alpha: AFC WT','24^o \alpha: AFC CFD SW1','24^o \alpha:
  AFC CFD SW2','24^o \alpha: AFC CFD SW3','24^o \alpha: AFC
  CFD SW4','24^o \alpha: AFC CFD SW5','Location','east')
% ylabel('C_M (% Reduction)')
% xlabel('C_\mu (%)')
% xlim([0 19])
% hold off
```

Appendix H. MATLAB Script: AFC Slot Extent Optimization

```
%% AFC Slot Extent Optimization
clear all; close all; clc; format compact; format short;
%% Baseline, Passive BLF and AFC Slot, Freestream M = 0.059,
   SW1, M1-M5 Wind Tunnel Uncorrected Data
alpha = 1;
Alpha_Baseline2=alpha+...
[-8.17894442052277;-7.16850773849801;-6.15464379090849;...
-5.04877209800816;-4.02932120636633;-3.00640352702020;...
-1.98382443346184;-0.870213403716582;0.153319187693818;...
1.17508365277160;2.19900159794485;3.30928370940170;...
4.32751503348324;5.34186930698045;6.44211101586254;...
7.45523765217682;8.46819102061274;9.56920569459411;...
10.6678210098701;11.6756459136262;12.7671846976348;...
13.7663130389622;14.8512817871214;15.9311893169993;...
17.0110707277628;18.0844673115262;19.1538944819053;...
20.2221014158863;21.3721215112022;22.4257937648188;...
23.5698166553147;24.6991922407033;25.7472428560031;...
26.8830239002552;28.0967117595190;29.2310840568254;...
30.4510280084815;31.6729762552610;32.9017417048610;...
34.2275325071614;35.4596797612262;36.7847709966838];...
CD_Base2=...
[0.0326396226315288;0.0273554591561591;0.02320762912...
52264;0.0184655617641355;0.0156734227994947;0.013931...
8232188933;0.0127460003513771;0.0110429698239139;0.0...
115328779992575;0.0132684007837646;0.01594624739861...
14;0.0186260816468254;0.0227511043823911;0.027425377...
8944443;0.0325465190807324;0.0391042044857320;0.0473...
291339011119;0.0578153893612589;0.0714274594986400;0...
.0882968225391222;0.107396801468250;0.12837527862316...
1;0.152008514898266;0.177050724527485;0.203713593209...
787;0.230608840670329;0.257527050009981;0.2850390953...
55441;0.311662701851170;0.335885212499362;0.35962757...
0078000;0.378102215918811;0.393975988177553;0.4094634...
43267234;0.422979456980625;0.438129375146260;0.452553...
360061481;0.469150907399056;0.488570671603892;0.51410...
4483039872;0.536274210618872;0.565069415967284];
CL_Base2=...
[-0.380686716946657,-0.335679522978898,-0.28809803698...
6591,-0.235205472140068,-0.180638051940071,-0.1234544...
23606297,-0.0655693172981972,-0.00446862170388157,0.0...
533671656873325,0.110388299123664,0.169693355141534,...
0.227263490287654,0.279476897333351,0.32863898256204...
2,0.375560539057904,0.422360052709387,0.4700363760260...
67,0.517777718341523,0.561913793013043,0.604151005786...
968,0.641842476206843,0.673795777863523,0.70451924645...
7192,0.729874924214394,0.754142327869694,0.7725926727...
70825,0.786833165496932,0.798718935717348,0.805103685...
529550,0.802634940849533,0.801598645011175,0.78608838...
7524569,0.776596912840933,0.767880111293073,0.7484587...
51498765,0.737187298271561,0.724400980387816,0.713740...
363550526,0.709249314247855,0.715390882106700,0.71448...
6482896382,0.719886109135885]';
CM_Base2=...
[-0.00241933648422381;-0.000994749356042714;0.00052513...
```

```
8889181397;0.000531995120895268;-0.000127610521605613;...
-0.00112181497128817;-0.00238738588975404;-0.004014823...
77348298;-0.00458591893002119;-0.00447507033838957;-0.0...
0570421624022764;-0.0063975922846427 3;-0.006060593543...
11681;-0.00452373994614179;-0.00254238263866779;-0.000...
802608455539601;0.000686585846786974;0.0019224715481...
3012;0.00305034068341110;0.00384085470805589;0.0046514...
9185638424;0.00533251814807207;0.00492217834961218;0.0...
0390892393185356;0.00131507381415635;-0.0018753227054...
2222;-0.00563731602852632;-0.0109907490359497;-0.016914...
9235037892;-0.0248236615415000;-0.0317363120696212;-0.0...
393746528162185;-0.0435606742506112;-0.043896906122957...
7;-0.0457089065451211;-0.0471099572765705;-0.04925656335...
62850;-0.0525805261396649;-0.0556579516727002;-0.0595181...
996791140;-0.0641550435894548;-0.0701361258272115];


Alpha_BLF_1=alpha+...
[-8.06594564259070;-7.14241231732519;-6.03905594741620;...
-5.01406378048430;-3.98721923601549;-2.87195351727540;...
-1.85058803650554;-0.831110322743736;0.275151806711067;...
1.29346471552093;2.31597900276951;3.42813304789199;...
4.45108375100950;5.55684707512697;6.57167414343638;...
7.58705903612775;8.69009006482263;9.70504580065541;...
10.7161174843277;11.2642436005670;11.8166774071110;...
12.2766843085277;12.8266085308312;13.3790159996166;...
13.8375751427264;14.3856475805125;14.9354617926899;...
15.3929723623862;15.9414105042531;16.4688861494385;...
16.9094889255359;17.4240418013865;17.9837233404080;...
18.4646453036484;18.9881016785306;19.5209239626320;...
20.0480920643511;20.4921008071506;21.0161537952655;...
21.5513155912465;21.9819661259102;22.4844514540255;...
23.0266031504895;23.4649469590941;23.9788010755111;...
24.4993216153161;24.9404098936923;25.4654301290090;...
25.9851110721517;26.4294113964856;26.9572368515206;...
27.4879036272060;27.9159749086103;28.4552397489093;...
28.9719941570135;29.4032901602970;29.9353877441201;...
30.4579590792370;30.8794429116547;31.4044874140582;...
31.9278672633083;32.3622515736385;32.8915967016012];
 CD_BLF_1=...
 [0.0331859562592513;0.0285589439023825;0.0225065331772370;...
 0.0189468223940387;0.0158403087605802;0.0131311169034887;...
 0.0122527914619488;0.0124686038531358;0.0121007596222725;...
 0.0139941157444537;0.0168024120917713;0.0202655564151916;...
 0.0245968486909978;0.0291105237603469;0.0348275369759939;...
 0.0415565640185381;0.0491966039352059;0.0596374268695133;...
 0.0712235463740903;0.0783859677428014;0.0880240892437888;...
 0.0983355252004903;0.108101954523449;0.118749897647422;...
 0.128576970063239;0.140223144052195;0.152845063683076;...
 0.165098099722719;0.178263738604623;0.190669762413875;...
 0.200917116172463;0.213283639422009;0.230302422336980;...
 0.251856410673102;0.265348318598858;0.280169649171469;...
 0.293079995746426;0.306468524342820;0.316087744265308;...
 0.331153701240424;0.339352993468659;0.343805149187245;...
 0.357367274638073;0.365487071651346;0.371746744842184;...
 0.378965080879246;0.387348160309275;0.396148794017582;...
 0.400919634435716;0.410355844881111;0.418992542285874;...
 0.429377784632715;0.432161428908286;0.445358004857721;...
```

```
0.449511061662298;0.454432235165533;0.466615637205070;...
0.473488130419345;0.473825618553497;0.483262801297828;...
0.490134615871489;0.495193519187196;0.506592291154017];
CL_BLF_1=...
[-0.354173691100548,-0.309063999932849,-0.259899691306692,...
-0.201576490582196,-0.140228135605584,-0.0784330946201286,...
-0.0228956859968763,0.0306396081385506,0.0818251136500848,...
0.134125047245865,0.190880848861979,0.249375733204867,...
0.306594385654906,0.357250871754507,0.405853817460111,...
0.455048376575644,0.503867637134175,0.552607044125295,...
0.596166557862589,0.617511770875898,0.642365030513726,...
0.663583807519691,0.685775470178208,0.710600796703577,...
0.730284120516020,0.750511830740319,0.773647392520254,...
0.791158054932682,0.811773620986288,0.811217504491707,...
0.810796219594365,0.796534564440700,0.829074572567749,...
0.871414723998235,0.866595878432624,0.870649689280734,...
0.869767400527153,0.872958391535774,0.867711724905650,...
0.875307331477488,0.864330969244883,0.837270800264997,...
0.851219132828200,0.848402048276708,0.833399307819857,...
0.824406222320952,0.825560420849990,0.821339590367901,...
0.811456051420846,0.816016858774003,0.814771168240697,...
0.817599478203143,0.803887629919240,0.814774241132624,...
0.802847471376179,0.792555675655018,0.796901461921134,...
0.790083394307436,0.769385076296350,0.766250555705866,...
0.760289976252899,0.754334128100513,0.754700161457019]';
CM_BLF_1=...
[-0.00645565729432271;-0.00543366737074639;-0.00497230375830425;...

-0.00626840903527524;-0.00812639164827980;-0.00967798053293440;...

-0.00945309222782101;-0.00865038220961338;-0.00670502210461011;...

-0.00488751112138329;-0.00454480696604581;-0.00481732423437155;...

-0.00548800757156123;-0.00442664971617944;-0.00282825806744191;...

-0.00138620542503159;-0.000204421890390911;...
0.000817753587349030;0.00130240859034837;0.00109615288671430;
0.000464851194557061;-0.00149193626706634;-0.00380972808029311;...

-0.00533306500332433;-0.00620595983241655;-0.00759321564382312;...

-0.00870105692850148;-0.0108249745414312;-0.0129892457825265;...

-0.00516853422314401;-0.000189350755310846;-0.00462159855872107;...

-0.0191437591914945;-0.0261932152732147;-0.0251904959472022;...

-0.0378876638882588;-0.0478485428343769;-0.0499899927653833;...

-0.0545965073248441;-0.0540169594750646;-0.0642403701311685;...

-0.0678397210048976;-0.0669126861227226;-0.0711347448349583;...

-0.0673556117123620;-0.0649522888342130;-0.0668780318358190;...

-0.0603695865129550;-0.0637109281367164;-0.0621148519578112;...
```

```
  -0.0619758111857658;-0.0662567712765227;-0.0668173655521368;...
  -0.0655033106457927;-0.0660623006320958;-0.0655506777401585;...
  -0.0645042350127906;-0.0634239194747829;-0.0619745103601840;...
  -0.0628071667857057;-0.0612590184216668;-0.0608586271989955;...
  -0.0620809601781004]+0.01;

Alpha_Slot_200_JD=alpha+...
[-8.13930569650318;-7.12694507515062;-6.02140811853273;...
-5.00170105594408;-3.98198111516462;-2.87036265170578;...
-1.84851324989122;-0.829147376904798;0.278405572171361;...
0.830926257583539;1.29568572893127;1.84718260035369;...
2.40197787987524;2.86990616314340;3.42386719604621;...
3.89045100146877;4.44232258507587;5.45367108933443;...
6.55597231268537;7.56639951144478;8.66928705589410;...
9.68113243597496;10.6947912580051;11.7961467191067;...
12.8093111578703;13.8364110334608;14.9500955001699;...
15.9579723471582;16.9664225058238;18.0282886988279;...
19.0036122250817;20.0556137860657;21.0148460077832;...
21.9702533986755;22.9384955211547;23.9902030711724;...
24.9551128961650;25.9233516796538;26.9910982455396;...
27.9409309963523;28.9897676706375;29.9562597573613;...
30.8989470972295;31.9683622607734;32.9188182156738];...
CD_Slot_200_JD=...
[0.0249842840892673;0.0195604134915005;0.0143834216638...
751;0.0108549143990608;0.00816881835012328;0.004879311...
46539239;0.00395781966804512;0.00365483992792561;0.004...
28241322482735;0.00474407790921938;0.0057582558648709...
8;0.00645273970293498;0.00751031094048318;0.0094122348...
9896528;0.0110575635340329;0.0132817317745282;0.015133...
5148856012;0.0188803112856184;0.0240003722774144;0.029...
4918706354342;0.0366716976789302;0.0443669347927839;0....
0532532582951283;0.0695916787031502;0.088008587337434...
5;0.108464773625040;0.136824436503663;0.16582820991150...
7;0.192436036579450;0.223461254556216;0.25112573246278...
7;0.280867767929434;0.301227165976154;0.32037888054629...
5;0.341135419249444;0.360932278333196;0.37833276340675...
3;0.395976505144352;0.419017614622716;0.43261089695018...
3;0.450796231404737;0.466349160853958;0.47795232912708...
8;0.500123088459546;0.510802744409361];
CL_Slot_200_JD=...
[-0.338646961351646,-0.292659862392328,-0.2411828826456...
14,-0.188464920242479,-0.134672726701926,-0.07674586574...
51916,-0.0206952235870607,0.0327214552553833,0.0852759...
690471117,0.111281942933680,0.136480593829496,0.161400...
738366892,0.188758512195716,0.217317919068340,0.244851...
486437686,0.271984976572820,0.297302530690163,0.341155...
632833166,0.389200881638037,0.433137445034258,0.481804...
530093597,0.527245178134752,0.573548540644765,0.620590...
739659397,0.667430345563330,0.729049497802401,0.789167...
505771261,0.829338662373363,0.871178430668242,0.876339...
382985236,0.883045943420430,0.877744734569981,0.866324...
720972384,0.851908768417901,0.851104984074884,0.845491...
955167970,0.841154026490747,0.839286128027530,0.850683...
644332506,0.830355379707657,0.821697577864173,0.819037...
```

```
753064181,0.790070686515306,0.803237872240048,0.783570...
560967676]';
CM_Slot_200_JD=...
[-0.0083497933857716 1;-0.00715681206848110;-0.0065466537...
4145752;-0.00688203234423188;-0.00779458060051240;-0.009...
27762017151896;-0.00966528705279758;-0.009567947808616 0...
9;-0.00825205444560790;-0.00753024158239537;-0.006931591...
21437764;-0.00624167419865799;-0.00627780524635620;-0.00...
677685305657774;-0.00714047929698264;-0.00719647138574...
427;-0.00666526788181024;-0.00520675806074079;-0.0033756...
8081036960;-0.00182896399677014;-0.000752203860571932;...
-8.69837691748233e
   -05;0.000220931046794505;-0.00394263893098121;-0.01545796...

10548854;-0.0286247777470567;-0.0421161886578441;-0.0526...
581066968622;-0.0622903713117134;-0.0649164366029284;-0....
0679676602655533;-0.0710301613427541;-0.073605044751386...
5;-0.0757827756531143;-0.0801753059813129;-0.08113066871...
99231;-0.0827144357251951;-0.0846946079541785;-0.0854294...
231628424;-0.0841215861740769;-0.0841665989358836;-0.084...
2169756662313;-0.0831993253281970;-0.0831674320221782;...
-0.0852008474669002];

Alpha_Slot_400_JD=alpha+...
[-8.14107995734776;-7.12810380397329;-6.02294002587198;...
-5.00100829505852;-3.98065584668460;-2.87139441735438;...
-1.84952770602303;-0.829170803599483;0.280451313638561;...
0.832112928356729;1.29695570220239;1.84800350937919;...
2.40181187810453;2.86816341968855;3.42161042868440;...
3.88872287648642;4.43966731528486;5.45162906889796;...
6.55437032751475;7.56363601108004;8.66657245565575;...
9.67845705484742;10.6909516992006;11.7958743891732;...
12.8114141249747;13.8346778549107;14.9378776008161;...
15.9387749238412;16.9346122624383;18.0179820522858;...
18.9964023200859;20.0620812411592;21.0303959822269;...
22.0041179249296;22.9715615402812;24.0260517121405;...
24.9988278640787;25.9736340670725;27.0422333311487;...
27.9946973069450;29.0418733935211;29.9959334967865;...
30.9671914337833;32.0001766548288;32.9663708286242];...
CD_Slot_400_JD=...
[0.00569768908582134;0.000653616631782971;-0.0040173...
3492747906;-0.00742990193772587;-0.0102174497790087;...
-0.0133023270693763;-0.0142207914583933;-0.014594291...
7647373;-0.0142093229799219;-0.0138959193545874;-0.01...
26582858300000;-0.0117907234379582;-0.01058897412493...
04;-0.00846719539239434;-0.00710909653460416;-0.00465...
318894119242;-0.00296639088322539;0.001052522621462...
43;0.00651350808441484;0.0117933998076995;0.01891820...
08004069;0.0261482628131217;0.0342962335695831;0.043...
8656700474776;0.0552077756509481;0.0693740477420460;...
0.105172507392724;0.139528921009682;0.1679357319248...
90;0.199834155989705;0.226344669145139;0.25453057310...
9369;0.277085828367057;0.300568277707328;0.322077310...
429307;0.346829752414292;0.367124558895408;0.3862760...
86830406;0.412179568299533;0.427395948086337;0.44643...
3916573160;0.462425886927703;0.482117157303679;0.493...
772336860829;0.513431234800692];
CL_Slot_400_JD=...
```

```
[-0.340528694281068,-0.293888778754073,-0.242807582020...
513,-0.187730196836646,-0.133267182896577,-0.077840128...
4080720,-0.0217711282459079,0.0326966095383901,0.08744...
56269616597,0.112540493770281,0.137827493036031,0.162...
271372214259,0.188582455220084,0.215469612627635,0.242...
458020182855,0.270152174087562,0.294486423567305,0.338...
989921342888,0.387501859615882,0.430206551500381,0.478...
925498707463,0.524407741473837,0.569476408715038,0.620...
301913918239,0.669660695436623,0.727211335640237,0.776...
209533096261,0.808978395884902,0.837441349306045,0.865...
408433204394,0.875399313732268,0.884603942028837,0.882...
816602113635,0.887824566473365,0.886173907128255,0.883...
512051474941,0.887516935802066,0.892614264341189,0.904...
916129219707,0.887378470447064,0.876959494318545,0.861...
114645048685,0.862448778909116,0.836979355690106,0.834...
003572518458]';
CM_Slot_400_JD=...
[-0.0095985070030111;-0.00874982906994464;-0.007907456...
16336122;-0.00881500204053227;-0.00980820493121330;-0.0...
110651682189337;-0.0113239431035566;-0.011840219262665...
1;-0.0108308275197412;-0.0103000706859604;-0.0095246466...
1322938;-0.0085719019079036 5;-0.00834770619569028;-0.00...
849964062857796;-0.00863106772547918;-0.00879291315863...
069;-0.00837630719200007;-0.00694002271937745;-0.005296...
62406811701;-0.00331477093293976;-0.00212958191237636;...
-0.00145238375830875;-0.000726417246053755;-0.00025042...
8208528577;-0.00158101230521345;-0.0119384093858803;-0...
.0278569646668860;-0.0391783362526073;-0.0469237967756...
573;-0.0566692689865733;-0.0616690489485235;-0.06525804...
91857559;-0.0682765276124359;-0.0731923881907869;-0.075...
6053897214873;-0.0829084605615219;-0.0854438243424612;...
-0.0882944149254450;-0.0890506385715564;-0.08978128770...
85074;-0.0915346082694105;-0.0921384186320555;-0.092891...
1886500812;-0.0935403064400923;-0.0928891979397311];...

Alpha_Slot_600_JD=alpha+...
[-8.15250305008806;-7.13851290714992;-6.03051364430308;...
-5.01117589838906;-3.99037918445528;-2.87932753037828;...
-1.85626236599775;-0.834814878555532;0.274142141001341;...
0.826066351573143;1.29116820600337;1.84275410005435;...
2.39770025991947;2.86382014537051;3.41749994600344;...
3.88381537566056;4.43571125667504;5.44782988317605;...
6.55176145418855;7.56357115087161;8.66644528646187;...
9.67834967266616;10.6916630962418;11.7982876029726;...
12.8131855970119;13.8340664829350;14.9467350593083;...
15.9674637590202;16.9845101257540;18.0875632637920;...
19.0966204643189;20.1633774635334;21.1396071845055;...
22.1110566367845;23.0677525891127;24.1201163602511;...
25.0488677017462;25.9941081509589;27.0518668176482;...
28.0270018230895;29.0770736345079;30.0501514516892;...
31.0001085712215;32.0467826847915;33.0096335195687];...
CD_Slot_600_JD=...
[-0.0130658913688246;-0.0180842416071628;-0.022456305...
0802255;-0.0257976158492426;-0.0287702976700154;-0.03...
20076226532163;-0.0324107936394564;-0.03261643771122...
30;-0.0319837811121743;-0.0315085156292136;-0.0299661...
090276477;-0.0291775542254593;-0.0280246271852704;-0....
0256038813179883;-0.0238580183687156;-0.021228450678...
```

```
7270;-0.0191196323640248;-0.0149694630879372;-0.009078...
06619669437;-0.00304101045471653;0.00383001613165229...
;0.0113398715173390;0.019705816947943 0;0.030249908478...
1012;0.0403212498678895;0.0524337189708148;0.06698199...
27082439;0.0825577218736728;0.103000268644405;0.13377...
6722358127;0.185679142766743;0.238490168158967;0.2693...
60459893327;0.299375454581163;0.324196829528256;0.351...
115142779436;0.367985743075838;0.376515906340747;0.39...
9577001851152;0.422730003720431;0.444102434599543;0.4...
65101086216071;0.483472381511884;0.501379222405195;...
0.518553198817997];
CL_Slot_600_JD=...
[-0.352643716618924,-0.304928391262603,-0.250839956313...
286,-0.198513681158485,-0.143579491215208,-0.086253772...
9155831,-0.0289137259544743,0.0267106567212663,0.08075...
42895829787,0.106127658431716,0.131689431538560,0.156...
703991061284,0.184221784490254,0.210863253686253,0.23...
8098553737877,0.264947411815210,0.290290735103814,0.3...
34960608009534,0.384734959325207,0.430137762522489,0....
478790626509576,0.524293854844864,0.570230897122041,0...
.622861303021514,0.671539470632569,0.726562931104796,0...
.785603513336904,0.839404996363596,0.890361669785317,0...
.939204378913497,0.981687959342012,0.992035968075043,0...
.998643041172583,1.00124086382455,0.988191524579992,0....
983274465995295,0.940587830428161,0.914328522403276,0....
915133143717022,0.921639764091660,0.914291915191565,0....
918616737493617,0.897359802082030,0.886408446997923,0....
879886809143175]';
CM_Slot_600_JD=...
[-0.00723738933360987;-0.00620776301636090;-0.00619294...
458505423;-0.00651444951696916;-0.00743876910006222;-0...
.00861584790279979;-0.00966118845439566;-0.0105746532...
004899;-0.00980569395259948;-0.00916198942512294;-0.00...
848389612122977;-0.00782406485606092;-0.0076584206531...
9508;-0.00782905371730899;-0.00814129622862258;-0.0082...
4703629731736;-0.00807708135388103;-0.006707450540029...
11;-0.00524683155342631;-0.00386734839632959;-0.002368...
46368680112;-0.00158201749017828;-0.00111774076086887...
;-0.000634937187145405;-0.00138717124650150;-0.0105812...
981760175;-0.0222199752206172;-0.0342678895374102;-0.0...
456083761608960;-0.0577344485022751;-0.06970409688556...
46;-0.0754547156471550;-0.0791776508059520;-0.08150487...
85559114;-0.0829557505717916;-0.0847154169596503;-0.08...
23035973940487;-0.0858402438505193;-0.084752948869612...
3;-0.0857334788596333;-0.0837092498012970;-0.085689331...
5450340;-0.0917963917474111;-0.0940930991685665;-0.097...
4335038708480];

Alpha_Slot_800_JD=alpha+...
[-8.16532994130786;-7.15071579092200;-6.04244860884083;...
-5.02099510922208;-4.00074350475546;-2.89013300970893;...
-1.86673672339860;-0.845557601359153;0.262744376454180;...
0.815668234712962;1.28098830005780;1.83392968241970;...
2.38963009158842;2.85600354947695;3.41124262157922;...
3.87728372488066;4.42928798070192;5.44207749788951;...
6.54701850023257;7.55851760590759;8.66181167361823;...
9.67231113504006;10.6858135558792;11.7945702669411;...
12.8095448979892;13.8303756931133;14.9434105377481;...
```

```
15.9616233762802;16.9770125159476;18.0751112575024;...
19.0870816918115;20.1944651800602;21.2080328942639;...
22.1973387095223;23.1762140686440;24.2493579805815;...
25.2214289083073;26.1923382924692;27.2178579547376;...
28.1285669372076;29.1882477121527;30.1384264568971;...
31.0873604704253;32.0796152955456;33.0318609966642];...
CD_Slot_800_JD=...
[-0.00681050693390072;-0.0126543294087441;-0.0182495...
693770797;-0.0214166231427484;-0.0251674028323114;-0...
.0284813491243448;-0.0295284521703782;-0.0300352983...
439126;-0.0297999387101721;-0.0295720385414848;-0.02...
82132488021699;-0.0273310852132612;-0.026210383664...
1072;-0.0240278454672732;-0.0220435932508557;-0.0190...
684670650371;-0.0168993698727356;-0.01216566243845...
81;-0.00643704479454368;-0.000469991253904901;0.0068...
1634235048144;0.0143941708545328;0.022555795883598...
0;0.0335793770283875;0.0439463538650867;0.0560009143...
510980;0.0702808537518199;0.0848501778814416;0.10300...
2466782877;0.128061227791715;0.152144243602451;0.182...
336909797974;0.215148357201335;0.275067267157616;0.3...
20558261523750;0.362479685381631;0.396531037918776;...
0.429234176477427;0.457465813635064;0.4677768042418...
04;0.494369876697358;0.510196123102673;0.52428205263...
3874;0.518416110561748;0.533085621458722];
CL_Slot_800_JD=...
[-0.366247569549657,-0.317870438818895,-0.2634978559...
96289,-0.208927669846718,-0.154571608219602,-0.09771...
37712223667,-0.0400225453233562,0.0153172162849387,...
0.0686661296398034,0.0950996977124353,0.1208928993...
96894,0.147345053057996,0.175662782841257,0.2025731...
84086938,0.231462205167657,0.258020120152550,0.2834...
78382821840,0.328859784193542,0.379704711000120,0.4...
24778109798272,0.473876342402648,0.517889545618680...
,0.564027033267523,0.618918797249851,0.667678243993...
874,0.722648579523156,0.782077615939359,0.833210844...
835199,0.882409908178346,0.925998118771882,0.971571...
395935769,1.02500675704765,1.07121349306802,1.09274...
928998711,1.10322282802753,1.12034462316562,1.12360...
156582039,1.12456603399776,1.09117884162421,1.02935...
696942839,1.03220012662585,1.01223881378076,0.98989...
6799890378,0.921229823462180,0.903460668486540]';
CM_Slot_800_JD=...
[-0.00271428206765456;-0.00189706750827400;-0.001585...
10093408801;-0.00257006623435670;-0.003639827594117...
15;-0.00377285117644621;-0.00528002084311486;-0.0060...
4783914821188;-0.00542639016919631;-0.0048547859236...
7664;-0.00467522918668672;-0.00464200994639661;-0.00...
484881943788308;-0.00517612644732052;-0.00576129489...
607823;-0.00558567933442236;-0.00544667475420462;-0....
00388856835124193;-0.00257735756993069;-0.001209129...
76751777;0.000188843218942158;0.00126966991609235;0...
.00194730019213918;0.00226867902786383;0.0020075243...
3835763;-0.00655633847238418;-0.0191938207372223;-0.0...
288876484116350;-0.0402225780133489;-0.0509736602055...
526;-0.0593875338193712;-0.0673592849128238;-0.074871...
3020188131;-0.0814793195538752;-0.0864569567583774;-0...
.0922018627535162;-0.0947708467128809;-0.09736442547...
76938;-0.0959300891773638;-0.0898902740886361;-0.0917...
```

```
042960490281;-0.0905853919434668;-0.089976876926054...
0;-0.0848269056017114;-0.0859492228960141];

Alpha_Slot_1000_JD=alpha+...
[-8.19296176515518;-7.17933574587292;-6.07141593961330;...
-5.05068766637736;-4.01478390175705;-2.90376884270189;...
-1.88070289398938;-0.858610138673839;0.251892829170128;...
0.805045079373169;1.27096880298182;1.82550033419823;...
2.29328670403366;2.84752853218911;3.40257829519855;...
3.86968238230243;4.42287620882581;5.43862308343971;...
6.54573182715474;7.55713986284914;8.66098722550410;...
9.67236449623901;10.6852903591628;11.7936837267243;...
12.8112788281600;13.8329825727792;14.9471087553110;1...
5.9664578225023;16.9791398538928;18.0817616704432;...
19.0886948118036;20.1847033352771;21.2029090750168;...
22.2183661266420;23.2279674798223;24.3299915044846;...
25.3283955867359;26.3157875287581;27.3957186622302;...
28.3760532549829;29.4314555943111;30.3576518649962;...
31.2810950601421;32.2836331725416;33.2135410784349];
CD_Slot_1000_JD=...
[-0.0193797893655357;-0.0259114877416335;-0.03258667...
37823424;-0.0372877316448054;-0.0409895595179842;-0.0...
451211540031038;-0.0465323825799716;-0.046985848615...
9102;-0.0470235007266426;-0.0471019968699758;-0.04558...
46122476344;-0.0447892744155420;-0.0432186377043500;...
-0.0416831615990399;-0.0400375162366334;-0.037384285...
6392081;-0.0350786936687696;-0.0303777956122959;-0.02...
17416728583107;-0.0157560312384841;-0.00811648099009...
559;-0.000582397437687672;0.00780414749527014;0.0186...
951181907445;0.0294869235072628;0.0417640755961384;...
0.0566192455906378;0.0718139381421382;0.08864026042...
94024;0.109696609944029;0.131368096438492;0.15524846...
0024663;0.184343329546123;0.215847194077492;0.248784...
760521435;0.293162365698196;0.352499161384842;0.4063...
87379826736;0.458282454622353;0.500207681789809;0.54...
2355888075449;0.570273045623037;0.586548858269573;...
0.595084080898688;0.601632791661711];
CL_Slot_1000_JD=...
[-0.395553132478767,-0.348223986795931,-0.29421982134...
7971,-0.240418790630072,-0.169462472469212,-0.1121755...
65857211,-0.0548346870548746,0.00147404922605309,0.05...
71572729111181,0.0838330672852779,0.110266492551626,...
0.138405114959061,0.166814012293967,0.19358481061487...
2,0.222273055606256,0.249958342381286,0.2766782314731...
33,0.325196125920342,0.378340100431535,0.423316912878...
281,0.473001955093872,0.517946139059006,0.56347214502...
0504,0.617978556741035,0.669517203304557,0.7254133653...
91840,0.785999845181785,0.838338127376218,0.884666105...
104343,0.933051366361309,0.973282227247636,1.01465360...
923606,1.06577930934517,1.11505039826875,1.1581110922...
4280,1.20586235163683,1.23704752376115,1.255492945757...
42,1.27981308396896,1.29183424562026,1.29013981004425...
1.24474333567583,1.19536645118314,1.13760565033506,1.0...
9614563559966]';
CM_Slot_1000_JD=...
[0.00507017714348937;0.00614418826676139;0.006842971...
85030537;0.00699513112022954;0.00437741572681731;0.0...
0282945856269266;0.00113340818135327;0.000333189608...
```

```
933874;0.000586231571137447;0.000924799225952278;0.0...
00824185731205280;0.000767407000762050;0.0003493200...
57341334;-0.000162324801487116;-0.00074296932765326...
5;-0.00125212658580521;-0.00147376228469160;-0.001264...
98499510802;0.00179972763032268;0.00314076315957652...
;0.00435342405830659;0.00526227344420236;0.006221210...
03062758;0.00675959969365219;0.00639421820758831;-0....
00220469951161398;-0.0136034339227159;-0.0230183035...
253696;-0.0325897625335028;-0.0410750732024380;-0.046...
7011262564439;-0.0522773449139122;-0.05960919917759...
88;-0.0671714951745267;-0.0740194214401699;-0.0823273...
039146220;-0.0909191500060944;-0.0970089485628756;...
-0.103913781913880;-0.108509186502984;-0.11207993050...
2852;-0.109408392847778;-0.105477991507032;-0.101058...
260651483;-0.0975542197429547];

%% Import Kestrel Data

[EX1] = importdata('EX1_forces.dat',' ',23);
[EX2] = importdata('EX2_forces.dat',' ',23);
[EX3] = importdata('EX3_forces.dat',' ',23);
[EX4] = importdata('EX4_forces.dat',' ',23);
[EX5] = importdata('EX5_forces.dat',' ',23);
[EX6] = importdata('EX6_forces.dat',' ',23);
[EX7] = importdata('EX7_forces.dat',' ',23);
[EX8] = importdata('EX8_forces.dat',' ',23);

SW_M = {EX1, EX2, EX3, EX4, EX5, EX6, EX7, EX8};
%% Axial Forces
Iter = 1000; %Number of iterations to average over
k = 0;
for i = 1:length(SW_M)
    I = SW_M{i};
    k=k+1;
    fx_I = mean(I.data(([length(I.data)-Iter:end]),33)); %
       Time Avg at 33
    fx(:,k) = fx_I;
end
fx_3_check = mean(EX3.data(([length(EX3.data)-Iter:end]),33));

%% Vertical Forces
k = 0;
for j = 1:length(SW_M)
    J = SW_M{j};
    k=k+1;
    fy_J = mean(J.data(([length(J.data)-Iter:end]),34)); %
       Time Avg at 34
    fy(:,k) = fy_J;
end
fy_3_Check = mean(EX3.data(([length(EX3.data)-Iter:end]),34));

%% Moment about the z-axis
x_cor = -1.28; % Correction for incorrect location of Moment
   Reference point in CFD Settings
k = 0;
for e = 1:length(SW_M)
    E = SW_M{e};
    k=k+1;
```

```
552      Mz_E = mean(E.data(([length(E.data)-Iter:end]),38))/x_cor;
             % Time Avg at 38
553      Mz(:,k) = Mz_E;
554  end
555   Mz_3_Check = mean(EX3.data(([length(EX3.data)-Iter:end]),38))
         /x_cor;
556
557  %% Lift
558  AoA = 24;
559  k = 0;
560  for p = 1:length(SW_M)
561      FX_L = fx(p);
562      FY_L = fy(p);
563      k=k+1;
564      L_P = FY_L*cosd(AoA)-FX_L*sind(AoA);
565      L(:,k) = L_P;
566  end
567  L_3_Check = fy(:,3)*cosd(AoA)+fx(:,3)*sind(AoA);
568
569  %% Drag
570  k = 0;
571  for q = 1:length(SW_M)
572      FX_D = fx(q);
573      FY_D = fy(q);
574      k=k+1;
575      D_P = FX_D*cosd(AoA)+FY_D*sind(AoA);
576      D(:,k) = D_P;
577  end
578  D_3_Check = fx(:,3)*cosd(AoA)+fy(:,3)*sind(AoA);
579
580  %% Pitching Moment
581  x_cm = 1.3; % in - Estimated distance from Aero Center
582  MomRef_L = 1; % in - NA
583  % PM_0 =  (Mz_0/MomRef_L)-(L_0*cosd(0)*x_cm)+(D_0*-sind(0)*
         x_cm);
584  k = 0;
585  for z = 1:length(SW_M)
586      L_PM = L(z);
587      D_PM = D(z);
588      Mz_PM = Mz(z);
589      k=k+1;
590      PM_Z = (Mz_PM/MomRef_L)-(L_PM*cosd(AoA)*x_cm)+(D_PM*-sind(
             AoA)*x_cm);
591      PM(:,k) = PM_Z;
592  end
593  PM_3_Check = (Mz(:,3)/MomRef_L)-(L(:,3)*cosd(AoA)*x_cm)+(D
         (:,3)*-sind(AoA)*x_cm);
594
595  %% Coeffiecient of Lift
596  k = 0;
597  for v = 1:length(SW_M)
598      L_CL = L(v);
599      k=k+1;
600      CL_V = (L_CL*2)/(0.67764*0.0009518*((3751.5/12)^2));
601      CL(:,k) = CL_V;
602  end
603  CL_3_Check = (L(:,3)*2)/(0.67764*0.0009518*((3751.5/12)^2));
604
```

```
%% Coeffiecient of Drag
% CD_0 =(D_0*2)/(0.67764*0.0009518*((3751.5/12)^2));
k = 0;
for w = 1:length(SW_M)
    D_CD = D(w);
    k=k+1;
    CD_W = (D_CD*2)/(0.67764*0.0009518*((3751.5/12)^2));
    CD(:,k) = CD_W;
end
CD_3_Check = (D(:,3)*2)/(0.67764*0.0009518*((3751.5/12)^2));

%% Moment Coeffiecient
c_bar = 9.66;
% CM_0 =(PM_0*2)/(0.67764*0.0009518*((3751.5/12)^2)*c_bar);
k = 0;
for x = 1:length(SW_M)
    PM_CM = PM(x);
    k=k+1;
    CM_X = (PM_CM*2)/(0.67764*0.0009518*((3751.5/12)^2)*c_bar)
        ;
    CM(:,k) = CM_X;
end
CM_3_Check =(PM(:,3)*2)/(0.67764*0.0009518*((3751.5/12)^2)*
    c_bar);

%% Momentum Cefficient (C_mu) and Blowing Ratio (BR)
    Calcualtion
V_inf = 3751.5; % in/s
C_mu = [7.332, 9.165, 5.499, 5.499, 3.666, 1.833, 7.332,
    5.499];
V_slot = [18196.02];

BR = V_slot/V_inf;

%% Percent Gain/Reduction CL/CD/CM
CL_Base_24AoA = 0.8021; % <--CFD, WT =0.8021
CD_Base_24AoA = 0.3503; % <--CFD, WT =0.3478
CM_Base_24AoA = -0.03129; % <--CFD, WT =-0.028291

CL_BLF_24AoA = 0.8505; %WT
CD_BLF_24AoA = 0.3567;  %WT
CM_BLF_24AoA = -0.06696; %WT

CL_AFC_WT = [0.8508, 0.8861, 0.98912, 1.10134, 1.14839,]; % 24
    AoA Wind tunnel values in order of Cmu (M1, M2, M3, M4, M5)
CD_AFC_WT = [0.3423, 0.32275, 0.32244, 0.31237, 0.24135,]; %
    24AoA Wind tunnel values in order of Cmu (M1, M2, M3, M4,
    M5)
CM_AFC_WT = [-0.08023, -0.0758, -0.08285, -0.08556,
    -0.07247,]; % 24AoA Wind tunnel values in order of Cmu (M1,
     M2, M3, M4, M5)

CL_Combine = [CL, CL_Base_24AoA, CL_BLF_24AoA, CL_AFC_WT];
CD_Combine = [CD, CD_Base_24AoA, CD_BLF_24AoA, CD_AFC_WT];
CM_Combine = [CM, CM_Base_24AoA, CM_BLF_24AoA, CM_AFC_WT];

CL_PerGain = 100*((CL_Combine-CL_Base_24AoA)/abs(CL_Base_24AoA
    ));
```

```
653
654 CD_PerRed = 100*((CD_Combine-CD_Base_24AoA)/abs(CD_Base_24AoA)
    );
655
656 CM_PerRed = 100*((CM_Combine-CM_Base_24AoA)/abs(CM_Base_24AoA)
    );
657
658 %% CD, CL, CM vs Alpha Plots
659 % figure()
660 % hold on
661 % plot(Alpha_Baseline2,CD_Base2, 'k',  'LineWidth',0.9)
662 % plot(Alpha_BLF_1,CD_BLF_1,'Color', [0.25 0.80 0.54],  '
     LineWidth',0.9)
663 % plot(Alpha_Slot_200_JD,CD_Slot_200_JD, 'r',  'LineWidth
     ',0.9)
664 % plot(Alpha_Slot_400_JD,CD_Slot_400_JD, 'g',  'LineWidth
     ',0.9)
665 % plot(Alpha_Slot_600_JD,CD_Slot_600_JD, 'b',  'LineWidth
     ',0.9)
666 % plot(Alpha_Slot_800_JD,CD_Slot_800_JD, 'm',  'LineWidth
     ',0.9)
667 % plot(Alpha_Slot_1000_JD,CD_Slot_1000_JD,  'LineWidth',0.9)
668 % plot(AoA,CD(:,1),'ro',AoA,CD(:,2),'go',AoA,CD(:,3),'bo',AoA,
     CD(:,4),'mo',AoA,CD(:,5),'o',AoA,CD(:,6),'ko','LineWidth
     ',0.9)
669 % colororder([0.9290 0.6940 0.1250]) % Marker with no color
     assigned is Orange (M5)
670 % xlim([23 25])
671 % xlabel('Angle of Attack (deg)')
672 % ylabel('Uncorrected Coefficient of Drag (-)')
673 % hold off
674 %
675 % title('Coefficient of Drag at 45 mph')
676 % legend('Baseline Model','Fence Model','Slot Model, C\mu
     =0.49%','Slot Model, C\mu=1.95%','Slot Model, C\mu=4.40%'
     ,'Slot Model, C\mu=7.82%','Slot Model, C\mu=12.22%','EX1','
     EX2','EX3','EX4','EX5','EX6','Location','best')
677 % %legend('Windtunnel Basic Model','Fence Model','Slot Model,
     600 SLPM%')
678 % %legend('Windtunnel Basic Model','CFD Basic Model','Location
     ','best')
679 %
680 % figure()
681 % hold on
682 % plot(Alpha_Baseline2,CL_Base2, 'k',  'LineWidth',0.9)
683 % plot(Alpha_BLF_1,CL_BLF_1,'Color', [0.25 0.80 0.54],  '
     LineWidth',0.9)
684 % plot(Alpha_Slot_200_JD,CL_Slot_200_JD, 'r',  'LineWidth
     ',0.9)
685 % plot(Alpha_Slot_400_JD,CL_Slot_400_JD, 'g',  'LineWidth
     ',0.9)
686 % plot(Alpha_Slot_600_JD,CL_Slot_600_JD, 'b',  'LineWidth
     ',0.9)
687 % plot(Alpha_Slot_800_JD,CL_Slot_800_JD, 'm',  'LineWidth
     ',0.9)
688 % plot(Alpha_Slot_1000_JD,CL_Slot_1000_JD,  'LineWidth',0.9)
689 % plot(AoA,CL(:,1),'ro',AoA,CL(:,2),'go',AoA,CL(:,3),'bo',AoA,
     CL(:,4),'mo',AoA,CL(:,5),'o',AoA,CL(:,6),'ko','LineWidth
```

```
    ',0.9)
690 % colororder([0.9290 0.6940 0.1250]) % Marker with no color
    assigned is Orange (M5)
691 % xlim([23 25])
692 % xlabel('Angle of Attack (deg)')
693 % ylabel('Uncorrected Coefficient of Lift (-)')
694 % hold off
695 % legend('Baseline Model','Fence Model','Slot Model, C\mu
    =0.49%','Slot Model, C\mu=1.95%','Slot Model, C\mu=4.40%'
    ,'Slot Model, C\mu=7.82%','Slot Model, C\mu=12.22%','EX1','
    EX2','EX3','EX4','EX5','EX6','Location','best')
696 % title('Coefficient of Lift at 45 mph')
697 % %legend('Windtunnel Basic Model','CFD Basic Model','Location
    ','best')
698 %
699 % figure()
700 % hold on
701 % plot(Alpha_Baseline2,CM_Base2, 'k',  'LineWidth',0.9)
702 % plot(Alpha_BLF_1,CM_BLF_1,'Color', [0.25 0.80 0.54], '
    LineWidth',0.9)
703 % plot(Alpha_Slot_200_JD,CM_Slot_200_JD, 'r',  'LineWidth
    ',0.9)
704 % plot(Alpha_Slot_400_JD,CM_Slot_400_JD, 'g',  'LineWidth
    ',0.9)
705 % plot(Alpha_Slot_600_JD,CM_Slot_600_JD, 'b',  'LineWidth
    ',0.9)
706 % plot(Alpha_Slot_800_JD,CM_Slot_800_JD, 'm',  'LineWidth
    ',0.9)
707 % plot(Alpha_Slot_1000_JD,CM_Slot_1000_JD,  'LineWidth',0.9)
708 % plot(AoA,CM(:,1),'ro',AoA,CM(:,2),'go',AoA,CM(:,3),'bo',AoA,
    CM(:,4),'mo',AoA,CM(:,5),'o',AoA,CM(:,6),'ko','LineWidth
    ',0.9)
709 % colororder([0.9290 0.6940 0.1250]) % Marker with no color
    assigned is Orange (M5)
710 % xlim([23 25])
711 % xlabel('Angle of Attack (deg)')
712 % ylabel('Uncorrected Pitch Moment Coefficient (-)')
713 % hold off
714 % legend('Baseline Model','Fence Model','Slot Model, C\mu
    =0.49%','Slot Model, C\mu=1.95%','Slot Model, C\mu=4.40%'
    ,'Slot Model, C\mu=7.82%','Slot Model, C\mu=12.22%','EX1','
    EX2','EX3','EX4','EX5','EX6','Location','best')
715 % title('Pitch Moment Coefficient at 45 mph')
716 % %The coeffcient curves are superimposed, providng evidence
    that the data is good
717
718
719 %% CL/CD/CM vs BR - Lines of Constant Slot Width
720
721 % figure ()
722 % hold on
723 % yline(CL_Base_24AoA, '--k')
724 % plot(BR(:,[1]),CL(:,[1]),'ro','LineWidth',0.9)
725 % plot(BR(:,[1]),CL(:,[2]),'go','LineWidth',0.9)
726 % plot(BR(:,[1]),CL(:,[3]),'bo','LineWidth',0.9)
727 % plot(BR(:,[1]),CL(:,[4]),'mo','LineWidth',0.9)
728 % plot(BR(:,[1]),CL(:,[5]),'o','LineWidth',0.9,'Color',[0.9290
    0.6940 0.1250])
```

```
729 % plot(BR(:,[1]),CL(:,[6]),'ko','LineWidth',0.9)
730 % legend('Baseline','EX1','EX2','EX3','EX4','EX5','EX6','
      Location','northwest')
731 % ylabel('Coeffiecient of Lift')
732 % xlabel('Blowing Ratio (V_{slot}/V_{\infty})')
733 % hold off
734 %
735 % figure ()
736 % hold on
737 % yline(CD_Base_24AoA, '--k')
738 % plot(BR(:,[1]),CD(:,[1]),'ro','LineWidth',0.9)
739 % plot(BR(:,[1]),CD(:,[2]),'go','LineWidth',0.9)
740 % plot(BR(:,[1]),CD(:,[3]),'bo','LineWidth',0.9)
741 % plot(BR(:,[1]),CD(:,[4]),'mo','LineWidth',0.9)
742 % plot(BR(:,[1]),CD(:,[5]),'o','LineWidth',0.9,'Color',[0.9290
      0.6940 0.1250])
743 % plot(BR(:,[1]),CD(:,[6]),'ko','LineWidth',0.9)
744 % legend('Baseline','EX1','EX2','EX3','EX4','EX5','EX6','
      Location','northwest')
745 % ylabel('Coeffiecient of Drag')
746 % xlabel('Blowing Ratio (V_{slot}/V_{\infty})')
747 % hold off
748 %
749 % figure ()
750 % hold on
751 % yline(CM_Base_24AoA, '--k')
752 % plot(BR(:,[1]),CM(:,[1]),'ro','LineWidth',0.9)
753 % plot(BR(:,[1]),CM(:,[2]),'go','LineWidth',0.9)
754 % plot(BR(:,[1]),CM(:,[3]),'bo','LineWidth',0.9)
755 % plot(BR(:,[1]),CM(:,[4]),'mo','LineWidth',0.9)
756 % plot(BR(:,[1]),CM(:,[5]),'o','LineWidth',0.9,'Color',[0.9290
      0.6940 0.1250])
757 % plot(BR(:,[1]),CM(:,[6]),'ko','LineWidth',0.9)
758 % legend('Baseline','EX1','EX2','EX3','EX4','EX5','EX6','
      Location','northwest')
759 % ylabel('Pitching Moment Coeffiecient')
760 % xlabel('Blowing Ratio (V_{slot}/V_{\infty})')
761 % hold off
762
763 %% Cmu VS Percent Gain with lines of Constant Slot Width
764 figure ()
765 hold on
766 plot(C_mu(:,[1]),CL_PerGain(:,[1]),'ro','LineWidth',2)
767 plot(C_mu(:,[2]),CL_PerGain(:,[2]),'go','LineWidth',2)
768 plot(C_mu(:,[3]),CL_PerGain(:,[3]),'bo','LineWidth',2)
769 plot(C_mu(:,[4]),CL_PerGain(:,[4]),'mo','LineWidth',1.5)
770 plot(C_mu(:,[5]),CL_PerGain(:,[5]),'o','LineWidth',2,'Color'
      ,[0.9290 0.6940 0.1250])
771 plot(C_mu(:,[6]),CL_PerGain(:,[6]),'ko','LineWidth',2)
772 plot(C_mu(:,[7]),CL_PerGain(:,[7]),'yo','LineWidth',2)
773 plot(C_mu(:,[8]),CL_PerGain(:,[8]),'co','LineWidth',2)
774 %line([0 C_mu(:,[7])],[0,CL_PerGain(:,[7])])
775 %line([0 C_mu(:,[8])],[0,CL_PerGain(:,[8])])
776 grid on
777 %legend('24^o \alpha: AFC CFD SW3 M_{slot}=0.8731 EX1','24^o \
      alpha: AFC CFD SW3 M_{slot}=0.8731 EX2','24^o \alpha: AFC
      CFD SW3 M_{slot}=0.8731 EX3','24^o \alpha: AFC CFD SW3 M_{
      slot}=0.8731 EX4','24^o \alpha: AFC CFD SW3 M_{slot}=0.8731
```

```
       EX5','24^o \alpha: AFC CFD SW3 M_{slot}=0.8731 EX6','24^o
      \alpha: AFC CFD SW3 M_{slot}=0.8731 EX7','24^o \alpha: AFC
      CFD SW3 M_{slot}=0.8731 EX8','Location','southeast')
778 legend('AFC CFD SW3 M5 EX1 = -0.25 to 0.75 x/c, \alpha = 24^o'
      ,'AFC CFD SW3 M5 EX2 = -0.25 to 1.0 x/c, \alpha = 24^o','
      AFC CFD SW3 M5 EX3 = -0.25 to 0.5 x/c, \alpha = 24^o','AFC
      CFD SW3 M5 EX4 = 0 to 0.75 x/c, \alpha = 24^o','AFC CFD SW3
       M5 EX5 = 0 to 0.5 x/c, \alpha = 24^o','AFC CFD SW3 M5 EX6
      = 0 to 0.25 x/c, \alpha = 24^o','AFC CFD SW3 M5 EX7 = 0 to
      1.0 x/c, \alpha = 24^o','AFC CFD SW3 M5 EX8 = 0.25 to 1.0 x
      /c, \alpha = 24^o','Location','southeast','Interpreter', '
      tex')
779 ylabel('C_L (% Gain)')
780 xlabel('C_\mu (%)')
781 xlim([0 14])
782 ylim([0 40])
783 hold off
784 %
785 % figure ()
786 % hold on
787 % plot(C_mu(:,[1]),CD_PerRed(:,[1]),'ro','LineWidth',0.9)
788 % plot(C_mu(:,[2]),CD_PerRed(:,[2]),'go','LineWidth',0.9)
789 % plot(C_mu(:,[3]),CD_PerRed(:,[3]),'bo','LineWidth',0.9)
790 % plot(C_mu(:,[4]),CD_PerRed(:,[4]),'mo','LineWidth',0.9)
791 % plot(C_mu(:,[5]),CD_PerRed(:,[5]),'o','LineWidth',0.9,'Color
      ',[0.9290 0.6940 0.1250])
792 % plot(C_mu(:,[6]),CD_PerRed(:,[6]),'ko','LineWidth',0.9)
793 % legend('EX1','EX2','EX3','EX4','EX5','EX6','Location','
      southeast')
794 % ylabel('Drag: Percent Reduction')
795 % xlabel('Momentum Coefficient')
796 % hold off
797 %
798 % figure ()
799 % hold on
800 % plot(C_mu(:,[1]),CM_PerRed(:,[1]),'ro','LineWidth',0.9)
801 % plot(C_mu(:,[2]),CM_PerRed(:,[2]),'go','LineWidth',0.9)
802 % plot(C_mu(:,[3]),CM_PerRed(:,[3]),'bo','LineWidth',0.9)
803 % plot(C_mu(:,[4]),CM_PerRed(:,[4]),'mo','LineWidth',0.9)
804 % plot(C_mu(:,[5]),CM_PerRed(:,[5]),'o','LineWidth',0.9,'Color
      ',[0.9290 0.6940 0.1250])
805 % plot(C_mu(:,[6]),CM_PerRed(:,[6]),'ko','LineWidth',0.9)
806 % legend('EX1','EX2','EX3','EX4','EX5','EX6','Location','
      southeast')
807 % ylabel('Pitching Moment: Percent Reduction')
808 % xlabel('Momentum Coefficient')
809 % hold off
810
811
812
813 % figure ()
814 % hold on
815 % %plot(0,CL_PerGain(:,[26]),'ko','LineWidth',2)
816 % % plot(0,CL_PerGain(:,[27]),'ks','Color', [0.25 0.80 0.54],'
      LineWidth',1.7) % BLF WT Gains
817 % %plot(C_mu(:,[1 2 3 4 5]),CL_PerGain(:,[28 29 30 31 32]),'k
      --h','LineWidth',0.9) %AFC WT Percent Gains
818 % plot(C_mu(:,[1 2 4 5]),CL_PerGain(:,[1 2 4 5]),'r--o','
```

```
     LineWidth',0.9)
819  % plot(C_mu(:,[6 8 9 10]),CL_PerGain(:,[6 8 9 10]),'g--v','
     LineWidth',0.9)
820  % plot(C_mu(:,[11 12 14 15]),CL_PerGain(:,[11 12 14 15]),'b
     --^','LineWidth',0.9)
821  % plot(C_mu(:,[16 17 18 19 20]),CL_PerGain(:,[16 17 18 19 20])
     ,'m--s','LineWidth',0.9)
822  % plot(C_mu(:,[21 22 24 25]),CL_PerGain(:,[21 22 24 25]),'--d
     ','LineWidth',0.9,'Color',[0.9290 0.6940 0.1250])
823  % grid on
824  % %legend('24^o \alpha: Baseline CFD','24^o \alpha: BLF CFD
     ','24^o \alpha: AFC WT','24^o \alpha: AFC CFD SW1','24^o \
     alpha: AFC CFD SW2','24^o \alpha: AFC CFD SW3','24^o \alpha
     : AFC CFD SW4','24^o \alpha: AFC CFD SW5','Location','east
     ')
825  % legend('24^o \alpha: AFC CFD SW1','24^o \alpha: AFC CFD SW2
     ','24^o \alpha: AFC CFD SW3','24^o \alpha: AFC CFD SW4
     ','24^o \alpha: AFC CFD SW5','Location','southeast')
826  % ylabel('C_L (% Gain)')
827  % xlabel('C_\mu (%)')
828  % xlim([0 14])
829  % ylim([0 0.4])
830  % hold off
```

Appendix I. MATLAB Script: Optimized AFC Slot Final Comparison

```
%% Final Comparison - Baseline WT, Passive BLF WT, AFC Cmu =12.22% WT, Optimal CFD Config
clear all; close all; clc; format compact; format short;
%% Baseline, Passive BLF and AFC Slot, Freestream M = 0.059, SW1, M1-M5 Wind Tunnel Uncorrected Data
alpha = 1;
Alpha_Baseline2=alpha+...
[-8.17894442052277;-7.16850773849801;-6.15464379090849;...
-5.04877209800816;-4.02932120636633;-3.00640352702020;...
-1.98382443346184;-0.870213403716582;0.153319187693818;...
1.17508365277160;2.19900159794485;3.30928370940170;...
4.32751503348324;5.34186930698045;6.44211101586254;...
7.45523765217682;8.46819102061274;9.56920569459411;...
10.6678210098701;11.6756459136262;12.7671846976348;...
13.7663130389622;14.8512817871214;15.9311893169993;...
17.0110707277628;18.0844673115262;19.1538944819053;...
20.2221014158863;21.3721215112022;22.4257937648188;...
23.5698166553147;24.6991922407033;25.7472428560031;...
26.8830239002552;28.0967117595190;29.2310840568254;...
30.4510280084815;31.6729762552610;32.9017417048610;...
34.2275325071614;35.4596797612262;36.7847709966838];...
CD_Base2=...
[0.0326396226315288;0.0273554591561591;0.02320762912...
52264;0.0184655617641355;0.0156734227994947;0.013931...
8232188933;0.0127460003513771;0.0110429698239139;0.0...
115328779992575;0.0132684007837646;0.01594624739861...
14;0.0186260816468254;0.0227511043823911;0.027425377...
8944443;0.0325465190807324;0.0391042044857320;0.0473...
291339011119;0.0578153893612589;0.0714274594986400;0...
.0882968225391222;0.107396801468250;0.12837527862316...
1;0.152008514898266;0.177050724527485;0.203713593209...
787;0.230608840670329;0.257527050009981;0.2850390953...
55441;0.311662701851170;0.335885212499362;0.35962757...
0078000;0.378102215918811;0.393975988177553;0.4094634...
43267234;0.422979456980625;0.438129375146260;0.452553...
360061481;0.469150907399056;0.488570671603892;0.51410...
4483039872;0.536274210618872;0.565069415967284];
CL_Base2=...
[-0.380686716946657,-0.335679522978898,-0.28809803698...
6591,-0.235205472140068,-0.180638051940071,-0.1234544...
23606297,-0.0655693172981972,-0.00446862170388157,0.0...
533671656873325,0.110388299123664,0.169693355141534,...
0.227263490287654,0.279476897333351,0.32863898256204...
2,0.375560539057904,0.422360052709387,0.4700363760260...
67,0.517777718341523,0.561913793013043,0.604151005786...
968,0.641842476206843,0.673795777863523,0.70451924645...
7192,0.729874924214394,0.754142327869694,0.7725926727...
70825,0.786833165496932,0.798718935717348,0.805103685...
529550,0.802634940849533,0.801598645011175,0.78608838...
7524569,0.776596912840933,0.767880111293073,0.7484587...
51498765,0.737187298271561,0.724400980387816,0.713740...
363550526,0.709249314247855,0.715390882106700,0.71448...
6482896382,0.719886109135885]';
CM_Base2=...
```

```
[-0.00241933648422381;-0.000994749356042714;0.00052513...
8889181397;0.000531995120895268;-0.000127610521605613;...
-0.00112181497128817;-0.00238738588975404;-0.004014823...
77348298;-0.00458591893002119;-0.00447507033838957;-0.0...
0570421624022764;-0.00639759228464273;-0.006060593543...
11681;-0.00452373994614179;-0.00254238263866779;-0.000...
802608455539601;0.000686585846786974;0.0019224715481...
3012;0.00305034068341110;0.00384085470805589;0.0046514...
9185638424;0.00533251814807207;0.00492217834961218;0.0...
0390892393185356;0.00131507381415635;-0.0018753227054...
2222;-0.00563731602852632;-0.0109907490359497;-0.016914...
9235037892;-0.0248236615415000;-0.0317363120696212;-0.0...
393746528162185;-0.0435606742506112;-0.043896906122957...
7;-0.0457089065451211;-0.0471099572765705;-0.04925656335...
62850;-0.0525805261396649;-0.0556579516727002;-0.0595181...
996791140;-0.0641550435894548;-0.0701361258272115];


Alpha_BLF_1=alpha+...
[-8.06594564259070;-7.14241231732519;-6.03905594741620;...
-5.01406378048430;-3.98721923601549;-2.87195351727540;...
-1.85058803650554;-0.831110322743736;0.275151806711067;...
1.29346471552093;2.31597900276951;3.42813304789199;...
4.45108375100950;5.55684707512697;6.57167414343638;...
7.58705903612775;8.69009006482263;9.70504580065541;...
10.7161174843277;11.2642436005670;11.8166774071110;...
12.2766843085277;12.8266085308312;13.3790159996166;...
13.8375751427264;14.3856475805125;14.9354617926899;...
15.3929723623862;15.9414105042531;16.4688861494385;...
16.9094889255359;17.4240418013865;17.9837233404080;...
18.4646453036484;18.9881016785306;19.5209239626320;...
20.0480920643511;20.4921008071506;21.0161537952655;...
21.5513155912465;21.9819661259102;22.4844514540255;...
23.0266031504895;23.4649469590941;23.9788010755111;...
24.4993216153161;24.9404098936923;25.4654301290090;...
25.9851110721517;26.4294113964856;26.9572368515206;...
27.4879036272060;27.9159749086103;28.4552397489093;...
28.9719941570135;29.4032901602970;29.9353877441201;...
30.4579590792370;30.8794429116547;31.4044874140582;...
31.9278672633083;32.3622515736385;32.8915967016012];
 CD_BLF_1=...
 [0.0331859562592513;0.0285589439023825;0.0225065331772370;...
 0.0189468223940387;0.0158403087605802;0.0131311169034887;...
 0.0122527914619488;0.0124686038531358;0.0121007596222725;...
 0.0139941157444537;0.0168024120917713;0.0202655564151916;...
 0.0245968486909978;0.0291105237603469;0.0348275369759939;...
 0.0415565640185381;0.0491966039352059;0.0596374268695133;...
 0.0712235463740903;0.0783859677428014;0.0880240892437888;...
 0.0983355252004903;0.108101954523449;0.118749897647422;...
 0.128576970063239;0.140223144052195;0.152845063683076;...
 0.165098099722719;0.178263738604623;0.190669762413875;...
 0.200917116172463;0.213283639422009;0.230302422336980;...
 0.251856410673102;0.265348318598858;0.280169649171469;...
 0.293079995746426;0.306468524342820;0.316087744265308;...
 0.331153701240424;0.339352993468659;0.343805149187245;...
 0.357367274638073;0.365487071651346;0.371746744842184;...
 0.378965080879246;0.387348160309275;0.396148794017582;...
 0.400919634435716;0.410355844881111;0.418992542285874;...
```

```
0.429377784632715;0.432161428908286;0.445358004857721;...
0.449511061662298;0.454432235165533;0.466615637205070;...
0.473488130419345;0.473825618553497;0.483262801297828;...
0.490134615871489;0.495193519187196;0.506592291154017];
CL_BLF_1=...
[-0.354173691100548,-0.309063999932849,-0.259899691306692,...
-0.201576490582196,-0.140228135605584,-0.0784330946201286,...
-0.0228956859968763,0.0306396081385506,0.0818251136500848,...
0.134125047245865,0.190880848861979,0.249375733204867,...
0.306594385654906,0.357250871754507,0.405853817460111,...
0.455048376575644,0.503867637134175,0.552607044125295,...
0.596166557862589,0.617511770875898,0.642365030513726,...
0.663583807519691,0.685775470178208,0.710600796703577,...
0.730284120516020,0.750511830740319,0.773647392520254,...
0.791158054932682,0.811773620986288,0.811217504491707,...
0.810796219594365,0.796534564440700,0.829074572567749,...
0.871414723998235,0.866595878432624,0.870649689280734,...
0.869767400527153,0.872958391535774,0.867711724905650,...
0.875307331477488,0.864330969244883,0.837270800264997,...
0.851219132828200,0.848402048276708,0.833399307819857,...
0.824406222320952,0.825560420849990,0.821339590367901,...
0.811456051420846,0.816016858774003,0.814771168240697,...
0.817599478203143,0.803887629919240,0.814774241132624,...
0.802847471376179,0.792555675655018,0.796901461921134,...
0.790083394307436,0.769385076296350,0.766250555705866,...
0.760289976252899,0.754334128100513,0.754700161457019]';
CM_BLF_1=...
[-0.00645565729432271;-0.00543366737074639;-0.00497230375830425;...

-0.00626840903527524;-0.00812639164827980;-0.00967798053293440;...

-0.00945309222782101;-0.00865038220961338;-0.00670502210461011;...

-0.00488751112138329;-0.00454480696604581;-0.00481732423437155;...

-0.00548800757156123;-0.00442664971617944;-0.00282825806744191;...

-0.00138620542503159;-0.000204421890390911;...
0.000817753587349030;0.00130240859034837;0.00109615288671430;
0.00046485119455706 1;-0.00149193626706634;-0.00380972808029311;...

-0.00533306500332433;-0.00620595983241655;-0.00759321564382312;...

-0.00870105692850148;-0.0108249745414312;-0.0129892457825265;...

-0.00516853422314401;-0.000189350755310846;-0.00462159855872107;...

-0.0191437591914945;-0.0261932152732147;-0.0251904959472022;...

-0.0378876638882588;-0.0478485428343769;-0.0499899927653833;...

-0.0545965073248441;-0.0540169594750646;-0.0642403701311685;...

-0.0678397210048976;-0.0669126861227226;-0.0711347448349583;...

-0.0673556117123620;-0.0649522888342130;-0.0668780318358190;...

-0.0603695865129550;-0.0637109281367164;-0.0621148519578112;...
```

```
155   -0.0619758111857658;-0.0662567712765227;-0.0668173655521368;...
156   -0.0655033106457927;-0.0660623006320958;-0.0655506777401585;...
157   -0.0645042350127906;-0.0634239194747829;-0.0619745103601840;...
158   -0.0628071667857057;-0.0612590184216668;-0.0608586271989955;...
159   -0.0620809601781004]+0.01;
160
161    Alpha_Slot_800_JD=alpha+...
162  [-8.16532994130786;-7.15071579092200;-6.04244860884083;...
163  -5.02099510922208;-4.00074350475546;-2.89013300970893;...
164  -1.86673672339860;-0.845557601359153;0.262744376454180;...
165  0.815668234712962;1.28098830005780;1.83392968241970;...
166  2.38963009158842;2.85600354947695;3.41124262157922;...
167  3.87728372488066;4.42928798070192;5.44207749788951;...
168  6.54701850023257;7.55851760590759;8.66181167361823;...
169  9.67231113504006;10.6858135558792;11.7945702669411;...
170  12.8095448979892;13.8303756931133;14.9434105377481;...
171  15.9616233762802;16.9770125159476;18.0751112575024;...
172  19.0870816918115;20.1944651800602;21.2080328942639;...
173  22.1973387095223;23.1762140686440;24.2493579805815;...
174  25.2214289083073;26.1923382924692;27.2178579547376;...
175  28.1285669372076;29.1882477121527;30.1384264568971;...
176  31.0873604704253;32.0796152955456;33.0318609966642];...
177  CD_Slot_800_JD=...
178  [-0.00681050693390072;-0.0126543294087441;-0.0182495...
179  693770797;-0.0214166231427484;-0.0251674028323114;-0...
180  .0284813491243448;-0.0295284521703782;-0.0300352983...
181  439126;-0.0297999387101721;-0.0295720385414848;-0.02...
182  82132488021699;-0.0273310852132612;-0.026210383664...
183  1072;-0.0240278454672732;-0.0220435932508557;-0.0190...
184  684670650371;-0.0168993698727356;-0.01216566243845...
185  81;-0.00643704479454368;-0.000469991253904901;0.0068...
186  1634235048144;0.0143941708545328;0.022555795883598...
187  0;0.0335793770283875;0.0439463538650867;0.0560009143...
188  510980;0.0702808537518199;0.0848501778814416;0.10300...
189  2466782877;0.128061227791715;0.152144243602451;0.182...
190  336909797974;0.215148357201335;0.275067267157616;0.3...
191  20558261523750;0.362479685381631;0.396531037918776;...
192  0.429234176477427;0.457465813635064;0.4677768042418...
193  04;0.494369876697358;0.510196123102673;0.52428205263...
194  3874;0.518416110561748;0.533085621458722];
195  CL_Slot_800_JD=...
196  [-0.366247569549657,-0.317870438818895,-0.2634978559...
197  96289,-0.208927669846718,-0.154571608219602,-0.09771...
198  37712223667,-0.0400225453233562,0.0153172162849387,...
199  0.0686661296398034,0.0950996977124353,0.1208928993...
200  96894,0.147345053057996,0.175662782841257,0.2025731...
201  84086938,0.231462205167657,0.258020120152550,0.2834...
202  78382821840,0.328859784193542,0.379704711000120,0.4...
203  24778109798272,0.473876342402648,0.517889545618680...
204  ,0.564027033267523,0.618918797249851,0.667678243993...
205  874,0.722648579523156,0.782077615939359,0.833210844...
206  835199,0.882409908178346,0.925998118771882,0.971571...
207  395935769,1.02500675704765,1.07121349306802,1.09274...
```

```
928998711,1.10322282802753,1.12034462316562,1.12360...
156582039,1.12456603399776,1.09117884162421,1.02935...
696942839,1.03220012662585,1.01223881378076,0.98989...
6799890378,0.921229823462180,0.903460668486540]';
CM_Slot_800_JD=...
[-0.00271428206765456;-0.00189706750827400;-0.001585...
10093408801;-0.00257006623435670;-0.003639827594117...
15;-0.00377285117644621;-0.00528002084311486;-0.0060...
4783914821188;-0.00542639016919631;-0.0048547859236...
7664;-0.00467522918668672;-0.00464200994639661;-0.00...
484881943788308;-0.00517612644732052;-0.00576129489...
607823;-0.00558567933442236;-0.00544667475420462;-0....
00388856835124193;-0.00257735756993069;-0.001209129...
76751777;0.000188843218942158;0.00126966991609235;0...
.00194730019213918;0.00226867902786383;0.0020075243...
3835763;-0.00655633847238418;-0.0191938207372223;-0.0...
288876484116350;-0.0402225780133489;-0.0509736602055...
526;-0.0593875338193712;-0.0673592849128238;-0.074871...
3020188131;-0.0814793195538752;-0.0864569567583774;-0...
.0922018627535162;-0.0947708467128809;-0.09736442547...
76938;-0.0959300891773638;-0.0898902740886361;-0.0917...
042960490281;-0.0905853919434668;-0.089976876926054...
0;-0.0848269056017114;-0.0859492228960141];

Alpha_Slot_1000_JD=alpha+...
[-8.19296176515518;-7.17933574587292;-6.07141593961330;...
-5.05068766637736;-4.01478390175705;-2.90376884270189;...
-1.88070289398938;-0.858610138673839;0.251892829170128;...
0.805045079373169;1.27096880298182;1.82550033419823;...
2.29328670403366;2.84752853218911;3.40257829519855;...
3.86968238230243;4.42287620882581;5.43862308343971;...
6.54573182715474;7.55713986284914;8.66098722550410;...
9.67236449623901;10.6852903591628;11.7936837267243;...
12.8112788281600;13.8329825727792;14.9471087553110;1...
5.9664578225023;16.9791398538928;18.0817616704432;...
19.0886948118036;20.1847033352771;21.2029090750168;...
22.2183661266420;23.2279674798223;24.3299915044846;...
25.3283955867359;26.3157875287581;27.3957186622302;...
28.3760532549829;29.4314555943111;30.3576518649962;...
31.2810950601421;32.2836331725416;33.2135410784349];
CD_Slot_1000_JD=...
[-0.0193797893655357;-0.0259114877416335;-0.03258667...
37823424;-0.0372877316448054;-0.0409895595179842;-0.0...
451211540031038;-0.0465323825799716;-0.046985848615...
9102;-0.0470235007266426;-0.0471019968699758;-0.04558...
46122476344;-0.0447892744155420;-0.0432186377043500;...
-0.0416831615990399;-0.0400375162366334;-0.037384285...
6392081;-0.0350786936687696;-0.0303777956122959;-0.02...
17416728583107;-0.0157560312384841;-0.00811648099009...
559;-0.00058239743768767 2;0.00780414749527014;0.0186...
951181907445;0.0294869235072628;0.0417640755961384;...
0.0566192455906378;0.0718139381421382;0.08864026042...
94024;0.109696609944029;0.131368096438492;0.15524846...
0024663;0.184343329546123;0.215847194077492;0.248784...
760521435;0.293162365698196;0.352499161384842;0.4063...
87379826736;0.458282454622353;0.500207681789809;0.54...
2355888075449;0.570273045623037;0.586548858269573;...
0.595084080898688;0.601632791661711];
```

```
CL_Slot_1000_JD=...
[-0.395553132478767,-0.348223986795931,-0.29421982134...
7971,-0.240418790630072,-0.169462472469212,-0.1121755...
65857211,-0.0548346870548746,0.00147404922605309,0.05...
71572729111181,0.0838330672852779,0.110266492551626,...
0.138405114959061,0.166814012293967,0.19358481061487...
2,0.222273055606256,0.249958342381286,0.2766782314731...
33,0.325196125920342,0.378340100431535,0.423316912878...
281,0.473001955093872,0.517946139059006,0.56347214502...
0504,0.617978556741035,0.669517203304557,0.7254133653...
91840,0.785999845181785,0.838338127376218,0.884666105...
104343,0.933051366361309,0.973282227247636,1.01465360...
923606,1.06577930934517,1.11505039826875,1.1581110922...
4280,1.20586235163683,1.23704752376115,1.255492945757...
42,1.27981308396896,1.29183424562026,1.29013981004425...
1.24474333567583,1.19536645118314,1.13760565033506,1.0...
9614563559966]';
CM_Slot_1000_JD=...
[0.00507017714348937;0.00614418826676139;0.006842971...
85030537;0.00699513112022954;0.00437741572681731;0.0...
0282945856269266;0.00113340818135327;0.000333189608...
933874;0.000586231571137447;0.000924799225952278;0.0...
00824185731205280;0.000767407000762050;0.0003493200...
57341334;-0.000162324801487116;-0.00074296932765326...
5;-0.00125212658580521;-0.00147376228469160;-0.001264...
98499510802;0.00179972763032268;0.00314076315957652...
;0.00435342405830659;0.00526227344420236;0.006221210...
03062758;0.00675959969365219;0.00639421820758831;-0....
00220469951161398;-0.0136034339227159;-0.0230183035...
253696;-0.0325897625335028;-0.0410750732024380;-0.046...
7011262564439;-0.0522773449139122;-0.05960919917759...
88;-0.0671714951745267;-0.0740194214401699;-0.0823273...
039146220;-0.0909191500060944;-0.0970089485628756;...
-0.103913781913880;-0.108509186502984;-0.11207993050...
2852;-0.109408392847778;-0.105477991507032;-0.101058...
260651483;-0.0975542197429547];

%% Import Kestrel Data
AoA = [0 10 14 16 18 20 22 24 26 28 30 32];

[AoA_0] = importdata('0_forces.dat',' ',23);
[AoA_10] = importdata('10_forces.dat',' ',23);
[AoA_14] = importdata('14_forces.dat',' ',23);
[AoA_16] = importdata('16_forces.dat',' ',23);
[AoA_18] = importdata('18_forces.dat',' ',23);
[AoA_20] = importdata('20_forces.dat',' ',23);
[AoA_22] = importdata('22_forces.dat',' ',23);
[AoA_24] = importdata('24_forces.dat',' ',23);
[AoA_26] = importdata('26_forces.dat',' ',23);
[AoA_28] = importdata('28_forces.dat',' ',23);
[AoA_30] = importdata('30_forces.dat',' ',23);
[AoA_32] = importdata('32_forces.dat',' ',23);

Opt_Config = {AoA_0, AoA_10, AoA_14, AoA_16, AoA_18, AoA_20,
    AoA_22, AoA_24, AoA_26, AoA_28, AoA_30, AoA_32};
%% Axial Forces
Iter = 1000; %Number of iterations to average over
k = 0;
```

```
for i = 1:length(Opt_Config)
    I = Opt_Config{i};
    k=k+1;
    fx_I = mean(I.data(([length(I.data)-Iter:end]),33)); % Time Avg at 33
    fx(:,k) = fx_I;
end
fx_3_check = mean(AoA_14.data(([length(AoA_14.data)-Iter:end]),33));

%% Vertical Forces
k = 0;
for j = 1:length(Opt_Config)
    J = Opt_Config{j};
    k=k+1;
    fy_J = mean(J.data(([length(J.data)-Iter:end]),34)); % Time Avg at 34
    fy(:,k) = fy_J;
end
fy_3_Check = mean(AoA_14.data(([length(AoA_14.data)-Iter:end]),34));

%% Moment about the z-axis
x_cor = -1.28; % Correction for incorrect location of Moment Reference point in CFD Settings
k = 0;
for e = 1:length(Opt_Config)
    E = Opt_Config{e};
    k=k+1;
    Mz_E = mean(E.data(([length(E.data)-Iter:end]),38))/x_cor; % Time Avg at 38
    Mz(:,k) = Mz_E;
end
 Mz_3_Check = mean(AoA_14.data(([length(AoA_14.data)-Iter:end]),38))/x_cor;

%% Lift
k = 0;
for p = 1:length(Opt_Config)
    FX_L = fx(p);
    FY_L = fy(p);
    AoA_L = AoA(p);
    k=k+1;
    L_P = FY_L*cosd(AoA_L)-FX_L*sind(AoA_L);
    L(:,k) = L_P;
end
L_3_Check = fy(:,3)*cosd(AoA(3))-fx(:,3)*sind(AoA(3));

%% Drag
k = 0;
for q = 1:length(Opt_Config)
    FX_D = fx(q);
    FY_D = fy(q);
    AoA_D = AoA(q);
    k=k+1;
    D_P = FX_D*cosd(AoA_D)+FY_D*sind(AoA_D);
    D(:,k) = D_P;
end
```

```
374 D_3_Check = fx(:,3)*cosd(AoA(3))+fy(:,3)*sind(AoA(3));
375
376 %% Pitching Moment
377 x_cm = 1.3; % in - Estimated distance from Aero Center
378 MomRef_L = 1; % in - NA
379 % PM_0 =  (Mz_0/MomRef_L)-(L_0*cosd(0)*x_cm)+(D_0*-sind(0)*
       x_cm);
380 k = 0;
381 for z = 1:length(Opt_Config)
382     L_PM = L(z);
383     D_PM = D(z);
384     Mz_PM = Mz(z);
385     AoA_PM = AoA(z);
386     k=k+1;
387     PM_Z = (Mz_PM/MomRef_L)-(L_PM*cosd(AoA_PM)*x_cm)+(D_PM*-
          sind(AoA_PM)*x_cm);
388     PM(:,k) = PM_Z;
389 end
390 PM_3_Check = (Mz(:,3)/MomRef_L)-(L(:,3)*cosd(AoA(3))*x_cm)+(D
       (:,3)*-sind(AoA(3))*x_cm);
391
392 %% Coeffiecient of Lift
393 k = 0;
394 for v = 1:length(Opt_Config)
395     L_CL = L(v);
396     k=k+1;
397     CL_V = (L_CL*2)/(0.67764*0.0009518*((3751.5/12)^2));
398     CL(:,k) = CL_V;
399 end
400 CL_3_Check = (L(:,3)*2)/(0.67764*0.0009518*((3751.5/12)^2));
401
402 %% Coeffiecient of Drag
403 % CD_0 =(D_0*2)/(0.67764*0.0009518*((3751.5/12)^2));
404 k = 0;
405 for w = 1:length(Opt_Config)
406     D_CD = D(w);
407     k=k+1;
408     CD_W = (D_CD*2)/(0.67764*0.0009518*((3751.5/12)^2));
409     CD(:,k) = CD_W;
410 end
411 CD_3_Check = (D(:,3)*2)/(0.67764*0.0009518*((3751.5/12)^2));
412
413 %% Moment Coeffiecient
414 c_bar = 9.66;
415 % CM_0 =(PM_0*2)/(0.67764*0.0009518*((3751.5/12)^2)*c_bar);
416 k = 0;
417 for x = 1:length(Opt_Config)
418     PM_CM = PM(x);
419     k=k+1;
420     CM_X = (PM_CM*2)/(0.67764*0.0009518*((3751.5/12)^2)*c_bar)
          ;
421     CM(:,k) = CM_X;
422 end
423 CM_3_Check =(PM(:,3)*2)/(0.67764*0.0009518*((3751.5/12)^2)*
       c_bar);
424
425 %% CD, CL, CM vs Alpha Plots
426 figure(1)
```

```
427 hold on
428 plot(Alpha_Baseline2,CD_Base2, 'k',  'LineWidth',0.9)
429 plot(Alpha_BLF_1,CD_BLF_1,'Color', [0.25 0.80 0.54],  '
       LineWidth',0.9)
430 plot(Alpha_Slot_800_JD,CD_Slot_800_JD, 'm',  'LineWidth',0.9)
431 plot(Alpha_Slot_1000_JD,CD_Slot_1000_JD,  'LineWidth',0.9)
432 plot(AoA,CD,'b--o','LineWidth',0.9)
433 colororder([0.9290 0.6940 0.1250]) % Marker with no color
       assigned is Orange
434 grid on
435 xlabel('\alpha (deg)')
436 ylabel('C_D (-)')
437 xlim([0 32])
438 ylim([-0.06 0.6])
439 hold off
440 legend('Baseline WT','BLF WT','AFC Slot WT, C\mu=7.82%','AFC
       Slot WT, C\mu=12.22%','AFC Slot CFD Opt Config C\mu=7.33','
       Location','northwest')
441
442
443 figure(2)
444 hold on
445 plot(Alpha_Baseline2,CL_Base2, 'k',  'LineWidth',0.9)
446 plot(Alpha_BLF_1,CL_BLF_1,'Color', [0.25 0.80 0.54],  '
       LineWidth',0.9)
447 plot(Alpha_Slot_800_JD,CL_Slot_800_JD, 'm',  'LineWidth',0.9)
448 plot(Alpha_Slot_1000_JD,CL_Slot_1000_JD,  'LineWidth',0.9)
449 plot(AoA,CL,'b--o','LineWidth',0.9)
450 colororder([0.9290 0.6940 0.1250]) % Marker with no color
       assigned is Orange
451 grid on
452 xlabel('\alpha (deg)')
453 ylabel('C_L (-)')
454 xlim([0 32])
455 ylim([0 1.4])
456 hold off
457 legend('Baseline WT','BLF WT','AFC Slot WT, C\mu=7.82%','AFC
       Slot WT, C\mu=12.22%','AFC Slot CFD Opt Config C\mu=7.33','
       Location','northwest')
458
459 figure(3)
460 hold on
461 plot(Alpha_Baseline2,CM_Base2, 'k',  'LineWidth',0.9)
462 plot(Alpha_BLF_1,CM_BLF_1,'Color', [0.25 0.80 0.54], '
       LineWidth',0.9)
463 plot(Alpha_Slot_800_JD,CM_Slot_800_JD, 'm',  'LineWidth',0.9)
464 plot(Alpha_Slot_1000_JD,CM_Slot_1000_JD,  'LineWidth',0.9)
465 plot(AoA,CM,'b--o','LineWidth',0.9)
466 colororder([0.9290 0.6940 0.1250]) % Marker with no color
       assigned is Orange
467 grid on
468 xlabel('\alpha (deg)')
469 ylabel('C_M (-)')
470 xlim([0 32])
471 % ylim([0 1.4])
472 hold off
473 legend('Baseline WT','BLF WT','AFC Slot WT, C\mu=7.82%','AFC
       Slot WT, C\mu=12.22%','AFC Slot CFD Opt Config C\mu=7.33','
```

```
    Location','southwest')

%% CL vs CD

figure(4)
hold on
plot(CD_Base2,CL_Base2, 'k',  'LineWidth',0.9)
plot(CD_BLF_1,CL_BLF_1, 'Color', [0.25 0.80 0.54], 'LineWidth'
    ,0.9)
plot(CD_Slot_800_JD,CL_Slot_800_JD,  'm',  'LineWidth',0.9)
plot(CD_Slot_1000_JD,CL_Slot_1000_JD,   'LineWidth',0.9)
plot(CD,CL, 'b--o','LineWidth',0.9)
colororder([0.9290 0.6940 0.1250]) % Marker with no color
    assigned is Orange
grid on
xlabel('C_D (-)')
ylabel('C_L (-)')
xlim([-0.05 0.51])
ylim([0 1.4])
hold off
legend('Baseline WT','BLF WT','AFC Slot WT, C\mu=7.82%','AFC
    Slot WT, C\mu=12.22%','AFC Slot CFD Opt Config C\mu=7.33','
    Location','southeast')
L_D_max = max(L./D);
```

Bibliography

1. R. J. Salmi, "Low-Speed Longitudinal Characteristics of a 45 degree Sweptback Wing of Aspect Ratio 8 with High-Lift and Stall-Control Devices at Reynolds Numbers from 1,500,000 to 4,800,000," *National Advisory Committee for Aeronautics*, vol. RM L51J04, 1952.

2. R. Seele, E. Graff, J. Lin, and I. Wygnanski, "Performance enhancement of a vertical tail model with sweeping jet actuators," *51st AIAA Aerospace Sciences Meeting including the New Horizons Forum and Aerospace Exposition 2013*, no. January, pp. 1–19, 2013.

3. M. M. Walker, K. Hipp, S. I. Benton, and J. P. Bons, "Control of Post Stall Airfoil Using Leading-Edge Pulsed Jets," *AIAA Journal*, vol. 55, pp. 365–376, 2017.

4. M. Walker and J. P. Bons, "The Effect of Passive and Active Boundary-Layer Fences on Swept-Wing Performance at Low Reynolds Number," in *2018 AIAA Aerospace Sciences Meeting*, 2018.

5. D. McDaniel, R. Nichols, and S. Morton, "Capabilities and Challenges in CFD: A Perspective from the DoD HPCMP Create-AV Kestrel Development Team," *23rd AIAA Computational Fluid Dynamics Conference, AIAA AVIATION Forum*, no. AIAA 2017-3789, 2017.

6. D. Stookesberry and R. Narducci, "An Industry Assessment of HPCMP CREATE-AV Kestrel," *53rd AIAA Aerospace Sciences Meeting, AIAA SciTech Forum*, no. SPR-2014-1146, 2014.

7. J. Winslow, H. Otsuka, B. Govindarajan, and I. Chopra, "Basic understanding of airfoil characteristics at low Reynolds numbers (104–105)," *Journal of Aircraft*, vol. 55, no. 3, pp. 1050–1061, 2018.

8. M. A. McVeigh and E. Kisielowski, "A Design Summary of Stall Characteristics of Straight Wing Aircraft," *NASA Contractor Report*, vol. 1648.

9. M. M. Walker, "Replicating the Effects of a Passive Boundary-Layer Fence via Active Flow Control," PhD Dissertation, The Ohio State University, 2018.

10. A. Busemann, "Aerodynamisher Aufrieb bei Uberschallgeschwindigkeit," *5th Volta Conference*, Rome, Italy, 1935.

11. P. Tewes, L. Taubert, and I. Wygnanski, "On the effect of sweep on separation control," *AIAA AVIATION 2014 -7th AIAA Flow Control Conference*, no. June, pp. 1–18, 2014.

12. E. C. Polhamus, "Sharp-Edge Delta Wings Based O N a Leading-Edge-Suction Analogy," *NATIONAL AERONAUTICS AND SPACE ADMINISTRATION For*, p. 18, 1966.

13. W. Shyy and H. Liu, "Flapping Wings and Aerodynamic Lift: The Role of Leading-Edge Vortices," *AIAA Journal*, vol. 45, no. 12, pp. 2817–2819, 2007.

14. I. Hamizi and S. Khan, "Cfd letters aerodynamics investigation of delta wing at low reynold's number," *CFD Letters*, vol. 11, pp. 32–41, 01 2019.

15. J. Jones, "Properties of low-aspect-ratio pointed wings at speeds below and above the speed of sound," *The Aeronautical Journal*, no. NACA Report No. 835, 1945.

16. C. P. Ellington, C. van den Berg, A. P. Willmott, and A. L. R. Thomas, "Leading-edge vortices in insect flight," *Nature*, vol. 384, no. 6610, pp. 626–630, 1996. [Online]. Available: https://doi.org/10.1038/384626a0

17. C. W. Smith, J. N. Ralston, and H. W. Mann, "Aerodynamic Characteristics of Forebody and Nose Strakes Based on F-16 Wind Tunnel Test Experience." *NASA Contractor Reports*, vol. 1, no. 3053, 1979.

18. K. Nickel and M. Wohlfahrt, *Tailless Aircraft*. New York, NY: AIAA, first edition, 1994.

19. D. A. Solfelt, M. D. Williams, M. F. Reeder, and R. C. Maple, "Model, Simulation and Flight Tests for a T-38 Talon with Wing Fences," *Journal of Aircraft*, vol. 47, p. 72, 2010.

20. G. L. Pratt and E. R. Shields, "Low Speed Longitudinal Characteristics of a 45 Degrees Swept Back Wing of Aspect Ratio 8," *NACA Research Memorandum*, vol. NACA-RM-L51J04, pp. 1–32, 1952.

21. L. Egenburg and A. Saweljew, ""Das G im Wörtchen "MiG": Michail Josifowitsch Gurjewitsch"." *Fliegerrevue*, vol. 1, 1993.

22. A. C. Demoret, "The Effect of Passive and Active Boundary-Layer Fences on Delta Wing performance at Low Reynolds Number," Thesis, Air Force Institute of Technology, 2019.

23. D. Greenblatt and A. E. Washburn, "Influence of finite span and sweep on active flow control efficacy," *AIAA Journal*, vol. 46, no. 7, pp. 1675–1694, 2008.

24. A. Seifert, A. Darabi, and I. Wygnanski, "Delay of Airfoil Stall by Periodic Excitation," *Journal of Aircraft*, vol. 335, no. 4, pp. 691–698, 1996.

25. L. G. Pack and A. Seifert, "Effects of sweep on the dynamics of active separation control," *Aeronautical Journal*, vol. 107, no. 1076, pp. 617–629, 2003.

26. T. Naveh, A. Seifert, A. Tumin, and I. Wygnanski, "Sweep effect on parameters governing control of separation by periodic excitation," *Journal of Aircraft*, vol. 35, no. 3, pp. 510–512, 1998.

27. M. F. Marzanek, "Separated Flows Over Non-slender Delta Wings," Thesis, Queen's University, Kingston, Ontario, Canada, 2019.

28. J. Luckring, "The discovery and prediction of vortex flow aerodynamics," *The Aeronautical Journal*, vol. 123, no. 1264, p. 729–804, 2019.

29. D. A. Solfelt, "CFD Analysis of a T-38 Wing Fence," *Air Force Institute of Technology Thesis*, Jun. 2007.

30. M. D. Williams, M. F. Reeder, R. C. Maple, and D. A. Solfelt, "Modeling, Simulation, and Flight Tests for a T-38 Talon with Wing Fences," *AIAA Journal of Aircraft*, vol. 47, no. 2, Mar. 2010.

31. R. M. Cummings, W. H. Mason, S. A. Morton, and D. R. McDaniel, *Applied Computational Aerodynamics: A Modern Engineering Approach.* Cambridge Uni- versity Press, Cambridge, United Kingdom, 2015.

32. J. Despirito, "CFD Aerodynamic Characterization of 155-mm Projectile at High Angles-of-Attack," *35th AIAA Applies Aerodynamics Conference, AIAA AVIATION Forum*, no. AIAA 2017-3397, 2017.

33. C. Liu and C. Hu, "Block-based adaptive mesh refinement for fluid–structure interactions in incompressible flows," *Computer Physics Communications*, vol. 232, pp. 104–123, 2018.

34. CREATE-AV, "HPCMP CREATE Kestrel User's Guide," 2020.

35. P. R. Spalart and S. R. Allmaras, "A One Equation Turbulence Model for Aerodynamic Flows," *AIAA Journal*, no. AIAA 92-0439, 1992.

36. M. L. Shur, P. R. Spalart, M. K. Strelets, and A. K. Travin, "A Hybrid RANS-LES Approach with Delayed-DES and Wall-Modeled LES Capabilities," *International Journal of Heat and Fluid Flow*, vol. 29, no. 6, pp. 1638–1649, 2008.

37. P. R. Spalart, *YOUNG-PERSON'S GUIDE TO DETACHED-EDDY SIMULATION GRIDS*. Tech. rep., Hampton, VA, 2001.

38. J. D. Anderson, *Fundamentals of Aerodynamics*, 5th ed. Boston: McGraw-Hill, 2010.

39. C. C. Critzos, H. H. Heyson, and R. W. Boswinkle, "Aerodynamic Characteristics of NACA 0012 Airfoil Section at Angles of Attack from $0°to180°."$ $LangleyField, VA$: $LangleyAeronauticalLaboratory, NACA - TN - 3361, 1955.$

40. *Pointwise Tutorial Workbook*. ANSYS, Inc., Canonsburg, PA, 2016.

41. D. Prosser, J. Forsythe, J. Laiosa, J. Lynch, C. Aallen, and T. Tully, *Kestrel CREATE Community Forum*. https://forum.create.hpc.mil/viewforum.php?f=26.

42. *DoD High Performance Computing Modernization Program, HPC Unclassified Systems, ONYX*. https://centers.hpc.mil/systems/unclassified.htmlOnyx.

REPORT DOCUMENTATION PAGE

Form Approved
OMB No. 0704–0188

1. REPORT DATE *(DD–MM–YYYY)*	2. REPORT TYPE	3. DATES COVERED *(From — To)*
25-03-2021	Master's Thesis	Sept 2019 - Mar 2021

4. TITLE AND SUBTITLE

Optimizing Design Parameters for Active Flow Control Boundary-Layer Fence Performance Enhancement on a Delta Wing

5a. CONTRACT NUMBER

5b. GRANT NUMBER

5c. PROGRAM ELEMENT NUMBER

6. AUTHOR(S)

Tedder, Nathan L., 1st Lt, USAF

5d. PROJECT NUMBER

5e. TASK NUMBER

5f. WORK UNIT NUMBER

7. PERFORMING ORGANIZATION NAME(S) AND ADDRESS(ES)

Air Force Institute of Technology
Graduate School of Engineering an Management (AFIT/EN)
2950 Hobson Way
WPAFB OH 45433-7765

8. PERFORMING ORGANIZATION REPORT NUMBER

AFIT-ENY-MS-21-M-322

9. SPONSORING / MONITORING AGENCY NAME(S) AND ADDRESS(ES)

Joint Aircraft Survivability Program Office

10. SPONSOR/MONITOR'S ACRONYM(S)

JASPO

11. SPONSOR/MONITOR'S REPORT NUMBER(S)

12. DISTRIBUTION / AVAILABILITY STATEMENT

DISTRIBUTION STATEMENT A:
APPROVED FOR PUBLIC RELEASE; DISTRIBUTION UNLIMITED.

13. SUPPLEMENTARY NOTES

14. ABSTRACT

Utilizing CFD simulations, the study progressed the investigation of replicating and improving upon the performance of a NACA 0012 cropped delta-wing at high angles-of-attack with an AFC fluidic fence via wall-normal, steady blowing from an optimized single chordwise slot. Data was generated using CREATE-AV Kestrel CFD software on the DoD HPC systems. The flight regime was constant at Mach 1.18 with a Re of 5.0x10^5, based on the c_{root}, using angles-of-attack ranging from 0° to 30°. Experimental and CFD performance results of three configurations (baseline, passive BLF and AFC slot) were compared to validate the CFD models. Computational optimization of the AFC slot parameters (slot width, length, and jet velocity) utilized peak performance gains to justify slot enhancement. Surface flow visualization assessed the unique flow features that contribute to spanwise flow reduction and performance gains. The use of AFC techniques to replicate and improve passive flow control methods provides a solution for flow separation leading to wing stall and undesirable delta-wing moment characteristics.

15. SUBJECT TERMS

active flow control (AFC), boundary layer fence (BLF) computational fluid dynamics (CFD), Computational Research and Engineering for Acquisition Tools and Environments-Air Vehicles (CREATE-AV), High Performance Computing (HPC), National Advisory Committee for Aeronautics (NACA), Reynolds Number (Re)

16. SECURITY CLASSIFICATION OF:			17. LIMITATION OF ABSTRACT	18. NUMBER OF PAGES	19a. NAME OF RESPONSIBLE PERSON
a. REPORT	b. ABSTRACT	c. THIS PAGE			LtCol Michael Walker, AFIT/ENY
U	U	U	UU	179	19b. TELEPHONE NUMBER *(include area code)* (312) 785-6565 x4745; Michael.Walker@afit.edu